UCL SCHOOL OF PHARMACY
BRUNSWICK SQUARE

Development of SLA 3D printed drug eluting medical implants for local cancer treatment

Ben Bowles

Supervisor: Dr Stephen Hilton

2019

This research project is submitted in part fulfilment of the requirements for the PhD degree, UCL School of Pharmacy Department of Pharmaceutical and Biological Chemistry

Abstract

The current dogma of drug formulation technology places heavy focus upon the use of systemic oral or intravenous routes, for the delivery of a medicine to a target tissue. An inherent problem with this approach is the requirement of a high dosing regimen to ensure that the drug reaches the site of interest for optimal therapeutic effect. However, this can lead to the prevalence of 'off-target' effects and poor compliance. In the case of cancer, the 'off-target' effects of cytotoxic chemotherapeutics can cause greater harm than benefit to the patient. The aim of this project is to develop a medical implant that obviates the requirement of systemic dosing by providing a method of local drug release to the target area. Through utilisation of SLA 3D printing, we aim to develop and produce a drug eluting device that provides unidirectional release of patient-specific payloads at pre-determined pharmacokinetic rates. However, before a specific focus could be placed on cancer, three major problems associated with SLA 3D printing pharmaceutics had to be solved. Firstly, SLA 3D printed materials have unsuitable physical properties for medical device applications. Secondly, photopolymer systems based on (meth)acrylate photopolymer systems are associate with toxicity and hence have limited use as pharmaceutics. Finally, commercial SLA 3D printers do not support the use of custom photopolymer systems. Solving each of these problems would provide solid groundwork for the development of SLA 3D printed drug eluting implants for local chemotherapy. To solve the issue of poor mechanical properties, a range of current and novel photopolymers were synthesised, characterised and compared against one another and reference materials. To solve the issue of material toxicity, different post-processing procedures were explored and utilised in attempt to render SLA 3D printed materials as biocompatible. Finally, an RT-FTIR spectroscopy tool was developed to bridge the gap between unprintable and printable photopolymer systems. Furthermore, extensive drug release studies were conducted with aim to characterise effect of different SLA 3D printed materials on drug release kinetics.

Impact statement

This present thesis pertains to the development of drug eluting implants, with applications in cancer therapy, using SLA 3D printing. Specifically, these devices are intended as an adjuvant therapy in combination with surgical removal or reduction of solid tumours. These devices would be placed in resection cavities post-surgery and would provide local release of cancer drugs with aim to eliminate residual cancer cells, and ultimately, prevent relapse. Current failings of pre-formed drug eluting implants for this application, are that they do not provide appropriate contact with resection cavity tissues, due to poor design, and hence drug penetration into tissues is suboptimal. The use of SLA 3D printing can overcome this problem, allowing for design of implants that have good surface contact with resection cavity tissues.

A number of different (meth)acrylate-functionalised monomers and macromers with different material and physical properties were developed and prepared, broadening the library of existing photocurable materials available for SLA 3D printing. Polyurethane dimethacrylate-based materials were identified as exceptional photopolymer systems, displaying superior mechanical properties to other existing and commercial materials. It is expected polyurethane dimethacrylate-based materials will facilitate the expansion of SLA 3D printing into a range of different applications, healthcare and other, attributed to overcoming poor mechanical properties that previously limited the applications of SLA 3D printable materials.

A method for rendering SLA 3D printed materials biocompatible (in the short-term) was also described. This allows for SLA 3D printed materials to be considered as potential options for medical devices, or for other applications where short-term biocompatible is essential.

A RT-FTIR spectroscopy-based tool is herein highlighted, effectively “bridging the gap” in the development timeline between monomer/macromer to 3D printable photopolymer formulation. This tool is shown to accurately predict

required additive contents for a certain monomer/macromer mixture to enable its successful 3D printing. Furthermore, this method is expected to allow optimisation of custom materials for any commercial SLA 3D printer, as long as an exemplar reference material is provided for that printer.

Finally, the drug release potential of a range of photocurable material formulations were detailed. These findings provide the foundations to the development of a photocurable material library, in which properties such as drug release kinetics for a range of different drugs and conditions are known and state. This would facilitate the future construction of sophisticated drug eluting devices with programmable drug release kinetics.

In April 2020, I provided consultancy for Scott Bader, a synthetic resin and composite materials company, who wished to enter the 3D printing field. The project involved reformulation of Scott Bader synthetic resins to yield materials that would be printable on Formlabs Form 2 SLA 3D printers. Printable resins were then used to fabricate a range of ventilator valves, with intention to provide and replenish NHS personal protective equipment (PPE) stock, in aid of the coronavirus pandemic. 3D printed ventilator valves are currently awaiting MHRA approval.

Acknowledgements

I would like to thank my supervisor Dr. Stephen Hilton who has guided me and taught me throughout this PhD and allowed me to reach my true potential by giving me the freedom to try out my own research ideas and supporting them.

I would like to thank my colleagues, current and old, Bruno, Alessandra, Zenobia, Zaid, Zi, Queenie, Rumintha and Marpin for all the fun times and help and support in the laboratory.

A special thanks to Dr Matthew Penny and Dr Ash Ishaq, who were always at hand to offer support and guidance to myself.

I would like to thank all the staff of the School of Pharmacy, especially Dr. Colin James for his assistance with using the NMR facility.

I would like to thank Dr Mehran Moazen at UCL for allowing me free access to his nanoindentation instrument, and Dr Arsalan Marghoub, also at UCL, who spent many hours operating the instrument so that I could get my results.

I would also like to thank Prof Julien Gautrot and Dr Khai Duong Quang Nguyen at Queen Mary University of London who allowed me access and taught me how to operate their photorheometer.

To my mum, grandparents and my sister, all of whom have supported me throughout my life. This PhD would not have been possible without you and I thank you for being my family.

Finally, to my wife Saniya, thank you for always being patient with me, for picking me up when I felt overwhelmed, and for always listening to me, regardless of whether I was making any sense or not!

Plagiarism Statement

I, Ben Jack BOWLES, hereby confirm that the work submitted in the thesis is my own. Any ideas submitted in this thesis are my own. Any ideas, quotations, and paraphrasing from other people's work and publications have been appropriately referenced. I have not violated the School of Pharmacy's policy on plagiarism.

Signature ..... Date .....

Abbreviations

°C	Degree Celsius
AJP	Aerosol jet printing
3DP	3D powder binding
APIs	Active pharmaceutical ingredients
BPAE	Bisphenol A ethoxylate
br	Broad
CAT	Computer axial tomography
CAD	Computer aided design
CTA	Chain transfer reagents
d	Doublet
DA	Diacrylate
DALY	Disability-adjusted life years
DBC	Double bond conversion
DBU	1,8-Diazabicyclo(5.4.0)undec-7-ene
DBTDL	Dibutyltin dilaurate
DCM	Dichloromethane
DLP	Digital light processing
DMA	Dimethacrylate
DMF	*N,N*-Dimethylformamide
DMSO	Dimethylsulfoxide
FFF	Fused filament fabrication
FTIR	Fourier transform infrared spectroscopy
h	Hours
HEMA	2-Hydroxyethyl methacrylate
HPLC	High Performance Liquid Chromatography
IBOA	Isobornyl acrylate
IJL	Inkjet-based lithography
IPDI	Isophorone diisocyanate
IPN	Interpenetrating network
IR	Infrared Spectroscopy
J	Joules
LED	Light emitting diode

M	Molar
m	Multiplet
MEHQ	4-methoxyphenol
mg	Milligrams
MHz	Mega Hertz
mL	Millilitre
mmol	Millimoles
MRI	Magnetic resonance imaging
MW	Molecular weight
N	Newtons
NMR	Nuclear magnetic resonance
Pa	Pascal
PCL	poly(caprolactone)
PEG	poly(ethylene glycol)
PGA	poly(glycolic acid)
Ph	Phenyl
PLA	poly(lactic acid)
PLGA	poly(lactic-co-glycolic acid)
ppm	Parts per million
PU	Polyurethane
q	Quartet
QALY	Quality adjusted life years
quin	Quintet
r.t.	Room temperature
s	Singlet
SLA	Stereolithography
SLS	Selective laser sintering
SO	Stannous octoate
t	Tertiary
t	Triplet
THF	Tetrahydrofuran
TMPTA	Trimethylolpropane triacrylate
TPO	Diphenyl(2,4,6-trimethylbenzoyl)phosphine oxide
UV	Ultra violet

List of Figures

List of Tables

Contents

1. Introduction

1.1. General Introduction

This present thesis is focussed on the development of a new paradigm approach to the treatment of cancer. Typical treatment approaches focus firstly on surgery followed by radiation therapy and chemotherapy. In a new approach, we aim to develop personalised drug releasing implants for patients so that a high local concentration of drug can be achieved next or within a tumour to obviate or supplement systemic dosing. In order to make the planned therapeutic approach personalised, we wish to take advantage of the possibilities available through 3D printing to develop complex architectures that can release drug at programmable rates, and that can be designed to match the particular contours associated with a patient or their requisite cancer type and shape. As such, the thesis opens with an introduction to cancer and current treatment strategies followed by newer approaches for the treatment of low prognosis solid tumour cancers, 3D printing and its applications in healthcare and as drug delivery systems.

1.2. Cancer

In 2015, there were over 17.5 million cancer cases reported worldwide with over 8.7 million deaths, making cancer the second leading cause of death behind cardiovascular diseases. Cancer caused over 208.3 million disability-adjusted life year losses (DALYs) in 2015[1]. At the global level, the odds of developing cancer are 1 in 3 for men and 1 in 4 for women, with tracheal, bronchus, and lung cancer, and colorectal cancer the most common incident cancers in men. The most common causes of cancer deaths for men following on from this were lung, liver, and stomach cancer respectively. For women in 2015, the most common incident cancers were breast, colorectal, and lung cancer, with the leading causes of cancer deaths being breast, lung, and colorectal cancer[1].

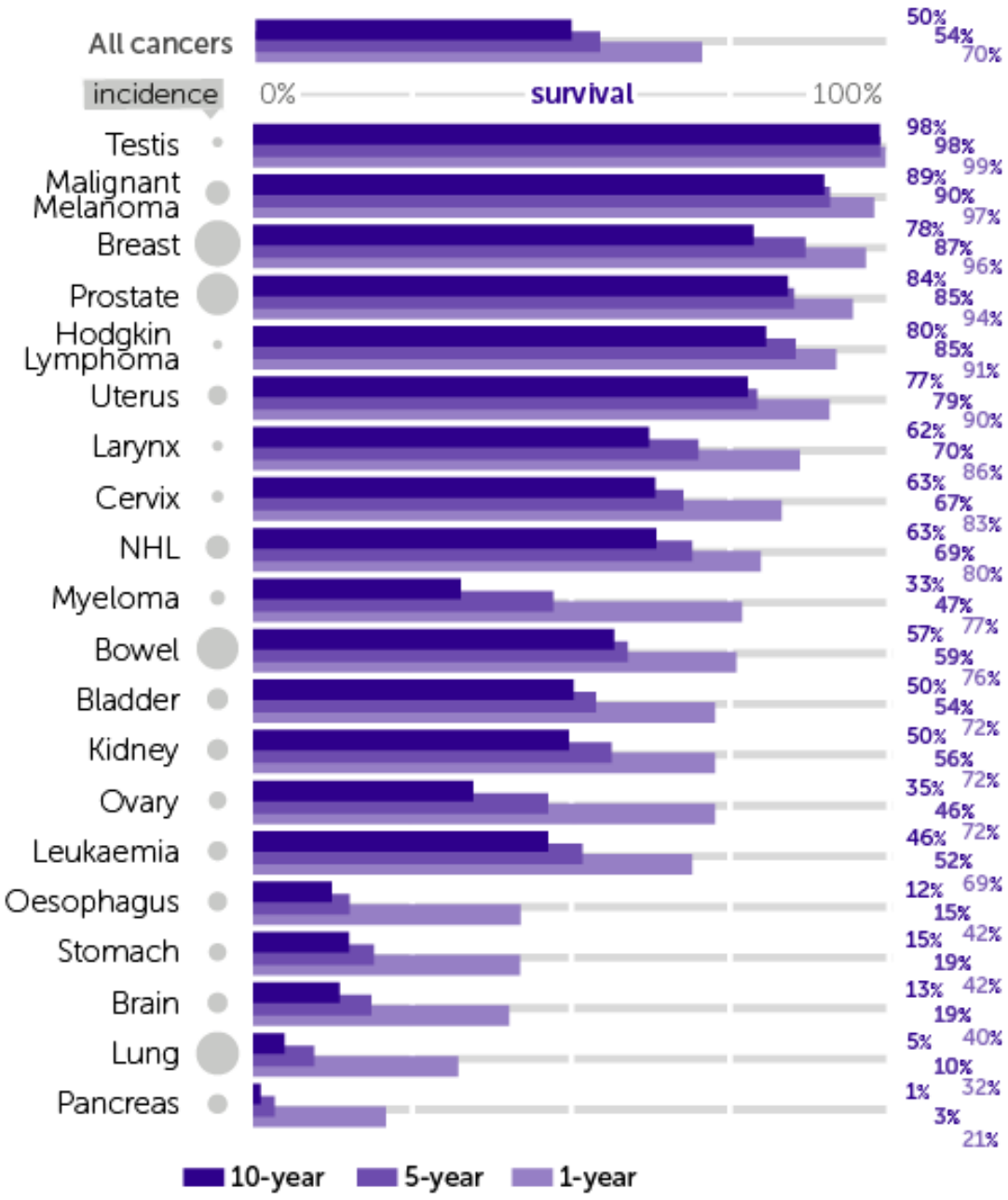

Figure 1 – One-, five- and ten-year survival rates for selected cancers of adults in the UK between 2010 and 2011. Reproduced from Cancer Research UK[2].

In the UK, there were 356,860 new cases of cancer with an estimated 163,000 deaths in 2014[3]. 50% percent of those afflicted by cancer survive for 10 or more years. However, there is a large variation in survival between different cancer types. For example, standardised 10-year survival rate for UK patients

with testicular cancer between 2010-2011 was 98% whereas the survival rate for patients with pancreatic cancer was 1%. Figure 1 illustrates the standardised survival rate variation between cancer types at 1-year, 5-year and 10-year time points[4].

Cancer also poses a huge economic burden on society with an estimated 25 million years of healthy life lost, costing the European Union (EU) €126 billion including €52 billion in lost productivity every year alone. Across the EU, approximately 5% of all health care expenditure goes on cancer, whilst in the UK 3.8% of total health care expenditure goes towards the treatment of cancer. The prevalence of cancer and the consequent demand for cancer services is expected to increase, due to an ageing population, and with it, an increased burden on patients, their families and society[5]. The total cost of cancer in the UK is estimated at £16.277 billion, with only a third due to the cost of healthcare, with other costs including lost hours of unpaid work (211 million hours)[6]. Every year since its inception, the budget for the NHS Cancer Drugs Fund (CDF) has increased, from £280 million in year 2014-2015 to over £340 million in 2015-2016. Furthermore, the actual total spend for 2015-2016 was £466 million, representing a £126 million overspend compared to the initial budget[7].

1.2.1. Current treatment pathways for solid malignant tumours

Solid tumours are defined as abnormal tissue masses and can either be benign (not cancerous) or malignant (cancerous), in contrast to those with liquid form such as leukaemia. How solid malignant tumours are treated depends on the stage of the cancer, its biological makeup, the risk versus benefits of planned therapy and expected clinical endpoints, patient treatment preference and the overall cost of treatment. Finding a compromise between therapeutic effectiveness and minimisation of treatment associated ‘off-target’ effects provides optimal care. The three cornerstones of cancer therapy are; surgery, chemotherapy and radiotherapy.

Surgery is frequently employed for cancer treatment, with excision of the tumour remaining the most effective way of treating and curing cancer. The Royal College of Radiologists (UK) estimate that of patients cured of all cancers, '49% are cured by surgery, 40% by radiotherapy and 11% by chemotherapy', when each modality is used as the main treatment component[8]. There are two general goals of surgery:

1) *Curative* – tumour resection/excision is most successful when the cancer is identified early, as the tumour is small and has limited dissemination. Typically, a margin of healthy tissue surrounding the tumour is excised to reduce the risk of cancer recurrence, as well as regional lymph nodes.
2) *Palliative* – tumours can be partially resected without curative intentions to relieve pain, haemorrhage or compression/obstruction of vital structures/organs e.g. spinal cord, trachea, gastrointestinal tract[9,10].

When possible, the primary objective of cancer treatment is to excise the cancer in its entirety, including all adjacent tissues into which cancers cells may have migrated. For superficial cancers such as early stage skin, mouth and testicular cancers, surgery offers a simple and effective method of curing cancers. For these reasons, such cancers are typically associated with good prognoses. For more advanced cancers that have spread, the surgeon will consider removal of the primary cancer and associated lymph nodes, which if possible and successful, is also associated with high cure rates. For example, treatment of breast cancer that is confined to the breast with early involvement of lymph nodes in the axilla often involves total removal of the breast and lymph nodes from the axilla, referred to as a radical mastectomy. For other "deep-seated" cancers including stomach, colon, rectum, uterus, ovary, oesophagus, lung and sometimes the pancreas, standard treatment also includes excision of the primary tumour along with nearby draining lymph nodes, however cure rate varies greatly for each cancer[11]. Combination of surgery with other modalities such as chemotherapy and/or radiotherapy has been shown to enhance the effectiveness of surgery. It is worth noting radiotherapy and/or chemotherapy can be used prior to surgery to shrink large

tumours or control regional disease, effectively ‘down-staging’ the cancer to increase the chances of successful surgery[12].

There are, however, limitations associated with surgical therapy[13]. Firstly, even if complete surgical resection is possible, small amounts of undetected cancer cells may remain and hence concurrent treatment with radiation and/or chemotherapy is necessary and recommended for aggressive cancer types to avoid recurrent tumour growth. For example, locoregional recurrence rates post-curative surgery is 27% and 11% for lung[14] and colon[15] cancers, respectively. Secondly, large, invasive tumours and cancers that have metastasised are often unresectable, although solitary metastases in the liver and lung can be sometimes resected.[16] Thirdly, patients with co-existing systemic disease or those who are in a poor condition due to their cancer are unlikely to be candidates for surgery. Finally, if the surgery required is extensive and would result in significant deformity or organ dysfunction, then it is likely the procedure would not be beneficial to the patient[13].

Radiotherapy utilises ionising radiation to kill cancer cells, which works in two ways; by damaging DNA within cells by dislodgement of electrons thereby inhibiting cell replication, and by generation of reactive oxygen species in the presence of water molecules that can further damage DNA, triggering cell death. There are different types of radiation therapy. The most common being external beam radiation therapy which features an external source of radiation. There are several methods of delivering external beam radiotherapy. Firstly, electromagnetic X-ray and gamma rays involve delivery of electromagnetic energy as photons generated by devices called linear accelerators or ^{60}Co units. This method provides deep tissue penetration and is therefore useful for deep-seated tumours. Secondly, particle beam radiation involves acceleration of particles such as electrons and protons and is a high precision method typically used for skin cancers. Another type of radiation therapy is brachytherapy. This is the temporary or permanent implantation of low energy electron, alpha or beta particle emitting radioactive isotopes such as ^{137}Ce, ^{192}Ir that are then directly inserted into a tumour[17]. Radiotherapy, whilst generally associated with lower 5-year survival rates than surgery, provides

an effective treatment for many skin cancers, some head and neck cancers, “deep-seated” cancers that cannot be totally removed by surgery, and for patients who are unable to tolerate surgery. Radiotherapy has the advantage of avoiding surgical operation, however treatment typically takes place over a period of weeks. Furthermore limited efficacy, acute and long-term toxicities, and occurrence of secondary malignancies prevents its routine use for all patients[11].

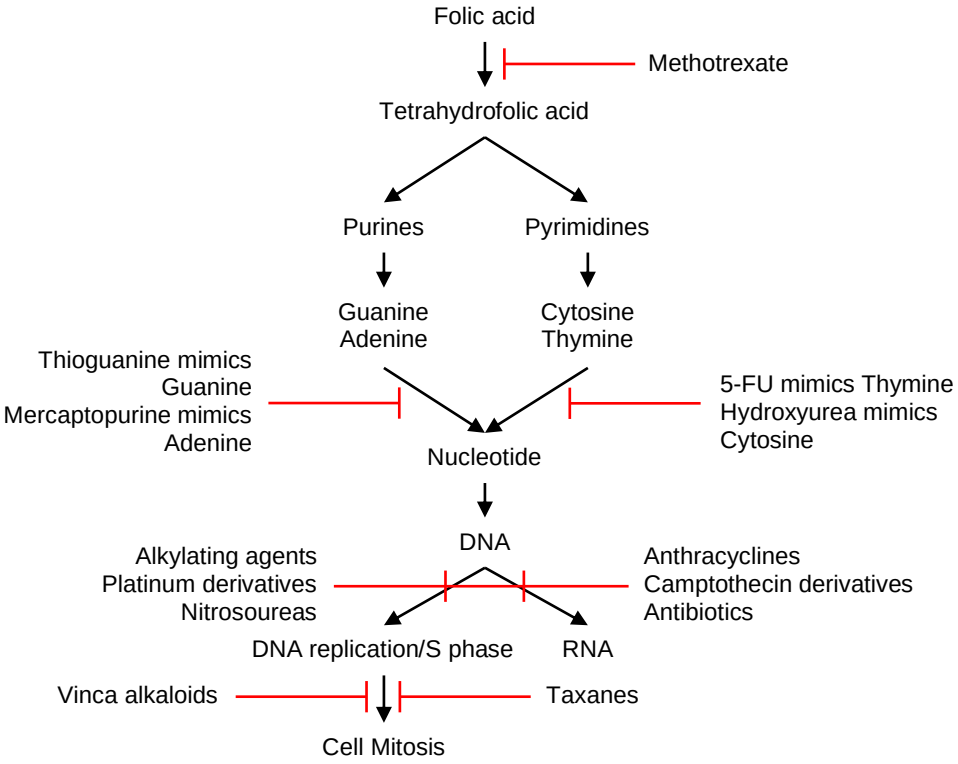

Figure 2 – Mechanisms of common chemotherapeutic agents. Adapted and modified from Baudino (2015)[18].

Chemotherapy is almost always a major component of cancer therapy, whether it be used alone or in combination to increase the effectiveness of surgery or radiotherapy. Unfortunately, unlike surgery and radiotherapy, treatment of cancer with chemotherapy as a single modality is not curative, and in general, this form of treatment is palliative. Palliative chemotherapy has the aim of prolonging life and making patients more comfortable (QALYs)[11].

On the other hand, chemotherapy (and radiotherapy) in combination with surgery, can be utilised post-surgery (adjuvant therapy) to eradicate small

numbers of malignant cells that may have spread, or prior to surgery (neoadjuvant or induction therapy) to help reduce tumour size and simplify excision. Adjuvant and neoadjuvant chemotherapy is often standard and can drastically improve prognosis of most cancers. Chemotherapeutic drugs have greatest effect on dividing cells. As cancer cells divide rapidly in comparison to normal healthy cells, they are more likely to be affected[11]. Figure 2 provides a summary of chemotherapeutics typically employed for cancer treatments and their mechanism of action[13,18]. Antimetabolites interfere with synthesis and metabolism of DNA and RNA. Examples of antimetabolites include methotrexate, 5-fluorouracil (5-FU), cytarabine, gemcitabine and 6-mercaptopurine. DNA damaging agents include alkylating agents such as cyclophosphamide and melphalan; antibiotics such as adriamycin and bleomycin; nitrosoureas such as carmustine (BCNU) and platinum derivatives such as cisplatin and carboplatin. Compounds that inhibit mitosis include vinca alkaloids such as vincristine and vinblastine and taxanes such as paclitaxel. In general, combinations of chemotherapeutic drugs are more effective than monotherapy, with considerable research having identified multiple optimal drug regimens of precise dose and timing schedules against different types of cancer[11].

However, there are limitations associated with chemotherapy. As with radiotherapy, therapy-associated toxicity is a major limitation. This is due to chemotherapeutic agents targeting cells in normal tissues that divide frequently, including mucosal cells lining the mouth, throat, stomach, bowel and airways, skin and growing hair cells, sex cells and blood cells in the bone marrow. Consequently, common toxicities include nausea and vomiting, alopecia, myelosuppression (perhaps most seriously) which results in reduced white blood cell and platelet production increasing risk of infection and bleeding, mouth sores, diarrhoea, infertility and like radiotherapy, secondary malignancies (especially from alkylating agents)[13]. Furthermore, some chemotherapeutic drugs can affect the function of the heart, lungs, kidneys, central nervous system (CNS) or peripheral nerves[11].

Poor penetration of anticancer drugs into malignant tumours presents another limitation. Despite an arsenal of potent chemotherapeutics, chemotherapy often fails as adequate therapeutic concentrations within cancer cells are not achieved which is due to poor penetration and non-uniform distribution of a drug. Tumours have a poorly formed vascular system with large intercapillary distance and hence drugs struggle to penetrate malignant tissue from the bloodstream. The imperfect vasculature also means regions of tumour have deficient supply of oxygen and nutrients and are dormant hence use of chemotherapeutics targeting cell replication are ineffective. Drug delivery to brain tumours is also typically inadequate due to poor penetration through the blood brain barrier[19].

Targeted therapies differ from traditional cancer treatments (surgery, radiotherapy, chemotherapy), instead targeting specific molecular changes which are unique to a specific cancer and/or cancer subtype. Hormonal therapy, or more correctly, anti-hormonal therapy is effective for cancers that are hormone dependent. For example, some breast cancers are dependent upon the female sex hormone oestrogen. Consequently, anti-oestrogen drug Tamoxifen, which binds to the oestrogen receptor and blocks the proliferative actions of oestrogen on mammary epithelium, is used for oestrogen receptor (ER) positive breast cancer[20]. Conversely, some prostate cancers are dependent on male sex hormones. Flutamide, is an anti-androgenic drug used for the treatment of metastatic prostate cancer. Flutamide binds to the androgen receptor and blocks the proliferative actions of testosterone and dihydrotestosterone on cancer cells[21]. Hormone manipulation has a distinct advantage over conventional chemotherapy, as hormones are less likely to cause serious side effects, especially in the short-term, or present drug-limiting toxicities[11].

Cancer immunotherapy, like hormone therapy, offers benefits over traditional chemotherapy due to fewer and less severe side effects. The main types of immunotherapy currently used to treat cancer are; monoclonal antibodies, immune checkpoint inhibitors, cancer vaccines and other non-specific immunotherapies such as cytokines. Monoclonal antibodies act through

multiple mechanisms, including recruitment and activation of the immune system (immunotherapy), inhibition of ligand-receptor interactions that are essential for cell survival and replication and/or by carrying lethal toxin/payloads (immunotoxins) to the cancer cells[18]. Some monoclonal antibody therapies that are clinically approved include Avastin which inhibits signalling of vascular endothelial growth factor (VEGF), a secreted glycoprotein that promotes angiogenesis and proliferation, and is overexpressed within cancer cells. Avastin is used to treat metastatic breast cancer, non-small cell lung cancer and colorectal cancer, where a study for the latter indicated survival duration was increased from 13.8 months to 21.5 months[22]. Another, Herceptin, binds to HER2, which disrupts intracellular signalling cascade inhibiting cell growth, downregulates HER2 and can increase the ability of the immune system to detect and kill cancer cells. Herceptin is useful for HER2-positive breast cancers.

Activation or inactivation of “checkpoint” proteins are often required to induce an immune response. Cancer cells sometimes exploit these checkpoints to avoid being attacked by the immune system. Clinically approved therapies that target checkpoint proteins include monoclonal antibodies pembrolizumab and nivolumab which are used in the treatment of melanoma, non-small cell lung cancer, renal cell carcinoma, bladder cancer, head and neck cancers and Hodgkin’s lymphoma[23].

Cancer vaccines can be used to prevent cancer, or to treat cancer. Preventative cancer vaccines aim to protect against certain viruses that are known to cause cancers. For example, human papilloma virus (HPV) has been linked to cervical, anal, throat and other types of cancer and hence vaccines against HPV are helpful in preventing some cancers[11]. Cancer treatment vaccines differ from those that work against viruses, instead stimulating the immune system to attack cancer cells. The only approved vaccine treatment is Sipuleucel-T, a cellular product based on enriched patient blood antigen presenting cells (APCs) which has been shown to improve survival by approximately 4.5 months in patients with prostate cancer[24]. Many more cancer vaccines are showing promise in clinical trials.

Cytokines, which are secreted by immune cells when stimulated by antigen, are potent non-specific stimulators of the hosts immune system and can be given systemically in certain cancers. Interleukin-2 (IL-2) is a potent mediator in antiviral therapy and is approved for adjuvant use in advanced melanoma and renal cell carcinoma[25], both cancers which show resistance to chemotherapy, whereas tumour necrosis factor alpha (TNF-α) is another cytokine used for adjuvant treatment of soft tissue carcinomas of the limb and melanoma[26]. Side effects of these medicines, like most cancer immunotherapies, are typically lesser than those associated with standard therapies with only rare potentially severe side effects.

Another class of targeted therapies, small molecule drugs, act by blocking specific enzymes and growth factor receptors (GFRs) that are involved in cancer cell proliferation[18]. Some small molecule drugs that are FDA approved are Gleevec, which works by targeting mutated enzyme c-Kit located on tumours, hence preventing abnormal cell growth, and is used for treatment of GIT stromal tumour[27], and Iressa which is an epidermal growth factor receptor (EGFR) inhibitor that is effective against cancers where EGFR is overexpressed such as non-small cell lung cancer[28].

Targeted therapies show great promise, offering better quality of life, higher survival rates and, whilst still substantial, decreased side effects compared to conventional treatments. Nevertheless, patient selection remains an important issue for targeted therapies to avoid treatment-related toxicity and cost in patients unlikely to benefit. This requires identification and validation of reliable biomarkers or diagnostics and larger roll-out of comprehensive screening programmes to identify patients most likely to profit from a given treatment.

1.2.2. Alternative drug delivery methods for cancer treatment

Variance between survival rates of certain cancers is partially attributed to the effectiveness of therapy and a balance between elimination of cancerous cells and preservation of normal cells. For some cancers such as pancreatic

locoregional cancers, surgery is often not possible and there is total reliance on radiotherapy and/or chemotherapy-based regimens for treatment. Oral and systemic chemotherapy for treatment of pancreatic cancers is often ineffective, hence the low survival rate[29]. Localised therapy can potentially offer a more effective and efficient treatment for such “hard-to-reach” cancers. Even cancers with high survival statistics could benefit from improved control of localised disease by limiting the extent of surgical resection, circumvention of harsh radiotherapy and/or chemotherapy-based regimens, and reduction of treatment toxicities, thereby reducing patient disablement and burden. Compared to systemic chemotherapy, localised delivery of chemotherapeutics can offer great utility against loco-regional early stage solid tumours by reducing systemic side effects, overcoming dose-limiting toxicities and thereby allowing optimal chemotherapeutic treatment[30].

Brachytherapy, the implantation of radioactive seeds, within or nearby malignant tissues, is a common localised therapy and has shown efficacy as a localised therapy option for treatment of inoperable tumours and prevention of local tumour recurrence post-resection. Seeds are typically composed of bio-inert stainless steel or titanium, and typically contain I^{125} or Pd^{103} as a radioisotope[31]. It has regular use for prostate cancer and shown great utility in others such as lung, cervical and breast cancer[32–34]. Although localised brachytherapy demonstrates remarkable benefits, its use is limited due to a number reasons including difficult method of administration, adverse bystander tissue effects and issues with radiation handling and toxicity[35].

Regional chemotherapy allows for high local drug concentrations, reduced systemic distribution and toxicity, and extended drug exposure. Beyond use as primary tumour treatment, it has shown great utility as a post-operative adjuvant therapy to prevent local recurrence of cancer, a major factor in patient relapse and post-operative patient death[29]. Regional chemotherapy also shows specific promise as a treatment modality for brain cancers, owing to the presence of the blood-brain barrier that prevents efficient treatment using traditional systemic chemotherapy[36]. There are many routes through which regional chemotherapy can be administered including intraarterial,

intraperitoneal, intrathecal/intraventricular and intravesical bladder routes[30]. Various regional chemotherapy strategies with clinical relevance are outlined below.

Intra-arterial chemotherapy involves injection or infusion of chemotherapy into arteries that feed directly into malignant tissue, thereby achieving high local drug concentrations with minimal systemic exposure. Abramson et al. developed an adapted ophthalmic intra-arterial infusion technique for delivery of melphalan (in combination with carboplatin and/or topotecan) to treat retinoblastoma. While lack of long-term studies and need for optimisation make it unclear whether this strategy is a first-line therapy, or a salvage therapy when conventional modalities such as systemic chemotherapy or radiotherapy fail, short-term studies demonstrate this method as a minimally invasive, safe and effective treatment with minimal side-effects[37].

Intracarotid chemotherapy is a type of intra-arterial treatment which involves delivery of chemotherapy through the carotid artery. This approach has become an established method for the treatment of patients with localised head and neck cancer. Intracarotid chemotherapy has mainly been use for maxillary sinus cancer as part of an interdisciplinary approach. Treatment results vary between countries, with 5-year survival rates in Japan ranging from 57-78.4% and those in Western countries ranging from 29.3-49%, and hence further studies are required to establish widespread clinical utility. The RADPLAT (radiotherapy and concomitant intraarterial cisplatin) regimen consists of intracarotid cisplatin infusion followed by an IV bolus of neutralising agent sodium thiosulfate and concomitant irradiation. One clinical trial indicated RADPLAT treatment of head and neck cancer is both feasible and effective in a multi-institutional setting[38]. From multiple studies, it is observed that primary breast cancer tumours are all supplied by branches of the internal mammary artery, and hence intra-arterial infusion is a viable treatment approach. Zhang et al. led a study where 28 patients with locally advanced breast cancer received intra-arterial chemoinfusion of docetaxel and epirubicin[39]. Findings indicated intra-arterial chemoinfusion shrunk tumours and metastatic lymph node volume in a short period of time and down-staged

tumours, allowing for surgical resection. Intra-arterial chemoinfusion could also reduce the number of treatment cycles and doses required of conventional IV chemotherapy, with markedly fewer side effects and reduced time to surgery[39]. Trans-arterial chemoembolisation (TACE) is an adapted intra-arterial treatment modality that involves the infusion of embolising agents in combination with chemotherapy, into the hepatic artery. The benefits of TACE are two-fold. Firstly, vasoconstriction of the tumour vasculature interrupts the tumour's blood supply and hence stunts tumour growth, and secondly, drug is accumulated in the tumour due to embolisation of the tumour vascular bed resulting in prolonged high local drug concentrations and reduced systemic exposure[40,41]. This method is typically used as a neoadjuvant therapy for treatment of colorectal cancer that has metastasised to the liver, showing improvement over systemic chemotherapy[42,43].

Intravesical therapy involves directly administering drug through a catheter into the bladder. Intravesical chemotherapy and immunotherapy are widely used adjuvant bladder cancer therapies after transurethral tumour resection for the prevention of cancer recurrence and progression. The rationale for intravesical therapy is maximising bladder cavity located tumour exposure to therapeutic agents whilst minimising systemic exposure and consequent toxicities. Bacille Calmette-Guérin (BCG) is a common immunotherapy administered intravesically and is first-line treatment for prophylaxis and treatment of carcinoma *in situ*. Intravesical administration of multiple chemotherapeutic agents and their combinations have also been evaluated in clinical trials and, in tandem with transurethral tumour resection, have demonstrated modest reduction in bladder cancer recurrence[44].

Intratumoural or intralesional administration involves direct application of anticancer agents into malignant tissues. The intratumoural route can also have advantages over other local/regional administration routes by addressing issues of poor vascularisation, stiffened extracellular matrix (ECM) and increased interstitial pressure that prevent sufficient penetrance and diffusion of drug into tumours. Intratumoural delivery of oncolytic virus immunotherapy has received considerable interest over the past decade, with numerous

clinical trials completed or under way and the recent FDA approval of oncolytic virus talimogene laherparepvec for treatment of advanced melanoma[45]. Talimogene laherparepvec, derived from herpesvirus, and other oncolytic viruses work through a combination of selective tumour cell killing and establishment of antitumour immunity. Intratumoural injection of talimogene laherparepvec in clinical trials have demonstrated significantly improved response rates in patients with melanoma compared to controls and even tumour regression in untreated lesions due to establishment of antitumour immunity[46]. Other clinical trials that have utilised various oncolytic viruses for treatment of cancers including pancreatic, malignant glioma, ovarian and prostate which have all shown positive response rates and good safety profiles, even at high doses, indicating that oncolytic viruses are potential emerging therapeutic agents in oncology[45].

The intratumoural/intralesional route has also shown significant utility in the treatment of malignant brain tumours[47], demonstrating increased penetration of chemotherapeutics into brain tissue when compared to systemic chemotherapy[48]. The general injection approach for treatment of gliomas can either be intracavitary, after resection of the tumour, or intratumourally, if the tumour is not resectable. A clinical trial investigated intratumoural injection of paclitaxel for the treatment of patients with recurrent grade III or IV gliomas. Whilst the results indicated treatment efficacy, with an average survival time of 7.5 months, the treatment was associated with severe treatment related adverse effects and neurological deterioration due to oedema and infection, preventing widespread clinical use[49]. Recently, intratumoural injection of iron oxide nanoparticles to facilitate heat ablation therapy, in combination with stereotactic radiotherapy, demonstrated an average survival time of 13.4 months in patients with recurrent glioma, without systemic side effects. Further trials are required to assess the efficacy of intratumoural injection of nanoparticle formulations for the treatment of glioma[50]. Convection-enhanced delivery (CED) involves pressure-driven bulk flow of a drug infusion through a catheter to facilitate intratumoural delivery of anticancer agents[51].

1.3. Cancer drug eluting polymer implants

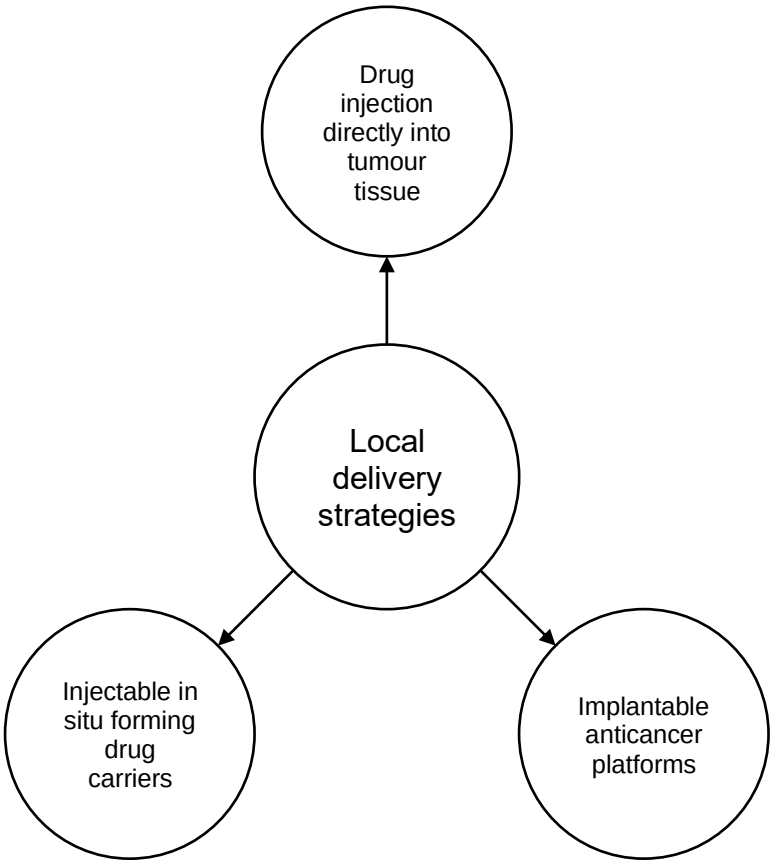

Figure 3 – Strategies of local delivery of anticancer agents. Adapted from Krukiewicz et al. (2016)[30].

Despite the relative clinical success of the loco-regional drug delivery strategies discussed, and their ability to minimise systemic side effects and hence circumvent dose limiting toxicities, there are still limitations that must be overcome to improve their efficacy. Although intravenous or regionally administered chemotherapeutics can afford high bioavailability when entering circulation, drug uptake by non-specific systems e.g. reticulo-endothelial systems or non-targeted cells can drastically reduce local bioavailability[52]. In addition, high interstitial pressure within solid tumours can prevent effective drug flow into the tumour centre[53,54]. Direct injection or infusion of anticancer agents into tumours can overcome, to an extent, these barriers, however this

method suffers from a lack of control of the amount of drug released in a specific time interval.

An alternative approach to increase and control drug dosage at the tumour site can be achieved with drug-eluting polymer implants. Drug-eluting devices can be implanted directly or adjacent to the site of disease and can offer multiple advantages over traditional systemic dosing and loco-regional chemotherapy injections/infusions[12,29,55,56]:

1. Drug-eluting implants can offer stabilisation and protection of contained anticancer agents, thereby preserving cytotoxic activity of payloads and facilitating treatment with unstable and/or short *in vivo* half-life therapies.
2. Controlled and prolonged drug release providing steady diffusion and uptake into cancer cells. Furthermore, tumour cell exposure to chemotherapy over multiple cell cycles has been shown to be more effective than bolus delivery.
3. Loading and release of chemotherapeutics that are incompatible with conventional dosing routes due to hydrophobicity and/or poor absorption.
4. Direct delivery of drug to malignant tissues resulting in minimisation of systemic toxicities and reduced drug wastage, whilst facilitating utilisation of “benched” potent, narrow therapeutic window therapies that are not used in clinic due to intolerable systemic adverse effects.
5. One-time installation of device compared to multiple repeated external administrations, improving patient compliance and avoiding adverse effects varying from irritation to local tissue necrosis associated with frequent injections/infusions. Local delivery systems are usually designed to be implanted immediately after a tumour debulking surgery, which omit the need of performing an additional surgery to place the therapeutic material in the patient.
6. Provide a large therapeutic coverage which can reduce the amount of resective surgery required thereby preserving tissue function.

With improvements in diagnostic technology, it is expected the number of patients diagnosed at earlier stages will increase. In response to this approach, the emphasis will likely shift from treatment, curative and/or palliative, of late stage disseminated disease to the prevention of local recurrence after initial curative surgery[12]. It is therefore likely local drug delivery implants represent the next generation of cancer treatments and will play a large role in increasing the number of long-term remission patients. There are two types of drug-eluting implants used for cancer therapy; injectable *in situ*-forming implants and pre-formed implants[29].

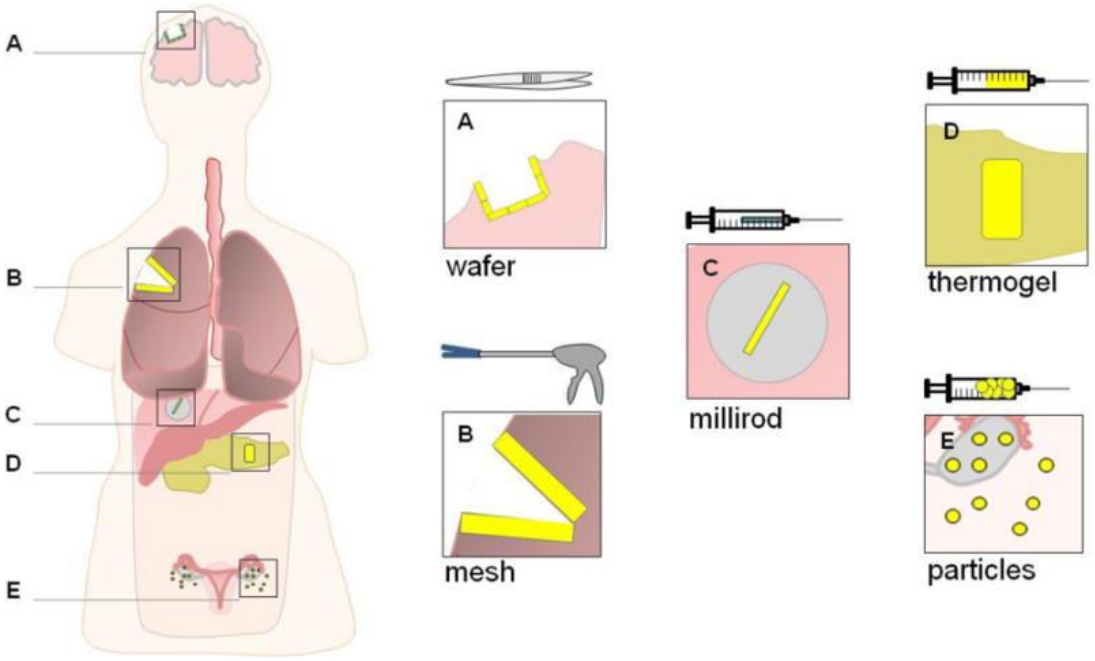

Figure 4 – Examples of localised chemotherapies at various treatment sites and different modes of administration. Reproduced from Wolinsky et al. (2012)[12].

1.3.1. Injectable *in situ* drug eluting polymer implants

In situ-forming polymer implants (ISFIs) typically consist of a solution or suspension of polymer matrix constituents and active agents that, after injection into a tumour site via a needle, solidify, in response to a certain

stimulus, to form a drug eluting depot[57]. These systems allow for easy non-invasive rapid, painless administration to a patient. Depending on their composition, these implants can release active agents, typically by either diffusion or degradation mechanisms, over periods ranging from hours to months[58]. ISFIs can be classified into two categories; *in-situ* crosslinking systems and *in-situ* phase separation systems[59]. This section briefly explores different types of ISFIs and discusses select examples that have been applied for the treatment of cancer in a pre-clinical or clinical setting.

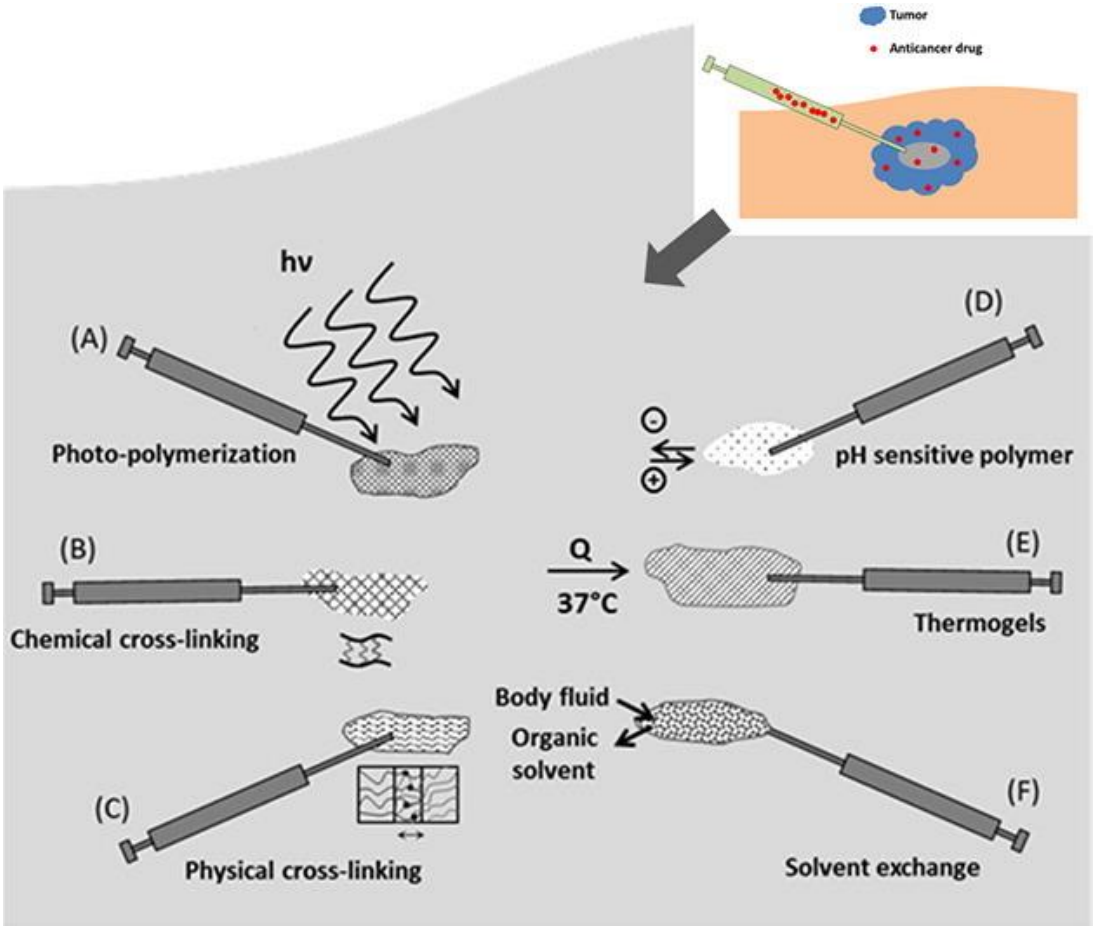

Figure 5 – Drug release platforms based on in situ cross-linking. Reproduced from Fakhari et al. (2015)[59].

Systems based on *in situ* cross linking prominently form by either photopolymerisation, chemical crosslinking or physical crosslinking (Figure 5). The photopolymerisation approach involves injection of liquid starting materials into the tumour site and subsequent irradiation with light to form a

drug-eluting implant. Requirements for these systems include cross-linkable polymers e.g. acrylates, methacrylates, vinyl ethers, a photo-initiator and visible or UV light[59]. Obara et al. developed a photocrosslinked chitosan-based hydrogel for gradual paclitaxel release through both diffusion of paclitaxel and biodegradation of the hydrogel. *In vivo* results from mouse models demonstrated greater prevention of induced tumour growth than subjects receiving intratumoural paclitaxel[60]. In another study, Sharifi et al. produced an *in situ* forming device based on photocrosslinkable PCL fumarate for sustained release of tamoxifen for the treatment of breast cancer. *In vitro* studies showed very slow release of drug (5% of payload after 400h) resulting in death of breast cancer cells[61]. Advantages of these systems include the formation of mechanically strong and stable implants. The main disadvantage of these systems includes generation of reactive species generated post-crosslinking, which can cause damage to surrounding tissues and affect anticancer agent activity and non-homogenous implant formation due to the limited depth penetration of visible and UV light, resulting in unpredictable drug release pharmacokinetics and leakage of toxic uncured monomers. To tackle the latter problem, Zhang et al. developed a PEG acrylate/TiO_2-multi-walled carbon nanotube based ISFI formulation for release of doxorubicin. After injection into a murine sarcoma tumour model, exposure to near-infrared light, which has a greater depth penetration than UV or visible light, resulted in rapid gelation *in vivo*. Alongside release of doxorubicin, additional laser irradiation led to generation of reactive oxygen species and local hyperthermia, resulting in increased cell death[62].

The chemical crosslinking approach requires starting polymers with functionalised terminal groups that undergo cross-linking when mixed with a cross-linking chemical such as benzyl peroxide and dialdehydes. Balakrishnan et al. developed a periodate-oxidised sodium alginate/gelatin system that crosslinked in the presence of sodium tetraborate[63]. This gel was found to be biocompatible and biodegradable with a high degree of customisation. Emoto et al. produced both an aldehyde-terminated and hydrazide-terminated hyaluronic acid based material which rapidly gelled when mixed. By altering the ratio of each polymer, the drug release rate of the resultant implant could

be tailored. This formulation was used to provide sustained release of cisplatin after intraperitoneal injection in a mouse model of peritoneal carcinomatosis. Tumour regression was observed in mice treated with the cisplatin loaded gel, whereas no regression was observed in mice treated with free drug[64]. Despite formation of stable implants, this approach is associated with high toxicity and poor biocompatibility, and a slow rate of crosslinking resulting in unpredictable drug release to surrounding tissues[59].

1.3.2. Pre-formed drug eluting polymer implants

Pre-formed polymer implants have been used for multiple applications ranging from adjuvant chemotherapy following brain tumour resection to palliative care for end-stage prostate cancer[65–67]. An advantage of such systems is that the shape can be designed to meet the specifications of the end application. Shape and surface area play an important part in drug diffusion and polymer degradation rate. The polymers used to form these implants can either be non-degradable or biodegradable. Non-biodegradable materials include silicone elastomers, polyethylene-based plastics and polyacrylates. Disadvantages of these devices are that they require removal at the end of treatment hence necessitating an invasive procedure[68,69]. Biodegradable materials, such as poly(lactic acid), poly(caprolactone) and poly(lactic-co-glycolic acid) (PLGA) can avoid such complications and have common use in clinical applications such as degradable sutures[70,71]. Degradation time can be suited to application (weeks to > 1 year) by tailoring of device geometry, porosity and chemical composition. Cisplatin and carboplatin, platinum-based anticancer agents with narrow therapeutic windows, have shown improved local effectiveness with minimal systemic side effects when entrapped as part of a pre-formed implant for intratumoural administration[72–74].

One example of a pre-formed drug eluting implant system is called the ‘millirod’, which consists of active agent entrapped into compressed PLGA microspheres. Designs range from monolithic, to multiple phase systems with programmable drug release profiles[75,76].Anti-tumour activity of doxorubicin-loaded millirods were evaluated in an in vivo ablated liver carcinoma model. It

was demonstrated that tumours in models treated with millirods were smaller compared to controls, however viable tumour cells were observed outside the ablation treatment area, associated with development of a fibrous capsule preventing effective drug penetration[77]. In a consequential study, the research group co-delivered doxorubicin and anti-inflammatory dexamethasone from millirods, with animal models showing improved anti-tumour efficacy compared to the previous study[78]. This was attributed to dexamethasone reducing the thickness of the fibrous capsule, permitting improved drug penetration. In another approach, millirods composed of biodegradable carboxyphenoxypropane and sebacic acid, and chemotherapeutic 5-FU were implanted into ablated rabbit liver models. Models treated with 5-FU eluting millirods showed reduced tumour volume compared to animals treated with ablation alone[79]. Polymer millirods in combination with radiofrequency ablation has shown promise for treatment of liver cancers, with one strategy involving insertion of multiple polymer millirods into a single ablated tumour to ensure adequate drug distribution throughout the malignant tissue[80].

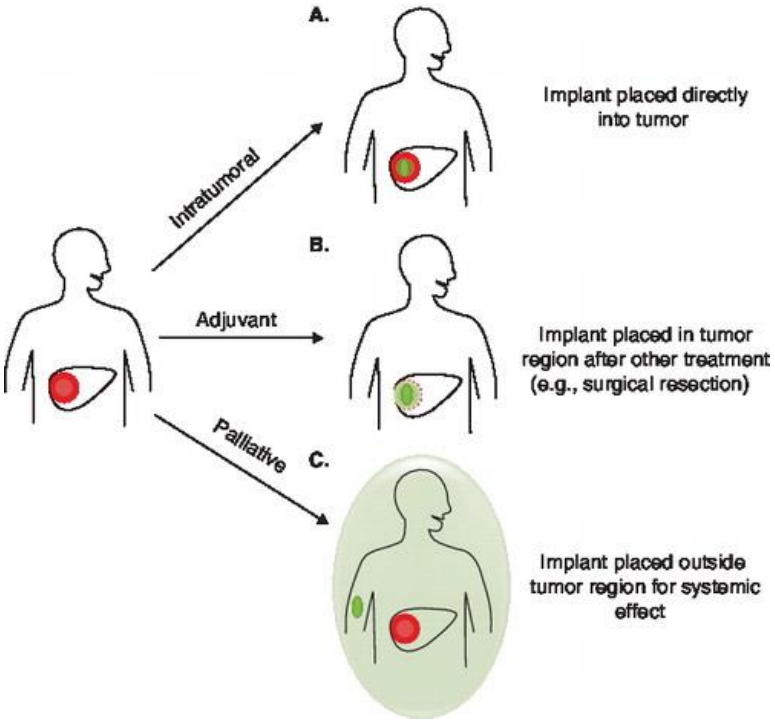

Figure 6 – Categories of drug-eluting implants in cancer chemotherapy. Reproduced from Exner et al. (2008)[29]

A major pitfall for local drug delivery is insufficient surface coverage, fixation and drug diffusion to tissues post-surgery where risk of local recurrence is high. Rigid materials are typically unsuitable to accommodate to the irregular shape of tissue post-surgery, and therefore soft and flexible materials are better suited to achieving optimal drug delivery[12]. In response, research has begun to focus on the development of drug-loaded flexible composite films which are fixed to tumour resection margins at the time of initial surgery. An example includes poly(glycerol monostearate-co- ε-caprolactone) films containing hydroxycamptothecin, a drug with poor pharmacokinetics when administered systemically, which were tested in a murine tumour model. In vitro drug release studies showed controlled release (0.5-2% per day) for at least 50 days without a significant initial burst. Furthermore, a significant in vitro inhibition of Lewis Lung carcinoma cell proliferation was achieved over the 50-day lifetime of the film. In a separate study, drug-loaded films were implanted into mice with established lung tumours. Local tumour growth was prevented in 86% of the implanted mice and no mice showed evidence of systemic toxicity[81]. Moreover, an investigation of films, where hydroxycamptothecin was substituted with paclitaxel, was undertook to assess their utility in preventing tumour recurrence after resective surgery. Mice implanted with paclitaxel-loaded films showed no tumour recurrence at the site of implant whereas controls treated with paclitaxel injections or unloaded composites all experienced local recurrence rates greater than 80%. Paclitaxel tissue concentrations achieved by the drug-loaded films were 3000-fold greater than those achieved by systemic administration, whilst plasma concentrations of the drug were negligible, demonstrating a promising safety profile. Paclitaxel-loaded films have also been investigated in a chondrosarcoma murine post-surgical recurrence model. Recurrence rates were 17% for animals with drug-loaded film implants whereas controls recurrence rate ranged from 69 to 89%. The average recurrence time for control groups ranged from 13 to 22 days, whereas ten of the twelve mice treated with drug-loaded films showed no evidence of recurrence over the 100-day experiment. Furthermore, overall survival was increased when compared to control groups (81 days vs. 48-56 days)[82].

Due to physiological barriers preventing effective treatment of brain malignancies with systemic treatment, methods that bypass these barriers and provide drug directly to the brain have been extensively researched[83]. These range from use of implantable controlled-release polymer systems, catheter devices for intracavitary drug delivery and convection-enhanced delivery. Ramachandran et al. demonstrated a temozolomide-loaded electrospun PLGA-PLA-PCL nanofibre wafer for treatment against glioblastoma[84]. Wafers displayed constant drug release over a month in a rat glioma model with negligible system leakage. 85% of animals implanted with these wafers showed prolonged survival of over three months with no sign of tumour recurrence. In another approach, Saini et al. developed mitoxantrone-loaded triangle shaped non-biodegradable ethylene-vinyl acetate implants for intratumoural treatment of glioma. In vivo studies in glioma rat models demonstrated these implants can significantly prolong survival[85]. Furthermore, combination of local glioma therapy with other modalities has shown improved survival rates in animal models, compared to monotherapy. For example, Ewend et al. highlighted that local carmustine therapy in combination with radiotherapy proved superior to each modality separately in four separate tumour animal models and was well tolerated[86]. Furthermore, Hsu et al. demonstrated that rat gliosarcoma models treated with both adriamycin-loaded wafers and intracerebrally injected IL-2 microspheres showed significantly improved survival times compared to models treated with each modality separately[87]. In another example, Bow et al. showed that rat glioma models treated with either radiotherapy or oral temozolomide, in combination with intracranial wafer-released minocycline, displayed significant extension in survival time for rat models[88]. The Gliadel wafer is an FDA approved example of a successful intracranial drug delivery implant for the treatment of glioma (Figure 6)[89,90]. It is made up of a biodegradable polyanhydride wafer containing carmustine. Treatment typically involves insertion of up to eight wafers into an orifice created by surgical resection of the primary brain tumour. In animal studies, wafers were shown to release carmustine in rat brains over a period of 5 days followed by complete degradation of the wafer 6-8 weeks post-implantation[91]. Clinical trial studies have shown the wafers together with surgical resection (and radiotherapy) significantly increase survival time for

both primary and recurrent disease[92], with a review of 19 studies show that Gliadel treatment can increase patient survival by an average of 2.2 months[93,94].

Several pre-formed drug eluting polymer implants are in current clinical use. Zoladex is a FDA approved PLGA-based pre-formed implant used to deliver goserelin acetate for palliative treatment of prostate and breast cancer. The use of the implant has been shown to extent the duration of drug action for up to three months[93]. Clinical trials showed that Zoladex in combination with a typical chemotherapy regimen showed added benefits, was well tolerated in patients and was associated with fewer acute toxicities than chemotherapy alone[95]. Histrelin acetate (Vantas) is a new gonadorelin analogue for palliative treatment of advanced prostate cancer which is administered annually. One clinical trial investigated use of Vantas in patients with advanced prostate cancer. One month after implantation, testosterone levels were within castration range, associated with disease control, for all patients. Testosterone levels remained suppressed throughout this year. The majority of patients received a second implant after one year. Between 52 weeks and 60 weeks (end of trial), testosterone levels remained suppressed. All reported adverse effects were manageable and did not lead to treatment discontinuation[96]. Another clinical study evaluated long term efficacy of Vantas in advanced prostate cancer patients. Testosterone levels remained within the castration range for 100% of patients at 3, 4 and 5 years, indicating Vantas as an effective long-term and well-tolerated method for treating patients with advanced prostate cancer[97]. Another device, Viadur, is a FDA approved non-resorbable, osmotically driven implant consisting of a titanium reservoir, polyurethane membrane, and a piston. Viadur can provide sustained release of leuprolide acetate for a period of one year for treatment of advanced prostate cancer. Clinical trials have shown the implantable leuprolide delivery system provides effective suppression of testosterone in patients with advanced prostate cancer[98]. Furthermore, TARIS Biomedical have developed GemRIS, a non-biodegradable drug-eluting device for treatment of bladder cancer. GemRIS is a small flexible device that continuously delivers gemcitabine into the bladder (intravesically) over 7 days through an osmotic pump made of silicone and

nickel alloy wire. Preclinical models have shown GemRIS is well tolerated without significant systemic side effects. Recently, GemRIS was evaluated for safety and tolerability in bladder cancer patients in combination with radial cystectomy. Patients in the clinical trials demonstrated tolerable treatment-related adverse effects without any systemic toxicities. 80% of patients experienced significant tumour reduction and 40% exhibited complete disease regression over the 4-week course of therapy. Further evaluation of GemRIS for treatment of bladder cancer is currently ongoing[99].

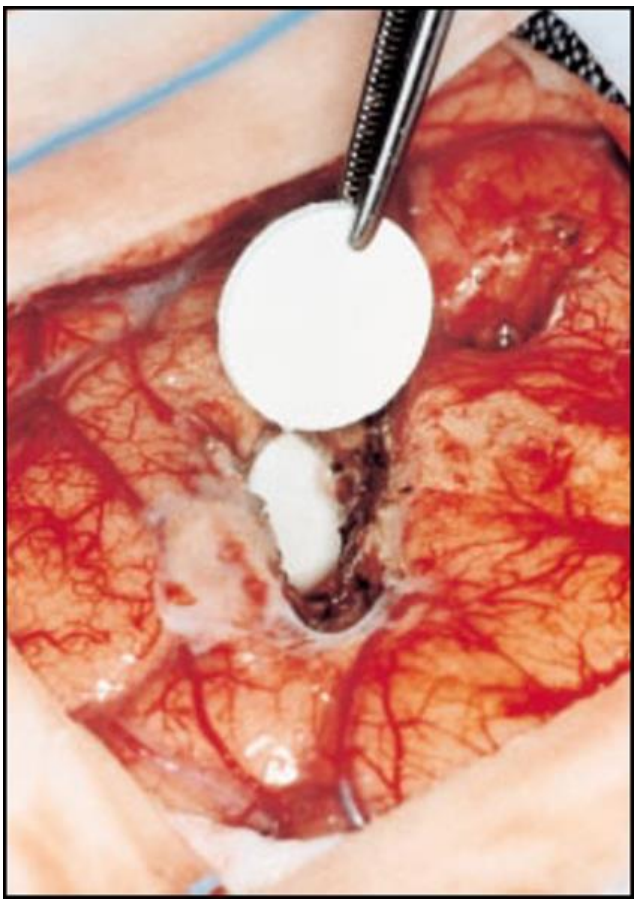

Figure 7 – Photograph showing implantation Gliadel wafers into a human brain following surgical resection of a malignant glioma. Reproduced from Fleming et al. (2012)[91].

The future for pre-formed drug eluting devices is promising, with many new, more sophisticated technologies entering development. For example, Struss

et al. developed a magnetically actuated microelectromechanical system (MEMS) drug delivery device that facilitated on-demand treatment of localised prostate cancer. Human prostate cancer xenograft mouse models treated with this device displayed reduced tumour growth rate and treatment side effects compared to IV and subcutaneous therapy controls[100]. A similar MEMS device containing temozolomide, developed by Masi et al. was assessed for efficacy in treatment of rodent glioma models[101]. In vivo efficacy studies highlighted treatment with this device resulted in the greatest extension of animal survival and the largest proportion of long term survivors compared to controls[102]. In another approach Ge et al. developed a biodegradable magnetic iron oxide microparticle/PLGA implant scaffold for targeted delivery of 5-FU loaded PLGA magnetic iron oxide nanoparticles. Magnetic scaffolds were implanted into a mouse tumour model, follow by injection of magnetic nanodrug into surrounding tissues. It was observed after 4 days a major fraction of injected nanodrugs had accumulated at the implantation site[103]. The combination of scaffold in vivo targeting, targeted cancer cell killing efficacy and sufficient durability and biocompatibility indicate the high potential of this device for treatment of bone cancer. Iontophoresis is a method where movement of hydrophilic and cationic/anionic drug molecules across a membrane is enhanced by an externally applied electrical field[104]. Byrne et al. developed an implantable iontophoretic system capable of deep chemotherapeutic delivery into solid tumours. Devices were implanted intratumourally and used to deliver and used to delivery FOLFIRINOX, a highly cytotoxic regimen containing folinic acid, 5-FU, irinotecan and oxaliplatin, for treatment of pancreatic cancer in a xenograft mouse model. Iontophoretic delivery of FOLFIRINOX was shown to increase tumour exposure by almost 10-fold compared to intravenous delivery, with mice treated with iontophoretic devices for 7 weeks demonstrating significantly greater tumour regression and negligible systemic toxicities compared to subjects receiving intravenous FOLFIRINOX therapy[105].

The immense range of materials, formulation methodologies and programmable controlled-release mechanisms allow for unprecedented opportunities for delivery of most chemotherapeutic agents using implantable technology, including utilisation of new and previously benched drugs that may

have previously failed with other administration routes[56]. Potential applications for drug-eluting polymer implants are diverse, including use as a first-line treatment for solid tumours, in cases where surgery is not possible and palliative care is required; use as a neoadjuvant therapy for downstaging of solid tumours to facilitate surgical resection and use as an adjuvant therapy to prevent metastasis post-surgery[106]. Furthermore, drug eluting polymer implants offer numerous clinical benefits over convention treatments with minimisation of patient risks, offering a new modality that displays significant synergistic combination with other therapies in the management of cancer[29]. Future development should focus on local delivery of combinational therapy with close consideration of factors such as drug concentration, exposure time, drug administration schedule and sequence of release. Additionally, while local delivery is a clear candidate for treatment of localised malignancies/lesions, treatment of tumours which are poorly localised or have spread, will likely require a carefully considered combinational approach of both local and systemic delivery[56].

1.4. 3D printing

Three-dimensional (3D) printing is an additive manufacturing (AM) technique that enables fabrication of 3D constructs based on computer aided designs (CAD) or even patient-specific medical images such as computer axial tomography (CAT) and magnetic resonance imaging (MRI). 3D printing allows fabrication of custom-designed, patient-specific objects from a variety of different materials with intricate internal and external geometries not achievable using other conventional techniques such as injection moulding and melt/solvent casting[107]. In addition, 3D printing can fabricate objects with complex shapes, compositions, gradients and functions in a single step, whereas conventional fabrication methods require multiple processing steps to achieve a final product with similar sophistication, enabling workflow simplification and improving cost efficiency[108]. 3D printing is an umbrella term for many different 3D printing processes that use various technologies, materials with different resolutions and build speeds[109]. The first 3D printing technique, stereolithography (SLA) was invented in 1986 with other

techniques invented shortly after[109]. Since the start of the 21st century, 3D printers have become progressively cheaper and easier to access due to patent expirations. For example, the cost of fused filament fabrication (FFF) printers has dropped from thousands of pounds to hundreds in the space of a decade and is available from a plethora of companies[107]. A common process exists for all 3D printing technologies. Firstly, the 3D models are designed using 3D CAD software or obtained from medical imaging such as CAT or MRI. The 3D model is converted into a file and sliced into a series of 2D cross-sectional layers which enables the 3D printer software to interpret and determine how layers are constructed. The 3D object is then printed in a layer-by-layer approach[109,110]. As an additive manufacturing (AM) technique, 3D printing has a shorter manufacturing time compared to subtractive fabrication techniques whilst enabling manufacture of complex, small volume objects, which is uneconomical using conventional manufacturing methods. In addition, 3D printing offers the following advantages: quick and easy customisation by changing materials and/or design; overall cost-efficiency, especially in the case of technologies such as FFF; minimal technical expertise is required to operate and adapt machines; on-demand fabrication suitable for in-house production or for fabrication in remote areas[110]. 3D printing has mainly been used as a rapid and cost-effective prototyping technique for a broad range of applications including aerospace, automotive, construction, jewellery, food and fashion[109]. Furthermore, 3D printing is becoming widely used for medical applications. More than 85 3D printed medical device products are currently marketed including implantable and non-implantable products including spinal cages, denture bases and surgical instruments[107]. 3D printing is expected to be an integral ubiquitous technology of the future, with a vision where objects or object components are developed using CAD or medical imaging, downloaded from the internet, and printed locally or at home using desktop 3D printers[108].

1.4.1 Common types of 3D printing

Below, a number of different 3D printing technologies are described and outlined. Stereolithography is omitted here and is instead discussed in greater detail later in the thesis.

Fused-deposition modelling

Fused filament fabrication (FFF) is an extrusion-based 3D printing technology. FFF was developed and founded in 1989 by the company Stratasys, and has become the most widely used 3D printing technology worldwide, with a plethora of applications in the pharmaceutical industry[111]. FFF fabricates 3D objects through deposition of layers of solidifying materials, until a desired object is formed (Figure 8). Materials utilised with this technology range from thermoplastic polymers to molten metals. Thermoplastics typically employed include polylactide (PLA), polyvinyl acetate (PVA), and acrylonitrile butadiene styrene (ABS). Feed materials are pre-processed as coiled filaments. The FFF printing process begins with mechanical feeding of thin filament into a heating element, which raises the material temperature to slightly above the glass transition or melting temperature of the feed material[108]. The (semi-)molten material is then extruded and deposited through a nozzle printhead in a layer-dependent pattern. After cooling and solidification of a layer, the print head moves vertically up and prints the next layer upon the previous. This process continues until the desired object is built[112].

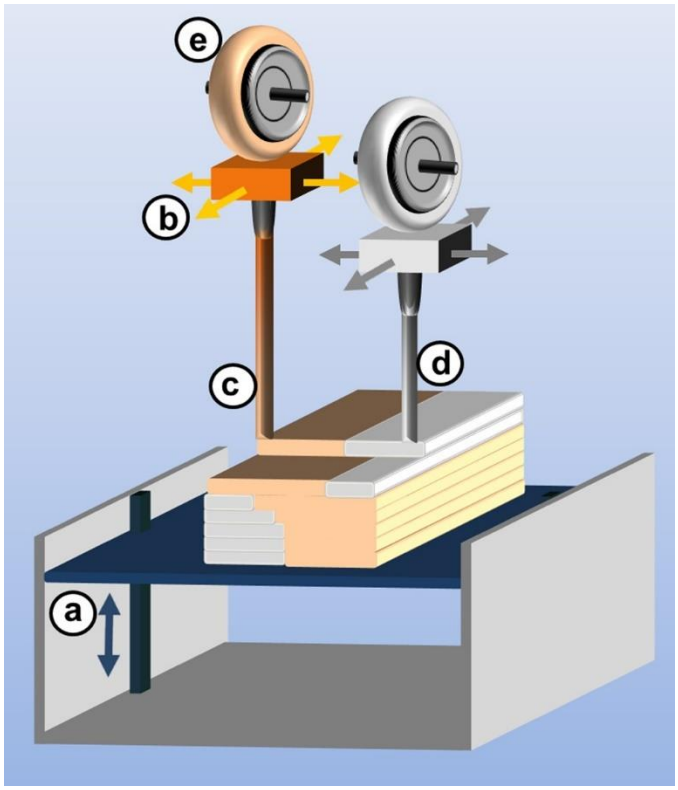

Figure 8 – Fused filament fabrication (FFF) comprising of (a) a vertically movable building platform, and (b) a tempered extrusion printing head for deposition of (c) model and (d) support material stored in (e) feedstocks containing filaments of thermoplastics wound on a spool. Reproduced from Ligon et al. (2017)[108].

Filaments of different blends of materials and additives, including amorphous solid dispersions, can be prepared through drug/organic solvent immersion or hot melt extrusion for use with an FFF apparatus. Polymer melt rheology, processing temperatures, build speeds, and CAD design dictate the success of an object build[108]. These parameters require fine-tuning for individual feed materials to not only ensure accurate material deposition, but also sufficient layer-to-layer bond formation to impart optimal structural strength[112]. An advantage of this method is that it does not require drying steps or post-treatment[109]. The main disadvantage of FFF is the requirement of high temperatures, typically 200 °C for material processing, which can lead to the degradation of additives such as APIs. The use of plasticisers, however, can

be added to polymer blends to decrease processing temperatures and better protect thermolabile constituents[112]. FFF also suffers from limited spatial resolution due to fixed printhead extrusion diameter requirements[108]. Another downside is that the FFF process builds product and support structure together, and the subsequent separation process can flaw end-object structural integrity and functionality[111].

Selective laser sintering

Selective laser sintering (SLS) was first introduced by Carl Deckard in 1986 and subsequently acquired and marketed by 3D Systems Inc[108]. SLS is a powder-based printing technology that uses a laser to sinter thin layers of powdered materials, layer by layer, to form a solid structure. SLS involves three building steps; powder deposition, powder solidification, and lowering of the build platform by one-layer thickness. These steps are repeated until the final object is formed. The process utilises a laser source to selectively scan over the powder surface, according to CAD-defined cross-sectional profiles, and locally irradiate powder particles within a thin layer. Laser absorption raises local powder temperature with subsequent sintering and fusion of adjacent particles, forming a solid mass[113]. The powder deposition step is conducted using a roller that distributes powder particles from a hopper across the building envelope[114]. The process chamber is kept a few degrees below material softening point to decrease processing time and reduce cooling-induced internal stresses and distortions. Loose powder particles remain on the build platform acting as support material, allowing for fabrication of intricate parts without support building[108].

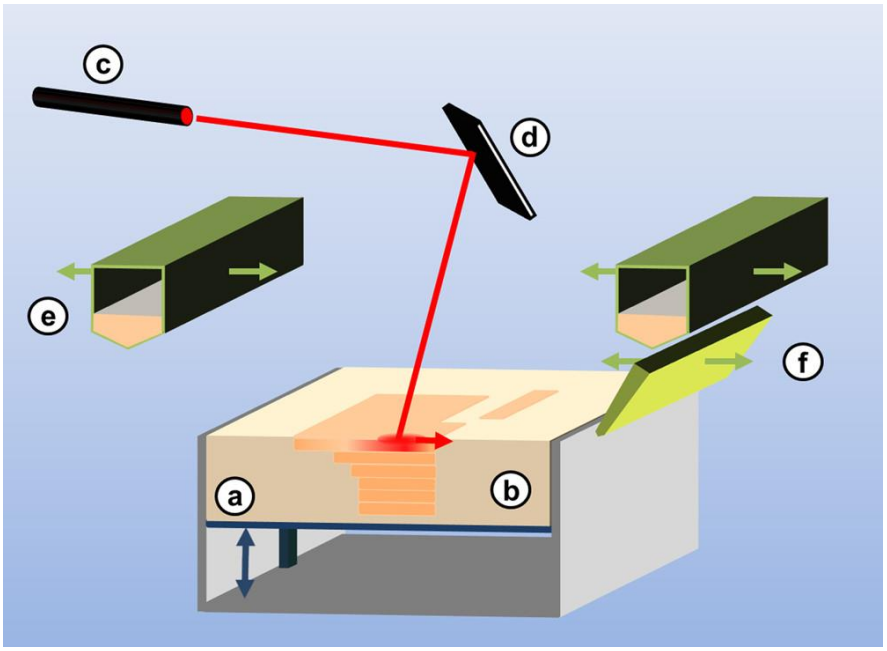

Figure 9 – (Selective) laser sintering process comprised of (a) vertically movable build platform, (b) powder bed with embedded, sintered model layers, (c) laser source and (d) laser optics, (e) powder feedstock and deposition hopper, and (f) blade for powder distribution and levelling. Reproduced from Ligon et al. (2017)[108].

The sintering process intrinsically fabricates objects with porous internal structures and rough surfaces. Post-processing steps such as isostatic pressing, infiltration with suitable resins, or additional sintering are utilised for objects requiring high mechanical strength[115], whereas procedures such as milling and coating are used to improve object surface properties[116]. SLS allows for processing with a wide range of materials, including polymer and ceramic based powders[116]. Polymeric powders are normally semi-crystalline thermoplastics, but can also be amorphous thermoplastics, two-component thermosets, and elastomeric thermoplastics, ranging from cheap, abundant materials with unremarkable material properties to high-end high-performance engineering polymers with excellent mechanical properties. Powder characteristics such as flowability, laser absorption, and sintering behaviour strongly affect the accuracy and structural integrity of fabricated parts. It is of paramount importance material suppliers produce powders with precise

control over size (< 100 µm), size distribution and morphology to ensure build quality[108,117]. Polyamides are by far the most commonly used commercial SLS material due to established history, ease of processability, and cost-effectiveness[118]. High-density polyethylenes (HDPEs) and polypropylenes (PPs) are also commercially available and are suitable for applications requiring low mechanical demands[117]. Polyether ether ketone (PEEK) is considered a high performance SLS material attributed to its high temperature and mechanical stability, making it suitable for medical applications[119]. More recently, SLS compatible thermoplastic elastomers have entered the market offering low strength but high flexibility with potential applications as elastomeric functional parts, such as patient-specific orthopaedic insoles[120].

Inkjet-based 3D printing

Droplet-based (or inkjet-based) printing is a commonly used additive manufacturing technique that utilises precise jetting of liquid droplets onto a 2D substrate in a layer-by-layer manner[107]. Several different inkjet-based technologies exist. One technology, thermal inkjet printing, applies heat to a liquid ink, forming and propelling an ink droplet out of a print head[108]. One example includes a system developed by Brothers Industries that jets liquid thermoset resin onto a heated support to form objects[121]. Inkjet-based lithography (IJL) combines lithographic methods, associated with high resolution parts, with thermal inkjet jetting, associated with fast build speeds and large build volume. A typical setup includes a horizontally-moving thermal inkjet printhead composed of hundreds of nozzles, which jets small droplets of photopolymer onto the build surface. After deposition of one layer, the droplets are solidified by UV light irradiation. Like FFF and SLA, a dense support is required for IJL builds with overhangs or voids, necessitating object post-processing[108]. However, unlike SLA, IJL allows for fabrication of multi-material objects, and hence it is possible to build easy-to-remove object support structures with water-soluble bicarbonate and wax-based materials[122]. As with SLA, IJL utilises photocurable materials such as acrylate and methacrylate-based monomers and polymers. However, IJL has a narrow processing window setting strict requirements regarding resin viscosity and surface

tension. Non-reactive and reactive diluents are regularly employed to reduce resin viscosity. Furthermore, resins must be able to withstand high temperatures and therefore epoxy resins are not compatible with IJL systems[108].

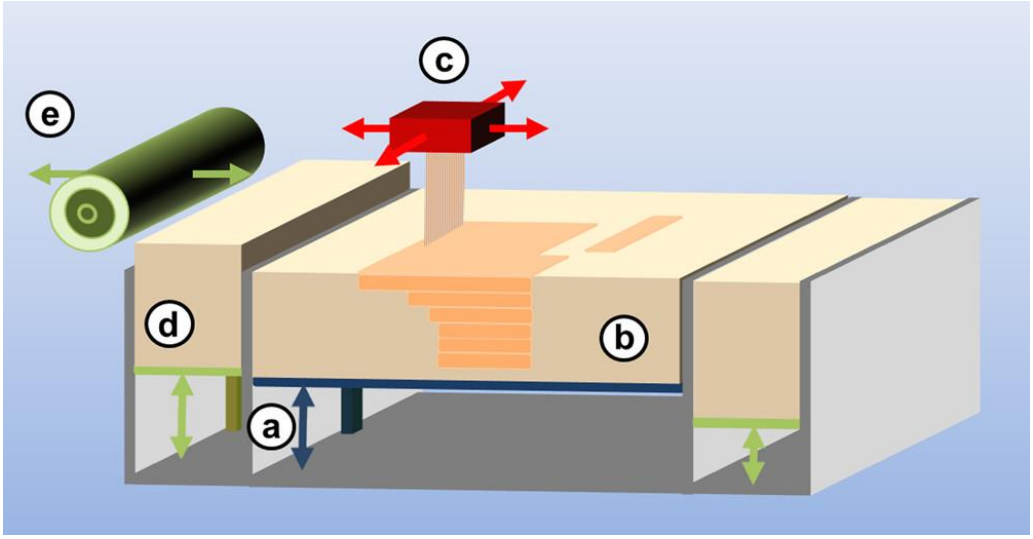

Figure 10 – 3DP comprised of (a) vertically movable build platform, (b) printed model embedded in supporting powder bed, (c) inkjet printing head for deposition of binder material, (d) support material feed stock, and (e) roller for powder distribution and levelling. Reproduced from Ligon et al. (2017)[108].

Aerosol jet printing (AJP) is another 3D material jetting technology based on atomisation of liquid solutions and dispersions in an aerosol chamber. The subsequent dense aerosol is transferred to a deposition head via an inert gas stream, which is focused and accelerated through a fine nozzle facilitating deposition of materials onto 3D substrates. Layer contours are printed by moving the build platform according to CAD data. Additional layers are deposited onto previously built structures[123]. Lateral resolutions of 1 – 10 µm and layer thicknesses of 100 nm can be achieved using AJP[124]. The high resolution and wide range of applicable materials, such as conductive, dielectric, and semiconductor inks, makes AJP particularly relevant within microfluidic and microelectronic fields. Other advantages of AJP include rapid build times and reduced material consumption[108].

3D powder binding (3DP) is a simple, versatile, cost-efficient, and high-speed 3D material jetting technology, first pioneered in 1986 and commercialised by Z Corp. Inc. (acquired by 3D systems in 2012)[125].The 3DP machine features a powder distribution unit, a vertically movable building platform, and an inkjet printing head enabling CAD guided material dispensing (Figure 10). In the first step, a layer of powder is deposited on the build platform. Next, the inkjet print head dispenses binder which binds particles together forming a solid mass. Finally, the build platforms move downwards by one-layer thickness, allowing for printing of a new layer on top of the previous[114]. Unlike other material jetting technologies, unbound powder particles remain on the building platform acting as a temporary support. 3DP fabricated objects are naturally porous and rough, and require post-processing procedures such as resin infiltration and coating to improve mechanical and surface properties. The main advantage of 3DP, as with IJL and AJP, is it allows for fabrication of objects with different binder inks within individual layers and is a popular technology for fabrication of 3D multicoloured models for 3D visualisation, planning, and concept modelling in medicine[108]. Materials utilised by 3DP include hydrophilic powders such as starch, plaster, and PVA that require aqueous binders such as water, whereas hydrophobic polymer particles such as PLA, PLGA and PCL can be bound together using organic solvents such as chloroform[126]. Binder printing inks can also contain metallic and ceramic powder particles such as silica or polymer solutions and dispersion to improve physical and end-use properties[108]. Drawbacks of the 3DP technique include difficulty in removing internal unbound powder from constructs designed to be porous, powder particle size dictates object layer thickness (usually 80 – 250 mm), and biomaterials for applications such as tissue engineering are not readily available in powder form and hence require pre-processing for 3DP[114].

1.4.2. Medical applications for 3D printing

The application of 3D printing in dentistry has existed since the late 1990s, where SLA was used to print wax moulds as templates for casting processes. More recently, due to progress of scanning technology and the advent of cheaper 3D printers and printable biomaterials, it is now possible to create

restorations such as fillings and crowns, physical models and guides, and orthodontic appliances such as braces and retainers using 3D printing[107]. Photopolymerisation and powder-based printing are the two most common techniques used within dentistry. SLA/DLP/IJL are used to create restorations, physical models and guides, and orthodontic appliances from photosensitive materials, commonly methacrylate-based resins, reinforced with metal or ceramic fillers. For example, Invisalign, a set of thin transparent plastic inserts designed using CAD software and manufactured using a SLA printed mould are a popular alternative to metal brackets with more than 100,000 parts made per day[108,127]. Reasons SLA/DLP are particularly useful for dentistry applications include rapid fabrication, high resolution, reasonable cost, good surface properties and the ability to print objects with intricate parts. However, parts fabricated using photopolymerisation-based additive manufacturing typically have poor mechanical properties, and restorations are therefore temporary[128]. Powder-based printing techniques including SLS and 3DP commonly utilise biocompatible metal alloys such as chrome, titanium, and steel alloys to make restorations. Polyamide powders are also used to create dental models and surgical guides. Long-term clinical studies are necessary to examine accuracy, reproducibility, and safety of 3D-fabricated dental devices[107].

The current focus of tissue engineering is to create functional tissues and organs for implantation and to develop tissue models to study tissue development/pathology and to perform drug screening and assess drug toxicity. Tissue engineered scaffolds provide structural support for cell attachment, migration, proliferation and an extracellular matrix. An ideal scaffold must be biocompatible, biodegradable, mechanically strong and porous to facilitate cell, nutrient and waste transport[107]. Conventional scaffold fabrication methods include freeze drying, leaching and electrospinning, but are not the best options for tissue mimicking constructs due to lack of tunability. 3D printing, however, offers precise control over features such as shape and size (using tomographic medical imaging), porosity, physical properties, and degradability[129,130]. A 3D-printing approach allows for scaffold cell seeding either post-print or pre-print, the latter referred to as ‘bioprinting’.

The most common methods for scaffold fabrication are FFF, 3D dispensing, SLS, 3DP and SLA/DLP/IJL[107], with popular materials including PCL, PLA and PLGA due to their biodegradable and biocompatible properties[108]. Only lithographic-based techniques and methods based on ambient temperature extrusion of water soluble polymers such as 3D dispensing are suitable for bioprinting, as other processes impact cell viability[108]. Hydrogels based on acrylate- or methacrylate-functionalised derivatives of PEG and biopolymers gelatin, chitosan and hyaluronic acid are common materials for bioprinting[108]. There are several commercially available tissue regeneration scaffolds. 4WEB medical, the world's first FDA-approved 3D-printed medical devices provider, offer a titanium alloy, web-structured post-print cell-seeded bone scaffold using direct metal laser sintering (DMLS), a process similar to SLS. The scaffolds design and structural strength promote bone healing and guide bone formation[131]. Another medical supplier, Stryker, developed the Tritanium LP – a posterior lumbar cage for treatment of degenerative disc disease constructed using DMLS[132]. A wide variety of tissues have been successfully bioprinted to date, including skin, bone, blood vessel, cardiac tissue, kidney, and liver, and even implanted into animal models[107,133]. Even larger companies such as L'Oreal have begun to explore bioprinting hair follicles as a treatment for hair loss[134].

Engineered human tissue models are an attractive pre-clinical platform for studying diseases and assessing effectiveness and safety of novel therapeutics[135]. Current pre-clinical platforms include patient-derived xenograft animal models, which is a lengthy and expensive process. Current fabrication methods, however, produce simplified, unrealistic constructs that affect model accuracy. 3D fabrication techniques allow for design of more sophisticated, biomimetic in vitro tissue models[136,137]. 3D printed models mimicking tumour microenvironments are ideal pre-clinical models, with inkjet-based, extrusion-based, and lithographic-based 3D printing techniques used to create such models[107]. For example, Zhao et al. used 3D dispensing to fabricate cervical tumour models with HeLa cells embedded in gelatin/alginate/fibrinogen hydrogels. The 3D-printed model demonstrated higher metalloproteinase protein expression, improved cell proliferation rate

and greater chemoresistance than a 2D culture, and more akin to a realistic tumour microenvironment[138]. Despite promising efforts, 3D fabrication techniques are currently unable to construct complex multicellular systems composed of cancer cells, immune cells, and vasculature that forms complete cancer microenvironments[107]. Liver tissue engineering is an emerging platform for drug testing and screening. For example, Chang et al. 3DP bioprinted a micro-liver model consisting of hepatocytes embedded in alginate, to study drug metabolism[139], whereas Matsusaki et al. utilised inkjet 3D fabrication to construct multi-layered hepatocyte/endothelial cells on a chip for evaluation of drug toxicity[140]. Beyond academic research groups, medical research companies have also developed engineered human tissues models using 3D bioprinting. For example, Organovo constructed a 3D bioprinted human liver tissue model comprised of parenchymal and non-parenchymal cells for pre-clinical drug testing[141]. 3D bioprinting has also been used to develop skin tissue models. For example, Lee et al. utilised an eight-channel droplet-based printer to build an accurate in vitro skin model from keratinocytes and fibroblasts embedded within a collagen matrix. The printed cells proliferated and formed a tissue through intercellular adhesion and communication[142]. Cosmetics company L'Oreal and Organovo bioprinted human skin tissues to evaluate effectiveness of topical cosmetic products[143]. As with tumour models, inability to 3D bioprint vasculature limits the size, lifespan and overall accuracy of 3D-printed tissues as pre-clinical platforms. However, recent studies have demonstrated the potential of 3D-bioprinted vasculature and the construction of a larger, perfused living tissue model[144].

3D fabrication techniques are also an attractive avenue for medical device construction. 3D printing allows for fabrication of personalised medical devices that are anatomically moulded to the patient. Firstly, several medical institutions have fabricated and utilised 3D fabricated medical instruments[107]. For example, Kunz et al. used FFF 3D printing to create surgical guides to assist repair of a patient's articular cartilage defect[145] and Rankin et al. fabricated a PLA-based sterilisable surgical retractor using FFF[146]. 3D printing has also been utilised for fabrication of customised implants and external orthoses/prostheses. Techniques such as SLS and 3DP are preferable for

such applications as they utilise biocompatible and implantable materials such as metal alloys, ceramics, PEEK, and UHMWPE, and form objects with high mechanical and surface properties. 3D-fabricated implants have been used in craniomaxillofacial, thoracic, spine, and orthopaedic surgery[107]. For example, ZCorp and DePuy Synthes have fabricated patient-specific implants based on PEEK and titanium for partial skull and mandibular reconstructions using 3DP and SLS[147,148]. PCL-based implants fabricated using SLS were used to prevent tracheal collapse in paediatric patients whilst facilitating airway growth. The implants provided mechanical airway support for several months and were gradually biodegraded[149]. A number of manufacturers have utilised electron beam melting (EBM), another 3D fabrication technique, to produce and market FDA-approved lightweight, high strength orthopaedic implants. Beyond implants, 3D printing has been used to manufacture assistive orthoses/braces and prostheses. Commonly produced devices include foot orthoses, ankle-foot orthoses and prosthetic sockets. Materials utilised include polyamide, ABS, and polypropylene, owing to their mechanical strength, and the primary 3D printing techniques used are SLS and FFF. Face, nasal and ear prostheses for aesthetic reconstruction utilise SLA, FFF, 3DP and SLS techniques for fabrication of high resolution moulds to cast silicone-based prostheses[107]. 3D printing has also revolutionised the hearing aid industry, primarily used to produce shells that hold hearing aid components. 3D printing is particularly useful as it allows for fabrication of personalised models that perfectly fit in the patient's ear. Today, approximately 99% of hearing aid shells worldwide are fabricated using SLA[150].

3D-printed anatomical models for pre-surgical planning and training are increasingly popular, as they allow printing on-demand from imaging techniques such as computer tomography (CT) and magnetic resonance imaging (MRI). Pre-surgical planning models have numerous applications in craniomaxillofacial, cardiothoracic, tumour and other surgeries[107]. In addition, 3D-printed models are incredibly valuable for assisting complex and rare case surgeries. Evidence has shown use of 3D-printed surgical models has led to increased confidence of surgeons and their success rate, and enhanced doctor-to-patient rapport. Studies also show 3D-printed models improve

anatomical learning experience and outcome for students[151]. A number of techniques can be utilised to produce medical models. Single-colour models can be produced using SLS and SLA techniques. FFF-printed models are cost-effective but have poor resolution and surface properties. 3DP and IJL allow for multi-colour, multi-material models that can improve tissue differentiation and simulate the texture of soft and hard tissues. Limitations of current models are they do not allow for dissection as printing materials are too hard or brittle and secondly, resolution of certain techniques do not allow for accurate fabrication of delicate, thin biological structures[107].

1.4.3. 3D printed drug delivery systems

The application of 3D printing in the field of drug delivery has also been investigated and more recently realised with the FDA approval of 3D printed orodispersible tablet, Spritam, in August 2015. Spritam, manufactured by Aprecia Pharmaceuticals, are highly porous, fast disintegrating tablets, produced using 3DP technology, for the treatment of epilepsy. API levetiracetam (60 – 90% w/w), cellulose, mannitol and colloidal silicon dioxide form the powder matrix of these tablets, bound together with a solution of water, PVP, glycerol and surfactant[152,153]. 3D printing can offer many benefits over conventional drug formulation methods. Firstly, 3D printing facilitates manufacture of systems and devices of varying polymer and additive compositions, containing single or multiple drugs, with modifiable geometries and internal structure, affording drug delivery systems with programmable drug-release profiles. In addition, by changing object dimensions and infill, and therefore solid material content, systems with variable pre-defined dosages can be easily produced[109,154]. Such benefits make 3D printing a desirable technology for personalised medicines, enabling rapid production of drug delivery systems with dosages and release profiles tailored for a specific patient group – paediatrics or geriatrics, a specific disease burden or even an individual patient. Furthermore, 3D printing allows for on-demand production of medicine for emergency use, or for immediate use of formulations with poor storage stability[112]. Other advantages include accurate control over special

distribution of multiple APIs within a dosage form, preventing drug-drug incompatibilities; fabrication of personalised dosage forms without high volume manufacture, reducing material wastage; and potential dosage form taste and aesthetic personalisation to improve patient adherence[112]. 3D fabrication techniques thoroughly explored for formulation development include 3DP, FFF and 3D dispensing.

In addition to Spritam, 3DP has been extensively applied for preparation of drug delivery systems[109]. Lin et al. manufactured three different subdermal implant designs for release of ethinylestradiol using 3DP. In vitro and in vivo studies demonstrated one design provided a steady level of drug release for 5 weeks before gradual decline and maintained structural integrity during a 5-month implantation period[155]. Antibiotic-eluting tricalcium phosphate-based scaffolds have also been developed by several groups using 3DP and have demonstrated several advantages over conventional drug-eluting scaffolds such as high sustained drug release rates, resorbable properties removing need for surgical removal and facilitation of multi-drug therapy[156,157]. 3DP fabrication of pharmaceuticals has also focused on dosage forms with layered 3D structures and variable drug loadings to achieve a variety of complex formulation designs such as core-shell, layered, multicompartment, and porosity/concentration gradient designs that enable drug release profiles such as fast-dissolving, zero/first-order, or pulsatile for single or multiple drugs[109]. For example, Katstra et al. fabricated cellulose-based delayed release tablets containing a chlorpheniramine-loaded layer, sandwiched between two non-drug layers[158]. Rowe et al. fabricated four different types of oral drug delivery systems with different drug delivery profiles, including immediate-extended release tablets, breakaway tablets, and (enteric) dual pulsatory tablets. Different drug delivery profiles were achieved by adjusting polymers used, and their concentrations, in the powder material and/or binder solution[158]. In another example, Yu et al. was able to fabricate controlled-release tablets with high drug loadings up to 68% w/w, by adding API to the powder bed instead of the binder solution[159]. Yu et al. further increased drug loading by incorporating drug both in the powder bed and in the binder solution. To prevent burst release associated with high-drug loadings, the outer edges of

the tablets were printed with a release-retardant binder solution, producing tablets that provided a high yet linear drug release[160].The high porosity and surface area of 3DP-printed tablets facilitates rapid tablet disintegration within the oral cavity, making them viable candidates as fast disintegrating tablets/oral disintegrating tablets (FDTs/ODTs). Lee et al. prepared mannitol-based oral fast disintegrating tablets containing captopril. Dispersion time of tablets could be decreased by reducing binder liquid content per tablet[161]. Drawbacks of the 3DP technique for drug formulation include poor mechanical properties, potential presence of residual organic solvent and low drug loading[109,162].

Drug formulations fabricated using FFF typically exhibit high precision and good mechanical strength, with hollow, porous or complex internal structures possible, allowing for tablets of different shapes with different controllable drug release profiles with drug loadings of 5 – 10%[109]. The FFF method can also produce drug delivery systems with multiple APIs. For example, Goyanes et al. fabricated paracetamol and caffeine formulations as layered caplets or caplet-in-caplet systems using FFF[163]. FFF printed devices prepared from antimicrobial nitrofurantoin-loaded PLA filaments have been investigated for use as personalised therapy devices such as catheters and implants[164,165]. Intrauterine systems based on either biodegradable PCL[166] or non-biodegradable ethylene-vinyl acetate (EVA)[167], containing anti-inflammatory indomethacin, have been prepared using FFF, with potential applications as contraceptives or local drug delivery devices. Pharmaceutical grade polymers have demonstrated compatibility with the FFF process including PVP, methacrylic polymers, cellulose derivatives, PCL-PVA-PEG triblock copolymer Soluplus and PVA-PEG deblock copolymer Kollicoat[109]. Drawbacks of the FFF process for drug formulation include limited pharmaceutical grade materials and incompatibility with thermolabile APIs[109,162].

3D dispensing has been utilised for development of a variety of novel controlled-release drugs such as multi-layered tablets, multi-drug multicompartment tablets, and local drug delivery patches. Unlike FFF, the extrusion-process is pressure-controlled and prevents degradation of

thermolabile API. Rattanakit et al. fabricated a drug delivery device by depositing PVA-dexamethasone paste between PLGA films using 3D dispensing. Controlled long-term release of drug was observed, where drug-release kinetics were determined by device geometry[168]. Khaled et al. utilised 3D dispensing to fabricate five-in-one multidrug polypills. The formulation displayed no drug-drug incompatibility due to physical separation of drug compartments, and demonstrated controlled drug release and acceptable mechanical properties[169]. 3D dispensing can also facilitate development of targeted cell therapy formulations. For example, Song et al. 3D printed PCL/PLGA strengthened alginate hydrogel containing cyclosporin A loaded PLGA microspheres for local anti-rejection therapy post-xenogeneic cell transplantation[170]. The device achieved suppression of immune rejection in treated mice. 3D dispensing has also been used to develop implantable scaffolds capable of drug delivery. Zhu et al. manufactured implantable bioactive scaffolds containing isoniazid and rifampicin, combining regenerative medicine and multi-drug therapy for the effective treatment of osteoarticular tuberculosis. Scaffolds demonstrated prolonged drug release and negligible systemic toxicity compared to traditional treatment[171]. Yi et al. fabricated a 5-FU loaded implantable biodegradable patch from a PLGA/PCL paste using 3D dispensing for local treatment of pancreatic cancer. In vivo studies indicated patches provided drug release over a period of four weeks and significantly supressed tumour growth in pancreatic cancer xenograft mouse models with minimal systemic side effects[172]. Drawbacks of this technique for drug formulation is associated with solvent use, with consequent object deformation and presence of residual organic solvent in products affecting drug release kinetics and biocompatibility, respectively[109,162].

Application of SLS and SLA for drug formulation development is less attractive than other 3D printing techniques. With SLS, limited pharmaceutical grade excipients and API compatible with SLS, extensive posttreatment requirements and lack of affordable SLS printers have lessened its impact within drug formulation development. Likewise, lack of materials of suitable biocompatibility and physical properties, risk of toxic unreacted resin in products and single resin per print restrictions diminish the utility of SLA in drug

delivery system creation. However, studies have indicated both their potential use. For example, Salmoria et al. fabricated a reservoir-type drug delivery system with model drug progesterone using SLS that demonstrated zero-order drug release[173], whereas Goyanes et al. fabricated PEGDA-based multi drug-loaded tablets with tailorable release[174]. Drug delivery systems fabricated using stereolithography will be discussed in broader terms later in the thesis.

1.5. Case study - 3D printing porous copper chloride polymer composite intrauterine devices

Before undertaking the current body of work, a separate project was conducted. The goal of this project was to develop and fabricate a contraceptive intrauterine device (IUD) using SLA 3D printing. Conventional IUDs are formed of a plastic T-shaped frame with pure metallic copper wire woven around the vertical section. Cupric ions are released from the device by corrosion of the copper wire. Cupric ions act as a spermicide within the uterus, inhibiting sperm motility and viability, preventing ova fertilisation. In addition, copper corrosion can induce endometrial inflammation, preventing implantation of fertilised ova. IUDs are an effective, inexpensive, and safe form of contraception and are considered a first-line contraceptive choice for any woman with no medical contraindications. However, the discontinuation rate of IUDs is relatively high (8 – 12% at one year) with the most common reasons for discontinuation being menstrual bleeding and pain following insertion. These adverse effects are highly associated with an initial burst release of cupric ions from the device, and hence efforts have been made to achieve IUDs with controlled zero-order release of cupric ions.

The aim for the project were to develop a porous IUD containing copper chloride, homogenously distributed throughout the device, as a source of cupric ions. A copper salt was used instead of metallic copper as literature suggested that cupric ions can remain trapped in metallic copper corrosion products, depleting the available payload and reducing device effectiveness. Furthermore, it was speculated controlling device porosity (through design)

and consequently, device surface area, would facilitate tailorable cupric ion release kinetics. Tailorable release kinetics could permit controlled and sustained diffusion of cupric ions over a period of years, as is required for an IUD.

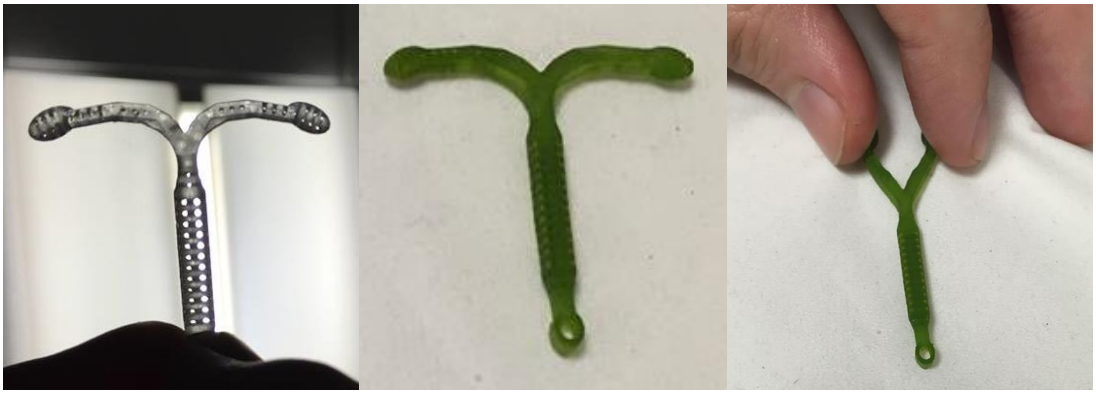

Figure 11 – Images showing SLA 3D printed IUDs. Left image highlights device porosity achievable through print design. Middle image shows an SLA 3D printed IUD containing copper chloride. Right image highlights flexibility of device.

Despite the apparent success of this project (Figure 11), three major problems became apparent during the course of this project. Firstly, the end device did not mechanical properties that are required for an IUD. This was attributed to the use of Formlabs Flexible resin (FLFLGR01), which produce materials with tensile strength below that required. Whilst other Formlabs resins can produce parts with suitable tensile strength, such parts are too stiff for use as an IUD. Furthermore, designed porosity and the inherent nature of SLA 3D printed parts meant IUDs were incredibly brittle, breaking with minimal manipulation. This is unacceptable, as such as device must be resistant to breaking during insertion and throughout its implantation lifetime. Secondly, due to the proprietary nature and therefore, unknown composition of Formlabs resins, properties such as short-term and long-term biocompatibility, vital for an IUD, are ambiguous. (Meth)acrylate-based monomers/macromers, the major constituent of most SLA 3D printing resins are considered irritants, meaning uncured monomers/macromers must be removed before a part can be considered biocompatible. Furthermore, “cleaned” (meth)acrylate-based parts

can still present toxicity issues, casting doubt over the use of such materials as IUDs. Finally, SLA 3D printing using Formlabs Flexible resin containing 1.5% w/w copper chloride (dihydrate), using the dedicated print settings for Formlabs Flexible resin was unsuccessful. Loading of IUDs with copper chloride were achieved through immersion of a “blank” SLA 3D printed IUD in a saturated 50:50 ethanol/IPA solution containing copper chloride dihydrate. Reasons for print failure were attributed to the addition of copper chloride to the resin, which likely affected the “curing” process of the resin ultimately leading to failed printing. Each of these problems require attention if fabrication of IUDs through SLA 3D printing is to be realised.

2. Aim of thesis

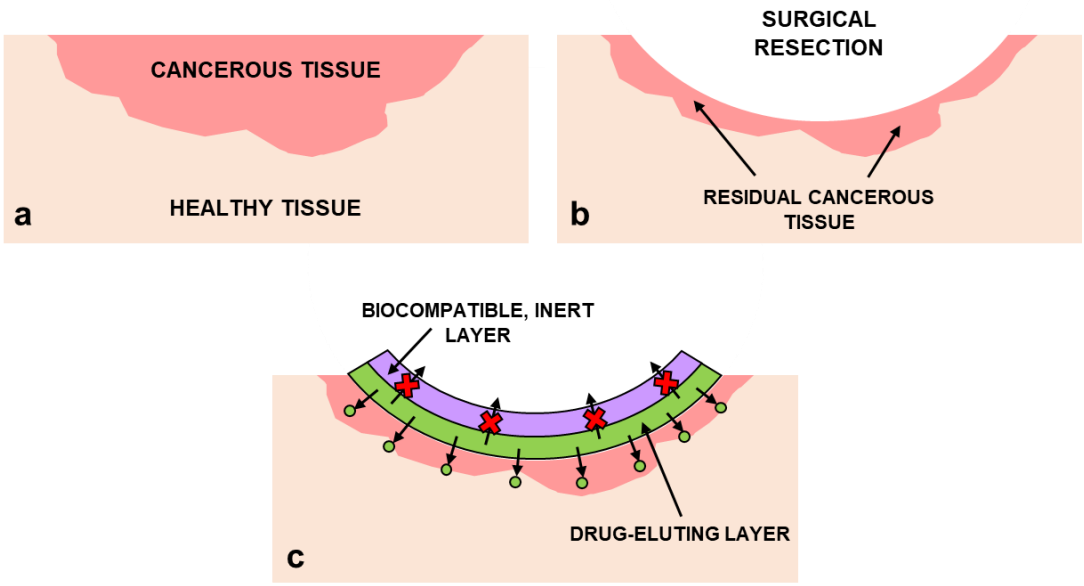

Figure 12 – Illustrations highlighting concept of proposed device. Surgical resection of cancer tissue (**a**) can result in a border of residual cancerous tissue (**b**), which, if left untreated, can lead to cancer recurrence. Proposed device could be custom fit to the resection cavity through SLA 3D printing, and could provide a unidirectional local release of chemotherapeutics, with aim to prevent cancer recurrence.

The initial aim of this project was to obviate the need for oral or intravenous systemic dosing of chemotherapeutics through development of a 3D printed drug-eluting implant for local treatment of solid tumours. The main intended application of this device would be as adjuvant therapy to tumour resection surgery. The device would be implanted into the cavity created from resective surgery and provide local release of chemotherapeutics, with aim to prevent recurrence of cancer through elimination of residual remnant cancer cells that remain post-surgery. This therapy could be used in combination with other adjuvant therapies. For example, a drug-eluting implant could be used to subsidise systemic chemotherapeutic dosing, allowing for reduction and management of dose-limiting toxicities associated with a systemically dosed treatment, whilst achieving high local drug concentrations and optimisation of chemotherapeutic treatment. The drug-eluting implant may also provide a

viable primary treatment option for non-resectable tumours. The device could be placed into a surgically created cavity near the malignant tissue and provide a certain degree of local drug release. In combination with other primary therapies, treatment may allow reduction of tumour size, facilitating surgical treatment, or simply alleviate patient discomfort and increase number of patient quality-adjusted life years (QALYs).

Before SLA 3D printing can even be considered for the fabrication of implantable devices with sophisticated, programmable drug release kinetics, the three issues raised from the IUD case study must be addressed, and hence form the basis of this thesis. The first issue of unsuitable mechanical properties is addressed through synthesis and characterisation of a range of current and novel photopolymers, which will be compared against reference materials, in attempt to identify suitable implantable materials. The second issue of material toxicity will be addressed through exploration and utilisation of different post-processing procedures to (meth)-acrylate-based materials biocompatible. Furthermore, alternative non-toxic photopolymer systems will be explored and assessed for potential use within the SLA 3D printing process. The final issue of incompatibility of custom resins with Formlabs SLA 3D printers will addressed through development of an RT-FTIR spectroscopy tool that should assist formulation of Formlabs-printable custom resins. In addition, an adapted printing setup will be developed for the Formlabs SLA 3D printer, with aim for increasing efficiency and output of these systems. Finally, extensive drug release studies will be conducted with aim to characterise effect of different SLA 3D printed materials on drug release kinetics.

3. Materials and methods

3.1. Materials

Reagents poly(ethylene glycol) ~400, ~1000, ~2000; poly(caprolactone) diol ~530, ~2000; poly(tetrahydrofuran) ~650, ~1000, ~2000; poly(propylene glycol) ~1200 and ~2000 were purchased from Sigma-Aldrich. Poly(caprolactone) diol ~1250 was purchased from Polysciences Europe and GmbH. Poly(propylene glycol) ~425 was purchased from Acros Organics. All other reagents were purchased from either Sigma-Aldrich, Fischer Scientific UK, Acros Organics, Alfa Aesar and ChemCruz.

Materials poly(ethylene glycol) diacrylate ~575 (PEG575DA), poly(ethylene glycol) dimethacrylate ~550 (PEG550DMA), 2,2′-(Ethylenedioxy)diethanethiol (dithiol CTA), trimethylpropane tris(3-mercaptopropionate) (trithiol CTA), pentaerythritol tetra(3-mercaptopropionate) (tetrafunctional CTA), ethyl lactate (EL) beta-carotene, diphenyl(2,4,6-trimethylbenzoyl) phosphine oxide (TPO), isobornyl acrylate (IBOA), bisphenol A ethoxylate (15EO/P) dimethacrylate and bisphenol A ethoxylate (2EO/P) diacrylate were purchased from Sigma-Aldrich. Hydroxyethyl acrylate (HEA), hydroxyethyl methacrylate (HEMA), isophorone diisocyanate (IPDI), hydroquinone (HQ) and α-tocopherol (AT) was purchased from Acros Organics. 4-methoxyphenol was purchased from Merck Millipore. Formlabs Clear Resin, Formlabs Dental Resin and Formlabs Flex Resin were purchased from Formlabs. Silmer ACR Di10, Silmer ACR Di50 and Silmer ACR D208 were kindly provided by Siltech, Canada. Sylanto-7MP (P3C-P) and Sylanto 7MS (P3C-Sb) were kindly provided by Synthos Chemical Innovations, Poland. Orasol Orange G dye was purchased from Kremer Pigmente, US.

Solvents toluene (extra pure, SLR, low in sulfur), hexane (extra pure SLR grade) and cyclohexane (extra pure) were purchased from Fischer Scientific UK. Dichloromethane (puriss), diethyl ether (puriss), acetone (puriss), tetrahydrofuran (HPLC grade, inhibitor free), ethanol (absolute, puriss), ethyl acetate (puriss), isopropanol (puriss) and acetonitrile (HPLC grade) were

purchased from Sigma-Aldrich. Solvents decalin (98%, mixture of cis and trans) and triethanolamine (99+%) were purchased from Acros Organics. Solvent dimethylformamide (PepSyn grade) was purchased from Rathburn Chemicals Ltd. Anhydrous solvents dichloromethane (≥99.8%), triethylamine (≥99.5%), toluene (99.8%), tetrahydrofuran (≥99.9%, inhibitor free) were purchased from Sigma-Aldrich. Anhydrous solvent acetone (99.8%, extra dry) was purchased from Acros Organics.

General lab reagents potassium carbonate, sodium hydroxide, magnesium sulphate and sodium chloride were purchased from Fischer Scientific UK. General lab reagent hydrochloride acid 37% was purchased from VWR Chemicals.

3.2. Compound synthesis

3.2.1. General methods

All reactions requiring the use of dry conditions were carried out under an atmosphere of nitrogen and all glassware was pre-dried in an oven (110 °C) and cooled under nitrogen prior to use. All reactions were followed by TLC and NMR analysis. FTIR spectra of compounds were acquired using a Bruker ALPHA Platinum FT-IR spectrometer with ATR sampling, USA. Samples were deposited onto the spectrometer optical window (< 5 mg) as a thin layer. Spectra were acquired at 4000 cm^{-1} to 400 cm^{-1}, at a resolution of 4 cm^{-1} and a sample and background scan time of 16 scans. ^{1}H NMR and ^{13}C NMR analyses of compounds were recorded on a Bruker AV400, operating at 400 MHz for proton and 101 MHz for carbon, or a Bruker AV500 spectrometer operating at 500 MHz for proton and 126 MHz for carbon. Chemical shifts (δ_H and δ_C) are quoted as parts per million downfield from 0. The multiplicity of a ^{1}H NMR signal is designated by one of the following abbreviations: s = singlet, d = doublet, t = triplet, q = quartet and m = multiplet. High resolution mass spectra of compounds were carried out at University of Swansea.

3.2.2. Preparation of telechelic diacrylate monomers

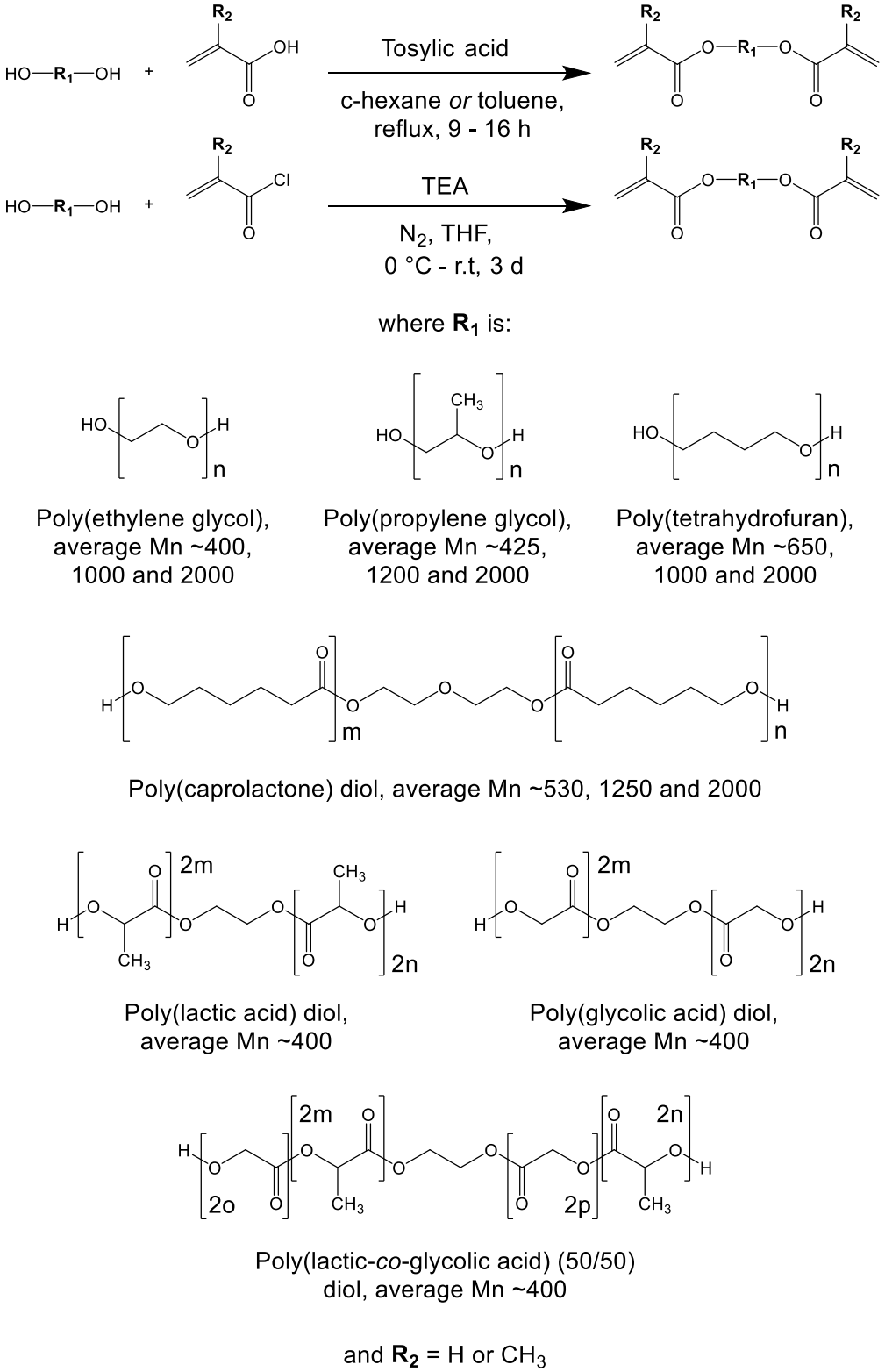

Figure 13 – Reaction scheme for preparation of telechelic diacrylate monomers via a tosylic acid/(meth)acrylic acid method or via a (meth)acryloyl chloride method

Tosylic acid/(meth)acrylic acid method

Synthetic route adapted from Guan et al. (2000)[175]. Poly(tetrahydrofuran) (PTHF) ~1000 Mn (60 g, 60.0 mmol, 1 equiv.), acrylic acid (10.79 mL, 157 mmol, 2.62 equiv.) or methacrylic acid (13.25 mL, 157 mmol, 2.62 equiv.), tosylic acid (1.054 g, 6.12 mmol, 0.102 equiv.), hydroquinone (0.211 g, 1.920 mmol, 0.032 equiv.) and cyclohexane (300 mL, 0.200 reaction molarity) were charged into a 500 mL round-bottom flask attached with a Dean-Stark water collector, condenser and a magnetic stirrer. The reaction mixture was refluxed at 110 °C until the amount of water distilled in the Dean-Stark equalled the theoretical yield (2.16 g, 120 mmol, 2 equiv.). The solution was treated with excess potassium carbonate until strongly basic and stirred for 3 h at 40 °C. The solution was filtered, and the filtrate washed repeatedly with 200 mL dilute 1M sodium hydroxide until the aqueous phase was colourless. The organic phase was washed with 200 mL water, 200 mL brine, and then dried using magnesium sulphate. Excess solvent was removed using a rotary evaporator and the product then further dried under high vacuum at room temperature for 2 days to afford a slightly yellow, viscous resin. Preparation of diacrylates with different spacers were carried out using reagents in the same equivalences as above. Diacrylates and dimethacrylates of PTHF ~650 Mn and ~2000 Mn were prepared using the same reaction conditions and workup. Diacrylates of poly(ethylene glycol) (PEG) ~1000 Mn and ~2000 Mn, and hydroxyl-capped poly(caprolactone) (PCL) ~530 Mn, ~1250 Mn and ~2000 Mn were reacted in toluene instead of cyclohexane due to insolubility of spacer reactants. Diacrylates of poly(propylene glycol) (PPG) ~425 Mn, ~1200 Mn and ~2000 Mn required a greater excess of acrylic acid (3.61 equiv.) tosylic acid (0.165 equiv.) and a longer reaction time to reach completion. Workups for diacrylates of PEG, PCL and PPG deviated from the above workup. For PEG diacrylates, upon reaction completion, the organic phase was dried using magnesium sulphate and filtered. Excess toluene was removed using a rotary evaporator. The crude product was re-dissolved in a minimum amount of dichloromethane (DCM) and precipitated into a large excess of diethyl ether (DE). This step was repeated three times. Precipitate was obtained by filtration and dried under

high vacuum for 2 days affording a white, waxy solid. For PCL diacrylates, after treatment with potassium carbonate, stirring at 3 h at 40 °C and subsequent filtration, the filtrate was diluted with a large volume of toluene before undergoing washes with dilute 1M sodium hydroxide thrice, 1:1 brine solution twice, water once and dried with magnesium sulphate. Excess solvent was removed using a rotary evaporator. The product was further dried under high vacuum at room temperature for 2 days to afford slightly yellow viscous resins or waxy solids. For PPG diacrylates, after treatment with potassium carbonate, stirring at 3 h at 40 °C and subsequent filtration, the filtrate was dried using magnesium sulphate and filtered. Excess cyclohexane was removed using a rotary evaporator. The product was further dried under high vacuum at room temperature for 2 days to afford slightly yellow resins of varying viscosities. Preparation of PTHF diacrylates utilised this workup at later stages.

PTHF650, 1000 and 2000 diacrylate (%) yields (actual yield/theoretical yield x 100%) = 75 – 85%. PPG425,1200 and 2000 diacrylate yields = 70 – 85%, PEG1000 diacrylate yields = 20 – 35%, PEG2000 diacrylate yields = 70 – 80%, PCL530 diacrylate yields = 10 – 25%, PTHF650 dimethacrylate yield = 78.51%.

(Meth)acryloyl chloride method

Hydroxyl-capped PCL ~530 Mn (24.70 mL, 50 mmol, 1 equiv.), triethylamine (20.91 mL, 150 mmol, 3 equiv.) and anhydrous THF (100 mL) were charged into an oven dried round-bottom flask under nitrogen and sealed with a rubber septum. The flask was then cooled to 0 °C. Acryloyl chloride (12.19 mL, 150 mmol, 3 equiv.) diluted in anhydrous DCM (25 mL) was added dropwise over 2 hours to the reaction vessel using a syringe pump. The solution was stirred for 12 h at 0 °C and then for 24 h at room temperature. Upon reaction completion the triethylamine chloride salts that had formed were removed by filtration over alumina. DCM was removed using a rotary evaporator and the crude product re-dissolved in 50 mL diethyl ether. Any further triethylamine hydrochloride salt precipitate was removed by filtration. Diethyl ether was

removed using a rotary evaporator and the crude product was precipitated into cold hexane. The mixture was frozen to allow removal of hexane by decanting and the product was dried under high vacuum for 2 days affording a viscous orange resin. Preparation of diacrylates with different spacers were carried out using the same reaction conditions and reagent equivalences as above. Crude products were dissolved in solvents such as diethyl ether, THF, acetone, ethyl acetate accordingly to aid removal of triethylamine hydrochloride salts by insolubility. Triethylamine hydrochloride salts were removed by additional filtration, and all products were precipitated into cold hexane. PLA, PLGA 50/50 and PGA dimethacrylates were synthesised utilising the same procedure as above, except for the use of methacryloyl chloride (15.68 mL, 150 mmol, 3 equiv.) instead of acryloyl chloride. Due to a lower tendency to auto-polymerise, a series of aqueous washes were performed prior to removal of DCM. The washes were as follows: saturated sodium bicarbonate (2 x 100 mL), ionised water (2 x 100 mL) and brine (100 mL). The organic phase was dried with magnesium sulfate before removal of DCM.

PLA dimethacrylate yields = 50 – 65%, PLGA(50/50) dimethacrylate yields = 40 – 50%, PGA dimethacrylate yields = 35 – 55%.

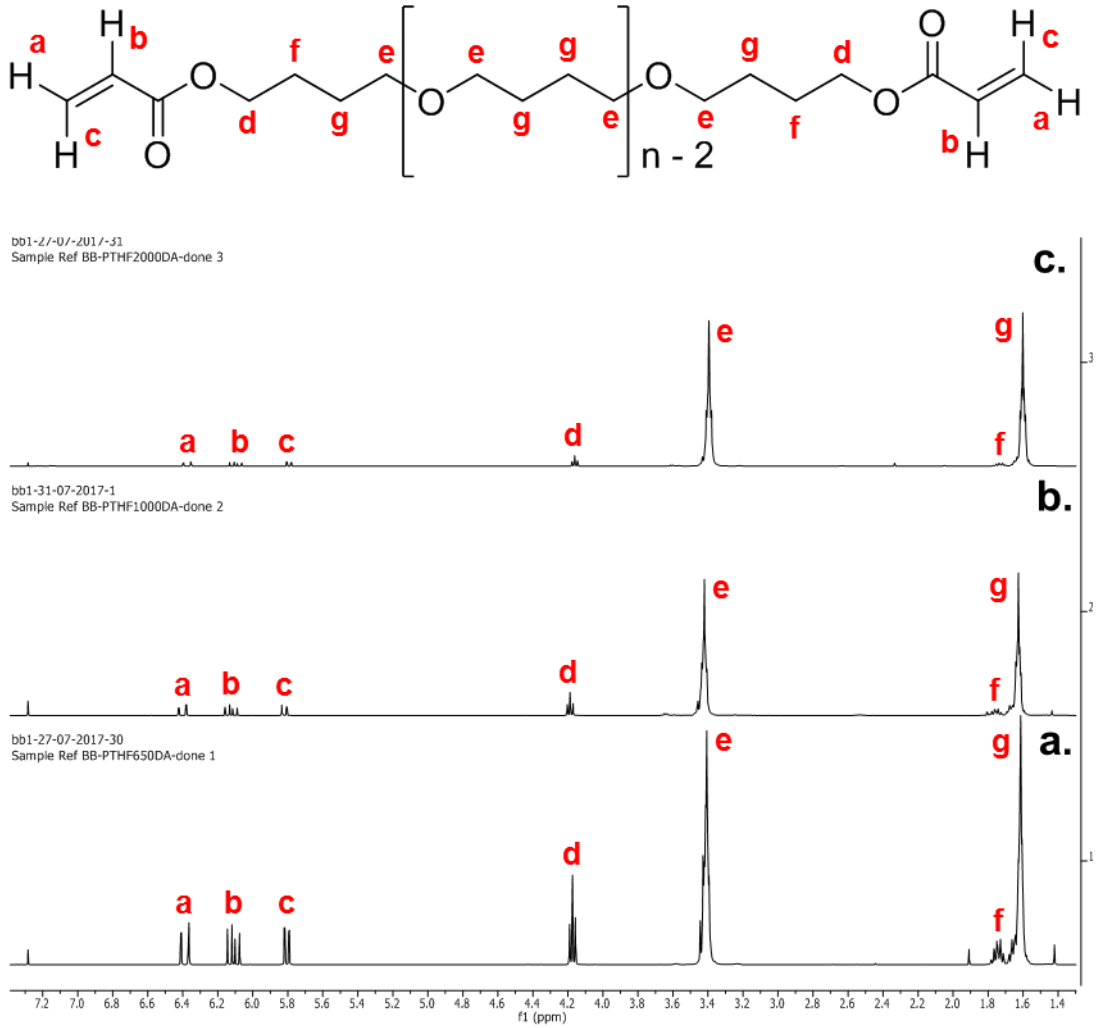

Figure 14 – Annotated ^{1}H NMR of synthesised PTHFDA compounds: **a.** PTHF650DA, **b.** PTHF1000DA and **c.** PTHF2000DA

PTHF diacrylate (PTHFDA) – ^{1}H NMR ($CDCl_3$; δ, ppm): 6.39 (d, 2H, C$\underline{H}_2$=CH), 6.10 (dd, 2H, CH_2=C$\underline{H}$), 5.80 (d, 2H, C$\underline{H}_2$=CH), 4.17 (t, 4H, CH_2), 3.41 (m, 4(n – 1)H, CH_2), 1.74 (m, 4H, CH_2), 1.61 (m, 4(n – 1)H, CH_2).

Theoretical n (n_t) value for PTHF average Mn ~650 (PTHF650) = 8.78. Integration of peaks **a**, **b** and **c** (6H) = 6 (set value); so H = 1. Integration of peak **e** (4(n – 1)H) = 32.02, calculated n (n_{nmr}) value = 9.01. If theoretical and calculated n values are the same, spacer compound has been fully functionalised with acrylate groups. Different n values indicate incomplete functionalisation but can also be due to inexact theoretical n values and/or inaccurate integration of peaks **a**, **b** and **c** due to small peak size.

Table 1 – Table showing theoretical and calculated n values for PTHFDA products

	n_t	Peak e integration value	n_{nmr}*
PTHF650	8.78	32.01	9.01
PTHF1000	13.64	62.64	16.66
PTHF2000	27.53	138.07	35.52

*Peaks **a**, **b** and **c** were integrated and values set to 6, for all spectra, to permit n_{nmr} calculation.

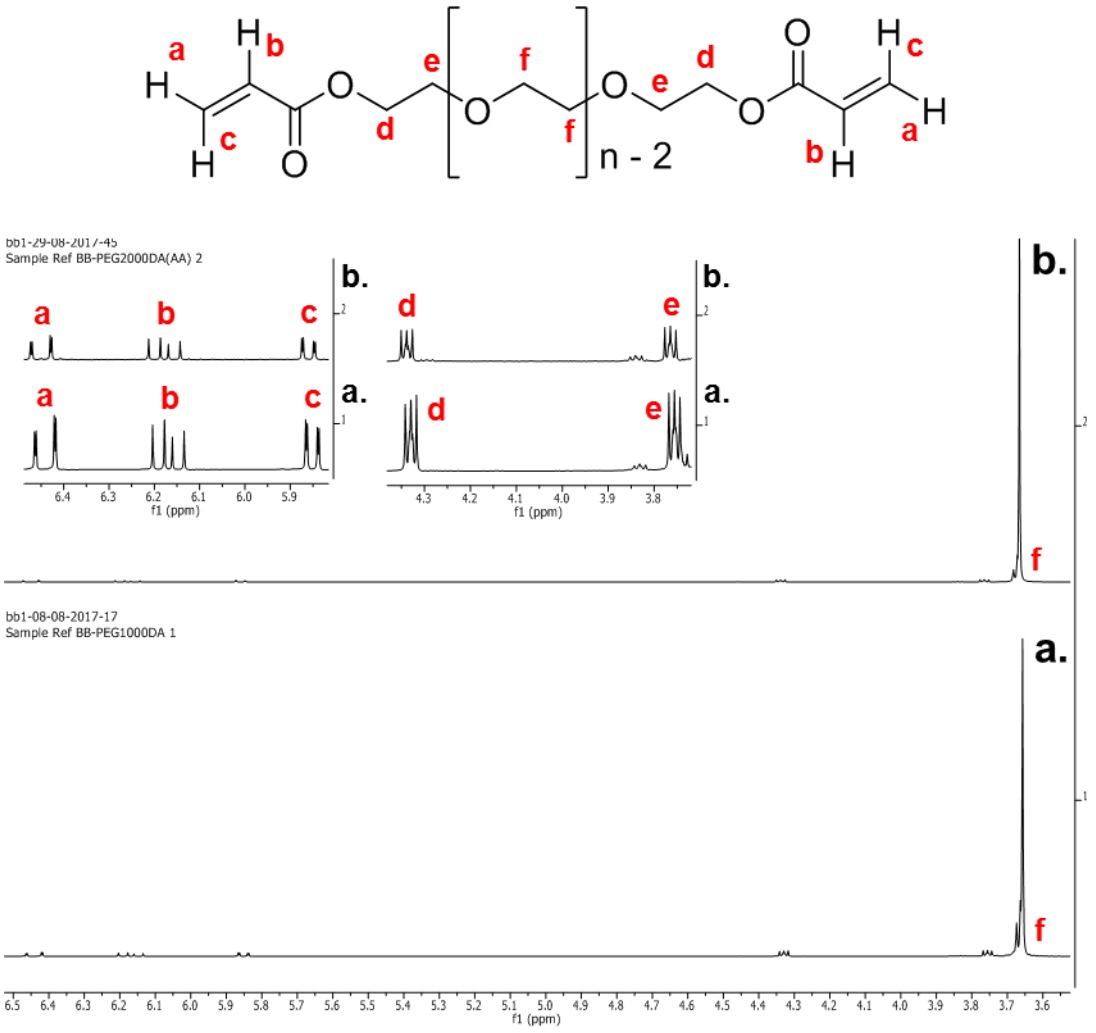

Figure 15 – Annotated ^{1}H NMR of synthesised PEGDA compounds including expansions: **a.** PEG1000DA and **b.** PEG2000DA

PEGDA – ^{1}H NMR ($CDCl_3$; δ, ppm): 6.44 (d, 2H, C<u>H</u>$_2$=CH), 6.16 (dd, 2H, CH_2=C<u>H</u>), 5.85 (d, 2H, C<u>H</u>$_2$=CH), 4.32 (t, 4H, CH_2), 3.75 (t, 4H, CH_2), 3.66 (s, 4(n – 2)H, CH_2).

Theoretical n (n_t) value for PEG average Mn ~1000 (PEG1000) = 22.32. Integration of peaks **a**, **b** and **c** (6H) = 6 (set value); so H = 1. Integration of peak **f** (4(n – 2)H) = 96.21, calculated n (n_{nmr}) value = 26.05.

Table 2 – Table showing theoretical and calculated n values for PEGDA products

	n_t	**Peak f integration value**	**n_{nmr}***
PEG1000	22.32	96.21	26.05
PEG2000	45.05	182.42	47.61

*Peaks **a**, **b** and **c** were integrated and values set to 6, for all spectra, to permit n_{nmr} calculation.

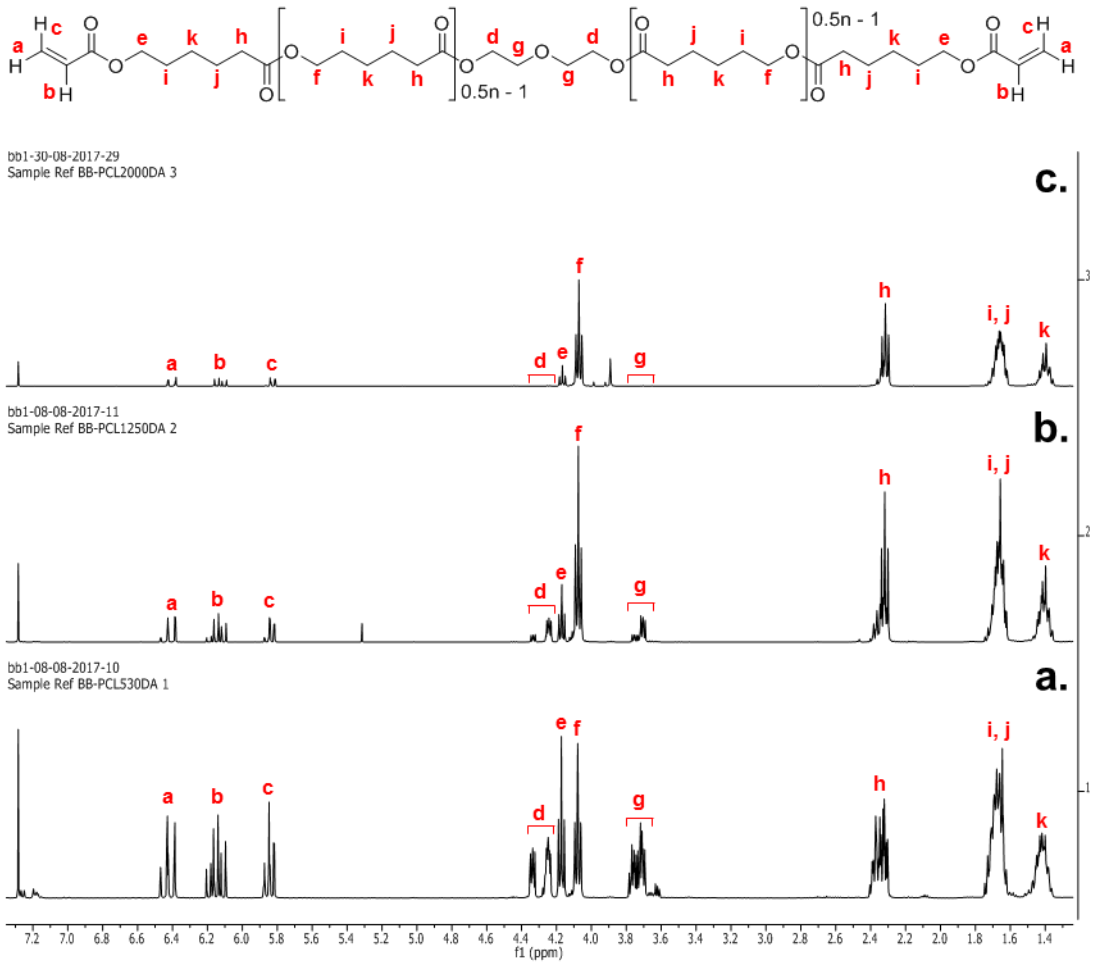

Figure 16 – Annotated ^{1}H NMR of synthesised PCLDA compounds: **a.** PCL530DA, **b.** PCL1250DA and **c.** PCL2000DA

PCLDA – ^{1}H NMR ($CDCl_3$; δ, ppm): 6.42 (d, 2H, $C\underline{H}_2$=CH), 6.12 (dd, 2H, CH_2=C$\underline{H}$), 5.83 (d, 2H, $C\underline{H}_2$=CH), 4.35 – 4.23 (m, 4H, CH_2), 4.17 (t, 4H, CH_2), 4.08 (t, 2(n – 2)H, CH_2), 3.78 – 3.69 (m, 4H, CH_2), 2.40 – 2.30 (m, 2nH, CH_2), 1.75 – 1.61 (m, 4nH, CH_2), 1.47 – 1.36 (m, 2nH, CH_2).

Theoretical n (n_t) value for PCL diol average Mn ~530 (PCL530) = 3.72. Integration of peaks **a**, **b** and **c** (6H) = 6 (set value); so H = 1. Integration of peak **h** (2nH) = 7.43, calculated n (n_{nmr}) value = 3.72.

Table 3 – Table showing theoretical and calculated n values for PCLDA products

	n_t	Peak h integration value	n_{nmr}*
PCL530	3.72	7.43	3.72
PCL1250	10.04	22.59	11.30
PCL2000	16.61	31.70	15.85

*Peaks **a**, **b** and **c** were integrated and values set to 6, for all spectra, to permit n_{nmr} calculation.

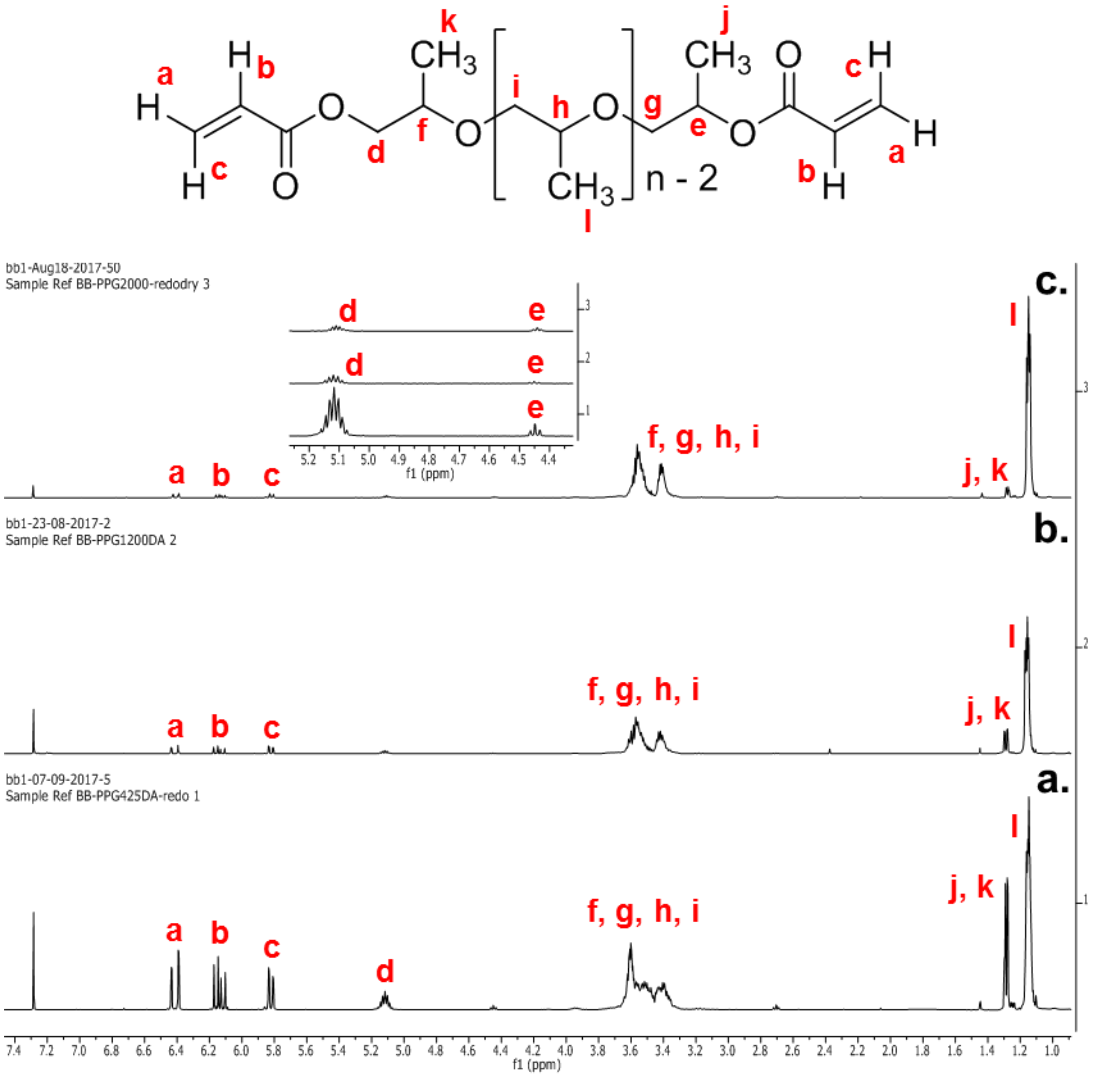

Figure 17 – Annotated ^{1}H NMR of synthesised PPGDA compounds: **a.** PPG425DA, **b.** PPG1200DA and **c.** PPG2000DA

PPGDA – ^{1}H NMR ($CDCl_3$; δ, ppm): 6.41 (d, 2H, C<u>H</u>$_2$=CH), 6.14 (dd, 2H, CH_2=C<u>H</u>), 5.82 (d, 2H, C<u>H</u>$_2$=CH), 5.12 (m, 2H, CH_2), 4.45 (m, 1H, CH), 3.68 – 3.33 (m; 1H, CH; 2H, CH_2; (n – 2)H, CH; 2(n – 2)H, CH_2), 1.29 (m, 6H, CH_3), 1.15 (m, 3(n – 2), CH_3).

Theoretical n (n_t) value for PPG diol average Mn ~425 (PPG425) = 7.02. Integration of peaks **a**, **b** and **c** (6H) = 6 (set value); so H = 1. Integration of peak **l** (3(n – 2)) = 18.37, calculated n (n_{nmr}) value = 8.12.

Table 4 – Table showing theoretical and calculated n values for PPGDA products

	n_t	**Peak l integration value**	**n_{nmr}***
PPG425	7.02	18.37	8.12
PPG1200	20.38	73.75	26.58
PPG2000	34.17	141.09	49.03

*Peaks **a**, **b** and **c** were integrated and values set to 6, for all spectra, to permit n_{nmr} calculation.

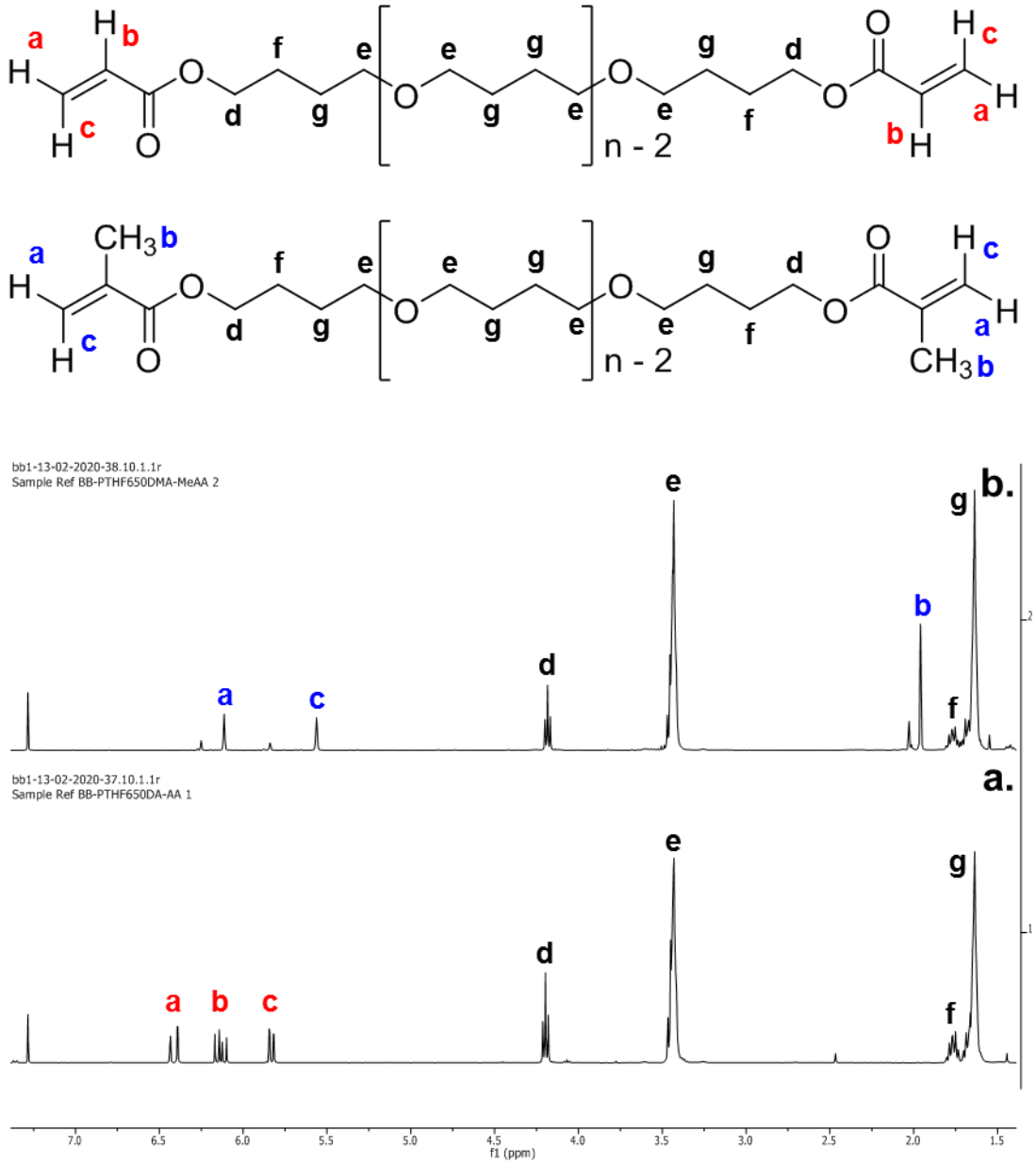

Figure 18 – Annotated ^{1}H NMR of **a.** PTHFDA and **b.** PTHFDMA

^{1}H NMR of synthesised compounds PTHF650DA (bottom), PTHF650DMA (top):

PTHFDA – ^{1}H NMR ($CDCl_3$; δ, ppm): 6.39 (d, 2H, $C\underline{H}_2$=CH), 6.10 (dd, 2H, CH_2=C$\underline{H}$), 5.80 (d, 2H, $C\underline{H}_2$=CH), **4.17 (t, 4H, CH_2)**, **3.41 (m, 4(n – 1)H, CH_2)**, **1.74 (m, 4H, CH_2)**, **1.61 (m, 4(n – 1)H, CH_2)**.

PTHF dimethacrylate (PTHFDMA) – ^{1}H NMR ($CDCl_3$; δ, ppm): 6.12 (s, 2H, C<u>H</u>$_2$=C), 5.57 (s), 2H, C<u>H</u>$_2$=C), **4.19 (t, 4H, CH_2)**, **4.08 (t, 4H, CH_2)**, **3.43 (m, 4(n – 1)H, CH_2)**, 1.96 (s, 6H, CH_3), **1.74 (m, 4H, CH_2)**, **1.63 (m, 4(n – 1)H, CH_2)**.

Peaks corresponding to spacer associated protons are in bold. Non-bold peaks were characteristic of dimethacrylate and diacrylate protons and were observed regardless of spacer used.

Theoretical n (n_t) value for PTHF average Mn ~650 (PTHF650) = 8.78. Integration of peak **b** (6H) = 6 (set value); so H = 1. Integration of peak **e** (4(n – 1)H) = 34.76, calculated n (n_{nmr}) value = 9.69.

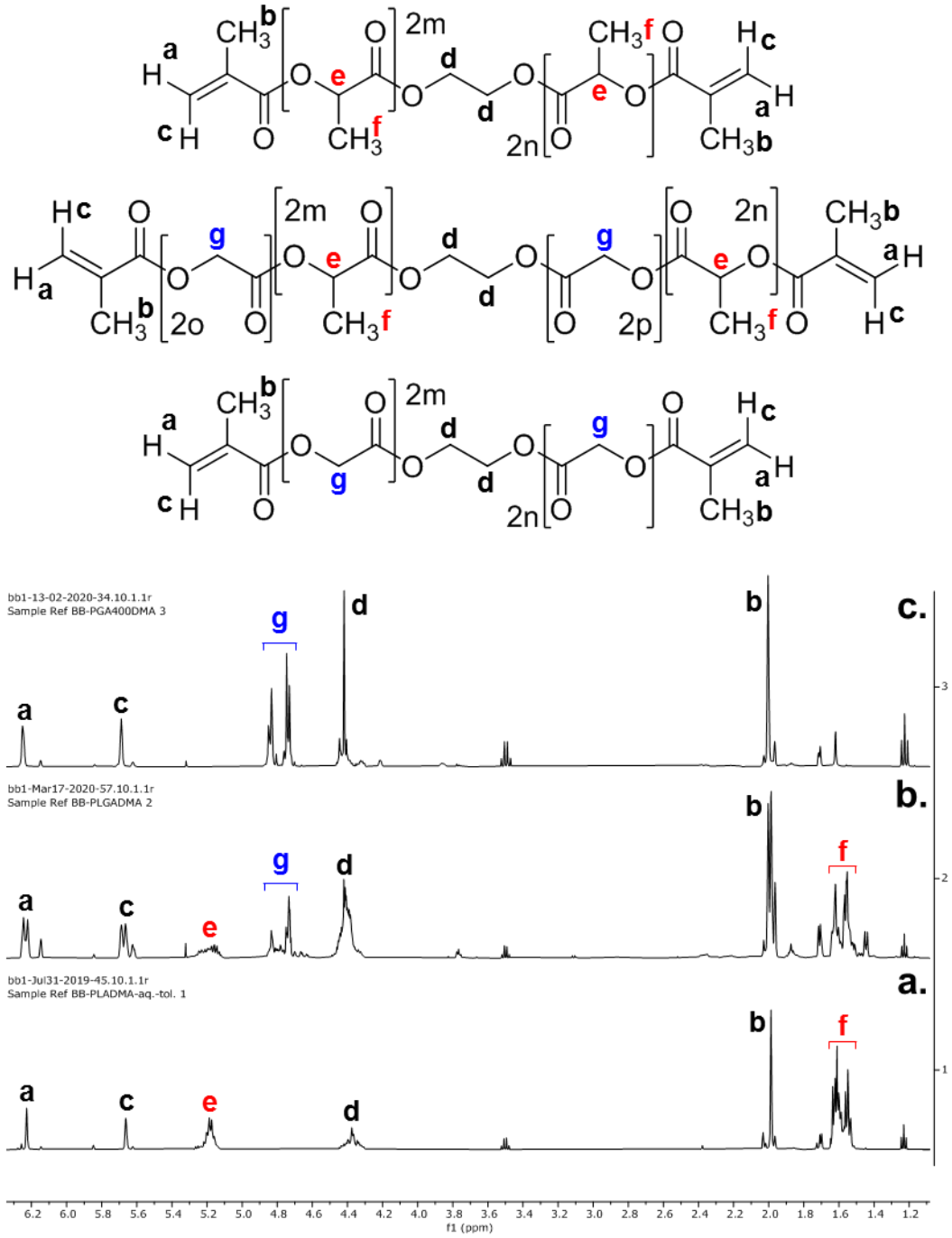

Figure 19 – Annotated ^{1}H NMR of synthesised polyester dimethacrylate compounds: **a.** PLADMA, **b.** PLGA(50/50)DMA and **c.** PGADMA

PLADMA – ^{1}H NMR ($CDCl_3$; δ, ppm): 6.23 (s, 2H, $C\underline{H}_2$=C), 5.66 (s), 2H, $C\underline{H}_2$=C), 5.18 (m, yH, CH), 4.40 (m, 4H, CH_2), 2.01 (m, 6H, CH_3), 1.65 – 1.51 (m, 3yH, CH_3). 2m + 2n = y

Integration of peak **b** (6H) = 6 (set value); so H = 1. Integration of peak **e** (yH) = 5.34, calculated y (y_{nmr}) value = 5.34. Calculated PLADMA molecular weight (Mn_{nmr}) = $MW_{ethylene\ glycol\ linkage}$ + $MW_{end\ groups}$ + y_{nmr} x $MW_{lactide\ repeating\ units}$ = 60 g/mol + 2 x 69 g/mol + 5.34 x 72 g/mol = 582.48 g/mol

PLGA(50/50)DMA – ^{1}H NMR ($CDCl_3$; δ, ppm): 6.24 (s, 2H, C$\underline{H}_2$=CH), 5.68 (s), 2H, C$\underline{H}_2$=C), 5.18 (m, yH, CH), 4.78 (m, 2zH, CH_2), 4.40 (m, 4H, CH_2), 2.01 (m, 6H, CH_3), 1.65 – 1.51 (m, 3yH, CH_3). 2m + 2n = y, 2o + 2p = z.

Integration of peak **b** (6H) = 6 (set value); so H = 1. Integration of peak **e** (yH) = 1.67, calculated y (y_{nmr}) value = 1.67. Integration of peak **g** (2zH) = 3.39, calculated z (z_{nmr}) value = 1.70. Calculated PLGA(50/50)DMA molecular weight (Mn_{nmr}) = $MW_{ethylene\ glycol\ linkage}$ + $MW_{end\ groups}$ + y_{nmr} x $MW_{lactide\ repeating\ units}$ + z_{nmr} x $MW_{glycolide\ repeating\ units}$ = 60 g/mol + 2 x 69 g/mol + 1.67 x 72 g/mol + 1.70 x 58 g/mol = 416.84 g/mol.

PGADMA – ^{1}H NMR ($CDCl_3$; δ, ppm): 6.24 (s, 2H, C$\underline{H}_2$=CH), 5.68 (s), 2H, C$\underline{H}_2$=C), 4.78 (m, 2zH, CH_2), 4.40 (m, 4H, CH_2), 2.01 (m, 6H, CH_3). 2m + 2n = z.

Integration of peak **b** (6H) = 6 (set value); so H = 1. Integration of peak **g** (2zH) = 7.37, calculated z (z_{nmr}) value = 3.69. Calculated PGADMA molecular weight (Mn_{nmr}) = $MW_{ethylene\ glycol\ linkage}$ + $MW_{end\ groups}$ + z_{nmr} x $MW_{glycolide\ repeating\ units}$ = 60 g/mol + 2 x 69 g/mol + 3.69 x 58 g/mol = 412.02 g/mol

Non-assigned peaks correspond to impurities such as solvents and triethylamine hydrochloride salts that were not removed (only reduced) despite use of purification procedures. Presence of impurities may affect testing results of these properties, and in future, it would be sensible to implement a more rigorous purification step to remove all impurities.

3.2.3. Preparation of polyurethane dimethacrylate monomers

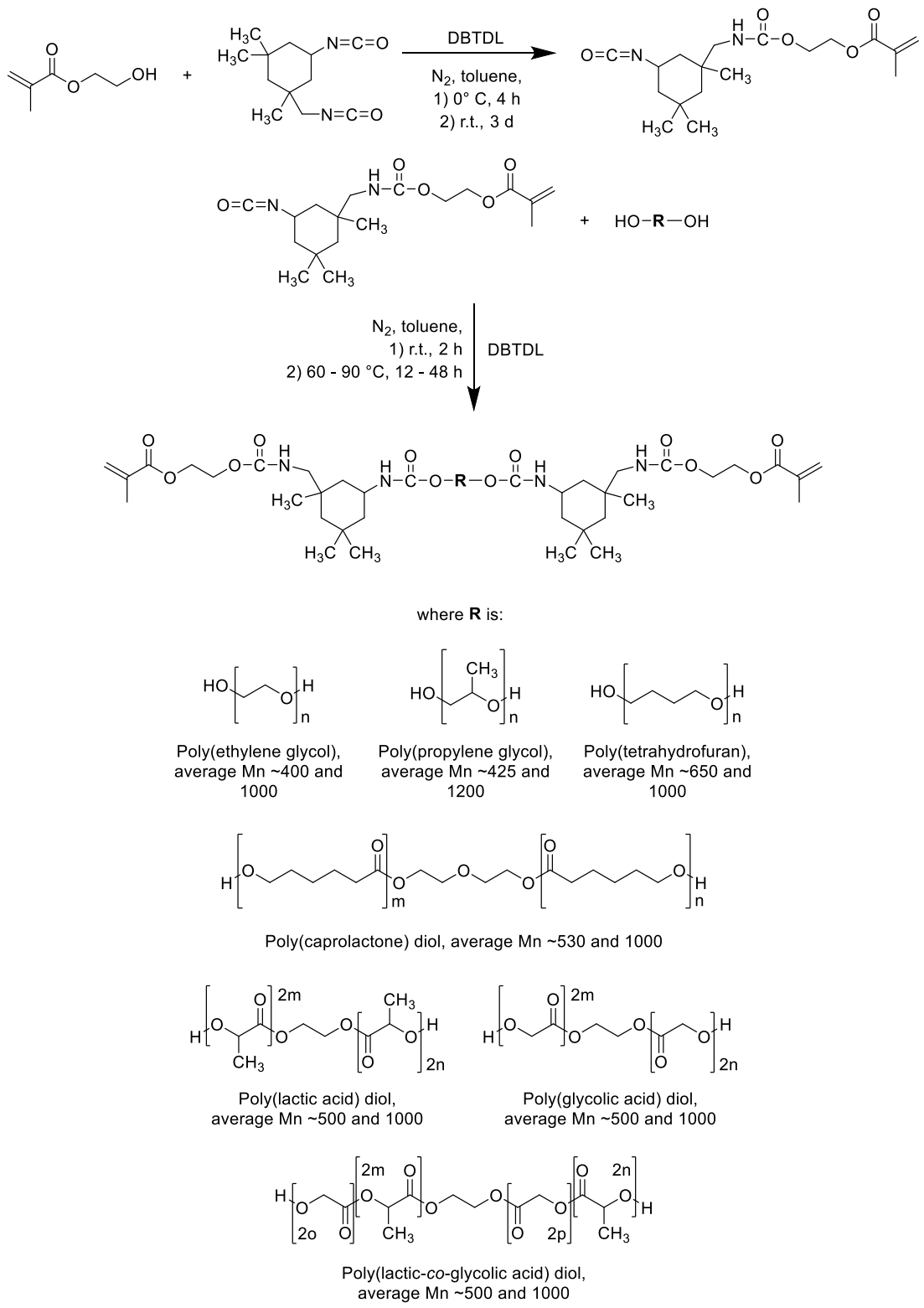

Figure 20 – Reaction scheme for preparation of polyurethane dimethacrylate monomers

The synthesis route was adapted from Sinh et al. (2016)[176], Patil et al. (2017)[177], Feng et al. (2014)[178] and Khudyakov (2004)[179]. IPDI (17.47 mL, 82 mmol, 2.0 equiv.), MEHQ (71 mg, 0.572 mmol, ~1000 ppm) and anhydrous toluene (50 mL) were fed into an oven dried 250 mL three-neck round-bottom flask under nitrogen. The reaction vessel was covered in foil to protect light-sensitive materials. HEMA (10 mL, 82 mmol, 2.0 equiv.) was added dropwise over 2 h at room temperature. The solution was stirred at 30 °C until IR analysis indicated disappearance of the O-H peak (~ 3 days for HEMA prepolymer). Preparation of the HEMA prepolymer in the initial step is referred to as the “reverse method”, and synthesis of all polyurethane dimethacrylates proceed via this route. DBTDL (67 µL) and anhydrous toluene (50 mL) were added directly to the reaction vessel. PEG ~1000 Mn (41 g, 41 mmol, 1.0 equiv.) diluted to 50 mL with anhydrous toluene, was added dropwise at room temperature. After 12 h stirring at room temperature, the reaction temperature was increased to 60 °C and the reaction continued until FTIR analysis indicated disappearance of the N=C=O peak (~16 h for PEG 1000 polyurethane dimethacrylate). Upon reaction completion (no observable N=C=O peak) solvent was removed using a rotary evaporator and the product was further dried under high vacuum for 2 days, affording a very viscous colourless resin. Preparation of polyurethane dimethacrylates with different spacers were carried out using the same reagent equivalences as above. Higher reaction temperatures (80 – 100 °C) were required to form polyurethane dimethacrylates based on PPG, PTHF and PCL in the final step. If after 48 h the N=C=O peak was still observable for any polyurethane dimethacrylate reaction, an additional 0.1 equiv. of respective spacer was added dropwise to complete reaction.

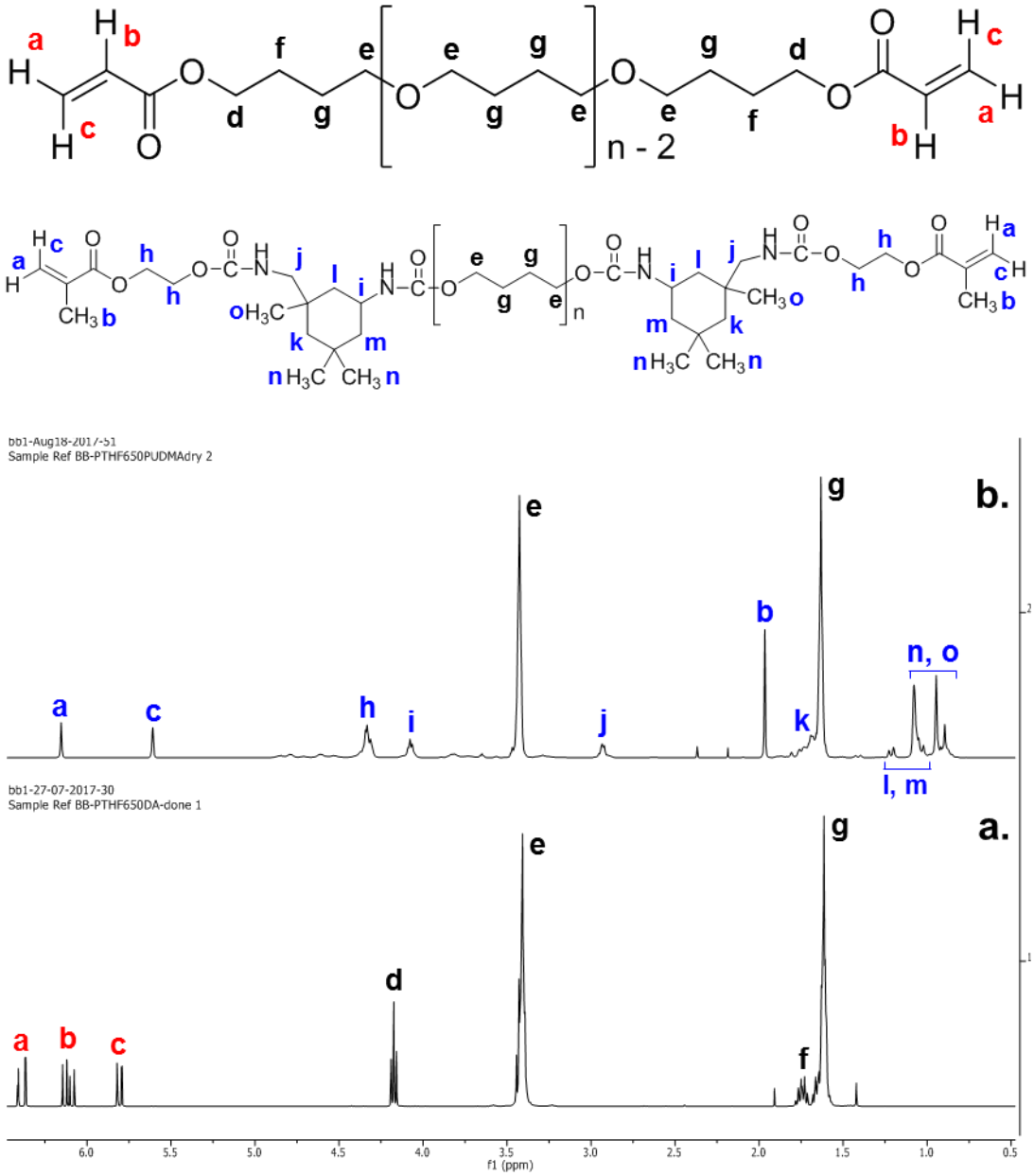

Figure 21 – Annotated ^{1}H NMR of synthesised compounds **a.** PTHF650DA and **b.** PTHF650PUDMA

PTHFDA – ^{1}H NMR ($CDCl_3$; δ, ppm): 6.39 (d, 2H, $C\underline{H}_2$=CH), 6.10 (dd, 2H, CH_2=C$\underline{H}$), 5.80 (d, 2H, $C\underline{H}_2$=CH), **4.17 (t, 4H, CH_2)**, **3.41 (m, 4(n – 1)H, CH_2)**, **1.74 (m, 4H, CH_2)**, **1.61 (m, 4(n – 1)H, CH_2)**.

PTHFPUDMA – ^{1}H NMR ($CDCl_3$; δ, ppm): 6.16 (s, 2H, $C\underline{H}_2$=CH), 5.61 (s), 2H, $C\underline{H}_2$=C), 4.33 (t, 4H, CH_2), 4.08 (t, 4H, CH_2), **3.43 (m, 4nH, CH_2)**, 2.93 (s, 4H,

CH_2), 1.96 (s, 6H, CH_3), 1.82 – 1.59 (m, 4H, CH_2), **1.63 (m, 4nH, CH_2)**, 1.25 – 1.00 (m, 8H, CH_2), 1.12 – 0.81 (m, 18H, CH_3).

Peaks corresponding to spacer associated protons are in bold. Non-bold peaks were characteristic of polyurethane dimethacrylate and diacrylate protons and were observed regardless of spacer used. Consequently, 1H NMR spectra for other polyurethane dimethacrylates are omitted here for brevity and instead included in the appendix.

3.2.4. Preparation of polyester diols

The synthesis route was adapted from Li et al. (2018)[180]. The following equation was used to calculate amounts of reactants required for a target molecular weight.

$$\frac{[M]_0}{[CTA]_0} = \frac{M_n^{\,t} - MW_{CTA}}{MW_M}$$

where, $[M]_0/[CTA]_0$ = feed molar ratio of monomer (DL-lactide and/or glycolide) to chain transfer agent (ethylene glycol), $M_n^{\,t}$ = target molecular weight of polyester, MW_{CTA} = molar mass of CTA and MW_M = molar mass of monomer. The below table (Table 5) shows reactant amounts for certain polyesters of different target molecular weights calculated using the above equation. $[M]_0/[CTA]_0$ for PLGA 50/50 was calculated by using the average molar mass of 50/50 PLGA as MW_M (PLA molar mass = 144.1 g/mol, PGA molar mass = 116.1 g/mol and PLGA 50/50 molar mass = 130.1 g/mol). Catalyst content (DBTDL, DBU, SO) was always 0.1% mol.

Table 5 – Reactant amounts for PLA, PLGA 50/50 and PGA diol preparation of different target molecular weights.

Polyester	M_n^t (g/mol)	[M]0/[CTA]0	Monomer content (g)		Ethylene glycol (mL)
			D,L-LA	GA	
PLA	200	0.957	10	-	3.71
	300	1.651	10	-	2.35
	400	2.345	10	-	1.66
	600	3.733	10	-	1.04
	800	5.121	10	-	0.76
	1000	6.509	10	-	0.60
PLGA 50/50	200	1.060	5	4.03	3.66
	1000	7.209	5	4.03	0.60
PGA	200	1.188	-	10	4.06
	1000	8.08	-	10	0.60

Example synthetic route and workup is for the preparation of PLA diol (M_n^t = 200 g/mol). D,L-lactide (10 g, 69.4 mmol), 0.1% mol DBTDL (41 µL, 69.4 µmol) and ethylene glycol (3.71 mL, 66.4 mmol) were fed into an oven dried 100 mL round-bottom flask fitted with condenser under nitrogen. The mixture was stirred at 130 °C for 48 h. The reaction mixture was cooled to room temperature and subsequently dissolved in a sufficient amount of chloroform to obtain a flowable mixture. This mixture was precipitated into ice-cold hexane dropwise over 30 min. Hexane was decanted off and crude material was stirred under high vacuum at 80 °C for 1 h to remove residual ethylene glycol to afford a colourless resin. Heating under vacuum was preferred to aqueous washings, which led to large losses of product. For reactions catalysed by DBU the crude product was dissolved into approximately 100 mL chloroform, filtered through a pad of silica, concentrated under reduced pressure and subsequently precipitated into ice-cold hexane.

3.2.5. Preparation of cationic photoinitiators

(η^6-Chlorobenzene) (η^5-cyclopentadienyl) iron hexafluorophosphate

The synthesis route was adapted from Wang et al. (2005)[181] and Abd-el-aziz et al. (1988)[182]. Ferrocene (7.44 g, 40 mmol, 1 equiv.), aluminium chloride

powder (10.67 g, 80 mmol, 2 equiv.), aluminium powder (2.16 g, 80 mmol, 2 equiv.), chlorobenzene (8.11 mL, 80 mmol, 2 equiv.) and decalin (60 mL) were charged into a round-flask connected to a reflux condenser and stirred under nitrogen at 150 °C. After 6 h, the dark green mixture was cooled to 0 °C and solvolysed with ice-cold water (approximately 80 mL), with stirring, to quench the reaction. Additional ice-cold water was added to the round-flask and sonicated to solvolyse any remnant crude product. Following filtration the aqueous layer of the filtrate was separated and washed with diethyl ether twice. A saturated aqueous solution of potassium hexafluorophosphate(V) (KPF_6) (11.04 g, 60 mmol, 1.5 equiv.) was added to the crude solution and the resultant precipitate obtained by filtration. The crude product was re-dissolved in 50 mL DCM, dried over magnesium sulfate, concentrated using a rotary evaporator and recrystallised from DCM/toluene to afford a dark green powder.

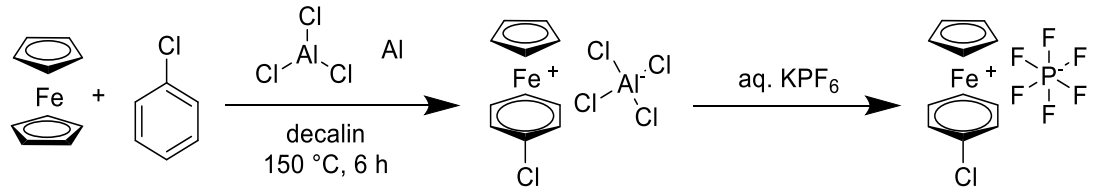

^{1}H NMR (acetone-d_6); δ, ppm): 6.90 (s, 2H, ArH), 6.68 (s, 2H, ArH), 6.55 (s, 1H, ArH), 4.64 (s, 5H, Cp). ^{13}C NMR (acetone-d_6; δ, ppm): 108.31 (CCl, ArC), 89.90 (2C, ArCH), 89.25 (2C, ArCH), 88.33 (C, ArCH), 80.0 (Cp). EI-MS (m/z): calcd for [C11H10ClFe]+, 232.9812, found: 232.9812 $[M]^+$. Peak at 829 cm^{-1}(strong, P-F) confirmed presence of PF_6 anion.

(η^6-Fluorobenzene) (η^5-cyclopentadienyl) iron hexafluorophosphate

The synthetic route and workup was identical to the preparation of (η6-chlorobenzene) (η5-cyclopentadienyl) iron hexafluorophosphate. Fluorobenzene was substituted for chlorobenzene.

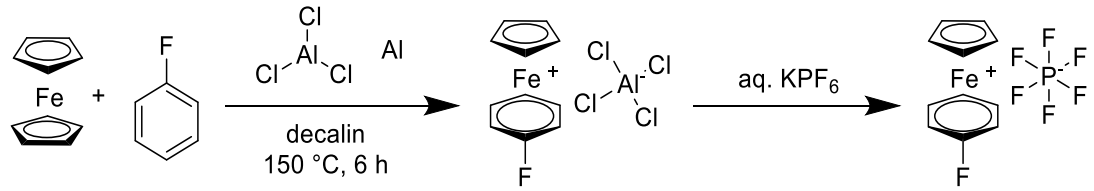

^{1}H NMR (acetone-d_6; δ, ppm): 6.85 (t, 2H, ArH), 6.60 (d, 2H, ArH), 6.41 (t, 1H, ArH), 5.37 (s, 5H, Cp). ^{13}C NMR (acetone-d_6; δ, ppm): 137.89 – 140.07 (CFl, quat., ArC), 89.33 (C, ArCH), 88.19 (2C, ArCH), 87.66 (2C, ArCH), 79.15 (Cp). EI-MS (m/z): calcd for [C11H10FFe]+, 217.0110, found: 217.0110 [M-PF_6^-]$^+$. Peak at 829 cm^{-1} (strong, P-F) confirmed presence of PF_6 anion.

(η^6-Diphenylmethane) (η^6-cyclopentadienyl) iron hexafluorophosphate

The synthetic route was reproduced from Wang et al. (2009)[183]. Ferrocene (9.3 g, 50.0 mmol, 1 equiv.), aluminium chloride powder (13.40 g, 100 mmol, 2 equiv.), aluminium powder (2.20 g, 82 mmol, 1.631 equiv.), diphenylmethane (25.05 mL, 150 mmol, 3.01 equiv.) and cyclohexane (60 mL) were charged into a round-bottom flask fitted with a reflux condenser and stirred at 90 °C under nitrogen. After 10 h the dark green mixture was cooled to 0 °C and solvolysed with ice-cold 15% aqueous methanol (approx. 80 mL), with stirring, to quench the reaction. Additional 15% aqueous methanol was added to the round-bottom flask and sonicated to solvolyse any remnant crude product. Following filtration the aqueous layer of the filtrate was separated and washed with diethyl ether twice. A saturated aqueous solution of KPF_6 (18.41 g, 100 mmol, 2 equiv.) was added to the crude solution in excess amounts and the resultant precipitate obtained by filtration. The crude product was redissolved in DCM, dried over $MgSO_4$, concentrated using a rotary evaporator and recrystallised from DCM/diethyl ether to afford a green-yellow powder.

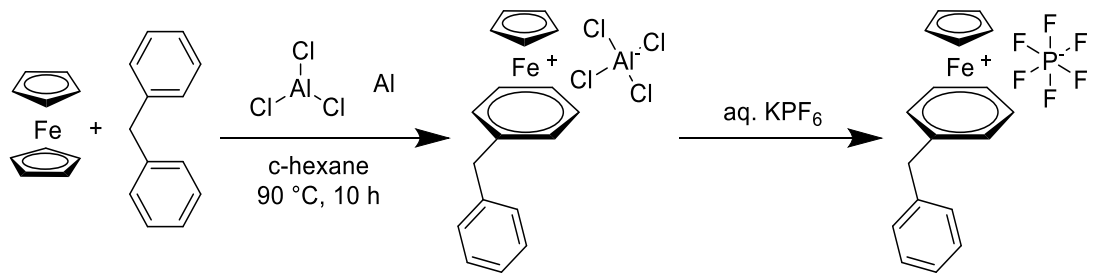

^{1}H NMR (acetone-d_6; δ, ppm): 5.23 (s, 5H, Cp); 6.65 – 6.47 (m, 5H, ArH), 7.41 – 7.18 (m, 5H, ArH). EI-MS (m/z): calcd for [C18H17Fe]+, 289.0674, found: 289.0674 $[M]^+$. Peak at 829 cm^{-1} (strong, P-F) confirmed presence of PF_6 anion.

(η^6-Benzophenone) (η^6-cyclopentadienyl) iron hexafluorophosphate

The synthetic route was reproduced from Wang et al. (2009)[183]. Ferrocene (9.30 g, 50.0 mmol, 1 equiv.), aluminium chloride powder (13.40 g, 100 mmol, 2.01 equiv.), aluminium powder (2.20 g, 82 mmol, 1.631 equiv.), diphenylmethane (25.05 mL, 150 mmol, 3.01 equiv.) and cyclohexane (60 mL) were charged into a round-bottom flask connected to a reflux condenser and stirred at 90 °C under nitrogen. After 10 h the dark green mixture was cooled to 0 °C and solvolysed with ice-cold 15% aqueous methanol (approx. 80 mL), with stirring, to quench the reaction. Additional 15% aqueous methanol was added to the round-bottom flask and sonicated to solvolyse any remnant crude product. Following filtration, the aqueous layer of the filtrate was separated and washed with diethyl ether twice. The water-soluble tetrachloroaluminate salt of the diphenylmethane complex was poured into 100 ml of aqueous potassium permanganate (7.90 g, 50.0 mmol, 1.000 equiv.) and stirred at 60 °C for 10 h. A saturated aqueous solution of KPF_6 (13.80 g, 75 mmol, 1.5 equiv.) was added to the crude solution in excess amounts and the resultant precipitate obtained by filtration. The crude product was re-dissolved in DCM, dried over $MgSO_4$, concentrated using a rotary evaporator and recrystallised from acetone/diethyl ether to afford a yellow powder.

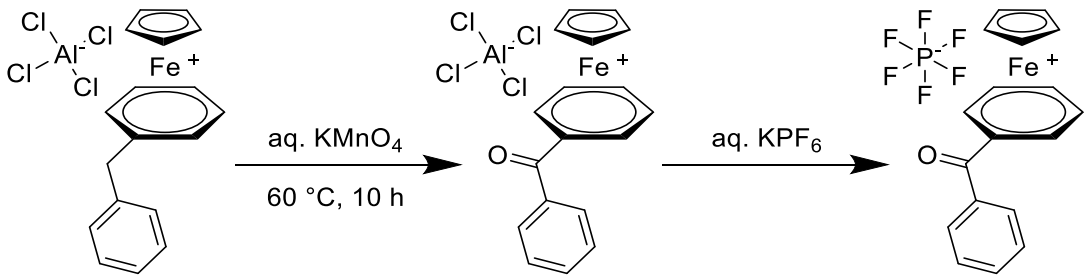

^{1}H NMR (acetone-d_6; δ, ppm): 7.41 – 7.18 (m, 5H, ArH), 6.65 – 6.47 (m, 5H), 5.23 (s, 5H, Cp. Small peaks observed at 5.32 (s, 5H, Cp); 6.95 – 6.76 (m, 5H), 7.81 – 7.63 (m, 5H, ArH). EI-MS (m/z): calcd for [C18H15FeO]+, 303.0466, found: 303.0466 $[M]^+$ (weak, mixture). Peak at 829 cm^{-1} (strong, P-F) confirmed presence of PF_6 anion. Peak at 1680 cm^{-1} (C=O) was not observed, indicating desired compound was not synthesised.

(η^6-3-Benzoyl-4-chlorodiphenylamine) (η^6-cyclopentadienyl) iron hexafluorophosphate

The synthetic route was reproduced from Li et al. (2010)[184]. (η6-Chlorobenzene) (η5-cyclopentadienyl) iron hexafluorophosphate (3.87 g, 10.25 mmol, 1 equiv.), 2-amino-5-chlorobenzophenone (2.38 g, 10.25 mmol, 1 equiv.), sodium hydride (60% dispersion in mineral oil) (0.82 g, 34.1 mmol, 3.33 equiv.) and dimethylformamide (40 mL) were charged into a 100 mL round-bottom flask and stirred for 14 h at room temperature under nitrogen. The solution turned from green-gold to yellow-brown. The reaction mixture was filtered through a sintered glass funnel into a 10% (v/v) HCl solution (60 mL), resulting in a granular orange precipitate. The precipitate was re-dissolved in water, filtered and treated with an excess of saturated KPF_6 solution resulting in a yellow granular precipitate. The precipitate was extracted with 50 mL DCM, washed with water (5 x 50 mL), dried with magnesium sulfate and then filtered. The solution was concentrated using a rotary evaporator and precipitated into diethyl ether affording a yellow granular powder.

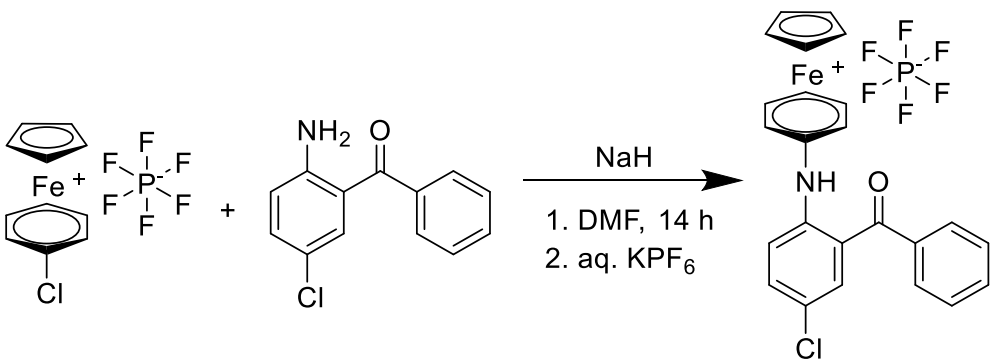

^{1}H NMR (acetone-d_6; δ, ppm): 8.46 (s, 1H, NH), 7.88 – 7.58 (m, 8H, ArH), 6.33 – 6.17 (m, 5H, ArH). EI-MS (m/z): calcd for [C24H19ClFeNO]+, 428.0496 found: 428.0496 [M-PF_6^-]$^+$. Peak at 829 cm^{-1} (strong, P-F) confirmed presence of PF_6 anion.

(E)-4-(((N,N-diphenyl)amino)-styryl)-phenyl-methyl-benzyl-sulfonium hexafluorophosphate (PAG 5)

The synthetic route was adapted from Zhou et al. (2011)[185], Jin et al. (2013)[186] and Zhou et al. (2002)[187]. Potassium *tert*-butoxide (4.04 g, 36 mmol, 1.82 equiv.) was charged into a solution of triphenylmethylphosphonium bromide (10.72 g, 30 mmol, 1.52 equiv.) in dry THF at 0 °C and stirred for 15 minutes at room temperature. 4-(Diphenylamino)benzaldehyde (5.41 g, 19.79 mmol, 1 equiv.) was added at 0 °C to the reaction mixture and the resulting mixture stirred at room temperature for a further 3 h. The crude product was extracted from the aqueous phase with ethyl acetate (3 x 50 mL). The organic phase was washed with brine (2 x 50 mL), dried over $MgSO_4$ and filtered. Ethyl acetate was removed using a rotary evaporator and the resultant white residue eluted through a column of silica with hexane. Hexane was removed using a rotary evaporator to afford 4-(*N,N*-diphenyl)aminestyrene as a pale-yellow powder.

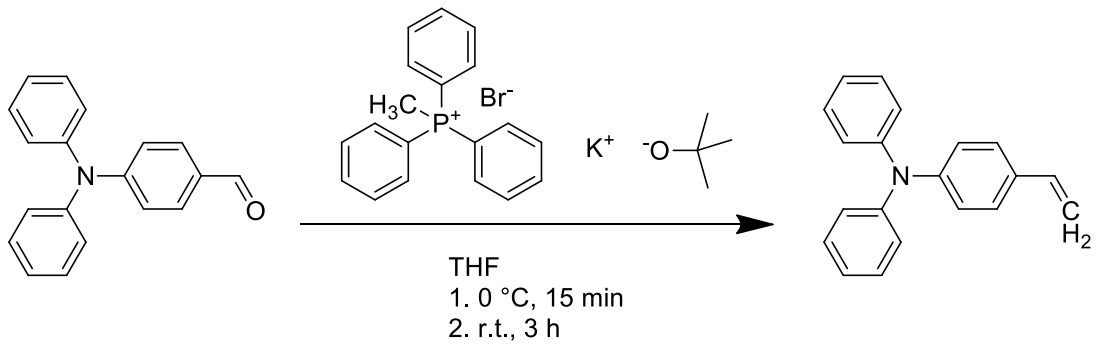

^{1}H NMR ($CDCl_3$; δ, ppm): 7.36 – 7.10 (m, 14H), 6.70 (dd, 1H, CH_2=C<u>H</u>), 5.68 (d, 1H, C<u>H</u>$_2$=CH), 5.19 (d, 1H, C<u>H</u>$_2$=CH).

^{13}C NMR ($CDCl_3$; δ, ppm): 147.65 (2C, ArCN), 147.52 (1C, ArCN), 136.26 (1C, **C**H=CH_2), 131.93 (1C, ArC), 129.27 (4C, ArCH), 127.08 (2C, ArCH), 124.41

(4C, ArCH), 123.65 (2C, ArCH), 122.94 (2C, ArCH), 112.15 (1C, CH=**C**H_2). IR (neat) cm^{-1}: 3085, 3061, 3033, 3003, 2976, 1625, 1592, 992, 841, 760.

Benzyl bromide (2.97 mL, 25.00 mmol, 1 equiv.) and 4-bromobenzenethiol (4.73 g, 25.00 mmol, 1 equiv.), potassium carbonate (4.15 g, 30.0 mmol, 1.2 equiv.) and acetone (125 mL) were charged into a round-bottom flask fitted with a reflux condenser. The reaction mixture was heated under reflux until all starting materials had been consumed, which was observed via thin-layer chromatography. Inorganic salts were filtered off and acetone was removed using a rotary evaporator. The crude product was recrystallised from ethanol to afford 4-(benzylthiol)-4'-bromobenzene as a white powder.

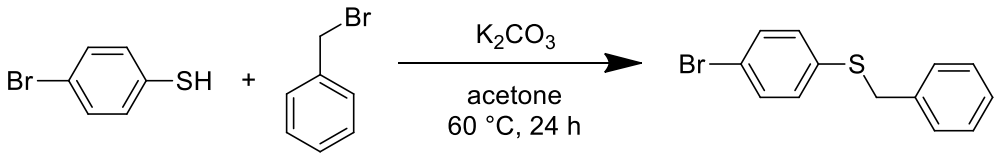

^{1}H NMR ($CDCl_3$; δ, ppm): 7.40 (d, 2H, ArH), 7.31 (m, 5H, ArH), 7.18 (d, 2H, ArH), 4.12 (s, 2H, CH_2).
^{13}C NMR ($CDCl_3$; δ, ppm): 137.07 (1C, ArC), 135.47 (1C, SArC), 131.88 (2C, ArCH), 131.52 (2C, ArCH), 128.80 (2C, ArCH), 128.58 (2C, ArCH), 127.34 (1C, ArCH), 120.35 (1C, BrArC), 39.13 (1C, SCH_2).

4-(*N,N*-Diphenyl)aminestyrene (1.76 g, 6.49 mmol, 1 equiv.), 4-(benzylthiol)-4'-bromobenzene (1.99 g, 7.13 mmol, 1.1 equiv.), palladium(II) acetate (0.015 g, 0.065 mmol, 0.01 equiv.) and triethanolamine (6.5 mL) were charged into a round-bottom flask fitted with a reflux condenser and the reaction mixture was heated at 120 °C under nitrogen. After 24 h, the reaction mixture was cooled and poured into 200 mL of water. The crude mixture was extracted with DCM washes (3 x 100 mL). The organic phase was washed with brine (2 x 100 mL), dried over magnesium sulfate and filtered through silica gel to remove the palladium catalyst. The solvent was removed using a rotary evaporator and the crude mixture was purified by column chromatography with DCM/hexane

(gradient – 4% DCM up to 32% DCM) as eluent to afford compound 5 as a yellow powder.

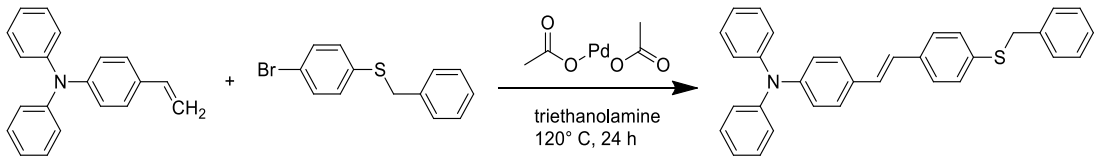

^{1}H NMR ($CDCl_3$; δ, ppm): 7.41 (d, 2H, ArH), 7.39 (d, 2H, ArH), 7.34 – 7.23 (m, 11H, ArH), 7.13 (d, 4H, ArH), 7.08 – 7.02 (m, 5H, ArH, CH=CH), 6.96 (d, 1H, CH=CH), 4.15 (s, 2H, CH_2).
^{13}C NMR ($CDCl_3$; δ, ppm): 147.46 (2C, ArCN), 147.35 (1C, ArCN), 137.45 (1C, ArC), 135.88 (1C, SArC), 135.16 (1C, ArC), 131.27 (2C, ArCH), 130.05 (2C, ArCH), 129.30 (2C, ArCH), 128.84 (2C, ArCH), 128.53 (2C, ArCH), 128.14 (2C, ArCH), 127.34 (2C, CH=CH), 127.22 (2C, ArC & ArCH), 126.67 (2C, ArCH), 126.24 (2C, ArCH), 124.53 (2C, ArCH), 123.52 (2C, ArCH), 123.08 (2C, ArCH), 39.13 (1C, SCH_2).

Due to the high sensitivity to ambient light, all preparation was carried out in darkness. Firstly, compound 5 (1.03 g, 2.19 mmol, 1 equiv.) and anhydrous DCM (10 mL) were charged into a 50 mL round-bottom flask and cooled to – 78 °C. Methyl trifluoromethanesulfonate (0.27 mL, 2.41 mmol, 1.1 equiv.) was added dropwise to the solution. The reaction mixture was stirred at – 78 °C for 2 h and then warmed to room temperature and stirred for a further 24 h. Subsequently, DCM was removed using a rotary evaporator and the residue was re-dissolved in acetonitrile. Diethyl ether was added to the solution dropwise and the resultant crystals were obtained by filtration and washed with diethyl ether. This step was repeated once more, affording PAG 5 as a yellow powder.

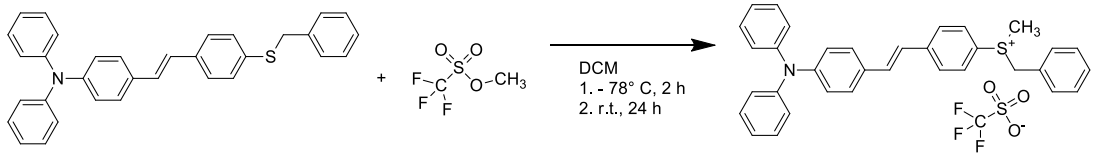

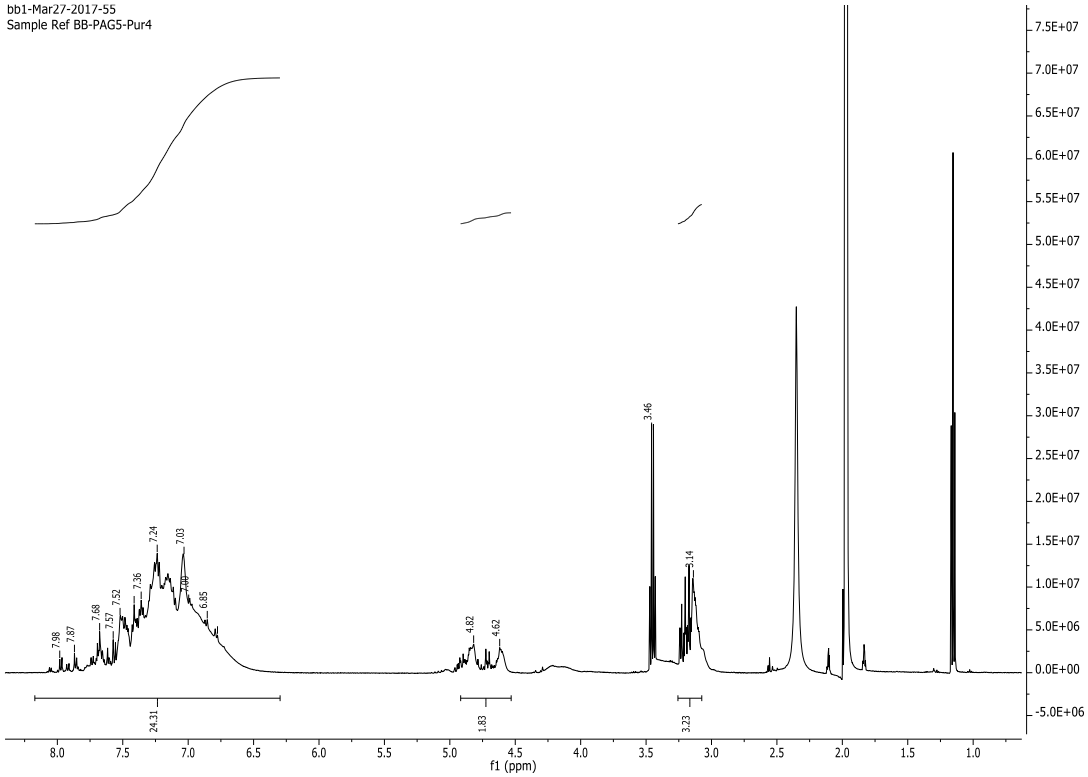

Figure 21 – ^{1}H NMR spectrum of synthesised compound PAG5

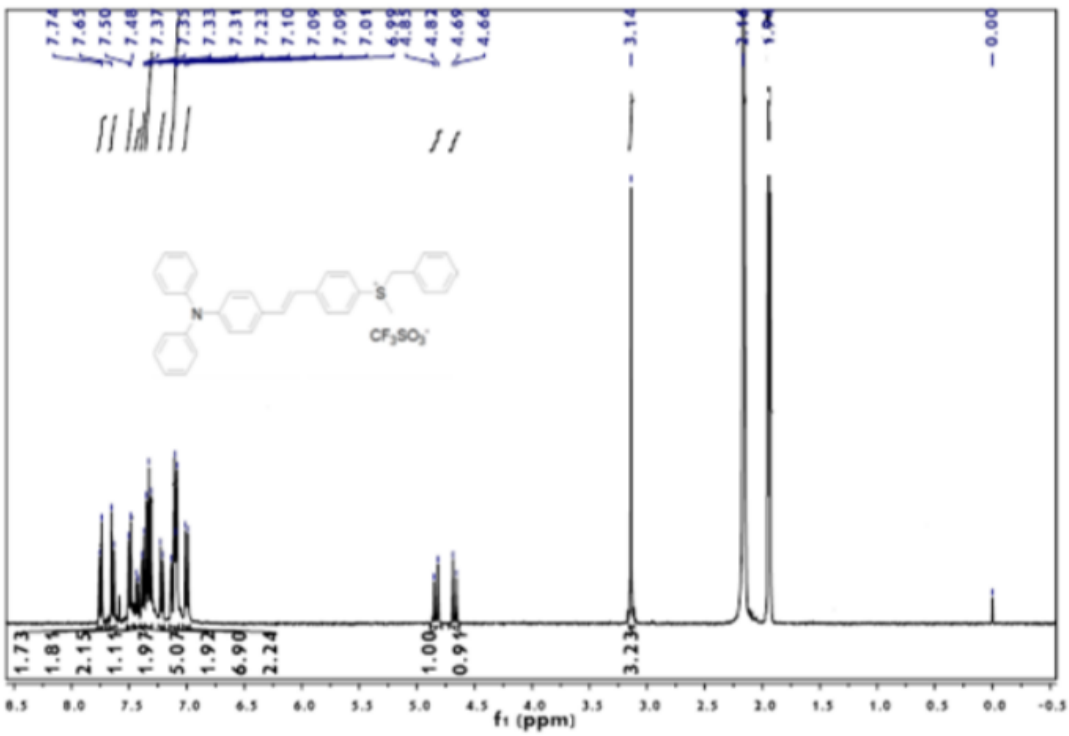

Figure 22 – 1H NMR spectrum of PAG 5 from Jin et al. (2013)[186]

Labelled peaks and integrals correspond with those from literature suggesting presence of desired compound, however presence of other peaks suggests sample is a complex mixture containing a number of impurities, including unreacted methyl triflate and solvents acetonitrile and diethyl ether. ^{13}C NMR (CD_3CN) of synthesised compound was inconclusive.

15 mL of a saturated aqueous solution of KPF_6 (0.844 g, 4.58 mmol, 2.09 equiv.) was added to a solution of PAG 5 (1.39 g, 2.19 mmol, 1.00 equiv.) and dissolved in acetone (15 mL). . The mixture was stirred for 2 h at room temperature in darkness. The precipitate was collected by filtration and re-dissolved in 15 mL of acetone. This anion-exchange step was repeated three times. The crude product was washed with water (3 x 10 mL) and diethyl ether (30 mL) and recrystallised from an acetone/diethyl ether system to afford PAG 5 PF_6 as a yellow powder.

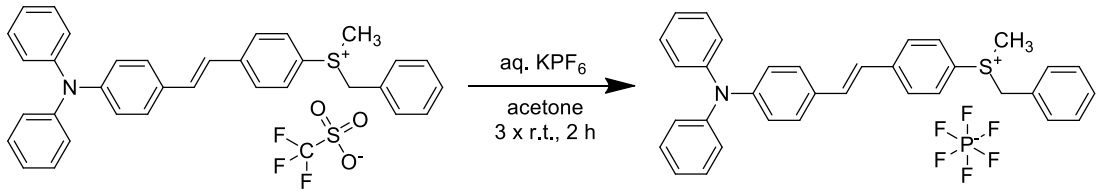

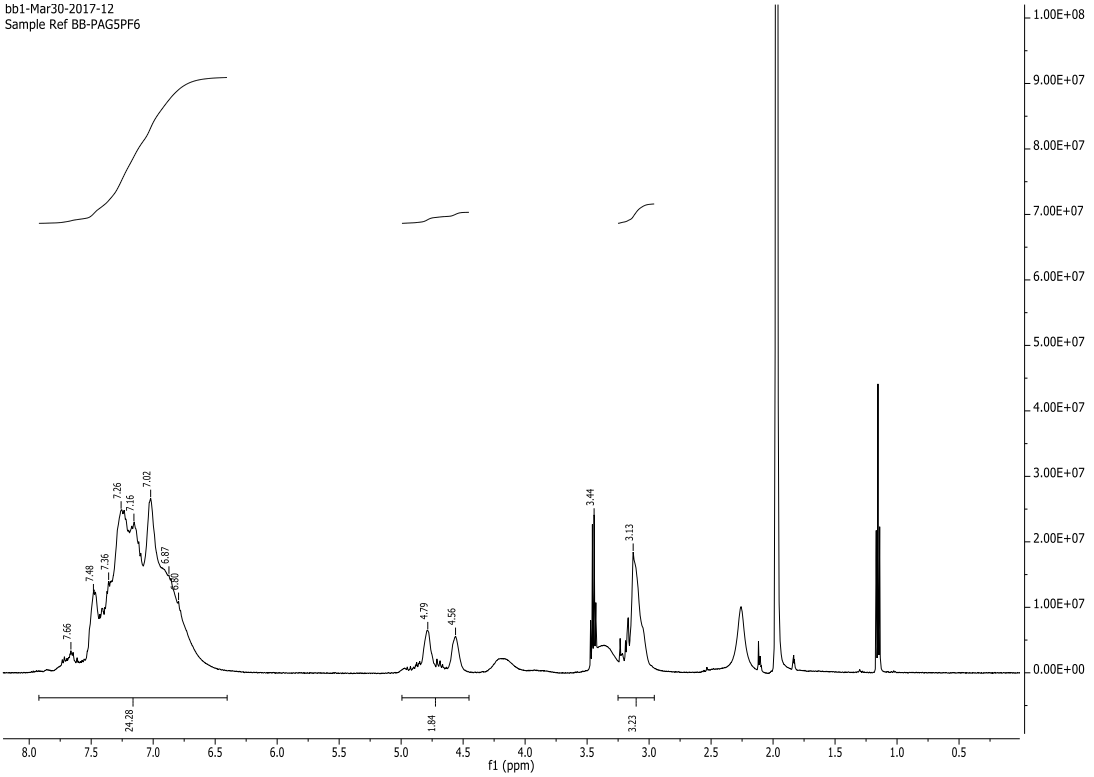

Figure 23 – ^{1}H NMR spectrum of synthesised compound PAG5 PF_6

Labelled peaks and integrals correspond with those from PAG5 PF_6 as expected, however with poor resolution. EI-MS (m/z): calcd for [C34H30NS]+, 484.2086, found: 484.2086 $[M]^+$ (v. weak, mixture). Peak at 829 cm^{-1} (strong, P-F) confirmed presence of PF_6 anion.

(E)-3-(((N,N-diphenyl)amino)-styryl)-phenyl-methyl-benzyl-sulfonium hexafluorophosphate (PAG 6)

The synthetic route was adapted from Zhou et al. (2011)[185], Jin et al. (2013)[186] and Zhou et al. (2002)[187]. Benzyl bromide (2.97 mL, 25.00 mmol, 1 equiv.) and 3-bromobenzenethiol (2.58 mL, 25.00 mmol, 1 equiv.), potassium carbonate (4.15 g, 30.0 mmol, 1.2 equiv.) and acetone (125 mL) were charged into a round-bottom flask fitted with a reflux condenser. The reaction mixture was stirred under reflux. The reaction was stopped when all starting materials were consumed as observed via thin-layer chromatography. Inorganic salts were filtered off and acetone was removed using a rotary evaporator. The crude

product was recrystallised from ethanol to afford white powder 3-(benzylthiol)-4'-bromobenzene.

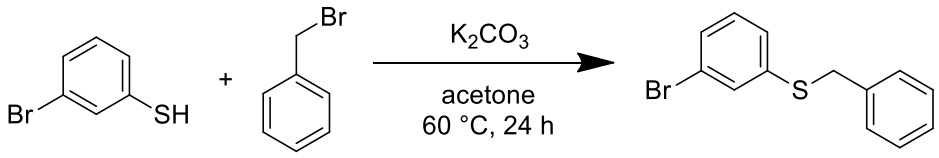

^{1}H NMR ($CDCl_3$; δ, ppm): 7.47 (t, 1H, ArH), 7.33 (m, 5H, ArH), 7.28 (d, 1H, ArH), 7.23 (dt, 1H, ArH), 7.13 (t, 1H, ArH), 4.15 (s, 2H, CH_2).
^{13}C NMR ($CDCl_3$; δ, ppm): 138.90 (1C, SArC), 136.77 (1C, ArC), 131.90 (1C, BrArC), 130.10 (1C, ArCH), 129.24 (1C, ArCH), 128.84 (2C, ArCH), 128.61 (2C, ArCH), 127.92 (1C, ArCH), 127.42 (1C, ArCH), 122.68 (1C, ArCH), 38.77 (1C, SCH_2).

4-(*N,N*-Diphenyl)aminestyrene (1.76 g, 6.49 mmol, 1 equiv.), 3-(benzylthiol)-4'-bromobenzene (1.992 g, 7.13 mmol, 1.1 equiv.), palladium(II) acetate (0.015 g, 0.065 mmol, 0.01 equiv.) and triethanolamine (6.5 mL) were charged into a round-bottom flask fitted with a reflux condenser and stirred at 120 °C under nitrogen. After 24 h, the reaction mixture was allowed to cool and poured into 200 mL of water. The crude product was extracted with three DCM washes. The organic phase was washed with brine (2 x 100 mL), dried over magnesium sulfate and filtered through silica gel to remove the palladium catalyst. Solvent was removed using a rotary evaporator. The crude product was purified by column chromatography with DCM/hexane (gradient – 4% DCM up to 32% DCM) as eluent to afford compound 6 as a light yellow powder.

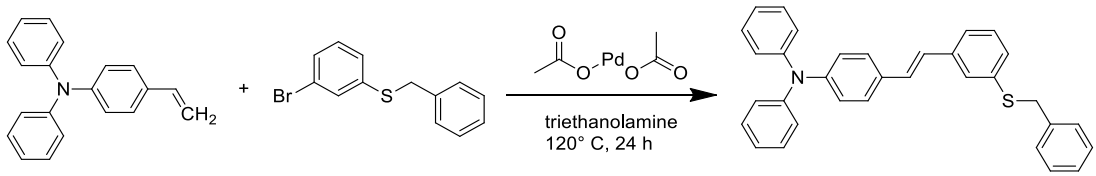

^{1}H NMR ($CDCl_3$; δ, ppm): 7.40 (s, 1H, ArH), 7.35 (d, 2H, ArH), 7.29 (d, 2H, ArH), 7.28 – 7.24 (m, 7H, ArH), 7.17 (t, 2H, ArH), 7.10 (d, 4H, ArH), 7.04 (d, 4H, ArH), 6.97 (d, 1H CH=C), 6.89 (d, 1H CH=C), 4.07 (s, 2H, CH_2).

^{13}C NMR ($CDCl_3$; δ, ppm): 147.51 (3C, ArCN), 138.31 (1C, ArC), 137.53 (1C, SArC), 136.72 (1C, ArC), 131.17 (1C, ArCH), 129.32 (2C, ArCH), 129.07 (2C, ArCH), 128.91 (2C, ArCH), 128.87 (2C, ArCH), 128.82 (2C, ArCH), 128.56 (2C, ArCH), 127.59 (2C, CH=CH), 127.42 (1C, ArC), 127.24 (1C, ArCH), 126.21 (2C, ArCH), 124.58 (2C, ArCH), 124.54 (2C, ArCH), 123.46 (2C, ArCH), 123.13 (1C, ArCH), 39.12 (1C, SCH_2).

Due to the high sensitivity to ambient light, all preparation was carried out in darkness. Firstly, compound 6 (0.95 g, 2.02 mmol, 1 equiv.) and anhydrous DCM (10 mL) were charged into a 50 mL round-bottom flask and cooled to – 78 °C. Methyl trifluoromethanesulfonate (0.25 mL, 2.23 mmol, 1.1 equiv.) was added dropwise to the solution. The reaction mixture was stirred at – 78 °C for 2 h, and then warmed to room temperature and stirred for a further 24 h. Subsequently, DCM was removed using a rotary evaporator and the residue was re-dissolved in acetonitrile. Diethyl ether was added to the solution dropwise and the resultant crystals were obtained by filtration and washed with diethyl ether. This step was repeated once more, affording PAG 6 as a light green powder.

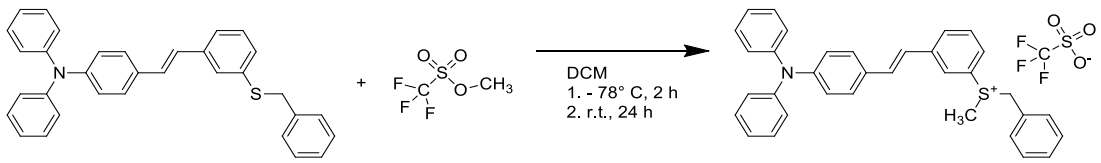

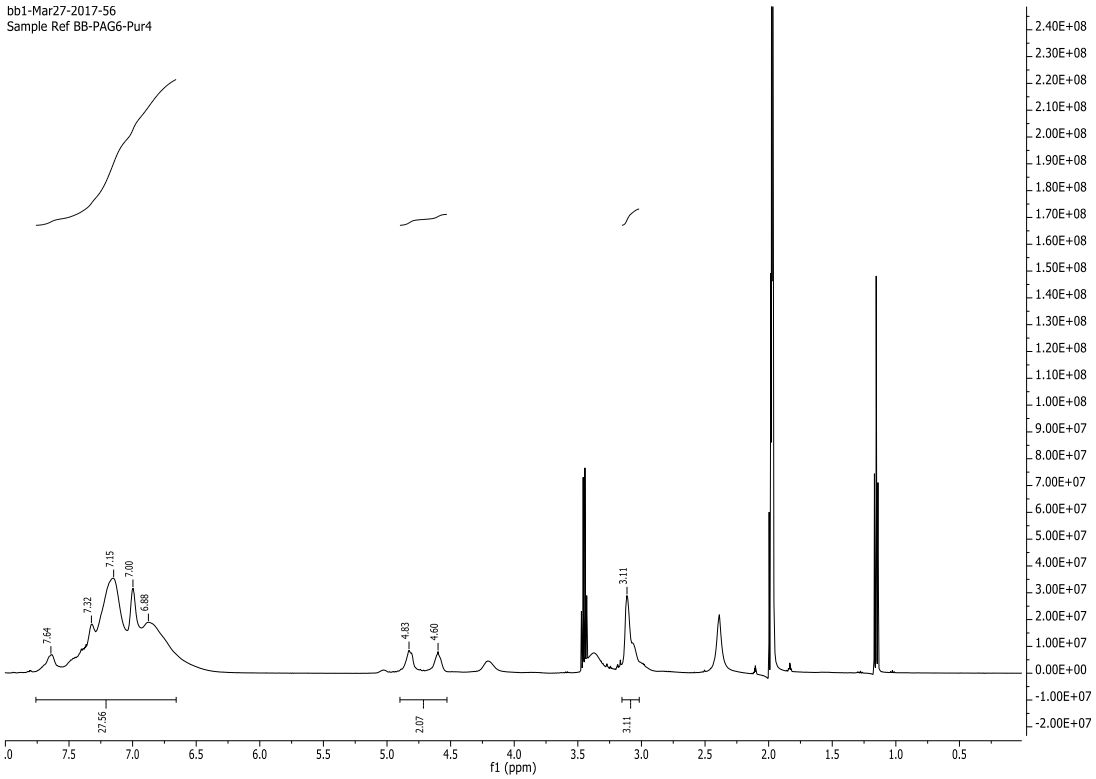

Figure 24 – ^{1}H NMR spectrum of synthesised compound PAG 6

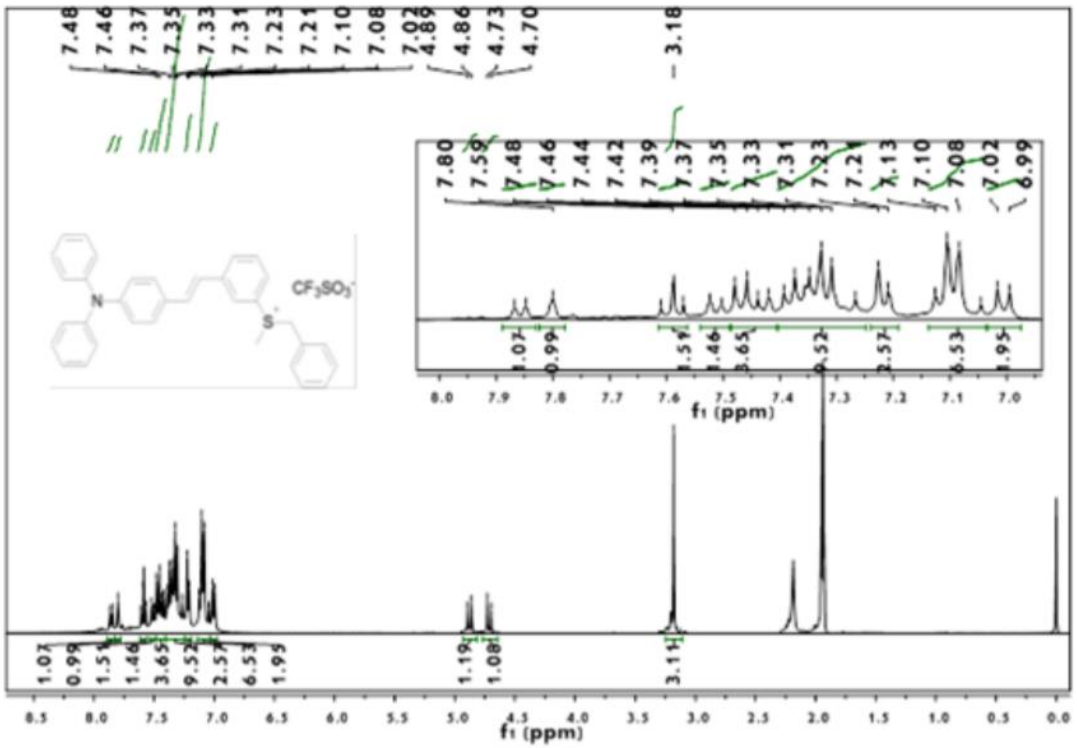

Figure 25 – 1H NMR spectrum of PAG 6 from Jin et al. (2013)[186]

Labelled peaks and integrals correspond with those from literature suggesting presence of desired compound, however presence of other peaks and poor

resolution suggests sample is a complex mixture containing a number of impurities, including unreacted methyl triflate and solvents acetonitrile and diethyl ether. ^{13}C NMR (CD_3CN) of synthesised compound was inconclusive.

15 mL of a saturated aqueous solution of KPF_6 (0.778 g, 4.23 mmol, 2.09 equiv.) was added to a solution of PAG 6 (1.28 g, 2.02 mmol, 1.00 equiv.) and dissolved in acetone (15 mL). The mixture was stirred for 2 h at room temperature in darkness. The precipitate was collected by filtration and re-dissolved in 15 mL of acetone. This anion-exchange step was repeated three times. The crude product was washed with water (3 x 10 mL) and diethyl ether (30 mL) and recrystallised from an acetone/diethyl ether system to afford PAG 6 PF_6 as a yellow powder.

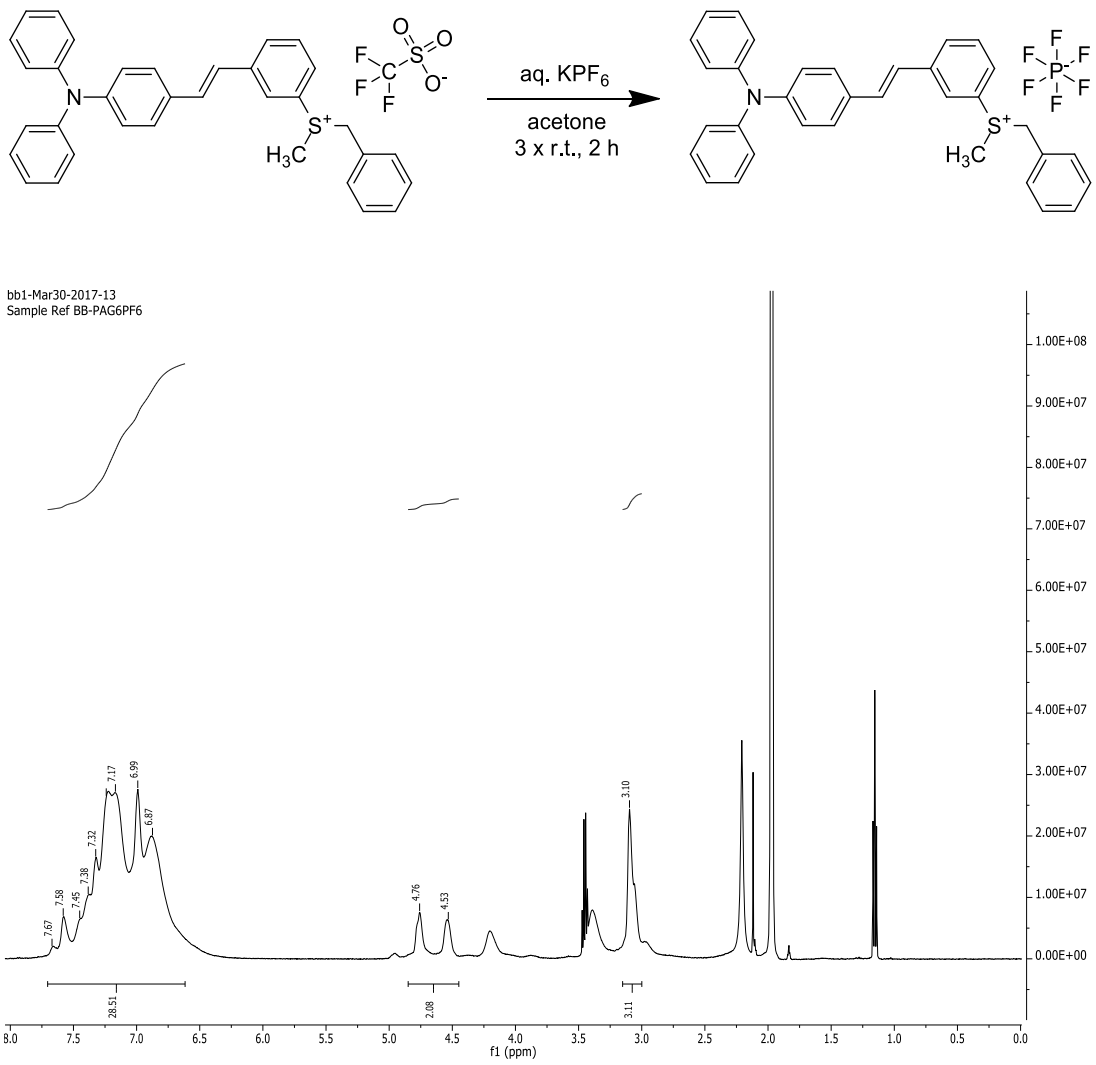

Figure 26 – ^{1}H NMR of synthesised compound PAG 6 PF6

Labelled peaks and integrals correspond with those from PAG 5 PF6 as expected, however with poor resolution. EI-MS (m/z): calcd for [C34H30NS]+, 484.2086, found: 484.2086 $[M]^+$. Peak at 829 cm^{-1} (strong, P-F) confirmed presence of PF_6 anion.

3.3. MALDI-TOF mass spectrometry

Matrix-assisted laser desorption/ionisation time of flight (MALDI-TOF) mass spectrometry was used to ascertain molecular weight of polyurethane dimethacrylate macromers. MALDI-TOF mass spectrometry was performed using a Bruker UltrafleXtreme MALDI-TOF/TOF with Smartbeam-II™ laser. The samples were acquired in positive ion reflectron mode (m/z range ~ 600-4000Da; potential mass resolution of up to R= 40,000). Samples were solvated in THF and mixed at a ratio of 1:24 with DCTB matrix (typically 10mg/ml in THF) with the addition of 1ul NaOAc solution to promote Na+ adduction.

3.4. Gel permeation chromatography

Gel permeation chromatography (GPC) was used to ascertain polydispersity of polyurethane dimethacrylate macromers. GPC was performed using a GPC system comprising of a Viscotek GPC max chromatograph, Waters 410 differential refractive index detector and a Gilson 831 column oven. Samples were prepared by dissolving a small amount of material in THF (approximately 3 mg/mL) with the addition of 2 µL/mL toluene as a flow marker. Two Polymer Labs PLgel Mixed E 3 µm columns (300 x 7 mm) were used and maintained at 40 °C. 100% THF (Fischer Scientific GPG grades) was used as mobile phase at a flow rate of 1.0 mL/min with an injection volume of 100 µL.

3.5. LC-MS

Liquid chromatography-mass spectrometry (LC-MS) analysis was used to quickly ascertain molecular weights of polyester diols. LC-MS analysis was performed using an Agilent 1260 Infinity with Agilent 6420A Triple Quadrupole LCMS MS System (Agilent Technologies, UK). Samples were prepared by

dissolving a small amount of material (1 – 2 mg) in approximately 1 mL methanol. The column used was Zorbax SB-C18 (2.1 x 50 mm, 1.8 µm) which was maintained at 40 °C. The flow rate of the mobile phase was set to 0.6 mL/min with an injection volume of 1 µL. Hydroxyl-terminated polyester samples were analysed using a mobile phase of water (+ 0.1% v/v formic acid) and acetonitrile (+ 0.1% v/v formic acid) in an isocratic elution mode at 35:65 ratio. The detection wavelength was set to 254 nm. A 100 – 2000 g/mol mass range was utilised with fragmentation of 125. Mass spectra were generated from chromatogram peak apexes.

3.6. Photorheology

Photorheology was used to elucidate gel points of a range of different photocurable monomers/macromers. Rheological measurements were performed on a Discovery hybrid rheometer (DHR-3, TA Instruments, USA) fitted with a UV accessory. The upper parallel plate and the bottom PMMA window, which permits transmittance of UV light, are both 20 mm in diameter. UV light irradiation was generated with an Omnicure S1500 mercury lamp (wavelength 280 – 600 nm) and was introduced into the rheometer UV chamber via a flexible light guide. The intensity of the UV light (2 mW) was measured using a radiometer for calibration and controlled by the advanced TRIOS software during experiments. Oscillations were set to controlled strain mode at 1 % strain. The photocurable formulations were sandwiched between two plates of the rheometer at a fixed gap of 200 µm. The axial force was controlled with a deviation of less than 0.1 N. A time sweep (10 min in total) with fast sampling mode of 25 Hz was utilised to facilitate accurate monitoring of rapid cross-linking progression. After 30 seconds, resin samples were irradiated for the remainder of the time sweep. Gel points were calculated from the crossover of elastic/storage (G') and viscous/loss (G'') moduli. Complex viscosity (Pa/s) and gap between plates (µm) were monitored during time sweeps to allow monitoring of change in material viscosity and material shrinkage.

3.7. Mould preparation

Various moulds were fabricated to allow for preparation of samples for physical properties testing. Utilising moulds for tensile testing and flexural testing as example. Firstly, sample shapes were generated using Tinkercad software. Chosen sample shape for tensile testing was dumbbell with dimensions: overall length – 50 mm; thickness – 3 mm; width at ends – 15 mm; width of narrow parallel-sided portion – 6 mm; length of narrow parallel-sided portion – 27 mm; and gauge length – 28 mm. Chosen sample shape for flexural testing was rod with dimensions: overall length – 50 mm; thickness – 3 mm; width – 6 mm; and lower support length – 20 mm. Moulds for sample mould preparation were FFF 3D printed using ABS. FFF 3D printed moulds were filled with equal parts PlatSil Gel-25 A and B, mixed and left to set overnight. Silicone rubber sample moulds were removed from FFF 3D printed moulds.

3.8. Tensile testing

Tensile testing was conducted to elucidate mechanical properties of a range of different photocured materials. Tensile testing was performed using a Shimadzu EZ-LX Test Compact Table-Top Universal/Tensile Tester fitted with a 5 kN EZ-Test-X load cell. The universal/tensile tester was fitted with an upper and lower tensile joint and a 5 kN non-shift manual type wedge grips with file teeth grip faces for flat specimens. Samples were first secured at the lower shoulder by the lower joint grip. The upper joint was lowered and gripped the upper shoulder of the sample ensuring a gauge length of 28 mm. Shimadzu Trapezium X software was used to design, execute, and analyse sample tests. Samples were loaded using force zero hold function to avoid inaccurate results. Test mode was set to single and test type was set to tensile. A pre-test force of 0.2 N was applied. Test speed was set at 10 mm/min. These parameters were selected as they allowed for accurate yet rapid testing of the range of materials tested. Test was stopped when sample break was detected. Stress-strain plots were generated in real-time during sample testing. Values for max force (N), max stress (tensile strength; MPa), elongation at break (mm) and energy (J) were automatically generated post-test whereas elongation at break (%) and (tensile) toughness (kJ/m^3) were calculated manually. All values

generated within 1 standard error (SE). Tensile testing was performed in triplicate for each resin formulation.

3.9. Flexural testing

Flexural testing was conducted to elucidate mechanical properties of a range of different photocured materials. Flexural testing was performed using a Shimadzu EZ-LX Test Compact Table-Top Universal/Tensile Tester fitted with a 5 kN EZ-Test-X load cell. The universal/tensile tester was fitted with a loading jig for compression and bending test compatible with a 5 kN load cell and a 2.5 kN 3 / 4 pt bending jig with infinitely adjustable span between 10 and 300 mm. Samples were placed onto the bending jig with a 30 mm lower support separation. Shimadzu Trapezium X software was used to design, execute and analyse sample tests. Samples were loaded using force zero hold function to avoid inaccurate results. Test mode was set to single and test type was set to 3-point bend. A pre-test force of 0.2 N was applied. Test speed was set at 20 mm/min. These parameters were selected as they allowed for accurate yet rapid testing of the range of materials tested. Test was stopped when sample break or sample displacement > 10 mm was detected. Stress-strain plots were generated in real-time during sample testing. Values for max force (N) and max stress (flexural strength; MPa) were automatically generated post-test. Elastic (flexural modulus; MPa) was manually generated by adjusting slope of the linear portion (elastic region) of the stress-strain curve. All values generated within 1 standard error (SE). Flexural testing was performed in triplicate for each resin formulation.

3.10. Nanoindentation

Nanoindentation was conducted to elucidate mechanical properties of a range of different photocured materials. Nanoindentation was performed using an Anton Paar Bioindenter (UNHT^3 Bio, Anton Paar, Austria). A standard linear loading-unloading mode was used. The nanoindentation tests were performed using a spherical indenter with 500 mm radius made of ruby, suitable for nanoindentation of soft materials. Square samples (10.0 mm x 10.0 mm, 0.5 mm thickness) were prepared from mould cured samples and SLA 3D printed.

Samples were stuck to a plastic dish with glue to prevent sliding during testing. An optical microscope was used to guide indentation placement, to avoid uneven surfaces that may give inaccurate results. 4 results were taken per sample at 50 µm apart. Test was load dependent with a maximum applied load of 1 mN. Load/unload speeds were 6 mN/min and a load hold of 5 seconds was applied before unloading. Values for indentation hardness (HIT, MPa), indentation modulus (EIT, MPa) and indentation creep (CIT, %) were automatically calculated post-test according to the Oliver and Pharr method. Shore A and D hardness values were calculated manually.

3.11. 3D printing

MakerBot and Ultimaker FFF 3D printers were used to fabricate moulds for tensile and flexural testing sample moulds. In addition, general lab equipment was also printed using FFF 3D printers. MakerBot Print and Ultimaker Cura software were used to orient MakerBot and Ultimaker prints respectively. PLA was used as feed material for FFF prints. Extruder temperature was 200 °C. Platform temperature was 60 °C. Reverse moulds for tensile and flexural testing sample moulds were printed on low quality, at a layer height of 0.30 mm, infill 10%, 2 shells with raft attached. A Formlabs Form 1+ SLA 3D printer was used to fabricate proof-of-printability objects. Formlabs PreForm software was used to elucidate ideal print orientation and generate build supports. Pre-set printing parameters for Clear V4 at 0.1 mm layer height were chosen for printing. No fine tuning (platform height offset = 0.00 mm) was required. The MiiCraft+ SLA 3D printer was also used to fabricated proof-of-printability objects. Miicraft Builder 1.1 software was used to elucidate ideal print orientation and generate build supports. Miicraft+ allows the user to control print speed (Fast, Normal. Slow), layer height (µm) and irradiation time per layer (s). No fine tuning (platform height offset = 0.00 mm) was required.

3.12. Differential scanning calorimetry (DSC)

DSC analysis was used to elucidate thermal properties of a range of photocured materials. DSC analysis was performed using a TA Q2000 DSC

(TA Instruments, USA), calibrated with indium (Tm = 156.6 °C, ΔHf = 28.71 J/g). The analysis was performed in a nitrogen atmosphere with flow rate of 25 mL/min. Tzero® pans with lids were used for all samples. Firstly, samples were cooled from room temperature to -80 °C and then heated to 200 °C at a heating rate of 10 °C/min. This cycle was repeated immediately afterwards to observe any differences after the first cycle. Melting temperatures (Tm) and crystallisation temperatures (Tc) were obtained at the peak of the melting endotherms and exotherms, respectively, whilst glass transition temperatures (Tg) were obtained at the inflexion point of the specific heat capacity. Samples were analysed in triplicate to confirm repeatability of measurements (n = 3).

3.13. Thermogravimetric analysis (TGA)

TGA analysis was used to elucidate thermal properties of a range of photocured materials. TGA analysis was performed with TA Discovery TGA (TA Instruments, USA) in a nitrogen atmosphere with a flow rate of 25 mL/min. Aluminium pans were used. In general, samples were heated to 600 °C at a step-rate of 10 °C/min. For others, whereby solvent loss was of key interest, samples were heated and held isothermal at 50 °C for 30 minutes, before heated to 600 °C at a step-rate of 10 °C/min Samples were analysed in triplicate to confirm repeatability of measurements (n = 3).

3.14. *In-vitro* drug release studies

Preliminary drug release studies

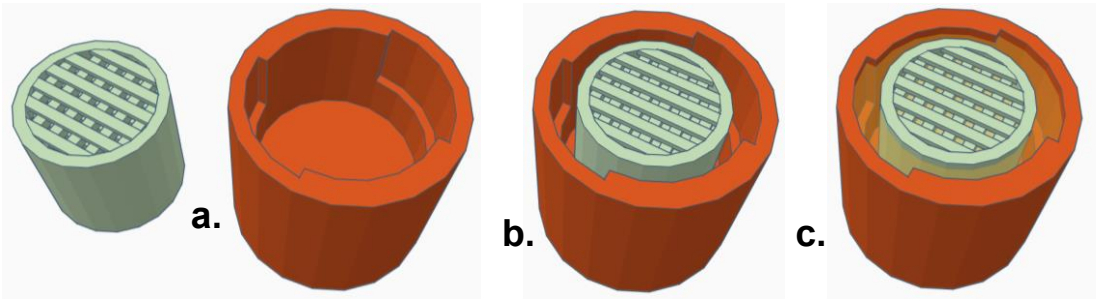

Figure 27 – Schematic for construction of unidirectional drug release device: **a.** sample and sample sleeves are SLA 3D printed separately **b.** sample is place inside the sample sleeve **c.** sample is fixed into place through addition and polymerisation of a TEGDVE formulation

Samples (cylindrical meshes – Ø 14.1 mm x 13.0 mm w/ 1.0 x 1.0 mm pore structure) were 3D printed using drug containing resins on a Formlabs Form 1+ SLA 3D printer. Samples were briefly washed with IPA and post-cured in a Form Cure UV oven at 60 °C for 60 min. Sample sleeves were 3D printed using a Formlabs Form 2 SLA 3D printer with Formlabs Dental Resin. Samples were fixed into 3D printed sleeves using a tetraethylene glycol divinyl ether (TEGDVE) formulation containing 1% w/w P3C-P and post-cured for a subsequent 60 min at 60 °C. Samples were suspended in glass scintillation vials (12.5 mL) and 10 mL of PBS (pH 7.4) was added. Magnetic stirrers were added, vials were capped and stirred at 150 rpm in an oil bath heated at 37 °C for 4 days. At regular intervals, 200 µL aliquots were withdrawn from each vial and replaced with an equal amount of PBS. Samples were frozen for later analysis by HPLC. Drug release studies for each sample were carried out in triplicate.

10 mg of aspirin powder was dissolved in 5 mL of acetonitrile. Aspirin was chosen as a model drug due to its documented use in drug release studies from SLA 3D printed samples[188]. The stock solution was serially diluted with PBS to produce the following calibration solution of concentrations: 2000, 1000, 500, 250, 100, 50, 25, 12.5, 6.25, 3.125 µg/mL. PBS was used as a control. These solutions were then analysed using HPLC (1260 Infinity, Agilent Technologies, UK). The column used was Phenomenex Synergi Hydro-RP (150 mm x 4.6 mm, 4 µm), which was maintained at an ambient temperature. The flow rate of the mobile phase was set to 1 mL/min with an injection volume of 10 µL. Samples were analysed using a mobile phase of water and acetonitrile in an isocratic elution mode at 55:45 ratio. The detection wavelength was set to 275 nm. The area under the curve (AUC) of chromatogram peaks corresponding to aspirin was used to generate a standard calibration curve and subsequently, facilitate quantification of drug release from samples.

Wider drug release studies

Samples (square films – 10.0 mm x 10.0 mm, 1.0 mm thickness) were 3D printed using a Formlabs Form 1+ SLA 3D printer. Samples were briefly washed with IPA and post-cured in a Form Cure UV oven at 60 °C for 60 min. Samples were placed into glass screw-cap vials (5 mL) and 2 mL of PBS (pH 7.4) was added. Vials were placed into an FFF-fabricated rack that was subsequently fixed into an Incu-Shake Incubating shaker (SciQuip, UK). The incubating shaker was set to shake at 150 rpm at a temperature of 37 °C for 28 days. At regular intervals 250 µL aliquots were withdrawn from each vial and replaced with an equal amount of PBS. Samples were frozen for later analysis by HPLC. Drug release studies for each sample were carried out in triplicate.

3 different drugs were used for wider drug release studies. Salicylic acid, a derivative of aspirin, was used instead of aspirin due to concerns aspirin may degrade over a long time period. Acetaminophen and naproxen were chosen as model drugs due to varying hydrophilicity and their documented use in drug release studies from SLA 3D printed samples[188]. 5 mg of each drug was dissolved in 1 mL and subsequently diluted 5-fold with PBS (pH 7.4). This stock solution was serially diluted with PBS to produce the following calibration solution of concentrations: 1000, 500, 250, 125, 62.5, 31.25, 15.625 µg/mL. As before, these solutions were then analysed using HPLC (1260 Infinity II, Agilent Technologies, UK). The column used was Poroshell 120 EC-C18 (3 x 150 mm, µm) which was maintained at 35 °C. The flow rate of the mobile phase was set to 0.5 mL/min. An injection volume of 5 µL was used for calibration solutions and samples containing salicylic acid and naproxen, whilst an injection volume of 1 µL was used for calibration solutions and samples containing acetaminophen. Calibration solutions and samples containing salicylic acid and acetaminophen were analysed using a mobile phase of water (+ 0.1% v/v) and acetonitrile (+ 0.1% v/v) in an isocratic elution mode at 50:50 ratio. Calibration solutions and samples containing naproxen were analysed using a mobile phase of water (+ 0.1% v/v) and acetonitrile (+ 0.1% v/v) in an isocratic elution mode at 40:60 ratio. The detection wavelength was set to 254 nm for all calibration solutions and samples. The area under the curve (AUC) of chromatogram peaks corresponding to each drug were

used to generate a standard calibration curve and subsequently, facilitate quantification of drug release from samples.

3.15. *In-vitro* cell viability studies

NIH 3T3 mouse embryonic fibroblast cells (passaged from 150 to 153) were purchased from HPA Culture Collections, Sigma-Aldrich, UK. Dulbecco's Modified Eagle Medium (DMEM, Gibco, Sigma-Aldrich, UK) with 4 mM L-glutamine, 4500 mg/L glucose, 1 mM sodium pyruvate, and 1500 mg/L sodium bicarbonate, supplemented with 10% v/v iron supplemented calf bovine serum (Sigma-Aldrich, UK) and 1% v/v penicillin and streptomycin solution (Sigma-Aldrich, UK) was used as a culture media to grow NIH 3T3 cells. Cells were passaged when they had reached approximately 80% confluence. NIH 3T3 cells were trypsinised with trypsin (0.25% w/v)-EDTA (0.53 mM) solution (2 mL). The trypsin solution was neutralised via addition of 4 times amount of complete culture media. The cell suspension was centrifuged for 5 min at 300 rpm. The cell pellet was resuspended and diluted with fresh culture media to 1,000,000 cells/mL. For general biocompatibility testing square samples were cut from solvent extracted mould cured film samples (5.0 mm x 5.0 mm, 0.5 mm thickness), sterilised in 70% v/v ethanol solution for 30 min and added to a well in a black 96-well plate. 100 µL of cell suspension (100,000 cells) was added to each well. This was done in triplicate and repeated six times. Positive controls (cell suspension only) and negative controls (media only) were subsequently ran. Plates were incubated at 37°C and 5% CO_2 for 24, 72 and 120 h (2 plates for each time interval). For Soxhlet drug leaching/biocompatibility testing square samples were cut from SLA 3D printed samples which had been continuously extracted for 0, 3, 8 and 24 hours with warm acetone (5.0 mm x 5.0 mm, 0.5 mm thickness). Samples were sterilised in 70% v/v ethanol solution for 30 min and added to a well in a black 96-well plate. 100 µL of cell suspension (100,000 cells) was added to each well in triplicate and repeated twice. Positive controls (cell suspension only) and negative controls (media only) were subsequently ran. Plates were incubated at 37°C and 5% CO_2 for 72 h.

Prestoblue™ Cell Viability Reagent (Prestoblue, Life Technologies Ltd, Thermo Fisher Scientific, US) was used to determine cell metabolic activity and ultimately viability. Each plate was equilibrated at room temperature for 30 min before addition of 11.1 µL (equal to 10% of culture medial volume per well) Prestoblue. Plates were shaken on a plate shaker for 2 min to ensure sufficient assay mixing and subsequently incubated at 37°C and 5% CO_2 for 1 h. Fluorescence was measured using a GlowMax Explorer plate reader (Promega, USA) at 1 s integration time. The average of the fluorescence values of negative control wells were subtracted from the fluorescence value of each experimental well. Fluorescence values from positive control wells were equated to 100% cell viability.

3.16. LIVE/DEAD Cell Staining

LIVE/DEAD Cell Imaging Kit (Invitrogen, UK) was used to qualitatively differentiate between live and dead NIH 3T3 cells at 24, 72 and 120 hours. The kit allows determination of cell viability based on intracellular esterase activity and plasma membrane integrity. Live Green (A) and Dead Red (B) dyes were thawed at room temperature. Subsequently, the contents of vial A were transferred to vial B and aspirated to produce a stock solution. 50 µL of this stock solution was added per well to the cultured cells (50 µL, 50,000 cells). The black 96 well-plate was then incubated at 25 °C for 15 min and subsequently observed under an inverted microscope. Pictures of each well were taken at 4x magnification by combining images of both GFP and Texas channels.

3.17. Determination of hydroxyl value

Two methods were utilised to ascertain the hydroxyl value (OHV) of polyester diols.

3.17.1. Acetylation method

This method was adapted from DGF C-V 17 a (53) and Ph. Eur. 2.5.3 Method A. In this method, the sample is acetylated with acetic anhydride in the presence of pyridine. Each hydroxyl group generates one mole of acetic acid and excess acetic anhydride reacts with water to create two mole of acetic acid. Acetic acid content is determined titrimetrically by difference between sample and blank values. The procedure is as follows:

Firstly, an acetylation mixture of 575 mL acetic anhydride and 1925 mL pyridine was prepared and stirred for 24 h before use. Sample weight and acetylation mixture used is based on predicted OHV. A polyester diol with Mn 400 g/mol will have a predicted OHV of 280.5 and hence a sample weight of 0.6 g and 5 mL of acetylation mixture was used. For example, a polyester diol with Mn 1000 g/mol will have a predicted OHV of 112 and hence a sample weight of 1.5 g and 5 mL of acetylation mixture was used. Sample and acetylation were both charged into a 250 mL round bottomed flask along with a magnetic stirrer. A glass funnel (width 40 mm) was installed to act as a reflux cooler. The flask was subsequently heated in an oil bath at 95 – 100 °C and stirred for 60 min. 1 mL of distilled water was added and stirred for another 10 min. The flask was removed from the oil bath and allowed to cool to room temperature. Condensed liquid on the funnel and flask neck were flashed with 5 mL neutralised alcohol. The mixture was titrated against phenolphthalein with 0.5N KOH solution in ethanol. A blind test without sample was conducted simultaneously. The hydroxyl value is calculated:

$$OHV = \frac{(b - a) \times 28.05}{E} + AV;$$

where, a = consumed 0.5N KOH solution in ethanol in sample test (mL), b = consumed 0.5N KOH solution in ethanol in blank test (mL), E = sample weight (g) and AV = acid value. Acid values for all polyester diols were determined to be negligible by dissolving sample in a 50:50 mixture of ethanol/toluene and titration against phenolphthalein with 0.5N KOH solution in ethanol. The hydroxyl value (OHV) indicates the necessary amount of KOH (mg) to neutralise the consumed amount of acetic acid of 1 g of sample during

acetylation and hence the units of OHV are mg KOH/g. The below equation was used to calculate polyester diol Mn from OHV (mg KOH/g):

$$M_{n\,(OHV)} = \frac{56.1 \times F}{OHV} \times 1000;$$

where, F = monomer hydroxyl functionality and OHV = hydroxyl value (mg KOH/g).

3.17.2. 19F NMR analysis

Method was adapted from "Quantification of hydroxyl group in polymers containing trace waterby19F NMR spectroscopy"[189]. The scope of this method comprises of reaction of sample hydroxyl groups with 4-fluorophenyl isocyanate in an NMR tube, followed by integration of peaks corresponding to the product versus internal standard α,α,α-trifluorotoluene in the 19F NMR spectra. The procedure is as follows:

A polyester diol (approx. 30 mg, 400 g/mol = approx. 0.075 mmol, approx. 1000 g/mol = approx. 0.03 mmol) was dissolved in deuterated chloroform (0.8 mL) in a NMR tube and (0.1 wt.%) DBTDL as catalyst and α,α,α-trifluorotoluene as an internal standard (30 µL, 0.244 mmol) were added. An excess amount of 4-fluorophenyl isocyanate (30 µL, 0.264 mmol, 3.52 equiv. to approx. 400 g/mol polyester diol) was added and after 15 min, the 19F NMR spectrum was recorded.^{19}F NMR ($CDCl_3$; δ, ppm): 62.73 (3F, s, CF3-Ph), 115.86 (1F, m, 4-F-Ph-NCO), 119.24 (1F, s, 4-F-Ph-NH-CO-OR). The hydroxyl value is calculated as so:

$$OHV = \frac{\left(\frac{3}{F} \times \frac{AUC_{sample}}{AUC_{standard}}\right) \times \left(\frac{V_{standard} \times 1.19}{146.11}\right)}{E} \times 1000;$$

where, F = monomer hydroxyl functionality, AUC_{sample} = area under peak corresponding to polyester-4-fluorophenyl isocyanate compound, $AUC_{standard}$ = area under peak corresponding to α,α,α-trifluorotoluene, $V_{standard}$ = volume

of α,α,α-trifluorotoluene (µL) and E = sample weight (mg). OHV units were mmol/g. The below equation was used to calculate polyester diol Mn from OHV (mmol/g):

$$M_{n\,(OHV)} = \frac{F}{OHV} \times 1000;$$

where, F = monomer hydroxyl functionality and OHV = hydroxyl value (mmol/g).

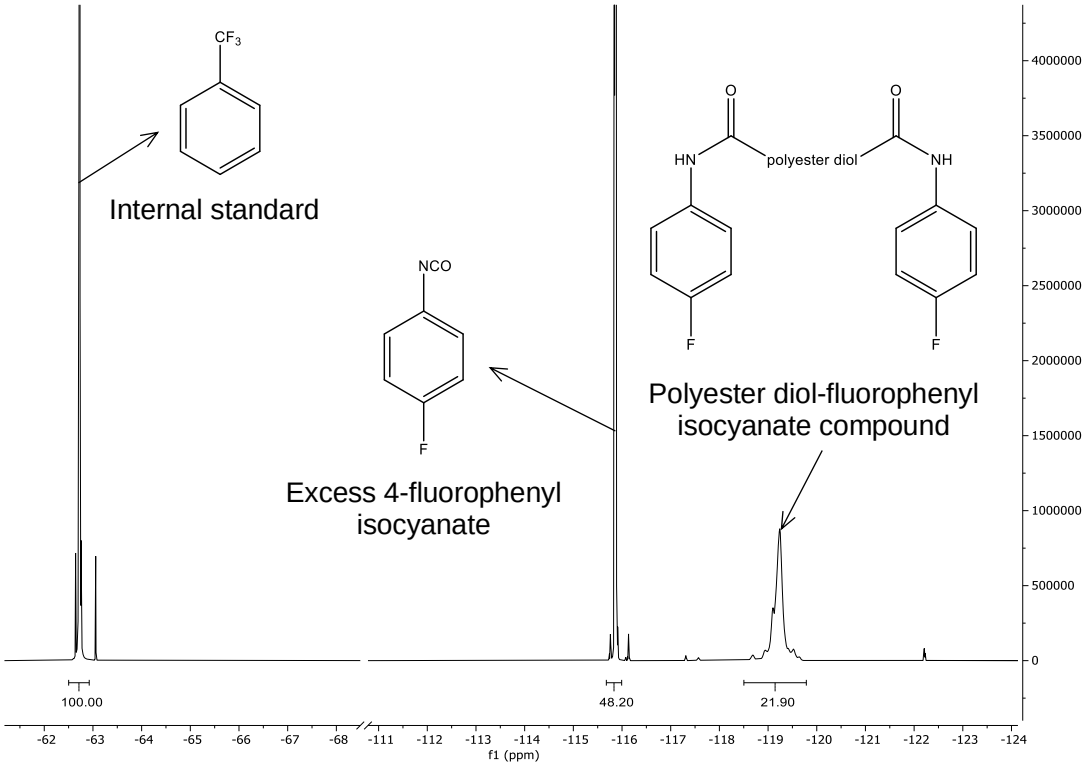

Figure 28 – ^{19}F NMR spectra analysing content of PLA400-4-fluorophenyl isocyanate compound versus internal standard α,α,α-trifluorotoluene

4. Material discovery, development, and characterisation

4.1 Introduction

Current scope of field of photopolymers

As described as part of a case study, porous IUDs containing approximately 100 mg of $CuCl_2 \cdot 2H_2O$ were successfully produced using a two-step process, whereby blank IUD structures were fabricated using FLFLGR01 resin and then loaded by immersion in a saturated $CuCl_2 \cdot 2H_2O$/solvent solution. Despite this success, resultant IUDs were extremely fragile and brittle, and would break when device arms were folded into an orientation required for intrauterine application. An absolute requirement of insertable/implantable devices is that they must withstand mechanical forces experienced during application, without failure or fracture[190]. Furthermore, the device must be able to withstand mechanical stresses and shocks encountered within the body, and also maintain tissue functionality and avoid causing discomfort by providing mechanical properties comparable to native tissue[190,191]. The tensile strength of the frame material of the TCu 380A IUD, a widely-used IUD, after sterilisation must exceed 13 MPa[192]. In comparison, the officially stated tensile strength of FLFLGR01 post-cured material ranges between 5.9 – 6.6 MPa[193]. Taking into consideration porosity, solvent immersion and $CuCl_2 \cdot 2H_2O$ content further decrease material tensile strength, FLFLGR01 resin is mechanically unsuitable for IUD fabrication. A possible solution is to use different resins which produce materials with high tensile strengths. For example, the officially stated tensile strengths of Formlabs Clear FLGPCL03 and Formlabs Durable FLDUCL01 post-cured materials are 31.8 and 65MPa, respectively[193]. However, the TCu 380 IUD must also exhibit a flexural modulus in the range of 133.5 MPa to 180.6 MPa[192], which neither of these materials achieve. It was therefore necessary to explore, discover and characterise new photopolymer systems that can produce materials with mechanical properties suitable for medical implants.

Toughness is an important physical property for implantable materials. Toughness is the ability of a material to deform plastically and to absorb energy in the process before fracture. Toughness relies on a good combination of strength and ductility. Toughness can be measured by calculating the area under the stress strain curve generated from a tensile test[194]. Materials of good toughness are paramount to prevent premature mechanical failure of implants which can lead to tissue injury, pain, additional surgical procedures and ultimately, treatment failure[195]. Most available SLA resins are based on low-molecular weight, multi-functional monomers, and highly crosslinked networks are formed. They form materials that are predominantly glassy, rigid and brittle with poor toughness, proving unsuitable for use as implantable materials[196]. Whilst some acrylate-based materials having good wear resistance for dental applications, this is achieved through highly crosslinked networks that lead to incredibly stiff materials. For photocurable materials requiring a low elastic modulus, this mode of strengthening is not applicable and hence, acrylate-based materials are plagued with unsuitable toughness due to an inherent trade-off between a low modulus and toughness[195]. The poor mechanical properties associated with (meth)acrylates are associated with underlying network structure. Epoxy resins are typically cured in the presence of amines or anhydrides (cationic) in a step growth manner leading to uniform, ordered networks that are tough and less brittle. In comparison, (meth)acrylate-based systems undergo radical chain growth polymerisation, which leads to highly irregular crosslinking due to a rapidly decreasing average kinetic chain length (propagation versus initiation and termination ratio) resulting in a brittle, non-tough inhomogeneous photopolymer network[197,198].

To improve (meth)acrylate-based material mechanical properties and toughness, it is necessary to optimise polymer architecture. Monomer composition plays a significant role in the determination of mechanical properties. (Meth)acrylate monomers that form interchain hydrogen bonds or are more polar, tend to polymerise at higher rates which leads to materials with improved mechanical properties. For example, Torres-Filho et al. demonstrated addition of 10% w/w of a hydrogen bond forming polyurethane diacrylate to a resin consisting of tri- and pentaacrylates improved material

mechanical properties, whereas addition the of short PEG-based diacrylates achieved the opposite[199]. Furthermore, polyurethane di(methacrylates) based on “soft” polyether/ester diols copolymerised with “hard” aromatic/aliphatic diisocyanates can also afford materials with improved toughness. This is associated with crystalline “hard” domains phase separating from “soft” domains, efficiently dissipating potential crack propagating forces and thereby improve material fracture toughness[200]. Photo-curing conditions and photoinitiator concentration also contribute to material toughness. Generally, material properties, including toughness, increase with double bond conversion (DBC) and hence it is necessary that photo-curing conditions are optimal to achieve maximum DBC. Real time FTIR (RT-FTIR) can be used to monitor DBC and hence it is utilised to adjust photocuring parameters such as light intensity, light wavelength, duration of irradiation, oxygen exposure and photoinitiator concentration, to ensure maximum DBC of (meth)acrylate-based systems[198].

Beyond monomer composition and photo-curing conditions, there are several other strategies that can improve toughness of photopolymer materials. Co-reactants that can regulate network formation have been investigated for improving toughness of (meth)acrylate-based systems. Thiol based chain transfer agents (CTAs) readily react with (meth)acrylates and other vinyl compounds and provide a versatile platform for regulation of cure kinetics and mechanical properties of the final polymer. Thiols act as potent hydrogen donors and generate thiyl radicals that can react with unsaturated carbon bonds in a “click” process. Reactivity of thiols with (meth)acrylates is considered intermediate, meaning generated radicals undergo chain transfer with thiol, but at a rate significantly less than (meth)acrylate propagation. In the presence of oxygen, this rate shifts in favour of chain transfer, due to the increased reactivity of thiols with peroxy radicals. Thiol-ene systems are less sensitive to oxygen inhibition than (meth)acrylate-based systems[201]. Polymers based on di-, tri- or tetra-thiols can react with (meth)acrylate-based monomers in a mixed chain growth/step-growth like manner, resulting in more uniform crosslink density and a higher final double bond conversion (> 90%). The more homogeneous composite network exhibits sharper, more defined thermal

glass transitions at lower temperatures, is less stiff and hard due to formation of flexible thioether bridges, and has improved toughness[202]. Thiols with different functionalities containing different functional groups such as urea, ester, ether also exist and can be used to modify material properties for different applications[198].

Another way to improve the toughness of photopolymer materials is through formation of an interpenetrating network (IPN). Mixtures containing both acrylates (with radical photoinitiators) and epoxides (with cationic photoinitiators) can undergo simultaneous polymerisation to form an IPN. Acrylates and epoxides do not copolymerise under these conditions, and instead, crosslinking locks the acrylate and epoxide polymers together non-covalently in an irreversible fashion[203]. A plethora of studies have investigated a number of different IPNs containing (meth)acrylate and epoxy-based systems, with increase of mechanical properties including hardness and toughness, compared to constituent parts, a commonly observed trend[198]. For example, Jansen et al. prepared a series of IPNs from monofunctional and difunctional (meth)acrylates and epoxides. A semi-IPN of poly(*p*-phenylene oxide)-based epoxide and monofunctional methyl methacrylate was found to have the highest toughness[204]. Additives used to toughen epoxy-based systems can also be applied to (meth)acrylate-based systems. Liquid rubbers and self-assembling block copolymers have demonstrated the ability to improve (meth)acrylate-based material toughness, albeit at the expense of stiffness and low viscosity. Furthermore, Sandmann et al. improved the mechanical properties of a polyurethane dimethacrylate/tetraethylene glycol dimethacrylate (TEGDMA) composite with core-shell nanoparticles. Success was attributed to effective adhesion of the nanoparticles within the TEGDMA matrix, and reduced polymerisation shrinkage of the polyurethane dimethacrylate[205]. However, other toughening additives such as core-shell and inorganic nanoparticles have proven unsuccessful in improving mechanical properties of (meth)acrylate-based systems. Nevertheless, by regulating and optimising polymer architecture using strategies discussed above, it is expected that the effectiveness of toughening additives will improve in (meth)acrylate systems[198].

It was decided to explore and prepare polyurethane (meth)acrylate systems based on a variety of different polyether and polyester diol “spacer” compounds copolymerised with an aliphatic diisocyanate, isophorone diisocyanate, and then analyse and compare their material mechanical properties against existing (meth)acrylate-based materials and medical grade implantable materials. Furthermore, “spacer” diol compounds were functionalised on terminal hydroxyl groups with acrylate groups. This was carried out in order to analyse how copolymerisation of spacer compounds with isophorone diisocyanate altered the mechanical properties by direct comparison of polyurethane dimethacrylate and acrylate monomers containing the same spacer compound. It was intended that a wide range of (meth)-acrylate-based heteropolymer systems would be prepared and characterised, with polyurethane dimethacrylates used as the main constituents. Minor constituents include reactive and non-reactive diluents and thiol-ene based CTAs. Heteropolymer polymerised materials were examined by mechanical testing including tensile testing and flexural testing using a universal testing machine, and hardness testing using nanoindentation, to further characterise and identify optimal implantable materials. Furthermore, nanoindentation, differential scanning calorimetry (DSC) and thermogravimetric analysis (TGA) were used to characterise other material properties such as glass transition temperatures, crystalline versus amorphous contents, residual solvent/resin contents, and porosity. The effect of certain conditions (temperature, catalyst amount) during different steps of polyurethane dimethacrylate preparation on mechanical properties, coupled with gel permeation chromatography (GPC) and MALDI-TOF-MS analysis, were investigated, with the aim being to further optimise polyurethane dimethacrylate synthesis. Low viscosity hydroxyl-terminated poly(lactic acid), poly(glycolic acid) and poly(lactic-co-glycolic acid) compounds were prepared and used to broaden the range of polyurethane dimethacrylate materials with tailorable biodegradable properties.

4.2. Results and Discussion

4.2.1. Polyurethane dimethacrylate synthesis

Poly(ethylene glycol) (PEG), poly(propylene glycol) (PPG), hydroxyl-terminated poly(tetrahydrofuran) (PTHF) and hydroxyl-terminated poly(caprolactone) (PCL), each of two different molecular weights (either between 400 – 650 g/mol or between 1000 – 1250 g/mol), were chosen as diol spacers molecules to produce di(meth)acrylate-based monomers. PEG was chosen due to it being a well-documented and commonly investigated polyether for biomedical applications, in addition to its inherent bioinert properties[206]. Furthermore, PEG-based materials are water-soluble, permitting 3D printing of hydrogel materials which can offer material properties similar to that of soft tissue, are compatible with hydrophilic APIs, and can offer widely programmable sustained drug-release profiles[207]. PPG, also a polyether, was chosen due to noted high flexibility properties which are desirable for implantable materials with the purpose being to mimic the material properties of soft tissue. In addition, PPG-based materials are reasonably water-soluble, imbue formulations with low viscosity, a desirable property for SLA resins, and are highly stable and bioinert[208]. PTHF-based materials, another polyether, are also highly flexible, stable and bioinert. PTHF, unlike PEG and PPG, is hydrophobic, and hence can cater as a vehicle for drug delivery of more hydrophobic APIs[175]. PCL, unlike PEG, PPG and PTHF, is a polyester and offers biodegradability through hydrolytic and enzymatic scission of ester groups. Degradation of PCL is slow due to hydrophobicity and crystallinity, facilitating extended and sustained drug release profiles. Many PCL-based medical and drug delivery devices have attained FDA approval due to their resorbable and bioinert properties[209,210].

Isophorone diisocyanate (IPDI) was chosen as the diisocyanate for polyurethane-based material synthesis for a few reasons. Firstly, IPDI, an aliphatic isocyanate, is more biocompatible than aromatic isocyanates such as toluene diisocyanate and methylene diphenyl diisocyanate [176,211]. Secondly, aliphatic isocyanate-based polyurethane materials tend to be less stiff and

rigid than those prepared using aromatic isocyanates, and are hence more suitable for fabrication of soft and flexible materials[212].

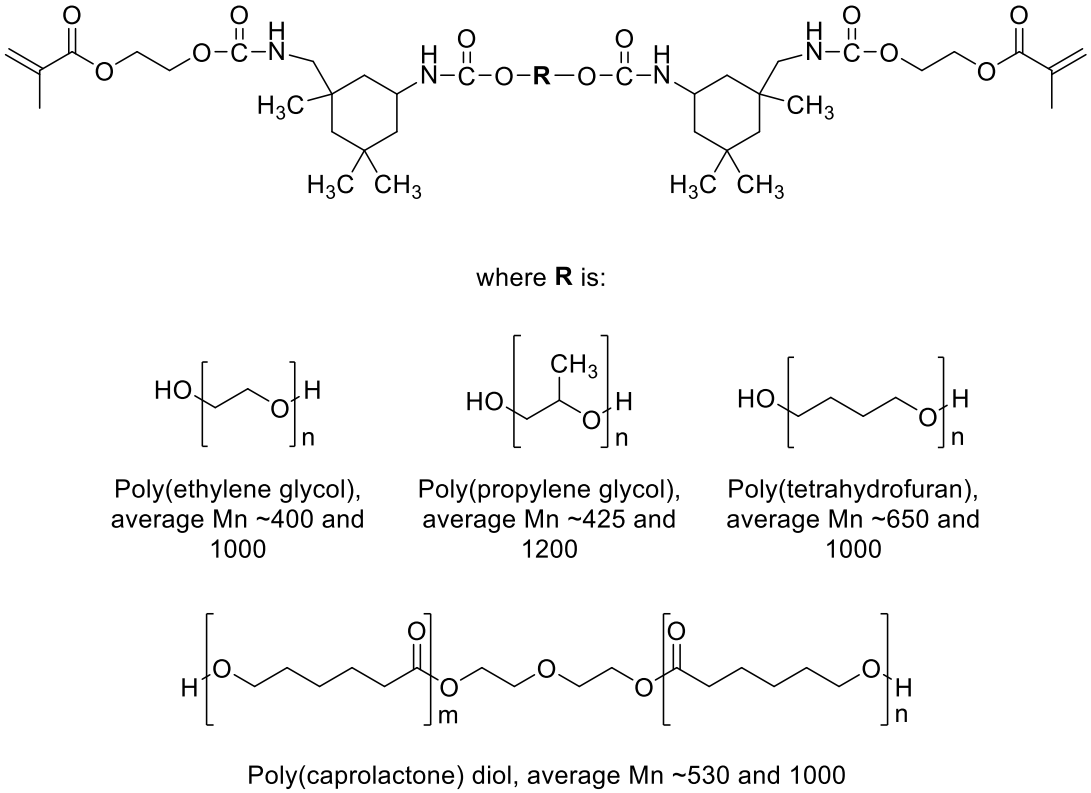

Figure 29 – Molecular structures of synthesised polyurethane dimethacrylates

Finally, the reactivity of the primary and secondary isocyanate groups of IPDI are unequal, unlike other aliphatic isocyanates such as hexamethylene diisocyanate, allowing for controlled synthesis of low molecular weight monomers of low polydispersity, meaning reproducible, uniform and low viscosity photocurable resins that are compatible with SLA 3D printing[212].

Both forward and reverse synthetic routes were considered for the preparation of polyurethane dimethacrylate monomers/oligomers. The forward route involves formation of the spacer-IPDI prepolymer before end-cap functionalisation with methacrylate groups. The reverse route instead involves formation of hydroxyethyl methacrylate (HEMA)-IPDI prepolymer, followed by end cap functionalisation of spacer-diols with prepolymer. Synthesis of

polyurethane dimethacrylates via the forward route was initially pursued due to the wealth of literature detailing the route of synthesis[176,177,213–217]. However, several issues arose when utilising this route that made it less desirable for the synthesis of an SLA 3D printable polyurethane-based resin.

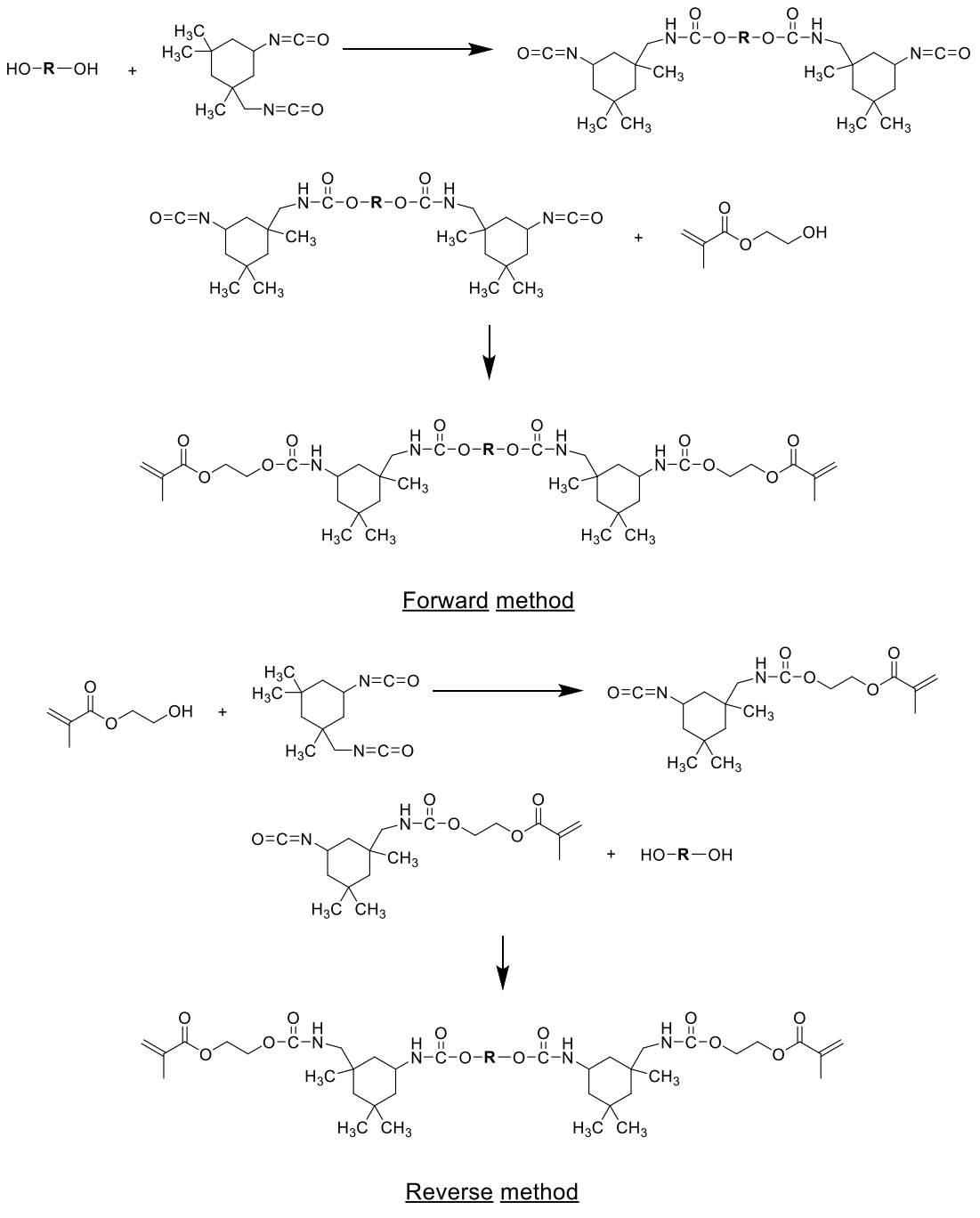

Figure 30 – Reaction schemes showing forward (top) and reverse (bottom) methods for preparation of polyurethane dimethacrylates

Firstly, different spacer compounds required different reaction temperatures for copolymerisation with isophorone diisocyanate. For example, formation of a PEG-IPDI prepolymer could be prepared at 60 °C, whereas formation of PPG-IPDI prepolymer required temperatures between 80 and 100 °C. This is speculated to be due to steric hindrance caused by the methyl side group on PPG[218]. This could lead to an increase in polydispersity and molecular weight of oligomers due to a decrease of selectivity of isophorone diisocyanate reactivity at elevated temperatures, leading to photocurable resins with non-uniform material properties and unsuitably high viscosities[219]. Secondly, it was difficult to track when prepolymer formation was complete via FTIR analysis due to incomplete consumption of the O-H (or any other) peak. Finally, the end-cap functionalisation final step with hydroxyethyl methacrylate required elevated temperatures to achieve completion. Consequently, premature polymerisation often occurred during reaction or work-up. For these reasons, a reverse route was instead preferred[212,220]. Synthesis of HEMA-IPDI prepolymer was consistent and achievable at room temperature, promoting a more consistent, low molecular weight prepolymer that acted as the precursor for all polyurethane-based monomers. Monitoring of HEMA-IPDI prepolymer synthesis progression and completion is observable through FTIR analysis (disappearance of O-H peak) (Figure 31). Furthermore, FTIR analysis was used to track progression and completion of the second step (disappearance of N=C=O peak). Additionally, the reverse route allowed use of elevated temperatures and catalyst without possible increase of monomer polydispersity and molecular weight[179].

Yields of products synthesised using the reverse route method were extremely high, ranging between 90 – 95%, attributed to a one-pot method and conservative work-up. This involved precipitation of the crude product in cold hexanes to remove/reduce catalyst component, redissolution in methanol to both quench any remaining unreacted isocyanate and to facilitate azeotropic removal of toluene, concentration by rotary evaporation and under high vacuum with periodic sonication and gentle heating.

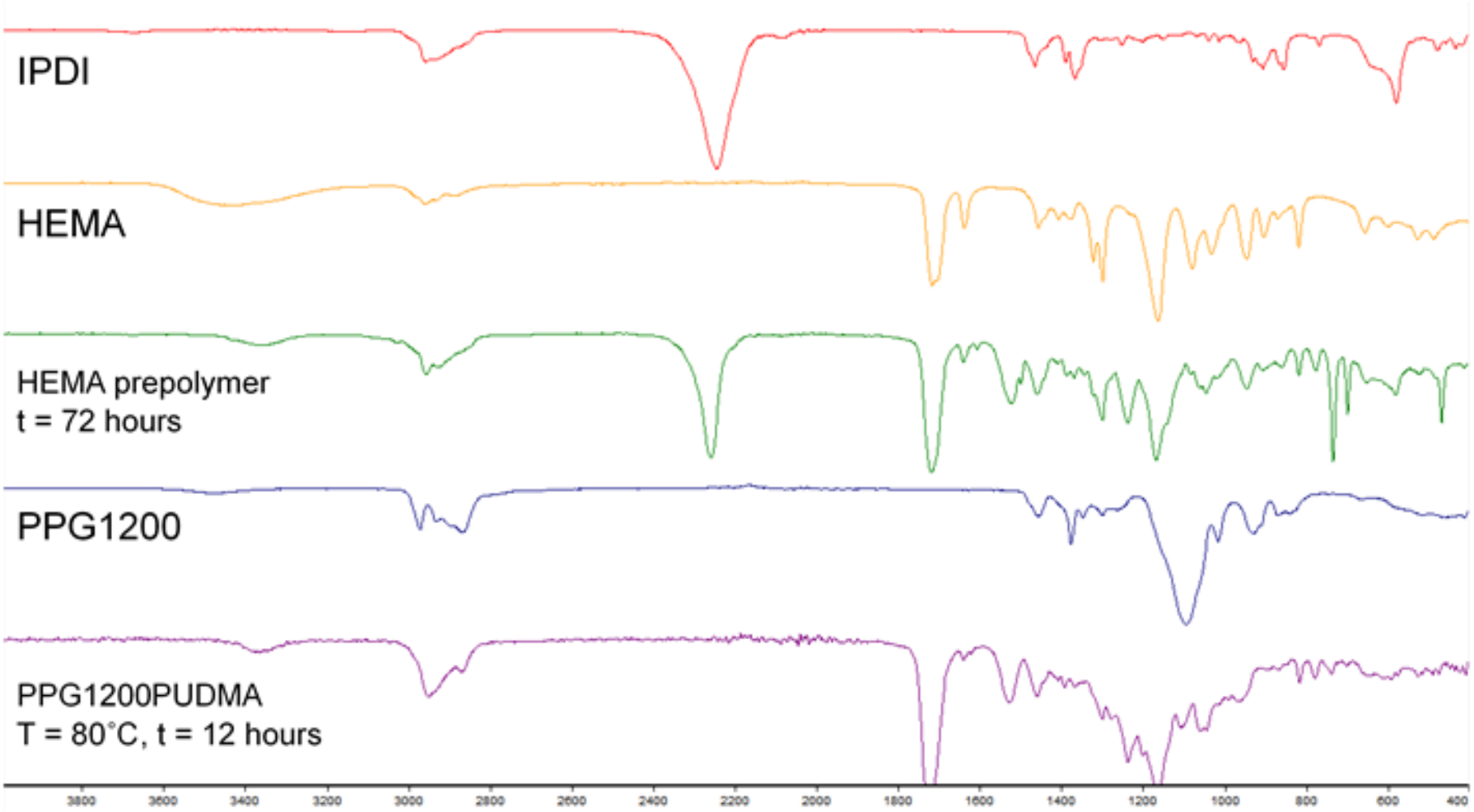

Figure 31 – FT-IR analysis of the step-by-step progression of polyurethane synthesis.

^{1}H NMR spectrum analysis of polyurethane dimethacrylate-based monomers corresponded with expected results based on ^{1}H NMR data of the starting spacer diols and isophorone diisocyanate, disappearance of peaks that correspond to alcohol groups (approx. 5 - 2 ppm) and appearance of peaks at 6.2 – 6.1 ppm (s), 5.7 – 5.6 ppm (s), 4.4 – 4.3 ppm (t), 3.85 – 3.8 ppm (t), 3.7 – 3.6 ppm (m), 2.95 – 2.9 ppm (d) 2.0 ppm (s), 1.85 – 1.5 ppm (m), 1.10 ppm (s) and 0.95 ppm (s).

4.2.2. Di(meth)acrylate synthesis

In addition to polyurethane dimethacrylate preparation, spacer compounds were functionalised on terminal hydroxyls with acrylate groups. For the synthesis of diacrylate monomers two synthetic routes were considered. Firstly, the end-group functionalisation of hydroxyl-terminated spacer molecules by catalytic esterification with acrylic acid[175,208,221] and secondly, end-group functionalisation by esterification with acryloyl chloride in the presence of triethylamine[210,222–225]. The latter method presented several issues.

Firstly, acryloyl chloride is considerably more expensive than acrylic acid. Secondly, the bi-product triethylamine hydrochloride salt and excess acryloyl chloride and triethylamine proved difficult to remove during work-up. Conversely, the by-product water and excess acrylic acid and tosylic acid were relatively easy to remove during work-up. Lastly, products produced via the acryloyl chloride method were heavily coloured and tended to auto-polymerise during work-up, despite the presence of the photoinhibitor 4-methoxyphenol (MEHQ). It was speculated this could have been due to removal of the photoinhibitor during work-up steps, and residual acryloyl chloride reacting with water to produce hydrochloric acid, post-removal of triethylamine and/or generation of impurities that sensitise the material to autopolymerisation. Products of the acrylic acid method were either colourless or slightly yellow

and did not auto-polymerise during work-up or storage. For these reasons, the acrylic acid method was utilised for the synthesis of all diacrylate monomers. Yields of products synthesised using the acrylic acid method varied depended on the spacer molecule used. Yields for PTHF diacrylates (PTHFDAs) products ranged between 75 – 85%. These high yields were attributed to a simple and straightforward synthetic route and work-up that did not deviate from that detailed in literature[175]. Yields for all PPG diacrylates (PPGDAs) were initially low, attributed to incomplete acrylation of starting materials and loss of product during work-up. Malucelli et al. noted that PPG products undergo hydrolytic chain cleavage by tosylic acid in the presence of water, yielding more hydroxyl groups that are then subjected to acrylation[208]. Insufficient reaction time and/or amount of acrylic acid therefore results in products with acrylate functionalities significantly lower than 2. It was also speculated that washing PPG diacrylate products with dilute 1M sodium hydroxide may also result in hydrolytic cleavage of PPG oligomer chains. To alleviate this problem, acrylic acid content was increased, reaction time extended and washing steps altered.

FT-IR and ^{1}H NMR analysis of monomers confirmed acrylate functionality increased to approximately 2 without significant impurities present. Product yields were improved to between 70 – 85% yield. Work-up of PEG diacrylate (PEGDA) products omit potassium carbonate treatment and aqueous washes, due to the aqueous solubility of PEGDA products. Instead, crude PEGDA products were dried, filtered and concentrated by rotary evaporation post-reaction and then precipitated into large excesses of diethyl ether thrice, yielding white waxy products. Yields for PEG2000 diacrylates (PEG2000DA) ranged between 70 – 80% with minimal impurities, whereas yields for PEG1000DA ranged between 20 – 35%. A lower yield for PEG1000 diacrylate was expected due to loss of product during diethyl ether washing. Yields for PCL diacrylate (PCLDA) products could not be improved above 10 – 25%, despite various work-up iterations. It was speculated that poor yields were due to hydrolysis of polyester chains during the reaction and/or work-up. Reaction

of hydrolysed polyester carboxylic acids with potassium carbonate led to a product that was poorly extracted by organic solvents, leading to loss of product.

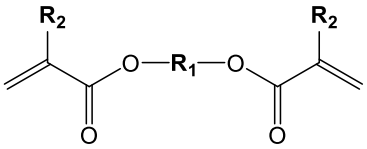

where $\mathbf{R_1}$ is:

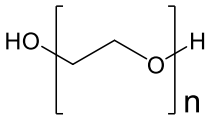

Poly(ethylene glycol), average Mn ~400, 1000 and 2000

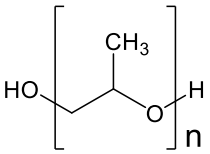

Poly(propylene glycol), average Mn ~425, 1200 and 2000

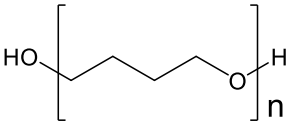

Poly(tetrahydrofuran), average Mn ~650, 1000 and 2000

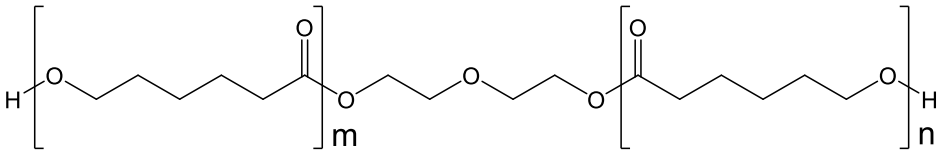

Poly(caprolactone) diol, average Mn ~530, 1250 and 2000

and $\mathbf{R_2}$ = H or CH_3

Figure 32 – Molecular structures of synthesised di(meth)acrylates

In this case, preparation of polyester di(meth)acrylates via the (meth)acryloyl chloride method may prove more successful, as dry conditions prevent hydrolysis of product. ^{1}H NMR analysis of diacrylate-based monomers corresponded with expected results based on ^{1}H NMR data of starting spacer diols, disappearance of peaks that correspond to alcohol groups (approx. 5 - 2 ppm) and appearance of three peaks at 6.5 – 6.4 ppm (d), 6.2 – 6.1 ppm (dd) and 5.9 – 5.8 ppm (d) that correspond to acrylate protons. Preparation of

PTHF dimethacrylates utilised the methacrylic acid method whereas preparation of PLA, PLGA(50/50) and PGA dimethacrylates utilised the methacryloyl chloride method. Preparation, work-up and resultant yields of PTHF dimethacrylates were near identical to those of PTHF diacrylates (78.51 %), albeit the substitution of acrylic acid with an equimolar amount of methacrylic acid. Preparation of PLA, PLGA(50/50) and PGA dimethacrylates via the methacryloyl chloride method were significantly more successful than synthesis of diacrylate compounds via the acryloyl chloride method. Products were afforded in greater yields, were less coloured and were less prone to autopolymerisation. The latter meant compounds could undergo more rigorous purification procedures and hence products contained fewer impurities. Nonetheless, products were still less stable than those prepared via the (meth)acrylic acid method. ^{1}H NMR analysis of dimethacrylate-based monomers corresponded with expected results based on ^{1}H NMR data of starting spacer diols, disappearance of peaks that correspond to alcohol groups (approx. 5 - 2 ppm) and appearance of three peaks at 6.30 – 6.15 ppm (s), 5.70 – 5.60 ppm (s) and 2.0 ppm (s) that correspond to acrylate protons.

4.2.3. Mechanical properties analysis

4.2.3.1. Tensile and flexural testing

Tensile testing and flexural testing strips were produced by curing resin in moulds. Silicone moulds were first produced by pouring fast curing platinum cure silicone into FFF 3D printed reverse moulds based on shapes and dimensions of specimens DIN EN ISO 527-3 (tensile test) and DIN EN ISO 178 (flexural test). All polyurethane based resins were diluted with 20% w/w reactive diluent isobornyl acrylate (IBOA) to reduce viscosity to allow easier dispensing of resin into moulds. PEG-polyurethane based resins were instead diluted with 20% w/w water-soluble hydroxyethyl acrylate (HEA) so that fabrication of polyurethane-based hydrogels could be an option. Once deposited, the resin was allowed to settle in the mould and then placed into a

Formlabs Form Cure and irradiated with 405 nm LEDs for 60 minutes at 60 °C. Heat was utilised to ensure resin was in a liquid state when polymerised. All cured samples were clear ranging from colourless to slightly yellow in colour. Samples produced from diacrylates of spacer compounds between 1000 and 1250 g/mol, and 2000 g/mol, went from clear to opaque minutes after curing. This was speculated to be due to uncured resin cooling and solidifying within the sample, or due to presence of crystalline regions, caused by increased chain length, which reduce opacity. This highlighted the importance of maintaining resins in a liquid state during curing. Formlabs materials were also investigated to provide an indication of the range of material properties available from commercial SLA resins. A range of materials prepared from formulations containing bisphenol A ethoxylate dimethacrylate (ethoxylate:phenol 15:1) (BPAEDMA 15:1) diluted with either bisphenol A ethoxylate diacrylate (ethoxylate:phenol 2:1) (BPAEDA 2:1) or trimethylolpropane triacrylate (TMPTA) in differing ratios, were also examined. These were described as soft engineering materials by Bens et al. suitable for broad biomedical applications involving short-term contact with the human body[226]. Finally, a range of polydimethylsiloxane-based diacrylates kindly provided by Siltech (Toronto, Canada) for mechanical analysis were compared against synthesised materials

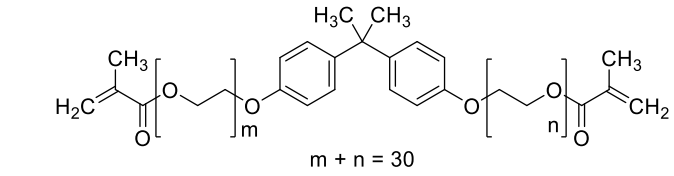

m + n = 30

Bisphenol A ethoxylate dimethacrylate, average Mn ~1700, EO/phenol 15

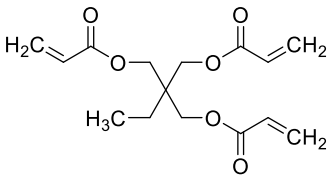

Trimethylolpropane triacrylate

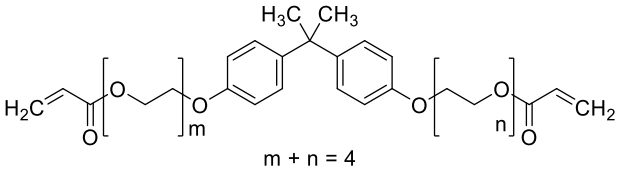

m + n = 4

Bisphenol A ethoxylate diacrylate, average Mn ~512, EO/phenol 2

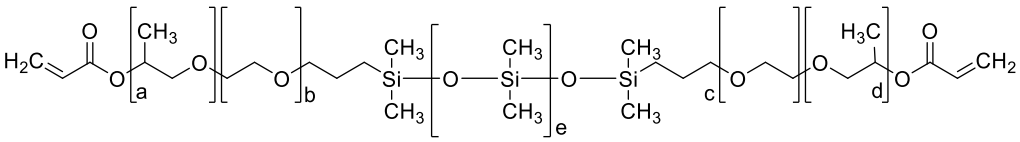

Silmer ACR Di10, average Mn ~1100; Silmer ACR Di50 Mn ~4100

Figure 33 – Chemical structures of known monomers/oligomers used to prepare samples for tensile and flexural testing

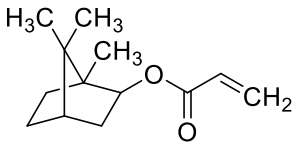

Isobornyl acrylate

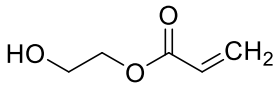

2-Hydroxyethyl acrylate

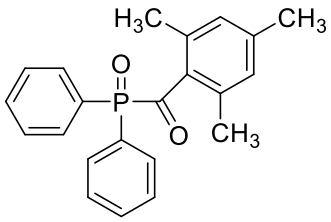

Diphenyl(2,4,6-trimethylbenzoyl)phosphine oxide

Figure 34 – Chemical structures for reactive diluents used in polyurethane dimethacrylate formulations and radical photoinitiator used in non-commercial formulations.

All materials, except Formlabs proprietary resin, were formulated with 1% w/w diphenyl(2,4,6-trimethylbenzoyl)phosphine oxide (TPO), a radical

photoinitiator which absorbs UV light at 405 nm, to enable near UV-visible light photopolymerisation of formulations. Tensile testing samples were measured with a universal testing machine (Shimadzu) according to DIN EN ISO 527-1, except with fewer samples (3 instead of 5) due to limited material, and increased thickness (< 1 mm to 2 mm). The latter was necessary due to poor material flow properties.

Figure 35 – Images of tensile testing samples (left), universal testing instrument set up for tensile testing (middle) and *in situ* tensile testing of a sample (right)

Mechanical properties of a range of implantable grade silicone rubbers (DOW CORNING C6-5XX, QP1-XX, Q7-XXXX) were considered as a benchmark reference for materials suitable for soft tissue implantation (see Table 6).

Table 6 – Mechanical data values for implantable grade silicone rubbers

Sample name	Tensile testing (± 1 SE)			
	Tensile strength (MPa)	Young's modulus (MPa)	Elongation at break (%)	Tensile toughness (kJ/m3)
DOW CORNING C6-5XX	8.30 – 9.12	1.10 – 5.83	386 - 796	-
DOW CORNING QP1-XX	6.1 – 8.5	1.2 – 5.7	290 - 680	-
DOW CORNING Q7-XXXX	6.44 – 9.45	-	300 - 540	-

Table 7 and 8 shows results obtained from tensile testing material samples. Four different values were calculated from stress-strain plots generated from

tensile testing samples. Tensile strength refers to the maximum amount of stress a material can withstand before breaking. Stress is calculated as:

$$\text{Stress} = \frac{\text{Force}}{\text{Area}}$$

where Stress is measured in N/mm^2 or Pascals (Pa, N/m^2), Force is measured in newtons (N) and Area is the cross-sectional area of the sample in mm^2. Formulations of Silmer ACR D208, Di10 and Di50 all produced materials too fragile for tensile testing, leading to their deselection as potential homopolymer systems for medical devices. It is worth noting that a requirement for a medical device/implant is maintenance of tissue functionality and avoidance of causing discomfort, which can be achieved by possessing mechanical properties comparable to native tissue[190,191]. Tensile strengths of implantable silicone rubber can range between 6.1 – 9.45 MPa (Table 6), therefore materials within this tensile strength range are acceptable for soft tissue applications. Materials that have tensile strengths above this range include samples prepared with Formlabs Clear Resin, PEG400PUDMA, PPG425PUDMA and PCL530PUDMA. These presented as stiff, rigid, homopolymer systems that are likely unsuitable for use within soft medical devices. Nevertheless, these polyurethane dimethacrylate materials may yet prove suitable for use as part of heteropolymer systems. Formlabs Clear Resin was considered unsuitable for use within heteropolymer systems due to unknown constituents. All other materials tested display tensile strengths between 6.1 – 9.45 MPa, indicating a range of materials that possess tensile strengths suitable for soft tissue applications.

Young's modulus or tensile modulus is a measure of a material's resistance to elastic deformation under load. Young's modulus is calculated as:

$$\text{Young's modulus} = \frac{\text{tensile stress}}{\text{tensile strain}} = \frac{F \times L}{A \times \Delta L}$$

where Young's modulus is measured in N/mm^2 or Pascals (Pa, N/m^2), F is Force and measured in newtons (N), L is initial gauge length of sample in mm, A is cross-sectional of the sample in mm^2 and ΔL is the change in gauge length under tension in mm. A high Young's modulus indicates a material is stiff, whereas a low Young's modulus value indicates a material is flexible. Implantable silicone rubbers possess Young's moduli of between 1.10 and 5.83 MPa. Materials that significantly fall outside of this range include Formlabs Clear, Formlabs Dental, BPAEDMA-based formulations diluted with above 20% w/w TMPTA, a 50/50 mix of water-soluble Silmer ACR D208 with PEG575DA and all polyurethane dimethacrylates based on low molecular weight spacer compounds (425 – 650 g/mol) (PET/PESXXXPUDMAs). Formlabs Clear, Formlabs Dental exhibited stiff and rigid mechanical properties, therefore rendering it unsuitable for soft tissue applications. Formulation of BPAEDMA with TMPTA, a tri-functional acrylate, increased both tensile strength and Young's moduli of resultant materials. While small quantities of TMPTA (< 20% w/w) can improve the mechanical properties of the resultant material, in large quantities (> 20% w/w) materials become too stiff and rigid for soft tissue applications. Formulation of Silmer ACR D208 with PEG575DA significantly also increased tensile strength and Young's moduli unsuitably, and hence dimethylsiloxane-based acrylates were abandoned as both homo- and heteropolymer systems for the present application. As mentioned previously, homopolymer systems of PET/PESXXXPUDMAs except PTHF650PUDMA are unsuitable for the present application and require reformulation to decrease both tensile strength and Young's modulus. Diacrylates based on spacer compounds of low (PET/PESXXXDAs), medium (1000 – 1250 g/mol) (PET/PES1XX0DAs) and large (2000 g/mol) (PET/PES2000DAs) molecular weights and polyurethane dimethacrylates based on medium molecular weight spacer compounds (PET/PES1XX0PUDMAs) all displayed Young's moduli within or near the desired range.

Elongation at break and tensile toughness are perhaps the most important mechanical values for consideration of viable candidates for the present application. An absolute requirement of insertable/implantable devices is that they must withstand mechanical forces experienced during application, without failure or fracture[190]. Furthermore, the device must be able to withstand mechanical stresses and shocks encountered within the body. Premature mechanical failure of implants can lead to tissue injury, pain, additional surgical procedures and ultimately, treatment failure. A material that exhibits high values for elongation at break and tensile toughness are resistant to mechanical failure and fracture. Implantable grade silicone rubbers exhibit very large values for elongation at break (290 – 796%) (and therefore tensile toughness). It is these properties that make such materials suitable for implantation. Elongation at break is the ratio between increased length and initial length after breakage and is related to the ability of a material to resist deformation without cracking. Elongation at break is calculated as so:

$$\text{Elongation at break} = \frac{\Delta L}{L} \times 100$$

where ΔL is change in gauge length at break in mm and L is the initial gauge length in mm. Elongation at break is measured in %. None of the tested materials achieved these values. Materials with low values for elongation at break (0 – 20%) include Formlabs Clear, Formlabs Dental, all BPAEDMA formulations, all diacrylates and PET/PESXXXPUDMAs, except PTHF650PUDMA. These materials break at low levels of applied strain, and their homopolymer may not be suitable as implantable materials. Formlabs Flex outperforms its Formlabs counterparts in terms of elongation at break. This is expected as Formlabs Flex possesses elastomeric properties, recommended for parts that bend and flex. PTHF650PUDMA unexpectedly has a far higher elongation at break than other PET/PESXXXPUDMAs. A potential reason is due to the longer chain length of PTHF650 compared to PCL530, PPG425 and PEG400. This trend was observed for diacrylates and

polyurethane dimethacrylates, where increasing spacer compound MW resulted in increased elongation at break. This observation may result from lower crosslinking density with increasing spacer compound molecular weight, where less crosslinking density permits greater flexibility within the polymer network[227]. PET/PES1XX0PUDMAs exhibited the best values for elongation at break (in between 50 and 80%) and may prove suitable as materials for implantation. The influence of hydrogen-bond forming urethane linkages and "soft" and "hard" domains on material elongation at break is significant. PET/PES1XX0PUDMAs exhibit an elongation at break increase of at least 500% in comparison to PET/PES1XX0DAs. This, as previously mentioned, is likely due to urethane linkage hydrogen bonding and phase separation of "soft" and "hard" domains resulting in dissipation of crack propagating forces[199,200]. Toughness relies on a combination of material strength and ductility. Toughness is related to the area (energy) under the stress strain curve. Toughness is calculated as so:

$$\text{Tensile toughness} = \left(\frac{\text{Energy}}{\text{T} \times \text{W} \times \text{L}}\right) \times 1 \times 10^{9}$$

where tensile toughness is measured in kJ/m^3, energy is measured in kilojoules (kJ), T is gauge thickness in mm, W is gauge width in mm and L is gauge length in mm.

Table 7 – Tensile testing data for all materials (1/2).

Sample name	Tensile testing (± 1 SE)			
	Tensile strength (MPa)	Young's modulus (MPa)	Elongation at break (%)	Tensile toughness (kJ/m3)
Formlabs Clear Resin	30.13 ± 1.10	1595.17 ± 46.01	5.42 ± 0.52	1113.53 ± 60.12
Formlabs Dental Resin	19.25 ± 1.87	1366.58 ± 87.12	3.79 ± 1.34	702.20 ± 129.48
Formlabs Flex Resin	2.71 ± 0.11	9.40 ± 0.27	33.14 ± 1.80	503.08 ± 41.73
60% BPAEDMA + 40% BPAEDA (EO-P 2) + 1% TPO	1.60 ± 0.12	26.73 ± 0.36	6.90 ± 0.46	69.26 ± 6.02
60% BPAEDMA + 40% TMPTA + 1% TPO	5.33 ± 0.32	341.14 ± 4.06	3.72 ± 1.01	227.93 ± 50.80
80% BPAEDMA + 20% BPAEDA (EO-P 2) + 1% TPO	0.98 ± 0.11	16.05 ± 1.44	7.94 ± 2.07	48.32 ± 17.89
80% BPAEDMA + 20% TMPTA + 1% TPO	2.87 ± 0.24	65.95 ± 3.11	6.08 ± 1.00	107.53 ± 26.38
Silmer ACR D208 + 1% TPO	*	*	*	*
Silmer ACR Di10 + 1% TPO	*	*	*	*
Silmer ACR Di50 + 1% TPO	*	*	*	*
50% PEG575DA + 50% Silmer ACR D208 + 1% TPO	2.93 ± 0.20	124.23 ± 4.64	5.01 ± 0.63	113.27 ± 22.17
PEG575DA + 1% TPO	1.18 ± 0.19	25.39 ± 1.34	5.05 ± 0.76	48.86 ± 18.56
PTHF650DA + 1% TPO	0.58 ± 0.09	13.68 ± 0.14	5.16 ± 0.58	19.95 ± 2.42
PPG425DA + 1% TPO	0.79 ± 0.05	20.31 ± 0.85	4.32 ± 0.26	25.40 ± 3.25
PCL530DA + 1% TPO	1.02 ± 0.04	21.70 ± 1.34	5.54 ± 0.53	33.44 ± 4.39
PEG1000DA + 1% TPO	0.81 ± 0.12	24.19 ± 9.42	4.11 ± 0.82	22.04 ± 1.39
PTHF1000DA + 1% TPO	0.77 ± 0.02	11.02 ± 0.30	8.79 ± 0.84	42.86 ± 6.42
PPG1200DA + 1% TPO	0.25 ± 0.04	3.80 ± 0.37	6.84 ± 1.10	11.39 ± 2.51
PCL1250DA + 1% TPO	0.77 ± 0.05	9.60 ± 0.72	8.94 ± 0.94	38.33 ± 5.92

Table 8 – Tensile testing data for all materials (2/2).

Sample name	Tensile testing (± 1 SE)			
	Tensile strength (MPa)	Young's modulus (MPa)	Elongation at break (%)	Tensile toughness (kJ/m3)
PEG2000DA + 1% TPO	0.68 ± 0.06	6.63 ± 0.52	10.68 ± 1.08	40.76 ± 7.70
PTHF2000DA + 1% TPO	0.56 ± 0.08	3.38 ± 0.19	20.20 ± 3.03	68.69 ± 18.79
PPG2000DA + 1% TPO	0.18 ± 0.01	2.08 ± 0.13	8.16 ± 0.24	8.71 ± 0.64
PCL2000DA + 1% TPO	0.57 ± 0.05	7.00 ± 1.07	9.60 ± 0.67	31.71 ± 2.83
PEG400PUDMA + 20% HEA + 1% TPO	32.42 ± 1.13	571.62 ± 24.61	12.57 ± 3.46	3241.69 ± 996.37
PTHF650PUDMA + 20% IBOA + 1% TPO	15.19 ± 0.83	203.54 ± 32.56	50.65 ± 5.76	6049.85 ± 466.98
PPG425PUDMA + 20% IBOA + 1% TPO	29.10 ± 3.45	499.86 ± 35.67	7.57 ± 0.96	1339.56 ± 211.99
PCL530PUDMA + 20% IBOA + 1% TPO	45.47 ± 1.73	732.97 ± 57.61	16.83 ± 3.27	5832.30 ± 1279.59
PEG1000PUDMA + 20% IBOA + 1% TPO	5.64 ± 0.34	21.41 ± 0.68	69.72 ± 2.83	2492.74 ± 257.69
PTHF1000PUDMA + 20% IBOA + 1% TPO	5.67 ± 0.41	31.89 ± 0.66	60.79 ± 5.15	2275.15 ± 337.15
PPG1200PUDMA + 20% IBOA + 1% TPO	5.10 ± 0.70	25.02 ± 1.67	56.19 ± 7.98	1891.69 ± 454.94
PCL1250PUDMA + 20% IBOA + 1% TPO	7.19 ± 0.45	23.07 ± 1.26	78.75 ± 3.57	3373.93 ± 281.75

* = Samples were too delicate to be gripped for tensile testing.

All diacrylates and BPAEDMA formulations with BPAEDA had a tensile toughness of below 100 kJ/m^3. These values are far below those that were recorded for reference materials and therefore these materials are unsuitable. BPAEDMA formulations with TMPTA do display an increased tensile toughness, however this is offset by an increase in tensile strength and Young's modulus, which is undesirable. Formlabs materials exhibit tensile toughness values ranging from 500 to 1200 kJ/m^3, which is a marked improvement over synthesised diacrylates and BPAEDMA-based formulations. However again, the toughest Formlabs materials are stiff and

rigid. Polyurethane dimethacrylates display the best values for toughness, with tensile toughness values for PET/PES1XX0PUDMAs ranging between 1800 and 3400 kJ/m^3, and PET/PESXXXPUDMAs ranging between toughness values of 1300 and 5900 kJ/m^3. Like elongation at break, the influence of hydrogen-bond forming urethane linkages and “soft” and “hard” domains on material tensile toughness is again significant. PET/PESXXXPUDMAs displayed an increase of between 500 and 3000% increase in tensile toughness compared to their diacrylate counterparts, whereas PET/PES1XX0PUDMAs displayed an increase of between 500 and 1500% compared to their diacrylate counterparts.

Figure 36 provides a visual illustration of the mechanical performances of BPAEDMA-based formulations and diacrylates based on PCL. Looking at the stroke force plots for BPAEDMA formulations, one can observe the influence of reactive diluents BPAEDA and TMPTA. Formulation with BPAEDA increases the amount of elongation the material can undergo before failure at the cost of tensile strength, whereas formulations with TMPTA increases material tensile strength at the cost of elongation. The same is observed between formulations of PCL530DA and PCL1250DA, where the diacrylate with a smaller MW spacer compound exhibits greater tensile strength but less elongation in comparison to the medium MW spacer compound. This is attributed to increased crosslinking density of the former material. All plots show in general show low values for tensile strength and elongation, indicating poor toughness of these materials. Figure 37 provides a visual illustration of the mechanical performances of Formlabs Clear and Flex materials and polyurethane dimethacrylates based on PCL. Like BPAEDMA and PCL diacrylate formulations, Formlabs Clear and Flex materials trade-off between tensile strength and elongation. Formlabs Clear can withstand a significant amount of force before failure but exhibits low values for elongation, whereas Formlabs Flex is able to undergo significant elongation but is unable to withstand high values of force.

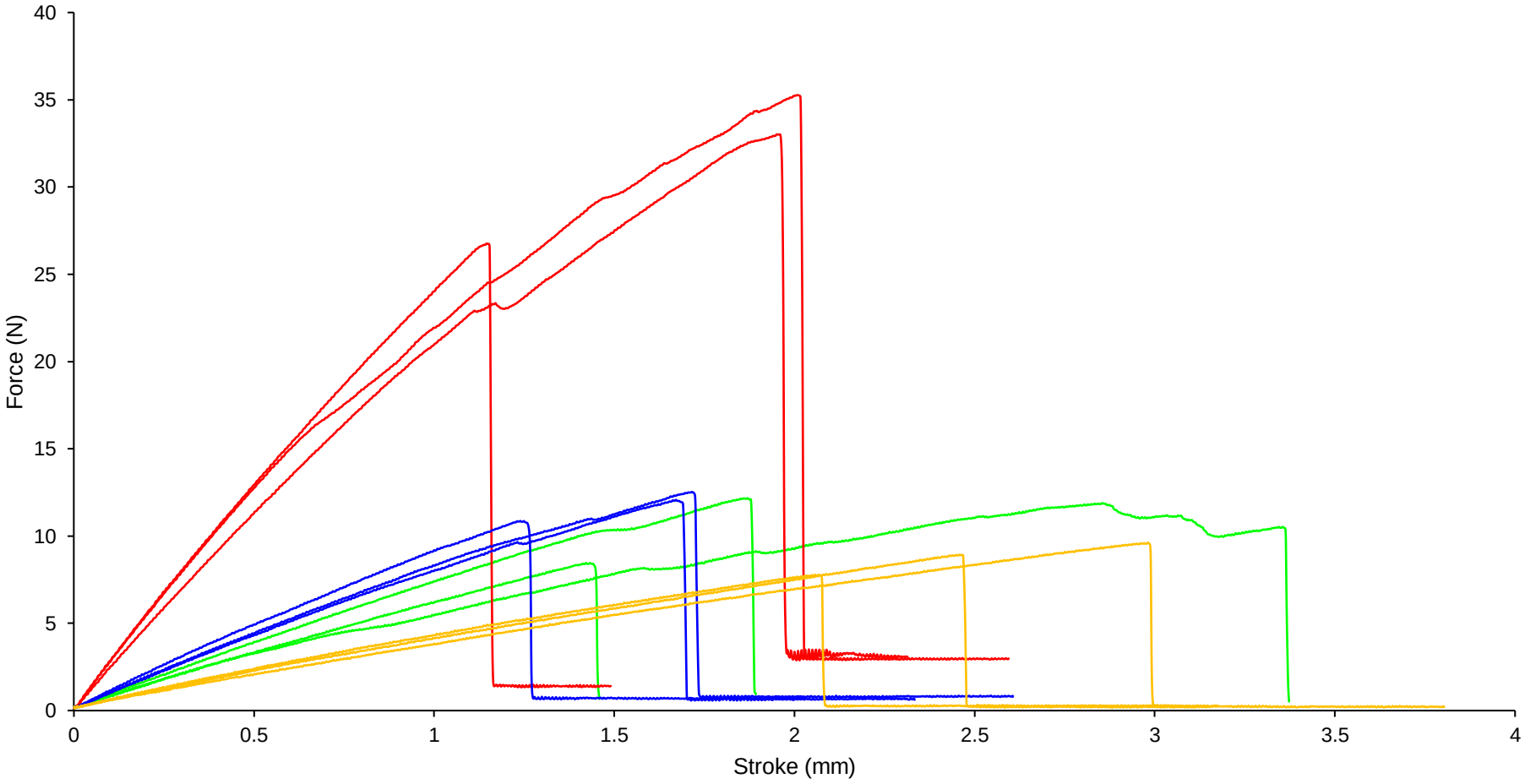

Figure 36 – Stroke force plots of select materials. Plot results shown are: (—) 80% BPAEDMA + TMPTA + 1% TPO; (—) 80% BPAEDMA + 20% BPAEDA (EO/P 2) + 1% TPO; (—) PCL530DA + 1% TPO; (—) PCL1250DA + 1% TPO.

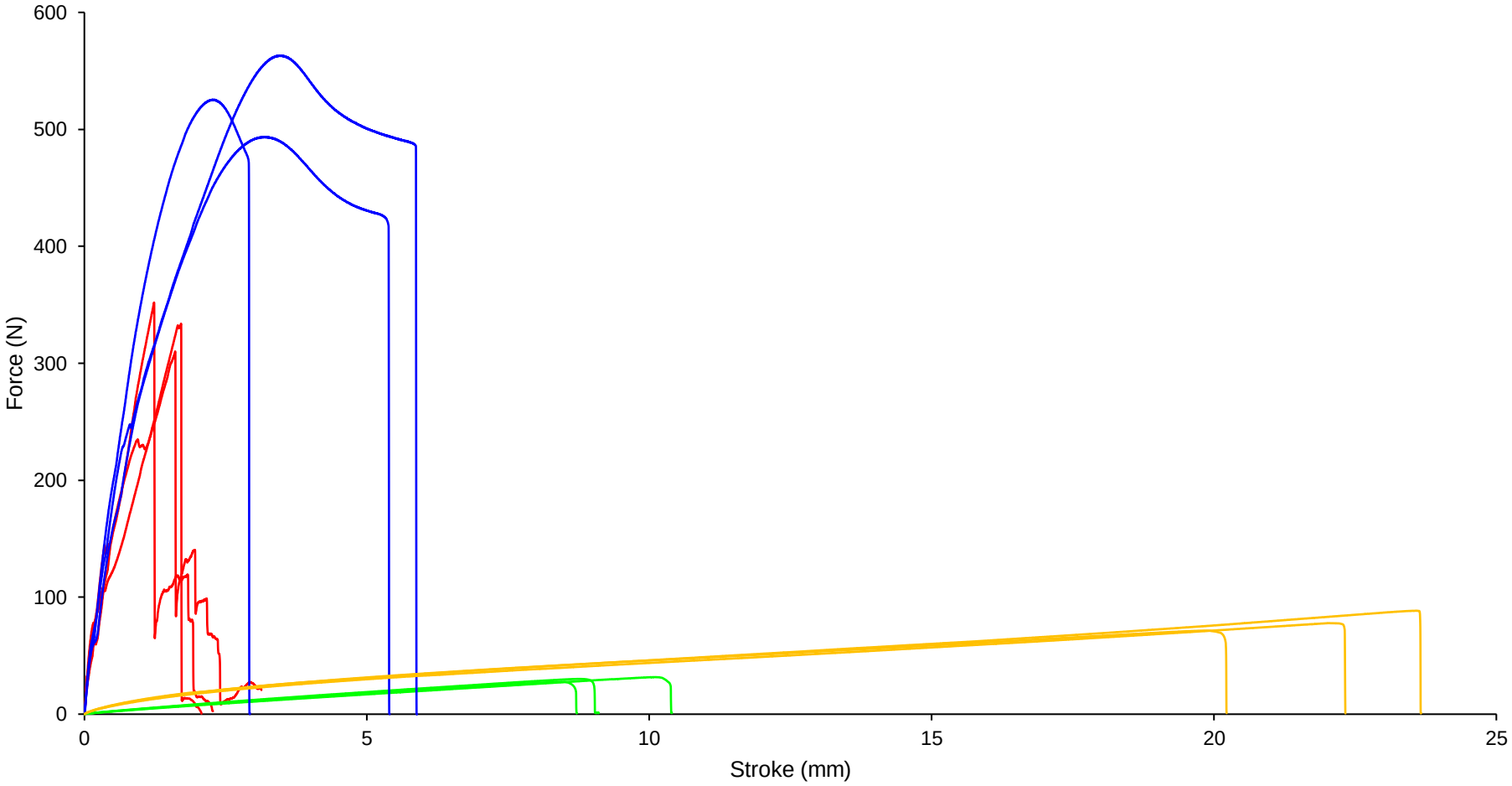

Figure 37 – Stroke force plots of select materials. Plot results shown are: (—) Formlabs Clear V1; (—) Formlabs Flex V1; (—) PCL530PUDMA + 20% IBOA + 1% TPO; (—) PCL1250PUDMA + 20% IBOA + 1% TPO.

It can be speculated that Formlabs Clear resin is based upon shorter chain, multifunctional photo-oligomers whereas Formlabs Flex resin is based upon longer chain, low functionality photo-oligomers. Influence of chain length on material properties is also visible for polyurethane dimethacrylates based on PCL, with materials based on PCL530PUDMA displaying high tensile strengths and materials based on PCL1250PUDMA exhibiting high values for elongation. Interestingly, it can be observed that PCL530PUDMA based materials display a yield point and undergoes significant plastic deformation before failure, indicating that the material is ductile and not brittle. Polyurethane based materials display a large area under their force stroke plots in comparison to other tested materials, highlighting their superior toughness.

Flexural testing samples were measured with a universal testing machine (Shimadzu) according to DIN EN ISO 178, except with lesser samples (3 instead of 5) due to sparsity of material.

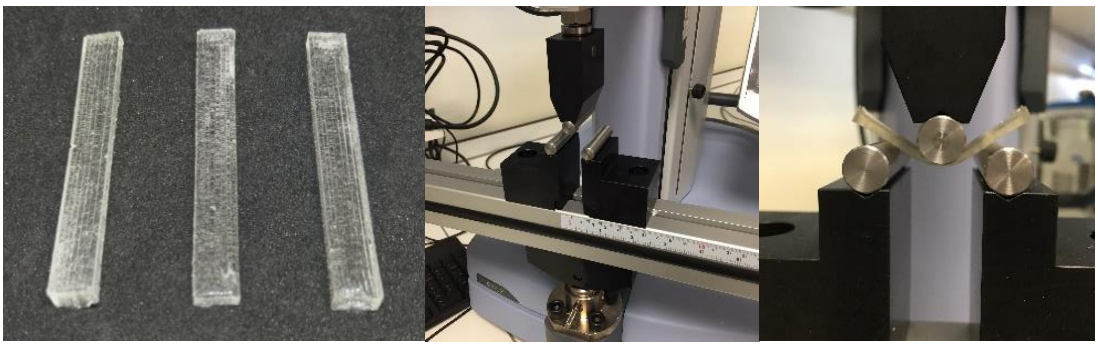

Figure 38 – Images of flexural testing samples (left), universal testing instrument set up for flexural testing (middle) and *in situ* flexural testing of a sample (right)

Table 9 shows results obtained from flexural material samples. It is worth noting that data obtained from flexural testing may be inaccurate, as some samples broke during testing, providing a definitive value for flexural strength, whereas some samples did not break therefore giving a value smaller than its actual flexural strength. This was attributed to material ductility. Regardless, results from flexural testing were analogous with those obtained from tensile

testing. Materials that were identified as stiff and rigid (Formlabs Clear and Dental, BPAEDMA formulations with > 20% w/w TMPTA, 50/50 SIlmer ACR D208 and PEG575DA and PET/PESXXXPUDMA except PTHF650PUDMA) with tensile testing, also displayed high flexural strengths and flexural moduli. These samples broke during testing, and therefore their values for flexural strength are accurate. Materials identified as elastomeric and soft (Formlabs Flex, BPAEDMA formulations diluted with BPAEDA and 20% w/w TMPTA, Silmer ACR Di 10 and 50, PTHF650PUDMA and PET/PES1XX0PUDMA) displayed low values for flexural strength and flexural modulus. These samples did not break and therefore values for flexural strength are inaccurate. As advised within DIN EN ISO 178, increasing sample thickness may allow precise measurement of flexural strength and other values for ductile materials. For both tensile and flexural testing, some results showed large variances that detracted from their accuracy. This may have been due to sample preparation, with some samples containing bubbles and uneven edges that required sanding. It is therefore prudent to treat the results as a guideline and elucidate true mechanical information from 3D printed samples, at a later point, that more closely adhere to specimen standards DIN EN ISO 527-3 and DIN EN ISO 178.

Table 9 – Flexural testing data for all materials

Sample name	Flexural testing (± 1 SE)		
	Break?	Flexural strength (MPa)	Flexural modulus (MPa)
Formlabs Clear Resin	YES	176.88 ± 10.38	3864.74 ± 305.21
Formlabs Dental Resin	YES	131.78 ± 9.96	2846.53 ± 146.80
Formlabs Flex Resin	NO	1.51 ± 0.15	14.48 ± 1.16
60% BPAEDMA + 40% BPAEDA (EO-P 2) + 1% TPO	NO	6.47 ± 0.01	69.19 ± 0.12
60% BPAEDMA + 40% TMPTA + 1% TPO	YES	34.33 ± 2.63	617.96 ± 10.76
80% BPAEDMA + 20% BPAEDA (EO-P 2) + 1% TPO	NO	2.93 ± 0.44	32.40 ± 5.20
80% BPAEDMA + 20% TMPTA + 1% TPO	NO	8.81 ± 0.06	107.14 ± 5.96
Silmer ACR D208 + 1% TPO	NO	0.87 ± 0.09	8.95 ± 0.69
Silmer ACR Di10 + 1% TPO	NO	0.80 ± 0.18	8.40 ± 1.80
Silmer ACR Di50 + 1% TPO	NO	0.26 ± 0.00	1.83 ± 0.04
50% PEG575DA + 50% Silmer ACR D208 + 1% TPO	NO	13.98 ± 1.28	188.74 ± 13.08
PEG575DA + 1% TPO	NO	4.46 ± 0.27	25.20 ± 1.42
PTHF650DA + 1% TPO	NO	3.03 ± 0.11	26.15 ± 1.10
PPG425DA + 1% TPO	NO	2.96 ± 0.41	25.89 ± 3.37
PCL530DA + 1% TPO	NO	2.44 ± 0.16	14.33 ± 0.96
PEG1000DA + 1% TPO	NO	1.75 ± 0.37	14.26 ± 4.17
PTHF1000DA + 1% TPO	NO	2.08 ± 0.12	18.81 ± 1.44
PPG1200DA + 1% TPO	NO	1.01 ± 0.03	7.19 ± 0.31
PCL1250DA + 1% TPO	NO	1.17 ± 0.20	7.28 ± 0.82
PEG2000DA + 1% TPO	NO	0.97 ± 0.07	4.23 ± 0.27
PTHF2000DA + 1% TPO	NO	0.81 ± 0.09	6.69 ± 0.86
PPG2000DA + 1% TPO	NO	0.60 ± 0.02	2.99 ± 0.27
PCL2000DA + 1% TPO	NO	1.03 ± 0.06	9.76 ± 0.87
PEG400PUDMA + 20% HEA + 1% TPO	YES	85.31 ± 4.80	1802.59 ± 64.11
PTHF650PUDMA + 20% IBOA + 1% TPO	NO	21.11 ± 1.12	348.91 ± 53.47
PPG425PUDMA + 20% IBOA + 1% TPO	YES	111.39 ± 2.65	2391.18 ± 10.02
PCL530PUDMA + 20% IBOA + 1% TPO	YES	69.89 ± 6.73	1348.70 ± 187.32
PEG1000PUDMA + 20% IBOA + 1% TPO	NO	2.75 ± 0.59	38.85 ± 8.42
PTHF1000PUDMA + 20% IBOA + 1% TPO	NO	3.24 ± 0.38	24.07 ± 2.57
PPG1200PUDMA + 20% IBOA + 1% TPO	NO	3.50 ± 0.19	46.17 ± 1.68
PCL1250PUDMA + 20% IBOA + 1% TPO	NO	3.99 ± 0.94	54.74 ± 11.79

Further tensile testing of heteropolymer systems

Having developed and identified a range of potentially viable base monomers/macromers for SLA 3D printing of implantable materials, it was decided to further investigate how different additives can adjust the physical properties of these materials, with a view to developing an expansive library of photocurable formulations that can be modified to be any drug delivery situation. It was considered how it might be possible to soften, harden and/or add porosity to a photocurable material. To soften materials, addition of monofunctional acrylates and thiol-based chain transfer reagents were utilised; to harden materials, addition of multifunctional reactive diluents, and to add porosity, addition of non-reactive diluents. In a different approach than before, monomers were dissolved in a carrier solvent, along with any additives, poured into a silicone mould, and the carrier solvent allowed to evaporate overnight. The resulting film was briefly irradiated in the Form Cure for 20 min, before removal from the mould and subsequent irradiation for 60 min at 60 °C. This was as opposed to heating the material and pouring it directly into the mould before curing. This was done for three reasons. Firstly, preparation of samples in this manner led to fewer observed defects than the previous method, thereby increasing the accuracy of subsequent physical property tests. Secondly, it allowed for preparation of films from base monomer/macromer only, which was previously not possible due to the high viscosity of base materials. Finally, it allowed for fabrication of films with thickness below 1 mm. This meant tensile testing samples met the < 1 mm thickness criteria as dictated by DIN EN ISO 527-1. Furthermore, subsequent sample preparation for nanoindentation, thermal and biocompatibility analysis was easier. All samples underwent a post-processing procedure that involved continuous residual monomer extraction with warm acetone for 20 h, and drying under high vacuum in a drying pistol at 60 °C. Samples were post-processed before testing to ensure formulations had sufficient physical integrity to endure the post-processing step, and also to clean the samples prior to other testing, which may be affected by trace amounts of residual monomer/macromer. In addition, the post-processing step facilitated removal of residual unreacted monomer and non-reactive diluents from materials.

Table 10 – Gel content (%) of select materials

Sample name	Gel content (%)
PCL1250PUDMA + 1% TPO	94.14
PCL1250PUDMA + 3% TPO	92.16
PCL1250PUDMA + 5% TPO	90.14
PCL1250PUDMA + 20% IBOA + 1% TPO	91.91
PCL1250PUDMA + 20% HDDA + 1% TPO	93.76
PCL1250PUDMA + 20% TMPTA + 1% TPO	93.88
PCL1250PUDMA + 10% PCL530 + 1% TPO	83.03
PCL1250PUDMA + 20% PCL530 + 1% TPO	75.52
PCL1250PUDMA + 30% PCL530 + 1% TPO	65.74
PCL1250PUDMA + 10% dithiol CTA + 1% TPO	90.49
PCL1250PUDMA + 10% trithiol CTA + 1% TPO	91.60
PCL1250PUDMA + 10% tetrathiol CTA + 1% TPO	92.73
PEG1000PUDMA + 1% TPO	94.49
PEG1000PUDMA + 3% TPO	93.14
PEG1000PUDMA + 5% TPO	91.52
PEG1000PUDMA + 20% HEA + 1% TPO	94.06
PEG1000PUDMA + 20% TEGDA + 1% TPO	93.67
PEG1000PUDMA + 10% PEG400 + 1% TPO	85.31
PEG1000PUDMA + 20% PEG400 + 1% TPO	75.84
PEG1000PUDMA + 30% PEG400 + 1% TPO	66.50
PEG1000PUDMA + 10% dithiol CTA + 1% TPO	81.61
PEG1000PUDMA + 10% trithiol CTA + 1% TPO	92.66
PEG1000PUDMA + 10% tetrathiol CTA + 1% TPO	95.24
PTHF1000PUDMA + 1% TPO	97.16
PTHF1000PUDMA + 3% TPO	94.43
PTHF1000PUDMA + 5% TPO	93.06
PTHF1000PUDMA + 20% IBOA + 1% TPO	95.25
PTHF1000PUDMA + 20% HDDA + 1% TPO	95.63
PTHF1000PUDMA + 20% TMPTA + 1% TPO	97.22
PTHF1000PUDMA + 10% PTHF650 + 1% TPO	86.77
PTHF1000PUDMA+ 20% PTHF650 + 1% TPO	77.66
PTHF1000PUDMA+ 30% PTHF650 + 1% TPO	69.32
PTHF1000PUDMA + 10% dithiol CTA + 1% TPO	92.15
PTHF1000PUDMA + 10% trithiol CTA + 1% TPO	95.48
PTHF1000PUDMA + 10% tetrathiol CTA + 1% TPO	95.03

Table 11 – Tensile testing data for PCL-based photocurable formulations.

Sample name	Tensile testing (± 1 SE)			
	Tensile strength (MPa)	Young's modulus (MPa)	Elongation at break (%)	Tensile toughness (kJ/m3)
PCL530PUDMA + 1% TPO	43.21 ± 1.09	1159.99 ± 138.70	16.98 ± 6.64	6211.61 ± 2719.85
PCL530PUDMA + 3% TPO	29.46 ± 0.94	930.30 ± 53.64	6.48 ± 0.58	1333.00 ± 213.43
PCL530PUDMA + 5% TPO	32.04 ± 1.79	910.13 ± 189.43	5.62 ± 0.74	1217.08 ± 195.47
PCL530PUDMA + 20% IBOA + 1% TPO	39.46 ± 4.88	1119.40 ± 72.44	12.02 ± 3.36	3585.96 ± 782.80
PCL530PUDMA + 10% PCL530 + 1% TPO	24.56 ± 0.49	836.55 ± 75.82	5.70 ± 1.40	1031.68 ± 333.82
PCL530PUDMA + 10% dithiol CTA + 1% TPO	11.57 ± 3.32	98.77 ± 7.13	112.55 ± 24.26	7605.27 ± 1948.95
PCL530PUDMA + 10% trithiol CTA + 1% TPO	20.20 ± 2.20	304.09 ± 37.09	129.97 ± 11.61	17317.30 ± 3038.99
PCL530PUDMA + 10% tetrathiol CTA + 1% TPO	28.39 ± 5.33	434.04 ± 46.17	112.85 ± 21.78	21072.09 ± 6287.84
PCL1250PUDMA + 1% TPO	10.29 ± 0.26	12.02 ± 1.02	112.20 ± 5.44	5463.54 ± 459.05
PCL1250PUDMA + 3% TPO	10.03 ± 0.98	16.44 ± 1.79	100.41 ± 8.58	4923.48 ± 783.95
PCL1250PUDMA + 5% TPO	10.92 ± 0.78	14.16 ± 0.43	111.68 ± 4.50	5541.35 ± 382.38
PCL1250PUDMA + 20% IBOA + 1% TPO	16.07 ± 1.02	23.26 ± 0.59	95.72 ± 4.43	6821.69 ± 618.81
PCL1250PUDMA + 20% HDDA + 1% TPO	9.21 ± 0.31	56.21 ± 0.18	38.22 ± 0.55	2061.24 ± 156.48
PCL1250PUDMA + 20% TMPTA + 1% TPO	15.14 ± 0.33	243.10 ± 19.53	25.16 ± 2.16	2667.86 ± 141.13
PCL1250PUDMA + 10% PCL530 + 1% TPO	6.56 ± 1.05	11.78 ± 0.08	81.78 ± 10.06	2833.34 ± 660.93
PCL1250PUDMA + 20% PCL530 + 1% TPO	5.60 ± 1.27	7.93 ± 1.79	102.65 ± 9.45	2763.26 ± 665.06
PCL1250PUDMA + 30% PCL530 + 1% TPO	4.23 ± 0.84	4.79 ± 0.43	115.27 ± 11.65	2529.92 ± 719.52
PCL1250PUDMA + 10% dithiol CTA + 1% TPO	1.22 ± 0.07	1.90 ± 0.12	94.90 ± 4.34	698.90 ± 20.09
PCL1250PUDMA + 10% trithiol CTA + 1% TPO	1.52 ± 0.12	2.13 ± 0.16	112.08 ± 6.25	985.10 ± 96.54
PCL1250PUDMA + 10% tetrathiol CTA + 1% TPO	1.62 ± 0.13	2.53 ± 0.09	83.79 ± 3.60	758.87 ± 12.30

Gel content is the content of “gelled” crosslinked solid within a sample. Gel content (%) is calculated as such:

$$\text{Gel content (\%)} = \left(\frac{W_{extracted}}{W_0}\right) \times 100\ \%$$

where $W_{extracted}$ is the weight of the sample (in g) after post-processing (continuous solvent extraction) and W_0 is the weight of the sample (in g) before post-processing. All formulations containing purely reactive compounds showed gel contents of above 90%. The fact that no single formulation had a gel content of 100% highlights the importance of this post-processing step, as the presence of unreacted monomers presents a toxicity risk. Furthermore, the gel contents of formulations containing non-reactive diluents (PCL530, PEG400 and PTHF650) correlate with their contents. This indicates the possibility of accurately controlling material porosity simply by adding varying amounts of non-reactive diluent.

This new method for sample preparation presented some problems. Due to the thinness of the films, stiff materials, particularly those formed from PET/PESXXXPUDMA monomers/macromers, tended to fracture when fashioned into specimens for tensile testing. This prevented accurate tensile testing of these samples; hence they were omitted. Nonetheless, certain samples prepared with PCL530PUDMA as base monomer showed little to no significant fracturing when cut into tensile testing specimens, indicating use of certain diluents made these materials less brittle, and hence were able to be tested. Table 11 displays tensile testing data for all formulations using PCL polyurethane dimethacrylates as base monomer/macromer. Samples prepared from PCL530PUDMA + 20% IBOA using the solvent evaporation method exhibit a lower tensile strength, a higher Young’s modulus, a shorter elongation at break and a lower toughness, than its counterpart prepared via the previous method. A stiffer, weaker material using the solvent evaporation method was speculated to be due to partial co-evaporation of isobornyl acrylate, leading to a highly crosslinked stiff material, and fracturing during cutting, as explained above. More so, samples prepared from

PCL1250PUDMA + 20% IBOA using the solvent evaporation method exhibited higher tensile strength, a similar Young's modulus, a higher elongation at break and a higher tensile toughness. Without cutting fracture adversely affecting material integrity, it appears samples prepared using the solvent evaporation method possess superior mechanical properties that those prepared via the other method.

As expected, the addition of multifunctional thiol CTAs significantly affect the mechanical properties of resultant materials. Firstly, they lower the tensile strength and Young's moduli of the material. In PCL530PUDMA formulations, dithiol CTA reduces tensile strength and Young's modulus the most, whereas tetrathiol CTA reduces their values the least. In PCL1250PUDMA, this graduation is not observed, with all thiol CTAs reducing tensile strength by almost ten-fold. In PCL530PUDMA formulations, elongation at break (%) is increased almost ten-fold, whereas elongation at break (%) in PCL1250PUDMA formulations was either unaffected or negatively affected. Furthermore, PCL530 formulations displayed a significant increase in tensile toughness when combined with CTAs, more so with the tetrafunctional thiol. Conversely, PCL1250 monomers/macromers when formulated with thiol CTAs exhibited reduced tensile toughness of almost 5-fold. It was noted that for these samples, there was a stoichiometric excess of thiol groups to dimethacrylate groups. For example, 90% w/w difunctional PCL1250PUDMA (1981.22 g/mol) versus 10% w/w difunctional thiol CTA (182.30 g/mol) results in a ratio of 1 to 0.83 methacrylate to thiol groups. It is therefore likely a sizeable content of thiol CTA remains unreacted within such samples, which may part explain the inferior mechanical properties, in comparison to their PCL530PUDMA counterparts.

Formulation of PCL530PUDMA with di- and trifunctional acrylates, and non-reactive diluents above concentrations of 10% w/w, led to materials too brittle to be cut into specimens. Formulation of PCL1250PUDMA with multifunctional acrylates bore expected observations. Formulation with trifunctional TMPTA resulted in a large increase in Young's modulus (approximately 10-15-fold) and decrease in elongation at break (approximately four-fold) when compared

to base material, whereas formulation with monofunctional IBOA resulted in a small increase in Young's modulus (less than two-fold) and an insignificant decrease in elongation at break. Formulation with multifunctional acrylates (di- and trifunctional) led to reduced material toughness. All these properties can be attributed to an increase in overall acrylate groups, resulting in a higher crosslinking density and a more irregular network, due to an increase in photoreactivity (acrylate reactivity > methacrylate reactivity). Formulation of PCL1250PUDMA with non-reactive diluents led to materials with decreasing tensile strength and Young's modulus (with increasing non-reactive diluent content), similar elongation at break and reduced tensile toughness (compared to base formulation; approximately 2-fold). An explanation for this observation is that the non-reactive diluent "dilutes" the polymer network, leading to a looser crosslinking. This results in a less stiff material, hence the lower tensile strength and Young's modulus, but a weaker material in all.

Table 12 – Tensile testing results for PEG1000PUDMA and PTHF1000PUDMA formulations produced from samples prepared by solvent evaporation method (1/2)

Sample name	Tensile testing (± 1 SE)			
	Tensile strength (MPa)	Young's modulus (MPa)	Elongation at break (%)	Tensile toughness (kJ/m3)
PEG1000PUDMA + 1% TPO	5.20 ± 0.19	13.76 ± 0.95	55.31 ± 1.48	1593.25 ± 75.93
PEG1000PUDMA + 3% TPO	4.82 ± 0.25	9.44 ± 0.59	70.75 ± 3.39	1764.66 ± 102.43
PEG1000PUDMA + 5% TPO	4.25 ± 0.48	8.36 ± 0.38	66.09 ± 8.20	1523.66 ± 340.60
PEG1000PUDMA + 20% HEA + 1% TPO	2.08 ± 0.09	5.17 ± 0.74	48.38 ± 3.40	559.73 ± 43.52
PEG1000PUDMA + 20% TEGDA + 1% TPO	3.60 ± 0.33	14.22 ± 2.04	28.44 ± 3.35	554.73 ± 95.73
PEG1000PUDMA + 10% PEG400 + 1% TPO	1.33 ± 0.05	3.51 ± 0.22	46.65 ± 2.91	357.22 ± 21.87
PEG1000PUDMA + 20% PEG400 + 1% TPO	4.68 ± 0.57	8.57 ± 0.42	84.00 ± 8.29	2159.91 ± 405.86
PEG1000PUDMA + 30% PEG400 + 1% TPO	1.43 ± 0.23	2.14 ± 0.18	77.33 ± 13.95	644.02 ± 266.92

Table 13 – Tensile testing results for PEG1000PUDMA and PTHF1000PUDMA formulations produced from samples prepared by solvent evaporation method (2/2)

Sample name	Tensile testing (± 1 SE)			
	Tensile strength (MPa)	Young's modulus (MPa)	Elongation at break (%)	Tensile toughness (kJ/m3)
PEG1000PUDMA + 10% dithiol CTA + 1% TPO	1.24 ± 0.06	2.22 ± 0.08	72.18 ± 3.55	587.69 ± 74.06
PEG1000PUDMA + 10% trithiol CTA + 1% TPO	1.33 ± 0.24	2.77 ± 0.15	70.16 ± 9.37	558.26 ± 139.49
PEG1000PUDMA + 10% tetrathiol CTA + 1% TPO	1.36 ± 0.01	3.23 ± 0.29	61.62 ± 4.54	487.75 ± 35.43
PTHF1000PUDMA + 20% IBOA + 1% TPO	13.30 ± 2.32	44.23 ± 1.81	93.57 ± 5.64	6255.28 ± 464.79
PTHF1000PUDMA + 20% HDDA + 1% TPO	8.57 ± 0.37	79.33 ± 5.86	31.04 ± 3.60	1727.49 ± 263.48
PTHF1000PUDMA + 20% TMPTA + 1% TPO	12.70 ± 1.28	208.44 ± 5.62	20.62 ± 2.08	1872.28 ± 145.02
PTHF1000PUDMA + 10% PTHF650 + 1% TPO	8.84 ± 0.53	20.59 ± 0.88	75.19 ± 6.11	3846.14 ± 633.44
PTHF1000PUDMA + 20% PTHF650 + 1% TPO	11.29 ± 0.67	31.70 ± 2.06	102.23 ± 3.05	6488.96 ± 459.03
PTHF1000PUDMA + 30% PTHF650 + 1% TPO	7.68 ± 0.47	24.23 ± 0.30	97.66 ± 5.24	4506.29 ± 366.45
PTHF1000PUDMA + 10% dithiol CTA + 1% TPO	1.71 ± 0.05	2.96 ± 0.07	93.01 ± 3.75	937.74 ± 65.60
PTHF1000PUDMA + 10% trithiol CTA + 1% TPO	2.52 ± 0.11	3.96 ± 0.05	105.91 ± 5.96	1521.15 ± 141.41
PTHF1000PUDMA + 10% tetrathiol CTA + 1% TPO	2.83 ± 0.28	3.96 ± 0.13	109.77 ± 11.89	1772.91 ± 331.78

4.2.3.2. Hardness testing

Hardness testing was utilised to supplement results obtained from tensile and flexural testing regarding properties such as strength and ductility. Furthermore, with the aim of developing “soft” biomimetic implantable materials, hardness testing is the best approach for evaluating a materials

hardness or “softness”. Hardness testing was performed on samples prepared by evaporation of a carrier solvent in a silicone mould.

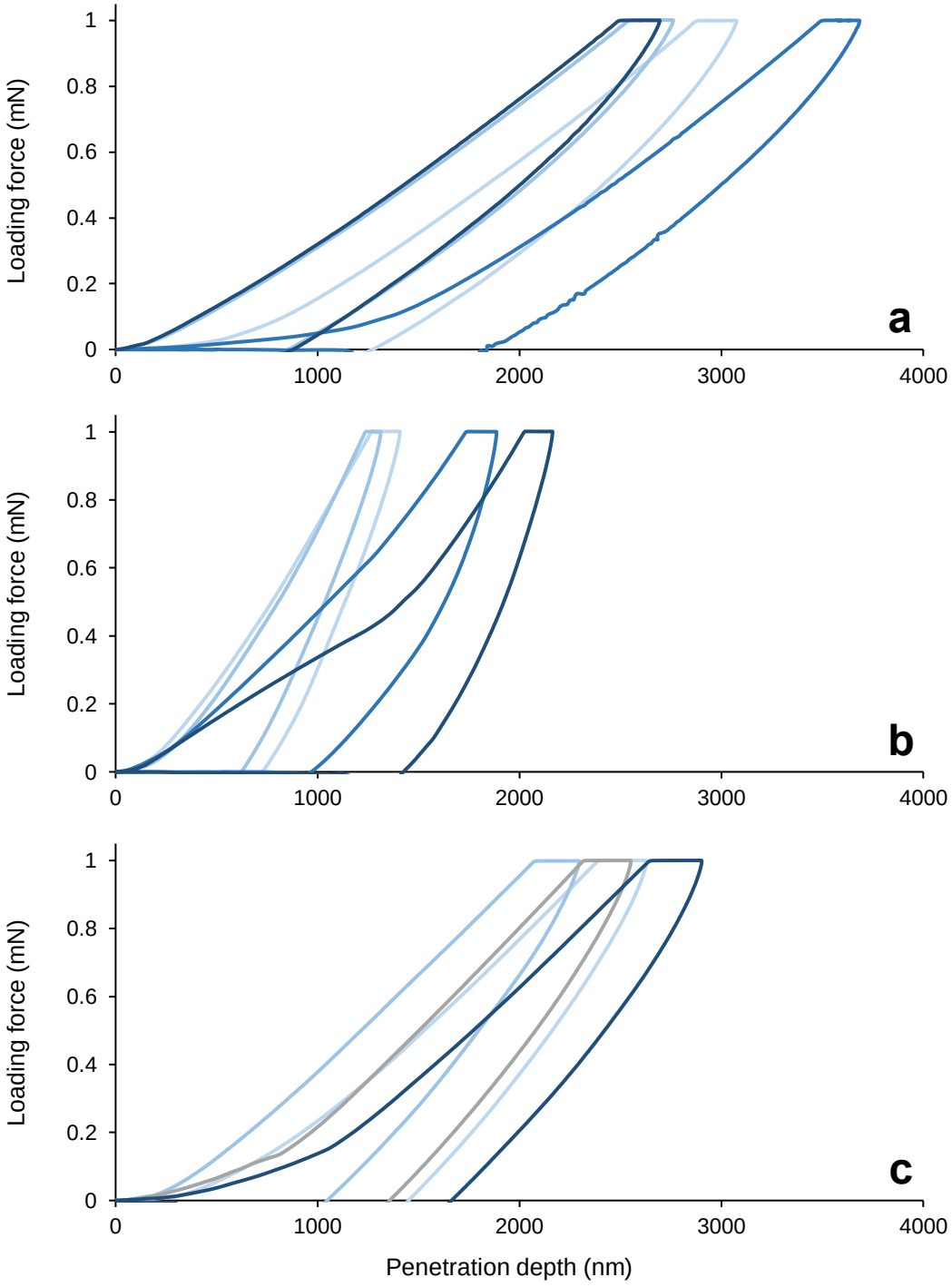

Figure 39 – Load versus penetration depth curves for load-unload nanoindentation testing. Plot results shown are: **a** = PEG1000PUDMA + 1% TPO, **b** = PTHF1000PUDMA + 1% TPO, **c** = PCL1250PUDMA + 1% TPO.

Durometer testing is typically used to measure hardness of polymers, elastomers and rubbers, however standard test methods (ASTM D-2240 Type A and Type M, and ISO-868) require samples of thickness above 1 mm. Instead, nanoindentation was employed. Nanoindentation is a technique for measuring the hardness of extremely small or thin samples.

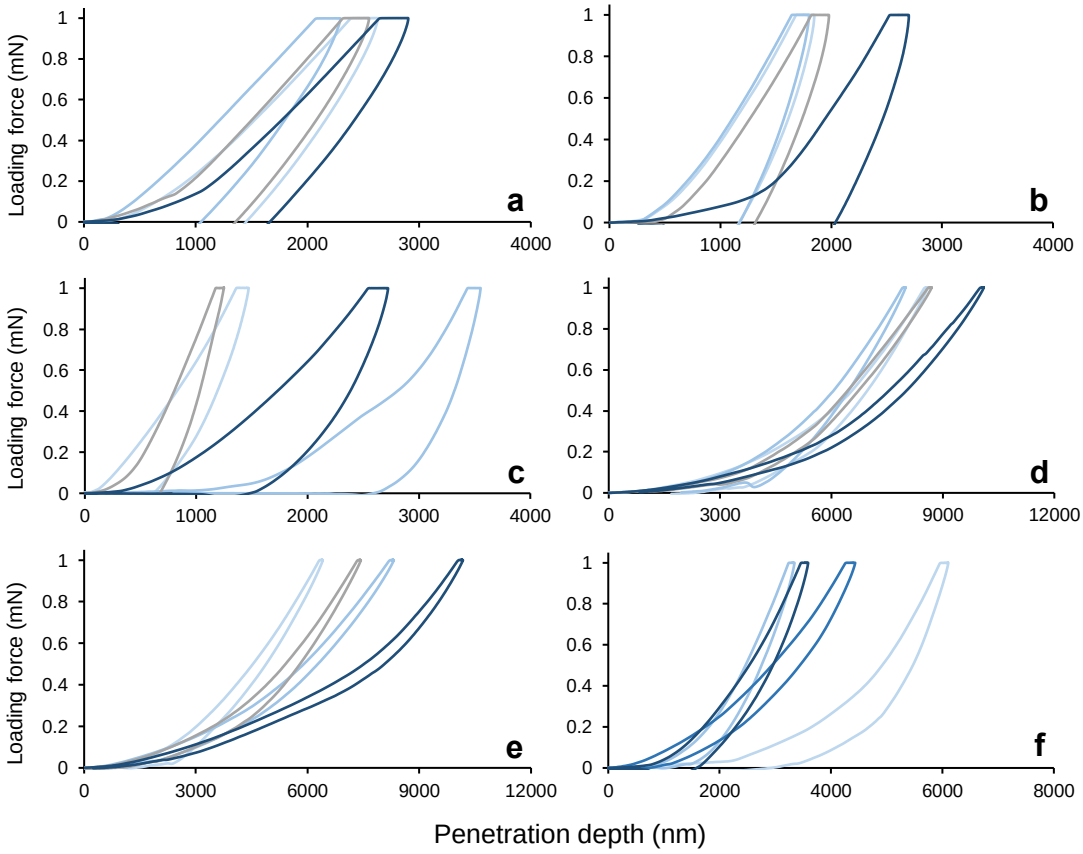

Figure 40 – Load versus penetration depth curves for load-unload nanoindentation testing of PCL1250PUDMA-based formulations (+ 1% w/w TPO). Plot results shown are: **a** = “PCL1250PUDMA”, **b** = “” + 20% IBOA, **c** = “” + 20% TMPTA, **d** = “” + 10% dithiol CTA, **e** = “” + 10% tetrathiol CTA, **f** = “” + 20% PCL530.

Figure 39, 40 and 41 show load versus penetration depth curves for mould cured polyurethane dimethacrylate materials, and Table 14 compiles values for indentation hardness (MPa), indentation modulus (MPa) and indentation creep (%), which were automatically calculated post-nanoindentation. In addition, approximate values for Shore A and Shore D were calculated from indentation moduli values using the following equation:

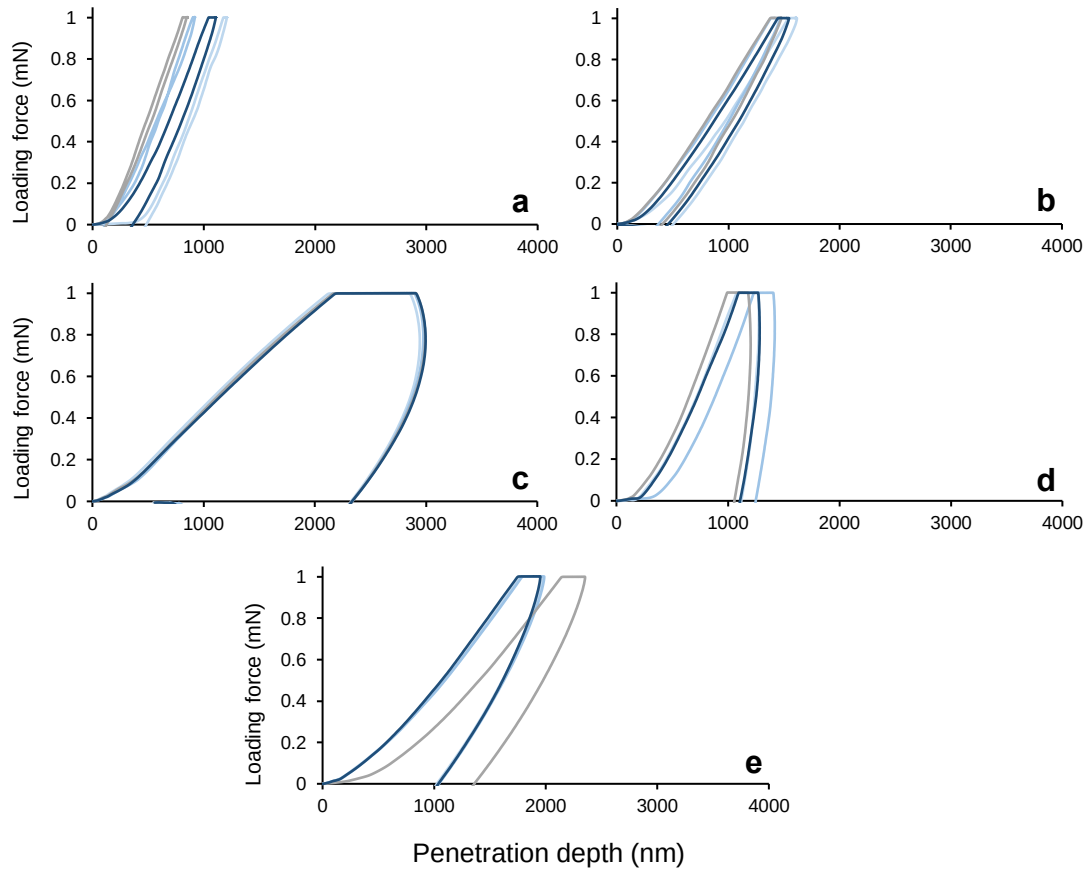

Figure 41 – Load versus penetration depth curves for load-unload nanoindentation testing of PCL530PUDMA-based formulations (+ 1% w/w TPO). Plot results shown are: a = “PCL530PUDMA”, b = “” + 20% IBOA, c = “” + 10% dithiol CTA, d = “” + 10% tetrathiol CTA, e = “” + 20% PCL530.

Figure 42 – Shore hardness scales. Reproduced from Albright Silicone webpage (2015)[228].

$$\ln E = 0.0235 \times S - 0.6403, \quad S = \begin{cases} S_A & \text{for } 20 < S_A < 80, \\ S_D + 50 & \text{for } 30 < S_D < 85, \end{cases}$$

where, S_A = ASTM D2240 type A hardness (Shore A), S_D = ASTM D2240 type D hardness and E = indentation modulus (MPa). Figure 42 shows a Shore A and Shore D durometer scale, which permits easy visualisation of a materials hardness based on its Shore A or Shore D value.

Table 14 – Nanoindentation results for all select polyurethane dimethacrylate photocurable formulations produced from samples prepared by solvent evaporation method. Results shown are within 1 SE.

Sample name	Indentation hardness (HIT, kPa)	Indentation modulus (EIT, MPa)	Tensile modulus (MPa)	Indentation creep (CIT, %)	Shore*	
					A	D
PEG1000PUDMA	143.52 ± 13.35	8.87 ± 0.37	13.76 ± 0.95	8.70 ± 0.87	67.57	-
PTHF1000PUDMA	246.67 ± 37.59	29.16 ± 0.84	30.21 ± 0.79	9.20 ± 1.16	-	39.58
PCL1250PUDMA	157.48 ± 10.25	12.95 ± 0.26	12.02 ± 1.02	11.43 ± 0.35	74.57	-
PCL1250PUDMA + 20% IBOA	179.99 ± 17.18	29.85 ± 1.55	23.26 ± 0.59	9.66 ± 0.73	-	40.01
PCL1250PUDMA + 20% TMPTA	211.24 ± 62.9	27.09 ± 3.74	243.10 ± 19.53	7.13 ± 1.39	-	38.22
PCL1250PUDMA + 10% dithiol CTA	48.66 ± 2.46	1.87 ± 0.15	1.90 ± 0.12	-2.18 ± 0.04	38.8	-
PCL1250PUDMA + 10% tetrathiol CTA	56.05 ± 6.15	2.06 ± 0.22	2.53 ± 0.09	1.19 ± 1.21	40.64	-
PCL1250PUDMA + 20% PCL530	95.80 ± 13.16	7.44 ± 0.98	7.93 ± 1.79	4.24 ± 0.44	64.33	-
PCL530PUDMA	622.88 ± 126.2	33.07 ± 2.61	1159.99 ± 138.70	5.12 ± 0.97	-	41.91
PCL530PUDMA + 20% IBOA	354.61 ± 11.80	18.00 ± 6.97	1119.40 ± 72.44	7.67 ± 0.58	-	30.66
PCL530PUDMA + 10% dithiol CTA	123.71 ± 2.69	19.18 ± 1.76	98.77 ± 7.13	35.59 ± 0.42	-	31.83
PCL530PUDMA + 10% tetrathiol CTA	263.41 ± 16.3	167.73 ± 33.15	434.04 ± 46.17	17.48 ± 1.04	-	71.91

Similar values for indentation modulus (MPa) and tensile (Young's) modulus are observed for materials with tensile moduli below approx. 50 MPa (Table 14). Materials with tensile moduli above this value, display much larger tensile moduli in comparison to indentation moduli. This indicates these materials do not respond to tensile and compressive (indentation) stress in a commensurate fashion. Indentation hardness and moduli of PCL1250PUDMA materials increase with addition of mono- and trifunctional acrylate. Vice versa, indentation hardness and moduli of PCL1250PUDMA materials decrease with addition of thiol CTAs and non-reactive diluents, attributed to presence of flexible thioether linkages and lower crosslinking density, respectively. PCL1250PUDMA materials containing thiol CTAs also display a lower indentation creep (%) than base homopolymer PCL1250PUDMA materials. Indentation creep (%) indicates material deformation, which can either occur as material fracture (unideal) or as plastic deformation, the latter being ideal. PCL1250PUDMA materials containing thiol CTAs, show low values for indentation creep (-2.18 ± 0.04 to 1.19 ± 1.21%), indicating under indentation loads, they exist within an elastic region. Conversely, PCL1250PUDMA homopolymer materials display an indentation creep of 11.43 ± 0.35%, suggesting these materials display a degree of plastic deformation under indentation loads. As expected, PCL530PUDMA homopolymer materials are harder than PCL1250PUDMA homopolymer materials, associated with greater crosslinking density. Interestingly, formulation of PCL530PUDMA with thiol CTAs led to materials exhibiting large indentation creep values. These values are attributed to significant plastic deformation of these materials under loading. Significant plastic deformation of these materials was also observed during tensile testing.

4.2.4. Thermal properties analysis

4.2.4.1. Differential scanning calorimetry analysis

Differential scanning calorimetry analyses were performed to evaluate the effect of polyurethane dimethacrylate functionalisation on spacer compounds and co-formulation of these polyurethane dimethacrylates with other

compounds on material thermal properties. Of greatest interest, were the glass transition of materials, and the temperatures at which these occur (Tg). These values indicate whether a material exists as glassy rigid systems or rubbery viscoelastic systems at room temperature, and therefore can provide explanation for a materials mechanical properties.

Figure 43 indicates all PET/PES1XX0 materials display glass transitions below room temperature, hence explaining their rubbery elastic properties at room temperature. All PET/PES1XX0 materials show an increase in Tg value compared to their spacer compound counterparts. This can be associated to isophorone diurethane linkage “hard segments” reducing network fluidity. It is worth noting glass transitions for most materials are not clear and somewhat speculative. For example, spacer compound Tg values hover between -90 and -65 °C. The DSC apparatus used has a maximum cooling temperature of -80 °C, and hence detection of these Tg values may not be possible. It is therefore entirely possible calculated Tg values are incorrect, and their true Tg values are much lower. To verify Tg values for these materials, or ascertain new Tg values, it may prove necessary to repeat DSC testing utilising different conditions until clearer, more accurate glass transitions are observed.

Tg values for different PCL1250PUDMA show no appreciable trends (Figure 44), other than a general decrease in Tg for all hetereopolymer materials. It is speculated network heterogeneity may result in greater network fluidity. Retesting with different heating procedures and DSC apparatus with lower cooling potential are necessary to verify calculated Tg values. PCL530PUDMA-based materials show a steep increase in glass transition temperatures (22.75 to 46.71 °C). This is attributed to an increased ratio of “hard” isophorone diurethane linkage hard segments to “soft” polyester segments, higher crosslinking density, and ultimately increased rigidity. Tg values close to room temperature also explain why these materials fractured when guillotined into testing samples.

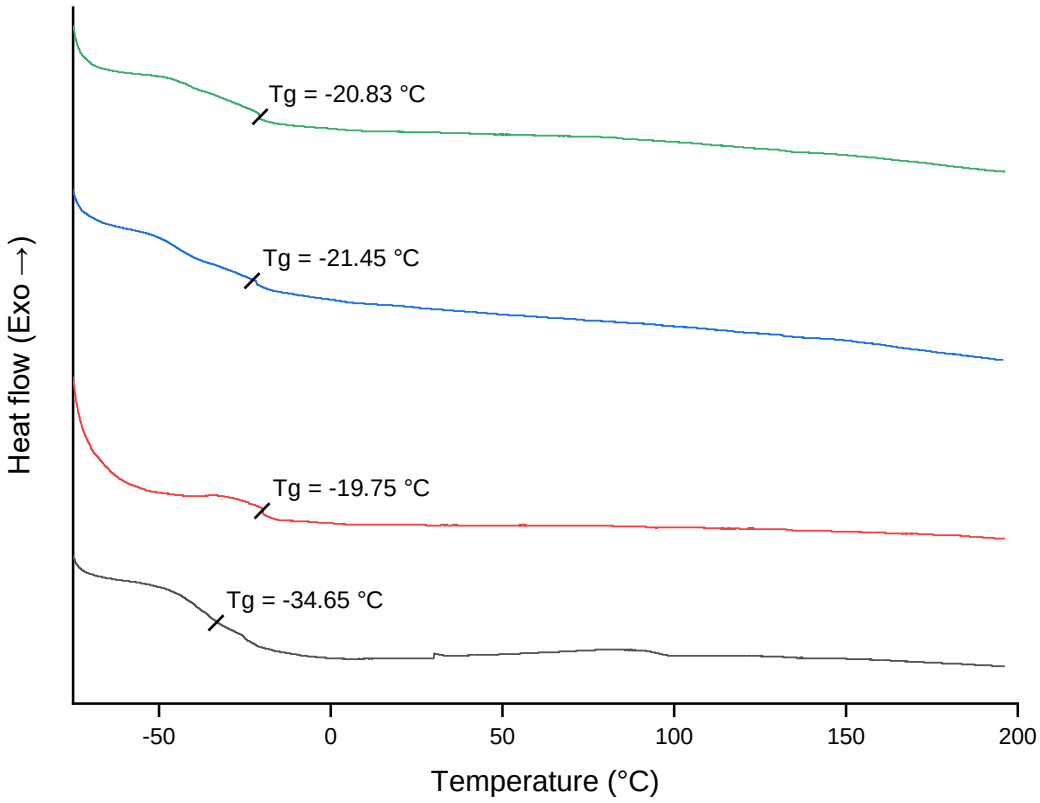

Figure 43 – DSC thermograms of base PET/PES1XX0 materials. Thermogram results shown are: (—) PEG1000PUDMA; (—) PTHF1000PUDMA; (—) PPG1200PUDMA; (—) PCL1250PUDMA.

Table 15 – Tg values for PET/PES1XX0 materials and spacer compounds.

Sample	Calculated Tg (°C)	Spacer compound Tg (°C)*
PEG1000PUDMA	-34.65	-67[229]
PTHF1000PUDMA	-19.75	-86[229]
PPG1200PUDMA	-45.05 or -21.45	-74[229]
PCL1250PUDMA	-20.83	-60[230]

* Tg values for spacer compounds were obtained from online polymer databases.

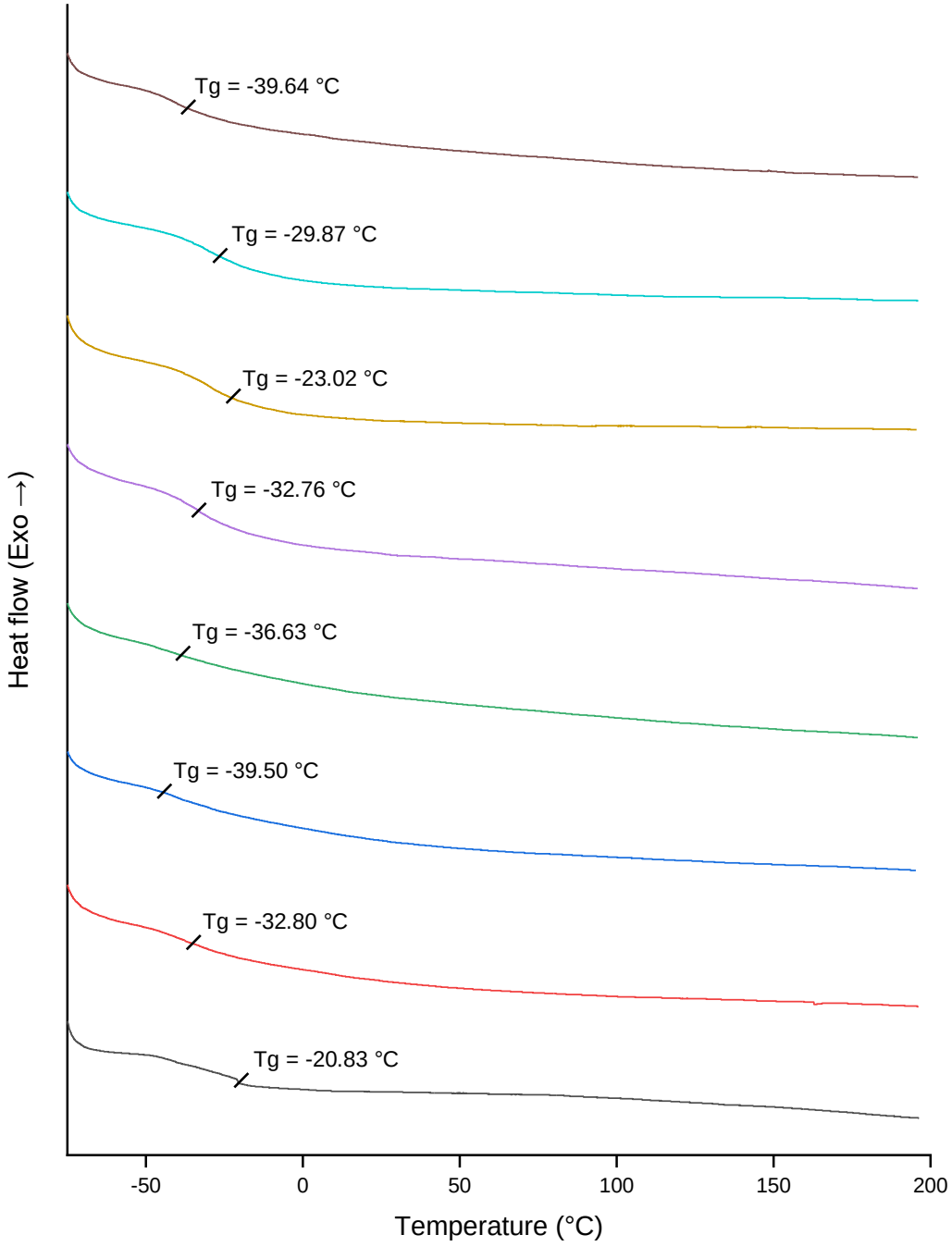

Figure 44 – DSC thermograms of PCL1250PUDMA-based materials. Thermogram results shown are: (—) PCL1250PUDMA + 1% TPO; (—) PCL1250PUDMA + 20% IBOA + 1% TPO; (—) PCL1250PUDMA + 20% HDDA + 1% TPO; (—) PCL1250PUDMA + 20% TMPTA; (—) PCL1250PUDMA + 10% dithiol CTA + 1% TPO; (—) PCL1250PUDMA + 10% trithiol CTA + 1% TPO; (—) PCL1250PUDMA + 10% tetrathiol CTA + 1% TPO; (—) PCL1250PUDMA + 20% PCL530 + 1% TPO.

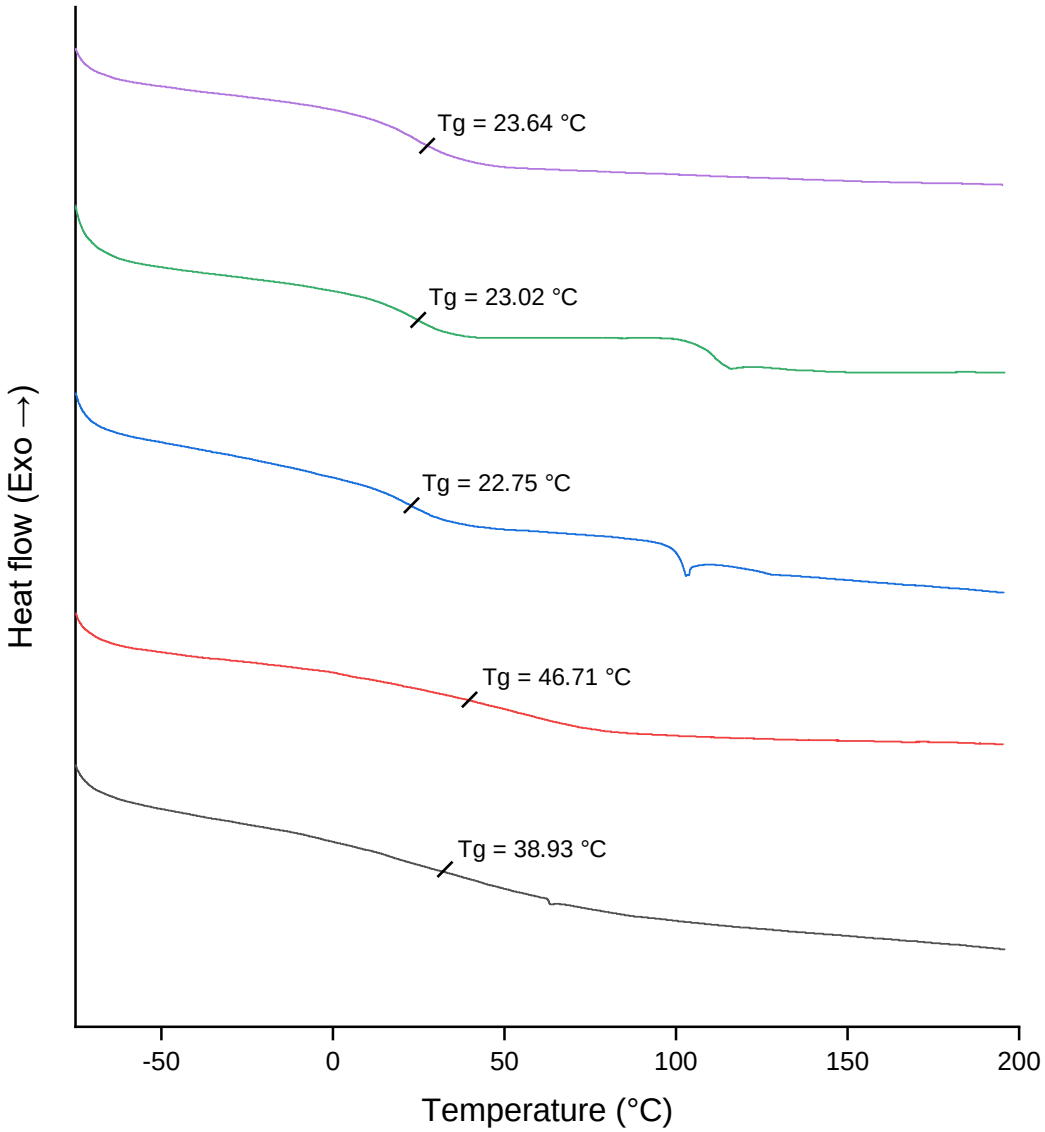

Figure 45 – DSC thermograms of PCL530PUDMA-based materials. Thermogram results shown are: (—) PCL530PUDMA + 1% TPO; (—) PCL530PUDMA + 10% dithiol CTA + 1% TPO; (—) PCL530PUDMA + 10% trithiol CTA + 1% TPO; (—) PCL530PUDMA + 10% tetrathiol CTA + 1% TPO.

4.2.4.2. Thermogravimetric analysis

Thermogravimetric analysis of select polyurethane dimethacrylate materials indicate good thermal stability. All materials exhibit onset of thermal

decomposition of between 328 and 360 °C. As reported by Feng at al. (2014), decomposition of polyether polyurethane occurs in one stage (175 – 400 °C) involving degradation of the carbamic ester (“hard” segment) and ether (soft segment). This correlates with thermal decomposition obtained from polyether polyurethanes (Figure 46). Feng et al. (2014) also report polyester polyurethanes display exhibited two stages of decomposition. The first decomposition °C (200 - 350 °C) begins with degradation of urethane hard segments followed by decomposition of polyester “soft” segments (200 - 350 °C)[178]. This does not correlate with obtained thermal decomposition data, with PCL polyurethane dimethacrylate materials displaying a single decomposition stage. This may be due to carbamic esters and PCL degrading at similar temperatures or indicates the heating step rate was too rapid too to allow detection of two separate decomposition stages. Weight loss (%) at 150 °C is attributable to volatiles.

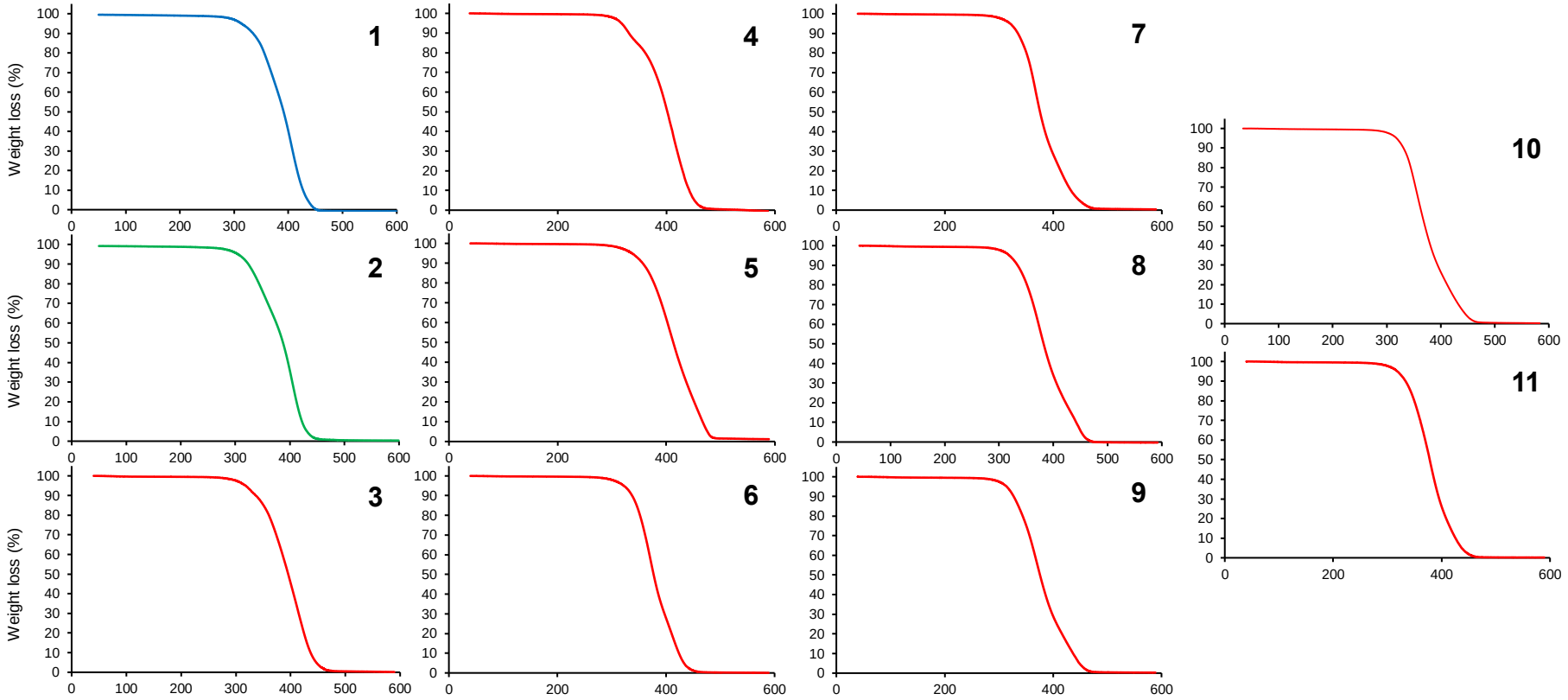

Figure 46 – TGA thermograms of select PCLPUDMA-based materials. Thermogram results shown are: **1** = PEG1000PUDMA ; **2** = PTHF1000PUDMA; **3** = “PCL1250PUDMA”; **4** = “” + 20% IBOA; **5** = “” + 20% TMPTA; **6** = “” + 10% dithiol CTA; **7** = “” + 10% tetrathiol CTA; **8** = “PCL530PUDMA”; **9** = “” + 20% IBOA; **10** = “” + 10% dithiol CTA; **11** = “” + 10% tetrathiol CTA.

Table 16 – Results obtained from TGA of PCLPUDMA-based materials (with PTHF1000PUDMA and PEG1000PUDMA-based materials as comparison).

Sample name	Weight loss (%)		Onset of thermal decomposition (°C)
	at 150 °C	at 600 °C	
PTHF1000PUDMA	0.784	100.805	353.26
PEG1000PUDMA	1.098	99.672	351.53
PCL1250PUDMA	0.435	99.916	349.41
PCL1250PUDMA + 20% IBOA	0.356	100.65	358.12
PCL1250PUDMA + 20% TMPTA	0.3	98.854	360.13
PCL1250PUDMA + 10% dithiol CTA	0.291	99.962	339.67
PCL1250PUDMA + 10% tetrathiol CTA	0.301	99.665	338.8
PCL530PUDMA	0.509	100.311	336.84
PCL530PUDMA + 20% IBOA	0.416	99.748	329.97
PCL530PUDMA + 10% dithiol CTA	0.417	99.829	338.25
PCL530PUDMA + 10% tetrathiol CTA	0.365	99.812	328.77

4.2.5. Polyurethane dimethacrylate preparation method and its effects

Gel permeation chromatography (GPC) and matrix-assisted laser desorption/ionisation time-of-flight (MALDI-TOF) mass spectrometry (MS) were used to assess polydispersity of PPG425 polyurethane dimethacrylates prepared with different reaction conditions. Table 17 lists the different reaction conditions used. For all reactions, PPG425PUDMAs were prepared using the reverse method. 0.1% w/w DBTDL was used in all instances. 80 °C was used during the second step to drive reaction to completion.

Table 17 – Table showing difference in reaction conditions for preparation of PPG425PUDMA.

Product	Temperature in 1st step	Time of catalyst addition
1	30 °C, 2h; then r.t.	2nd step
2	30 °C, 2h; then r.t.	1st step
3	60 °C, 2h; then r.t.	2nd step
4	60 °C, 2h; then r.t.	1st step

*r.t. = room temperature

Reaction work-up was carried out using the same protocol for polyurethane dimethacrylates, as previously discussed. The below figure (Figure 47) displays the MALDI-TOF mass spectrum and gel permeation chromatogram for Product 2. Table 18 shows molecular weight averages and processed peaks integrations for Product 2, generated from GPC.

Table 18 – Data generated from GPC for PPG425PUDMA Product 2

Peak No	M_{nGPC}	Peak polydispersity	Peak area
1	2845	1.06538	5151.28
2	1430	1.04476	11194.3
3	710	1.00704	1239.82
4	483	1.0207	2549.82
5	146	1.03425	90.1198
6	5	2	16410.6

A limitation of GPC is that molecular weight averages (M_{nGPC}) generated are affected by the instrument reference standards. As polystyrene reference standards were used, M_{nGPC} values were not accurate. To ascertain accurate M_n values, MALDI-TOF MS was performed in tandem to ensure peaks were accurately allocated to their associated compound/oligomer. Figure 48 shows possible compounds/oligomers within all products. FTIR spectra confirmed lack of a peak at 2270 cm^{-1} hence product is unlikely to contain a significant content of isophorone diisocyanate. Due to stoichiometric equivalents of poly(propylene glycol) and (hydroxyethyl)methacrylate (1:2) being used, any formation of compound **A** (see Figure 48) will lead to an stoichiometric equivalent amount of poly(propylene) glycol within the product.

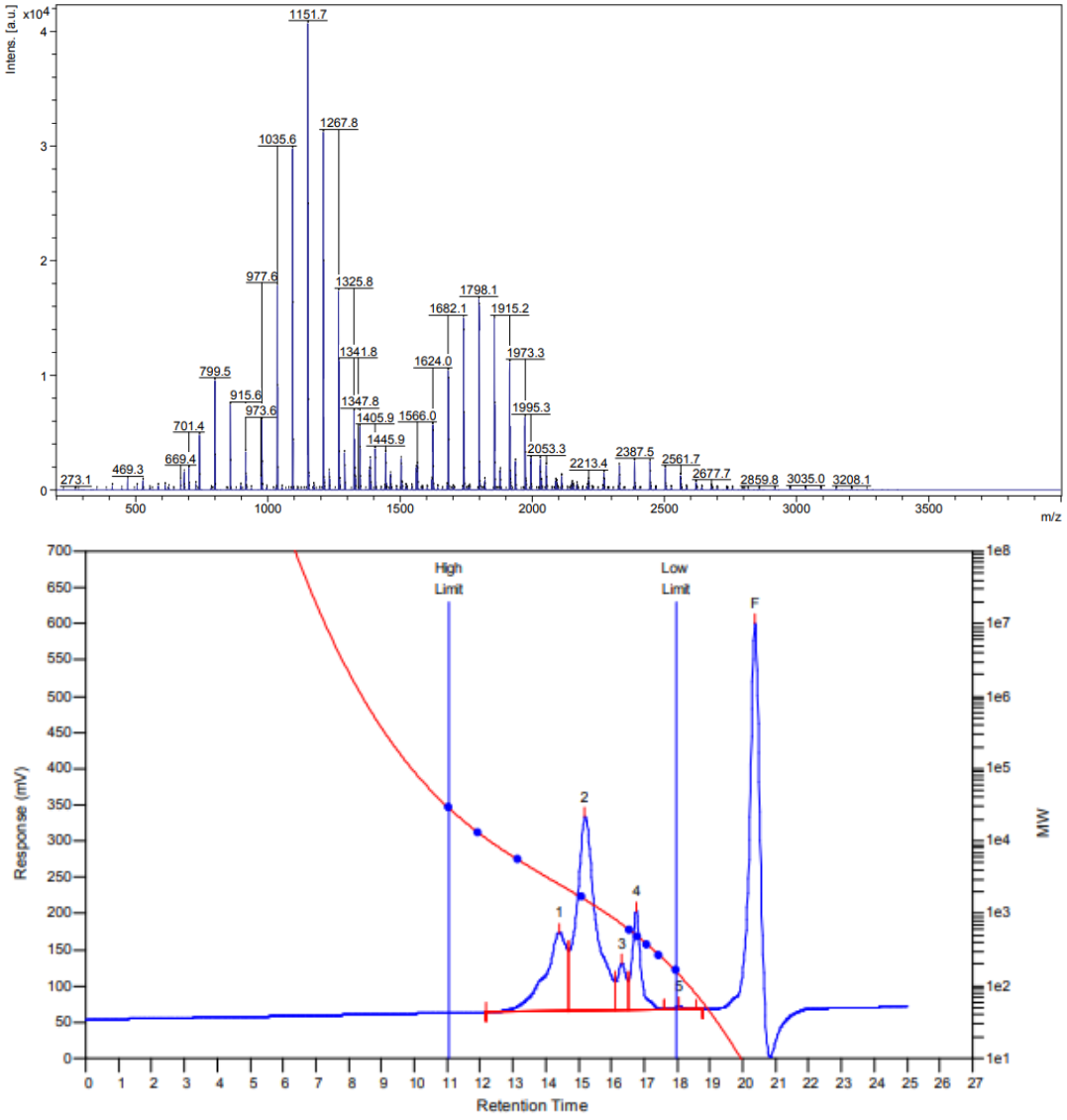

Figure 47 – MALDI-TOF mass spectrum (upper) and gel permeation chromatograph (lower) reported for PPG425PUDMA Product 2 (1st step - 30°C w/ cat).

The intended oligomer is compound **B**, with structure HEMA – IPDI – PPG – IPDI – HEMA.

Despite best efforts, the formation of compound **C** and **D** (and increasing molecular weight iterations) will occur. The purpose of this investigation was to determine which preparation method produced products with a larger content of compound **B** and minimisation of starting materials and compound **A**, **C** and **D**. From Table 18, peak **1** was allocated to compound **C** and **D** (and

larger oligomers), peak **2** was allocated to compound **B**, peak **3** was allocated to compound **A**, peak **4** was allocated to poly(propylene glycol) and peak **5** was allocated to (hydroxyethyl)methacrylate. Peak **6** was toluene which is used as a flow marker for GPC. This process for peak allocation was applied to all products, and compound **B** percentage content for each product was detailed in Table 19.

Table 19 – Compositions and compound **B** content (%) of PPG425PUDMA Products 1 – 4

	Area of GPC peak			
	Product 1	**Product 2**	**Product 3**	**Product 4**
Compound **B**	6690.46	11194.3	7104.81	9497.97
(Hydroxyethyl) methacrylate	79.0304	90.1198	88.9865	51.941
Poly(propylene glycol)	3143.59	2549.82	3386.74	2632.81
Compound **A**	704.647	1239.82	675.043	940.08
Compound **C**	3791.21	5151.28	4142.97	6288.65
Compound **D** (and larger MW oligomers)	2892.39		3495.13	
Compound **B** content (%)	38.67	55.35	37.60	48.93

As can be observed from Table 19, product 2 contained the greatest compound **B** content (%). Experiments that did not add catalyst during the initial reaction step display the lowest content of compound **B** content (%). The method of preparation for product 2 utilised a lower temperature in the first step (0 °C) and addition of catalyst in the first step. This observation aligns with the findings of Lömolder et al. regarding the influence of reaction conditions. Lömolder et al. found catalysis of IPDI with DBTDL promoted a higher degree of selectivity for mono-addition (and hence a greater probability

of compound **B** synthesis), even with increased temperature, than could be achieved without DBTDL at low temperatures[219].

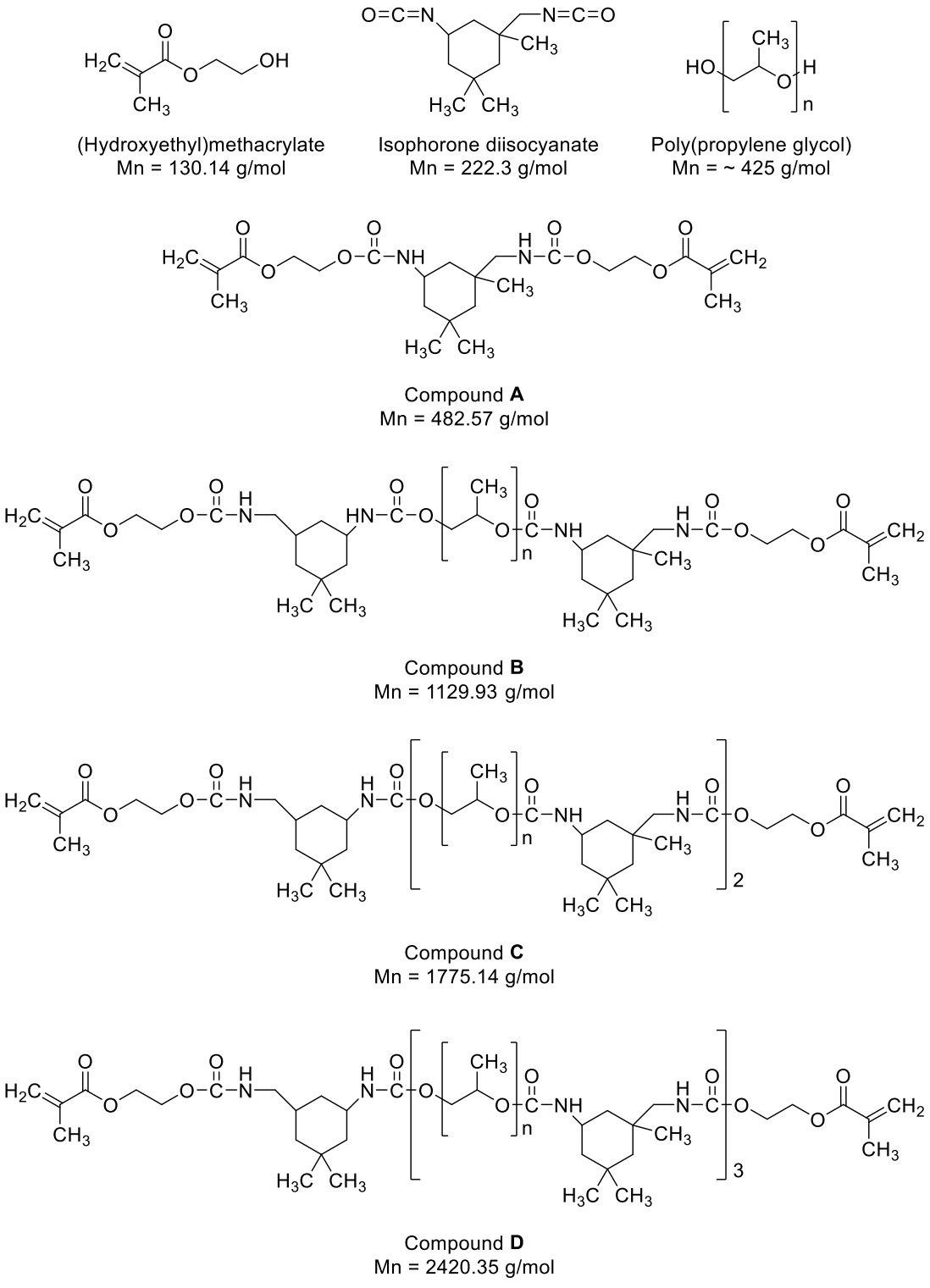

Figure 48 – Molecular structures showing possible compounds/oligomers within poly(propylene) polyurethane dimethacrylate products

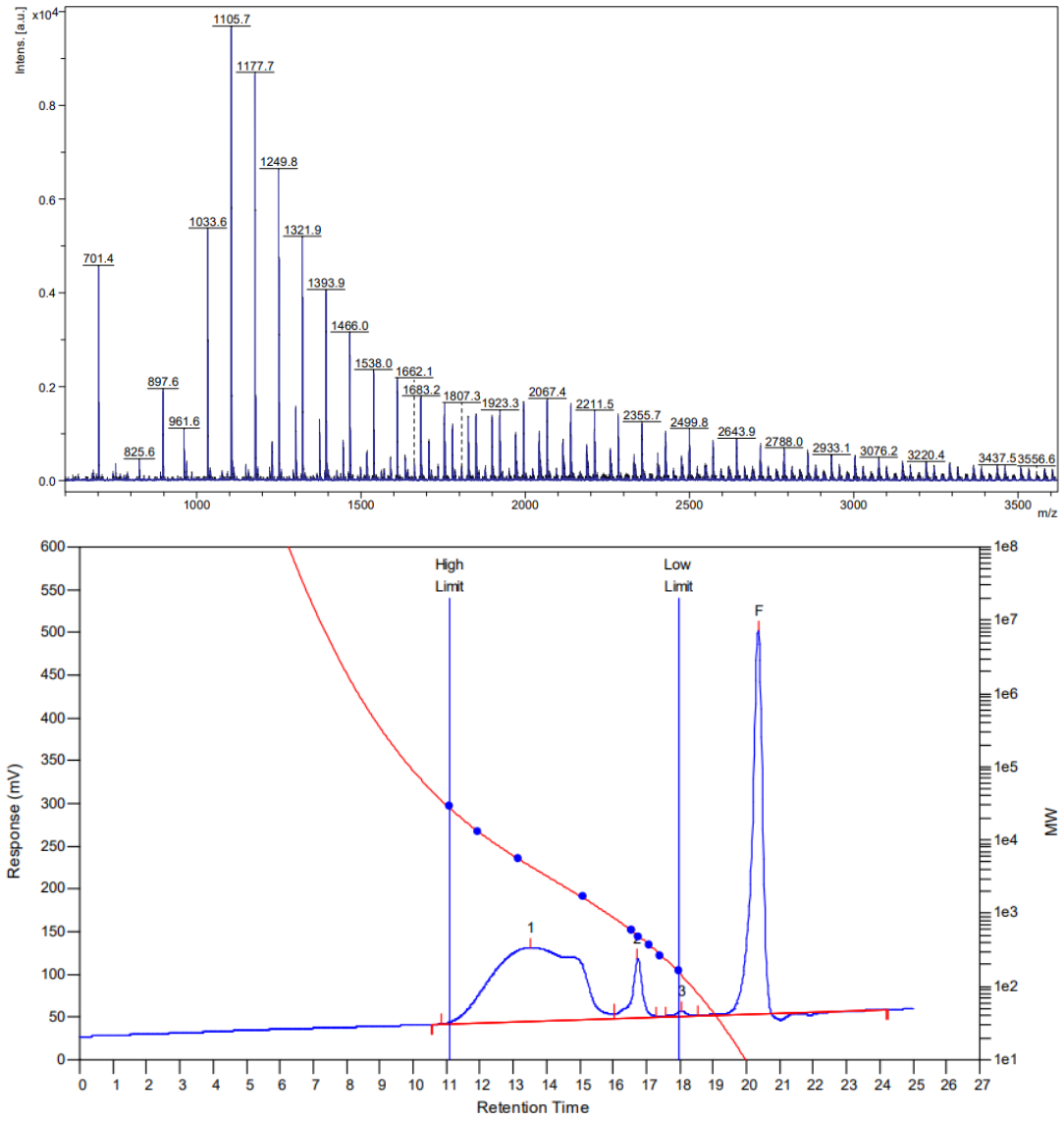

Figure 49 – MALDI-TOF mass spectrum (upper) and gel permeation chromatograph (lower) reported for PTHF650PUDMA Product 2 (1st step – 30 °C w/ cat).

This indicates that ideal reaction conditions for producing polyurethane dimethacrylates with high contents of oligomer with structure HEMA – IPDI – PET/PES – IPDI – HEMA, is through addition of catalyst and use of low temperatures during the first step. This experiment was repeated for polyurethane dimethacrylates prepared from PTHF650. This was done to ensure repeatability of this observation, and to afford materials that require minimal dilution to attain a photocurable formulation of workable viscosity (PPG425PUDMA materials displayed high viscosity). Product numbers were

allocated to their preparation conditions as before except Product 1 (30 °C wo/ cat) was omitted, due to time constraints.

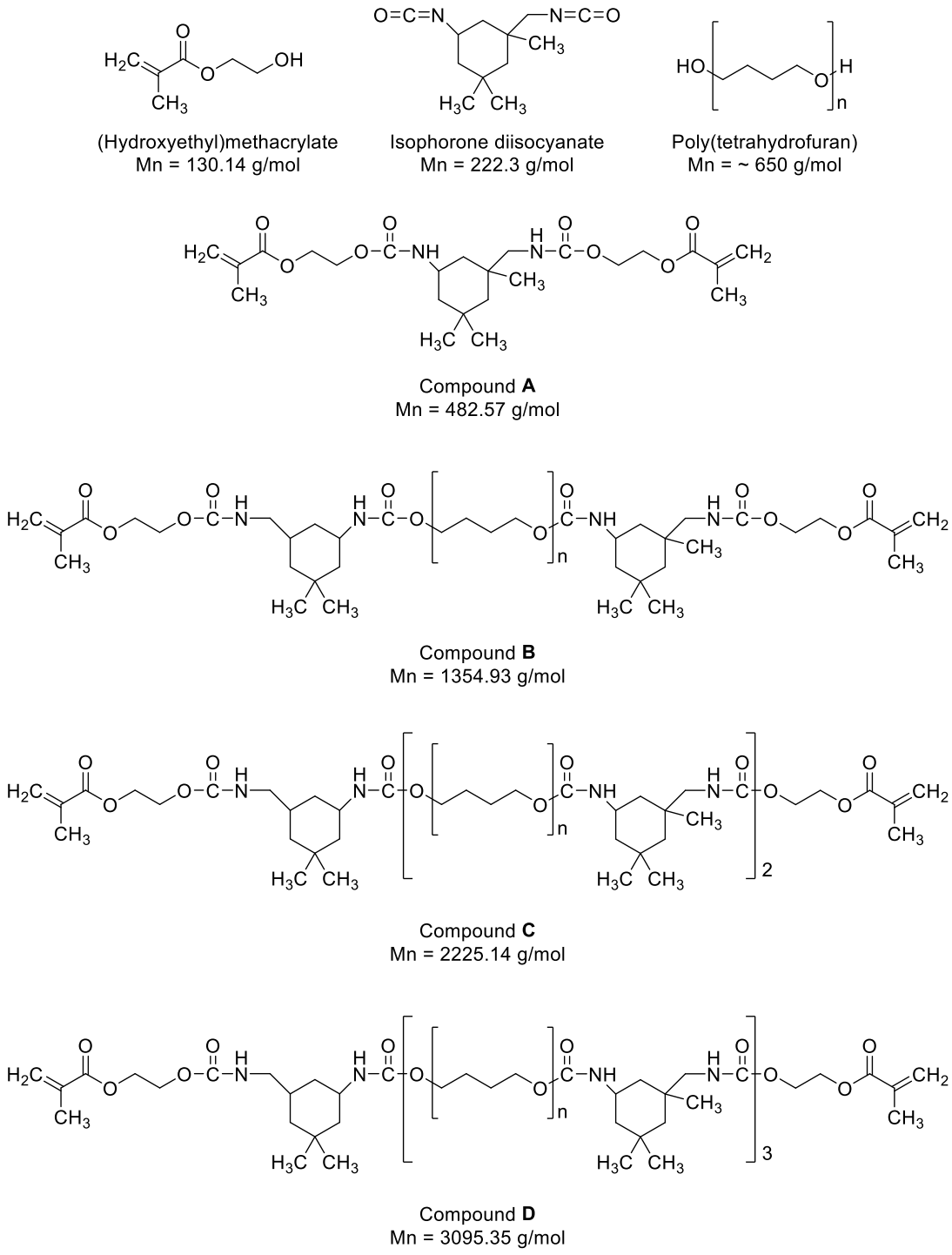

Figure 50 – Molecular structures showing possible compounds/oligomers within poly(tetrahydrofuran) polyurethane dimethacrylate products

Table 20 – Data generated from GPC for PTHF650PUDMA Product 2

Peak No	Mn	Peak polydispersity	Peak area
1	3280	1.5003	15544.7
2	517	1.03288	1533.5
3	145	1.04138	149.071
4	5	1.2	10141.5

For PTHF650PUDMA products, fewer GPC peaks were present. This was due to the merging of peaks corresponding to compound **B** (see Figure 50) and compounds **C**, **D** (and increasing molecular weight iterations). This explains the increase in peak polydispersity. Also, the peak corresponding to unreacted spacer does not appear, likely owed to a more controlled addition of spacer in Step 2 of the reaction. Unlike Table 19, Table 21 highlights the percentage content of compound **A** instead of compound **B**. This is due to the lack of separation of the compound **B** peak. In this case, lower percentage content of compound **A** indicates higher percentage content of compound **B**, as compounds **C**, **D** and higher are more likely to arise with higher compound **A** content. This is further supported by increasing compound **B**, **C**, **D** and higher peak polydispersity from Product 2 to 4 (1.5003, 1.51178 and 1.59613), which arises due to increase in content of compounds **C**, **D** and higher in comparison to compound **B**.

Table 21 – Compositions and compound **1** content (%) of PTHF650PUDMA Products 2 – 4

	Area of GPC peak		
	Product 2	**Product 3**	**Product 4**
Compound **A**	1533.5	1754.81	2102.47
(Hydroxyethyl) methacrylate	149.071	159.492	116.073
Compound **B**, **C** and **D** (and larger MW oligomers)	15544.7	14242.9	14290.3
Compound **A** content (%)	8.90	10.86	12.74

Products **2** – **4** were formulated together with 20% w/w HDDA and 1% w/w TPO and SLA 3D printed into tensile testing samples (55.0 mm x 8.0 mm, 0.8 mm thickness). Samples were post-cured and "cleaned" via continuous acetone extraction using a Soxhlet apparatus for 24 h.

Table 22 – Gel content (%) values for PTHF650PUDMA-based formulations prepared via different conditions.

Sample name	Gel content (%)
Product 2 + 20% HDDA + 1% TPO	92.08
Product 3 + 20% HDDA + 1% TPO	87.65
Product 4 + 20% HDDA + 1% TPO	83.07

Table 22 shows products with a higher compound **1** content have a lower gel content. An explanation for this observation is that formation of compound **1** in Step 1 of the polyurethane dimethacrylate synthesis, lowers the amount of end-capping (hydroxyethyl) methacrylate in Step 2. This results in fewer end-capped monomers/macromers within the product which do not exist as part of the materials polymer network/gel content.

Table 23 – Mechanical data obtained from tensile testing SLA 3D printed PTHF650PUDMA-based formulations prepared via different conditions.

Sample name	Tensile strength (MPa)	Young's modulus (MPa)	Elongation at break (%)	Tensile toughness (kJ/m3)
Product 2 + 20% HDDA + 1% TPO	7.24 ± 0.13	41.96 ± 1.20	32.91 ± 0.46	1603.37 ± 21.74
Product 3 + 20% HDDA + 1% TPO	7.04 ± 1.08	44.23 ± 1.17	30.19 ± 4.27	1465.12 ± 406.65
Product 4 + 20% HDDA + 1% TPO	5.13 ± 0.89	41.70 ± 2.56	25.74 ± 4.96	959.42 ± 334.21

Product 4, the material with the highest compound **1** content and lowest (%) gel content, displays the poorest and most variable mechanical properties, whereas Product 2, the material with the lowest compound **1** content and highest (%) gel content, displays the best and less variable mechanical properties. This observation can be attributed to lower gel content and greater

network heterogeneity due to increased material polydispersity. These factors can result in a greater propensity for material “weak spots” and ultimately, weaker material properties.

4.2.6. Polyester diol synthesis

To facilitate release of drug via mechanisms other than diffusion, polyester-based materials were first investigated. Polyester-based materials have the property of biodegradability, permitting release of drug through ester hydrolysis degradation of the polymer matrix. A range of polyesters exist, including poly(caprolactone), poly(butyrolactone), poly(lactide) and poly(glycolide). The degradation rates of these materials are determined by two major factors, hydrophilicity and crystallinity. For example, poly(lactide) materials have a faster degradation rate than poly(caprolactone) due to increased hydrophilicity, water diffusion and ultimately, ester hydrolysis. Conversely, poly(lactide-*co*-glycolide) materials have similar degradation rates to poly(glycolide) materials, despite a lower hydrophilicity. This is associated to higher crystallinity of poly(glycolide) materials, which hinders water diffusion, and hence ester hydrolysis[231]. Co-polymers of these compounds can be prepared to achieve materials with tailorable degradation rates. For the present application, degradation rates ranging from hours to weeks are desirable, and hence faster degrading materials such as poly(lactide) and poly(glycolide) are better suited. Most literature detailing the preparation of polyester-based compounds focuses on high molecular weight compounds (> 2000 g/mol). Such high molecular weight polyesters display either high viscosity or are solids at room temperature, rendering them incompatible with the SLA 3D printing process. Ideally, non-solid polyester compounds (which are typically < 1000 g/mol) are preferable, as these, in theory, will afford low viscosity photocurable materials compatible with the SLA 3D printing process. Another consideration pertains to polydispersity of prepared polyesters. Polyester materials of high polydispersity will offer inconsistent properties such as viscosity, end-material mechanical strength and end-material degradability. It is therefore necessary to identify a preparation method that yields polyester compounds with low molecular weights (< 1000 g/mol) with a low

polydispersity. Two preparation methods were considered: polycondensation and ring-opening polymerisation.

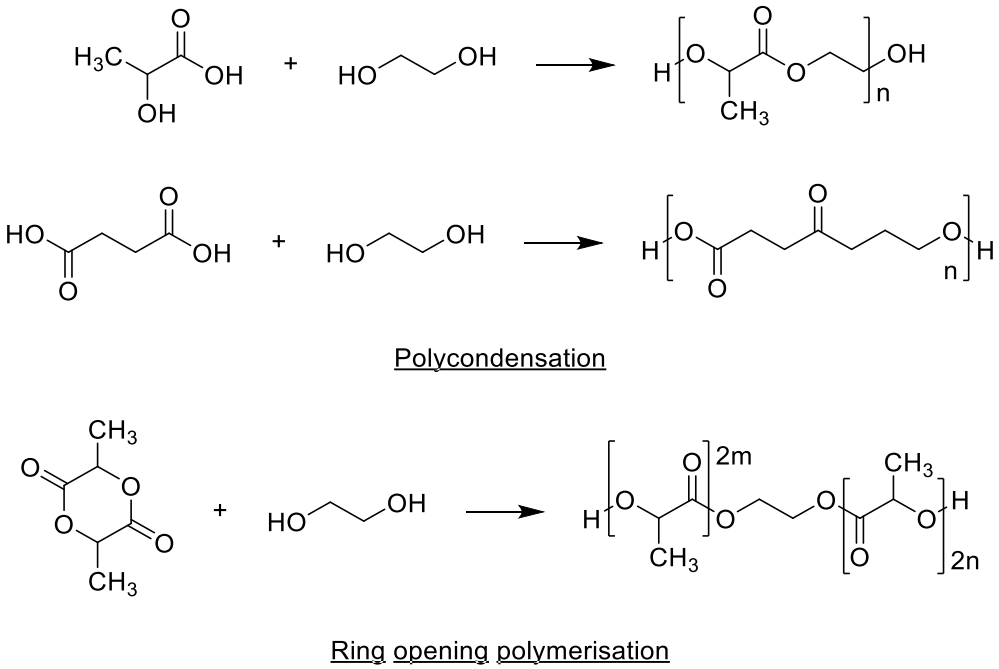

Figure 51 – Schemes showing two alternative routes to polyester materials

Polycondensation preparation of polyester materials involves reaction of (di)carboxylic acids with alcohols. The resulting polymer is a copolymer of the (di)carboxylic acid and the alcohol. If a monocarboxylic acid is reacted with dialcohol, both terminals of the copolymer will possess alcohol functionalities, whereas if a dicarboxylic acid is reacted with an alcohol, one terminal of the copolymer possesses an alcohol. An issue with this synthetic route is that the resulting compound contains different terminal functional groups. Each terminus will display a different reactivity towards acid chloride and isocyanate reactants and will form different products. This could potentially lead to photopolymer materials with low uniformity and high polydispersity, and a significant side product content. In contrast, ring opening polymerisation (ROP) preparation of polyester materials involves a chain-growth polymerisation initiated by an alcohol, where the terminal end group of a polymer chain acts as a reactive centre where further cyclic monomers can be added by ring-opening and addition of the broken bond. The resulting polymer is a homopolymer of acyclic monomer repeats containing an initiator (ethylene

glycol) core. Both terminals of the homopolymer possess alcohol functionalities, and hence high uniformity and low side product content is expected. Furthermore, for the above reaction between *rac*-lactide and ethylene glycol, polymer repeat chains are the same as pure poly(lactic acid) and hence, in theory, a faster degrading material can be expected. For these reasons, in addition to ease of preparation and breadth of literature detailing synthetic protocols, an ROP method was pursued for the preparation of polyester-based materials.

Due to cost and availability, oligomers based on *rac*-lactide were initially prepared to allow finetuning of the preparation method. The goal was to achieve oligomers with discrete target molecular weights of 400 and 1000 g/mol, with low polydispersity. This was achieved through adjusting the ratio between monomer (*rac*-lactide) and chain transfer agent (CTA, ethylene glycol) ($[M]_0/[CTA]_0$). These target molecular weights were chosen to ensure these materials had sufficiently low viscosities to allow for SLA 3D printing. Three reaction variables were explored to elucidate their impact on preparation of polyester materials with the above specifications: reaction time, temperature and catalyst. Temperatures ranging from 130 to 160 °C were first investigated. At higher temperatures, the reaction reached completion in less time (3 – 6 h) whereas at lower temperatures (130 °C) a larger amount of time was required before ^{1}H NMR analysis confirmed reaction completion (48 h). In addition, lower temperatures generally led to crude products with a higher content of starting materials in comparison to higher temperatures. A drawback of higher temperatures (160 °C) was products tended to be more coloured than those produced at lower temperatures (130 – 140 °C). For future syntheses, reaction conditions of 130 °C for 48 h and 140 °C for 6 h were used. Three different catalysts were tested: stannous octoate (SO), dibutyltin dilaurate (DBTDL) and 1,8-diazabicyclo[5.4.0]undec-7-ene (DBU). To assess how different catalysts influenced polyester synthesis, ^{1}H NMR and an acetylation-based hydroxyl value (OHV) test were used to calculate average molecular weight of products. Table 24 shows average molecular weights (M_n) of hydroxyl-terminated PLA calculated using different methods. ^{1}H NMR analysis of products were carried

out before and after material work-up. Prior to work-up, all PLA diol compounds were reasonably close to their target molecular weight.

Table 24 – Average molecular weights of hydroxyl-terminated PLA oligomers prepared using different reaction conditions

Rx time (hours)	Rx temp (°C)	Catalyst	Molecular weight (g/mol)				
			Target	1H NMR		OHV	
				before work-up	after work-up	acetylation	19F NMR
48	130	SO	400	441	445	520	564
48	130	DBTDL	400	437	447	481	553
48	130	DBU	400	462	593	774	738
48	130	SO	1000	958	958	1552	1513
48	130	DBTDL	1000	973	966	1422	1179
48	130	DBU	1000	963	1371	2967	-
6	140	DBU	400	-	456	-	-
6	140	DBU	1000	-	1231	-	-

PLA diol compounds with target M_n of 400 g/mol displayed higher $M_{n(1H\ NMR)}$, whereas compounds with target M_n of 1000 g/mol displayed a lower $M_{n(1H\ NMR)}$. It can be speculated that this was due to the gradual increase in reaction mixture viscosity which prevented further chain extension. After work-up, PLA diol compounds utilising SO and DBTDL as a catalyst displayed a similar $M_{n(1H\ NMR)}$ to before work-up. However, PLA diol compounds utilising DBU as a catalyst displayed an increase in $M_{n(1H\ NMR)}$ after work-up. This was attributed to different work-ups utilised. PLA diol compounds prepared using SO and DBTDL were purified by precipitation into cold hexanes. This step was carried out to remove both SO and DBTDL, which are soluble in hexane, from the product. PLA diol compounds prepared using DBU were purified by column chromatography, using a short silica. It was speculated that column chromatography was inefficient in removing DBU from the product. This meant during the subsequent drying step under high vacuum, intended for removal of excess ethylene glycol and *rac*-lactide, DBU further catalysed ROP leading to increased oligomer M_n. This trend was also observed from M_n values generated from acetylation-based OHV testing, where DBU catalysed products showed greater variance between $M_{n(acetylation\ OHV)}$ and $M_{n(1H\ NMR)}$ than for SO and DBTDL catalysed products. Values for $M_{n(acetylation\ OHV)}$ were

greater, especially for PLA diol oligomers with target M_n of 1000, than those calculated using 1H NMR. This was speculated to be due to the hydrolysis of PLA diol oligomers by ethanolic potassium hydroxide during titration. This would lead to the generation of new carboxylic acids, lowering the pH and artificially extending the titration endpoint. This was observed when the solution would turn from pink (endpoint) to colourless after a few seconds. Ultimately, this led to highly variable results. An alternative method for calculating hydroxyl value was sought. Moghimi et al. (2013) developed a method for determining hydroxyl value of polymers using 19F NMR[189]. The method involves reaction of free hydroxyl groups with fluorophenyl isocyanate, and then quantification with 19F NMR analysis against an α,α,α-trifluorotoluene.

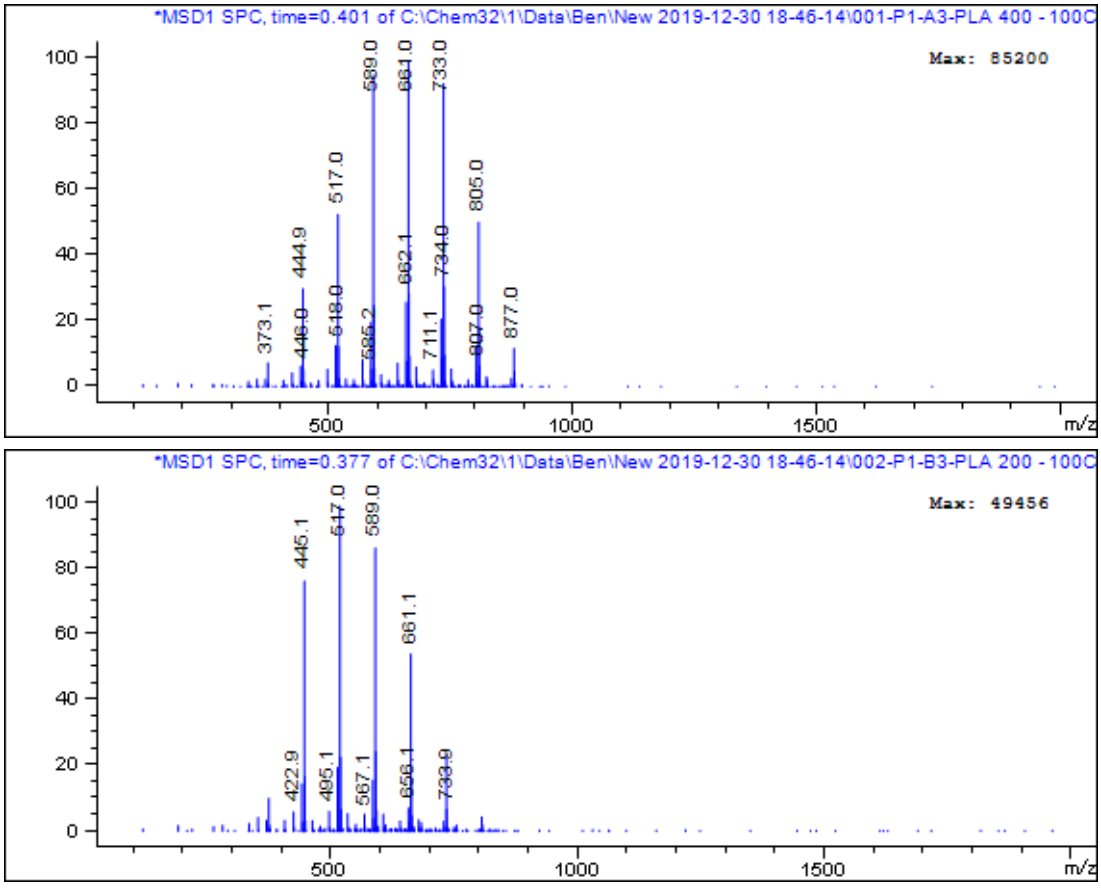

Figure 52 – Mass spectra generated from LC-MS analysis of PLA samples. Top spectra = dried PLA diol (M_n^t = 400 g/mol), bottom spectra = dried PLA diol (M_n^t = 200 g/mol).

This method produced similar values for M_n as with the acetylation method but once again, results varied heavily and had low reproducibility. Furthermore, lack of access to an NMR spectrometer with a 19F probe prevented the development and improvement of this method. As a result, neither of these methods could accurately identify the optimal catalyst for polyester diol preparation. DBTDL was ultimately chosen as the catalyst of choice. This was due to materials catalysed with DBU undergoing a molecular weight increase during drying under vacuum and materials catalysed with SO possessing a hazy appearance after work-up. Nonetheless, materials catalysed with DBTDL showed an unacceptable increase in viscosity after drying, suggesting an increase in molecular weight.

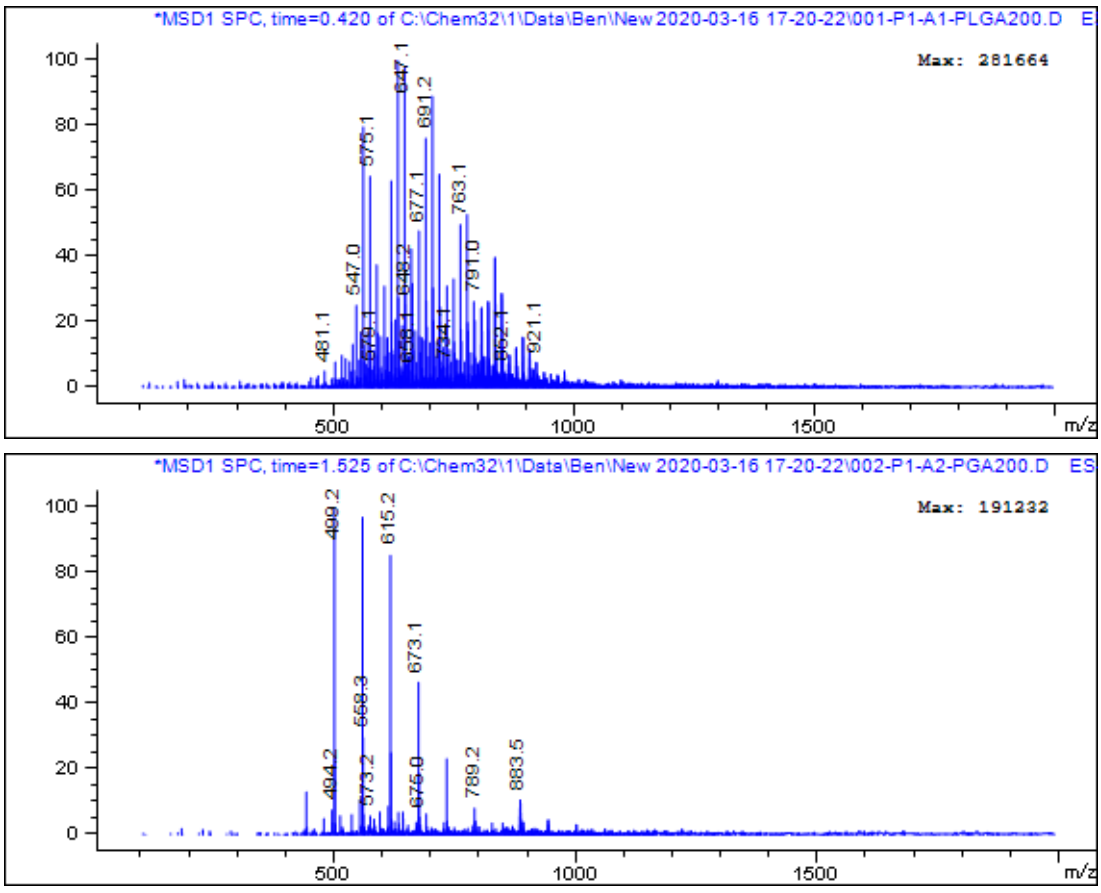

Figure 53 – Mass spectra generated from LC-MS analysis of PLGA and PGA samples. Top spectra = dried PLGA diol (M_n^t = 200 g/mol), bottom spectra = dried PGA diol (M_n^t = 200 g/mol).

LC-MS was chosen to monitor molecular weight distribution of materials catalysed with DBU. Figure 52 shows mass spectra for two dried PLA diols, one with M_n^t = 400 g/mol and one with M_n^t = 200 g/mol. As observed, the major $[M+Na]^+$ species in the PLA diol (M_n^t = 400 g/mol) spectra were 589.0, 661.0 and 733.0 Da whereas the major $[M+Na]^+$ species in the PLA diol (M_n^t = 200 g/mol) spectra were 445.1, 517.0 and 589.0 Da. The latter are far closer to the desired M_n of 400 g/mol and this was noted by the much lower viscosity of PLA diol (M_n^t = 200 g/mol). This material was functionalised with terminal methacrylate groups, and PLGA(50/50) and PGA diols were prepared with target molecular weight of 200 g/mol.

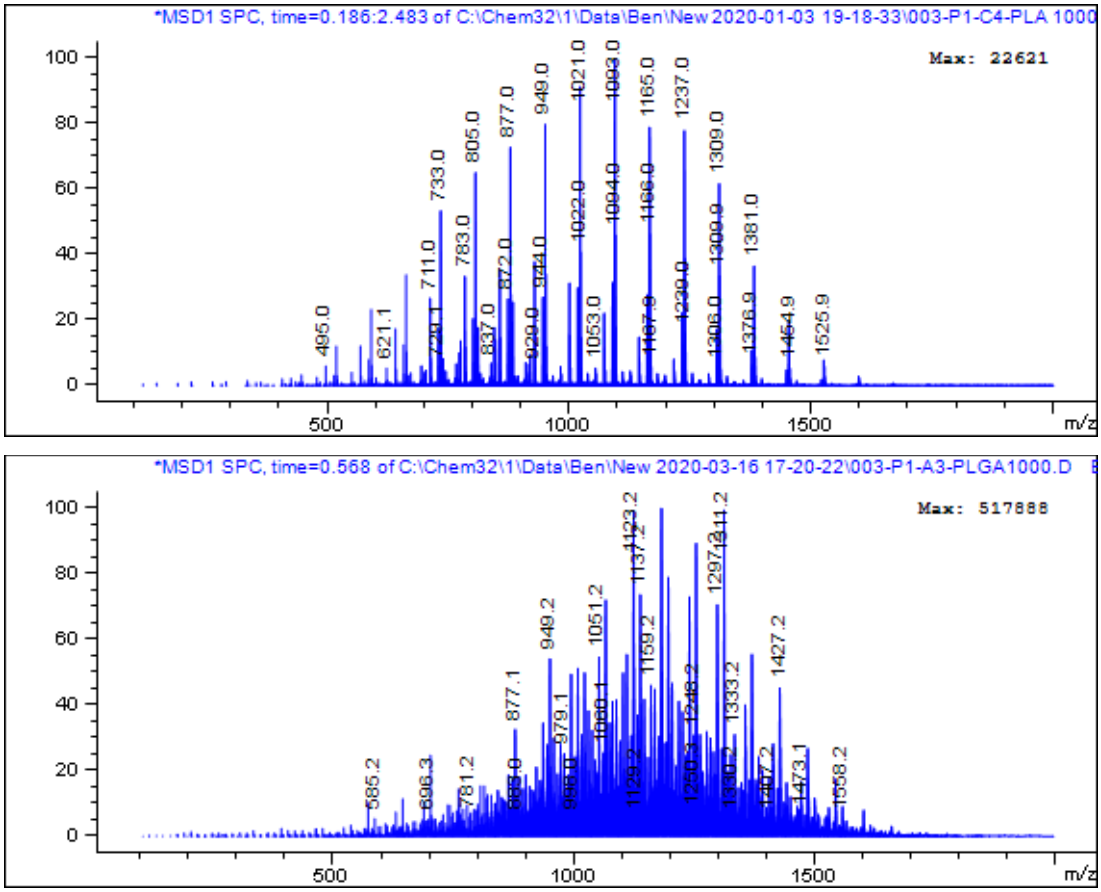

Figure 54 – Mass spectra generated from LC-MS analysis of PLA samples. Top spectra = dried PLA diol (M_n^t = 1000 g/mol), bottom spectra = dried PLGA diol (M_n^t = 1000 g/mol).

Their respective mass spectra can be observed in Figure 53. Major $[M+Na]^+$ species in the PLGA diol (M_n^t = 200 g/mol) spectra were 575.1, 647.1 and 691.2 Da and 499.2, 558.3 and 615.2 Da for PGA diol (M_n^t = 200 g/mol). These

materials displayed an acceptable viscosity and were functionalised with terminal methacrylate groups. For preparation of polyester diols with target molecular weight 1000 g/mol, utilising ($[M]_0/[CTA]_0$) for PLA diols of M_n^t = 1000 g/mol led to mass spectra displayed in Figure 54. Major $[M+Na]^+$ species in the PLA diol (M_n^t = 1000 g/mol) were 949.0, 1021.0 and 1093.0 Da, and 1123.2, 1159.2 and 1311.2 Da for the PLGA diol (M_n^t = 1000 g/mol). Both materials were utilised as spacers in polyurethane dimethacrylate reactions. Preparation of PGA with target molecular weight 1000 g/mol was not possible using current reaction conditions due to an exceptionally high melting point. It is worth noting that the abundance of cation species in a mass spectra does not equate to their actual sample content and hence spectra were used as a rough guideline for selecting acceptable materials for functionalisation.

4.3. Conclusions and Future Work

This chapter introduces and describes successful synthetic protocols for the preparation of a range of different photopolymers based on different polyether and polyester “spacer” compounds. Polyurethane dimethacrylate-based materials display reduced brittleness and improved toughness in comparison to all other materials tested, signifying a marked improvement in terms of material properties in comparison to existing photocurable systems, and possibly indicating the next generation, in terms of base monomers/macromers, in the development of high-performance SLA 3D printable materials. In addition, characterisation of heteropolymers, composed of polyurethane dimethacrylate macromers and diluents such as multifunctional acrylates and CTAs, and non-reactive diluents, reveal a broad range of materials with tailorable hardness, stiffness, toughness, and porosity. This bolstered library not only offers materials with acceptable mechanical properties for use as implantable materials but could also permit the emergence of SLA 3D printing in other fields, where lack of suitable varied materials previously prevented so.

Continuations of this work could involve further optimisation of the polyurethane dimethacrylate reaction with aim to control and investigate the role of polydispersity on material properties such as viscosity, and mechanical properties. In addition, the range of monomers and macromers could be further expanded with preparation of polyurethane dimethacrylates based on polydimethylsiloxanes and different polyesters to afford materials with bioinert properties and tailored biodegradability, respectively. Furthermore, (meth)acrylate-based systems containing pendant group drug conjugates could be developed, introducing a new approach for development of drug-eluting SLA 3D printed devices. Finally, further exploration of heteropolymer systems containing different diluents could be undertook, to further improve material properties. For example, material toughness could be improve through use of other CTAs such as thiocarbonylthio compounds, formation of IPNs through addition of epoxide systems and/or the addition of additives such as liquid rubbers, core-shell and inorganic nanoparticles.

5. Toxic to non-toxic – rendering SLA 3D prints biocompatible

5.1. Introduction

Few implantable devices fabricated using SLA 3D printing have been reported. The primary reason for this is associated to unreacted (meth)acrylate-based monomers that remain trapped within the printed part. Residual unreacted monomers that migrate demonstrate a propensity to undergo Michael addition reactions with free amino and thiol groups of proteins and/or DNA giving noncleavable adducts, causing local irritation and toxicity[232,233] (see Figure 55). In one of the few examples, Matsuda et al. SLA 3D printed structures from an acrylate-based poly(trimethylene carbonate-co-e-caprolactone) resin containing anti-inflammatory drug indomethacin. No adverse effects were observed which was attributed to slow release of anti-inflammatory drug indomethacin from the implant that attenuated foreign-body induced inflammation caused by residual (meth)acrylate-based monomers[224].

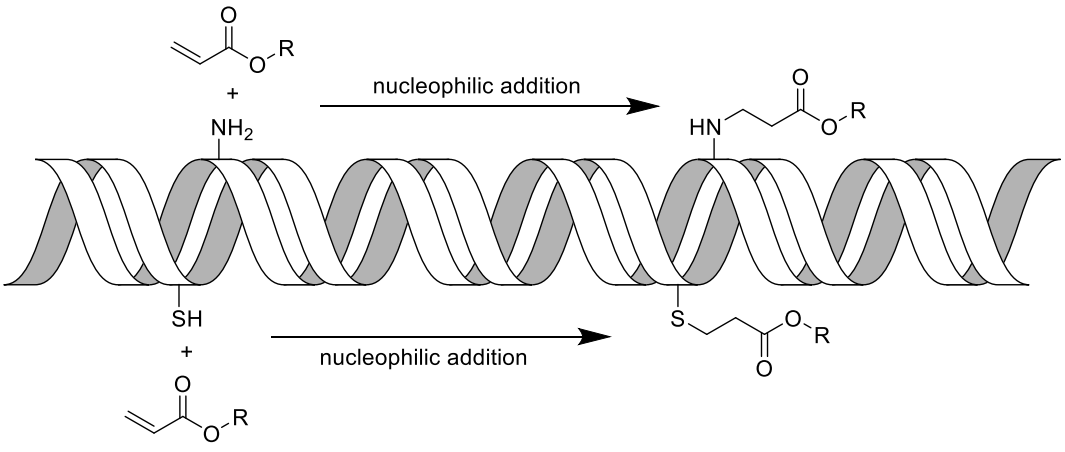

Figure 55 – Interaction of acrylate monomer/oligomers with DNA

Methacrylates are less reactive towards amines than acrylate, and are hence considered more biocompatible than acrylates[108]. Several studies have explored ways to improve biocompatibility of parts prepared from (meth)acrylate monomers. Schuster et al. evaluated different mono and multi-acrylated monomers as reactive diluents for 3D printing of bone replacement

materials. They noted that the whole structure of the monomer, rather than just (meth)acrylate functional groups were responsible for biocompatibility. They found that polymers obtained from acrylates with urethane units and amide linkages, and trimethylolpropane triacrylate gave outstanding biocompatibility[234]. In a following study, Schuster et al. also demonstrated the excellent biocompatibility of isobornyl acrylate compared to other reactive diluents, attributed to its camphor-like structure[235]. Beyond customisation of the backbone chemistry of (meth)acrylate monomers, carefully managed post-cleaning and post-curing processes and/or coating of surfaces with various biocompatible compounds can reduce leaching of unreacted monomers, additives and photoinitiator residues and ultimately improve biocompatibility[236]. Post-cleaning is typically the first post-processing step used to reduce residual monomer content. For example, parts printed from Formlabs Dental SG biocompatible resin require rinsing in a bath of 90%+ isopropyl alcohol for 10 minutes followed by removal and immediate re-immersion in fresh 90%+ isopropyl alcohol before drying and post-curing. Formlabs have developed the Form Wash instrument to automate this process. It is routine practice to store dentures and orthodontic appliances made using proprietary resins in water for up to 24 h to allow uncured compounds to be washed out[237]. Water storage times can be reduced by utilising an ultrasonic cleaner[238]. In addition, Alifui-Segbaya et al. demonstrated that treatment of SLA printed parts in 99% ethanol, which increased the biocompatibility of some printed parts using a zebrafish model, a fish embryo test designed to determine acute toxicity of monomers on embryonic states of zebrafish[239]. Post-curing, of SLA printed parts by additional UV light irradiation is another method used to reduce residual monomer content. For example, parts printed from Formlabs Dental SG biocompatible resin require exposure for 10 minutes to 108 watts each of Blue UV-A (315 – 400 nm) and UV-Blue (400 – 550 nm) light, in a heated environment at 60 °C[240]. Formlabs have developed the Form Cure to automate this process, featuring a rotating inner table and several floodlights that project from the inner walls and ceiling that maximise printed part UV light exposure. Oskui et al. demonstrated that post-curing SLA 3D printed structures on each side for 30 min improved their biocompatibility towards a zebrafish model[241].

Furthermore, alternative compounds can be used to replace those that exhibit high toxicity in photopolymer resins. For example, Nguyen et al. used riboflavin as an alternative photoinitiator. Parts printed containing riboflavin demonstrated improved biocompatibility over parts created containing commercial PIs such as Irgacure 2959 and Irgacure 369[236]. Other techniques for reducing toxicity of SLA 3D-printed parts include a high temperature heat treatment that removes cytotoxic material by sublimation and diffusion in a nitrogen atmosphere[242], and extraction of toxic residues using supercritical carbon dioxide[243]. However, both methods are unattractive due to impaired material transparency and high cost, respectively.

No matter how effective aforementioned detoxification techniques prove, they do not completely eliminate toxicity associated with (meth)acrylate-based materials. This is due to generation of toxic degradation products. (Meth)acrylate-based materials degrade via ester linkage hydrolysis to afford poly(carboxylic acid)s and low molecular weight alcohols. Small molecules are readily cleared from the body whereas macromolecules typically persist. In this case, macromolecular acids persist, leading to prolonged pH changes, biomaterial precipitation and further irritation and toxicity[108,233,244]. Potential non-toxic alternatives to (meth)acrylates that also undergo free radical polymerisation include vinyl esters, vinyl carbonates and vinyl carbamates. These monomers are widely used for biomedical applications such as materials for soft contact lenses but are relatively unexplored as photo-crosslinking systems[232]. Firstly, Heller et al. demonstrated that vinyl ester, vinyl carbonate and vinyl carbamate monomers were one and at least two orders of magnitude less cytotoxic than methacrylate and acrylate monomers, respectively[233]. Furthermore, materials based on vinyl esters and vinyl carbonates also degrade via ester hydrolysis, affording macromolecular poly(alcohol)s as a degradation product. Unlike poly(carboxylic acid)s, poly(vinyl alcohol)s are considered non-toxic and safe for pharmaceutical use. Vinyl carbamates, unlike vinyl esters and carbonates, are quite stable under hydrolytic conditions and are often considered non-degradable[108,232,244]. Divinyl esters, vinyl carbonates and vinyl carbamates have 8 and 100-fold greater compatibility compared to dimethacrylates and diacrylates,

respectively[108]. Vinyl esters and vinyl carbonates demonstrate photoreactivity between that of acrylates and methacrylates and DBC rates comparable with acrylates (approximately 70%). Difunctional vinyl carbamates show slightly lower photoreactivity and DBC (approximately 55%) which is comparable to that of methacrylates[108,233,245]. PEG-based vinyl esters, vinyl carbonates, and vinyl carbamates demonstrate significantly lower photoreactivity due to enhancement of chain transfer reactions of these monomers that contain hydrogen abstractable domains such as ethylene glycols[232,244]. However, Husár et al. demonstrated that the combination of vinyl esters and carbonates with thiol-based chain transfer reagents can increase photoreactivity and DBC of the resultant thiol-ene system[244]. Both vinyl esters and carbonates produce parts with mechanical properties comparable with (meth)acrylate-based materials and biodegradable thermoplastic (PLA and PCL) standards. In addition, structures were manufactured from vinyl ester and carbonate-based formulations using SLA[246] and displayed *in vivo* biocompatibility and osteointegration exceptionally well, when implanted into rabbit femoral bone[233,245,247,248]. Moreover, structures were also 3D printed from a vinyl carbamate-based resin and exhibited superior mechanical strength compared to PLA and PCL references[245]. However, compared to (meth)acrylates, only a few vinyl esters exist commercially and only one is difunctional. Furthermore, vinyl carbonates and carbamates are not available commercially. The main reason contributing to the limited availability of these monomers is due to complicated synthetic routes. For example, most common synthetic route to vinyl esters is through reaction of appropriate carboxylic acids with vinyl acetate using mercury(II) acetate as catalyst, however this method can be dangerous and restricts monomer design to non-ester-based backbones[233]. The most common synthetic route to vinyl carbonates and carbamates involves conversion of alcohols and amines with vinyl chloroformate, an extremely expensive reagent[232]. Other synthetic routes to these monomers involve the use of expensive and/or toxic reagents and/or require multiple steps and difficult purification processes that result in poor yields[232,244,247]. Nevertheless, recent patents have described the synthesis of these monomers from cheap reagents such as carboxylic acids, alcohols, amines and acetylene

gas in the presence of (rare) metal complex catalysts, and therefore may afford a broader, more affordable range of monomers in the future[232,249].

Other notable photopolymers that may prove suitable replacements are epoxides and vinyl ethers, that unlike other discussed monomers, undergo cationic photopolymerisation. Cationic photopolymerisable systems such as epoxides and vinyl ethers are characterised by absence of toxicity or irritant properties[250]. Furthermore, epoxide and vinyl ether monomers do not contain hydrolysable ester linkages and therefore do not form potentially toxic degradation products[251]. Cationic photopolymerisation systems have several distinct advantages such as a lack of inhibition by oxygen, low shrinkage and shrinkage induced stress due to the ring opening nature of epoxide and vinyl ether monomers, and good adhesion to inorganic substrates[251]. Furthermore, cationic photopolymerisation continues after UV-vis irradiation has ceased, with cationic reactions progressively penetrating parts of the component not directly exposed to UV-vis radiation. This phenomenon is known as “shadow curing” and provides a substantial post cure effect due to the prolonged lifetime of the cation[252]. Unfortunately, cationic photopolymerisation systems have not received as much interest or development in UV-curing and 3D printing applications attributed to their low cure speed (especially epoxides), moisture sensitivity, propensity for side-reactions, inconsistent product properties, high cost and difficult synthesis, and a limited choice of monomers and photoinitiators[253]. Considering the latter, extremely few cationic photoinitiators operate within the near UV light spectrum, severely limiting the usage of epoxide and vinyl ether-based materials with available SLA systems[254]. However, vinyl ethers may yet be applicable with SLA processes, with certain multi-functional monomers exhibiting homopolymerisation rates similar free radical photopolymerisation systems[250], an ability to co-polymerise with (meth)acrylate monomers and drastically improved DBC and biocompatibility of consequent materials[255]. Furthermore, the development of a green, safe and cost-effective one-pot method for synthesis of multi-functional vinyl ether monomers has recently been reported[256,257].

The aim of this chapter is to develop biocompatible SLA 3D printed parts, utilising a range of methods discussed above

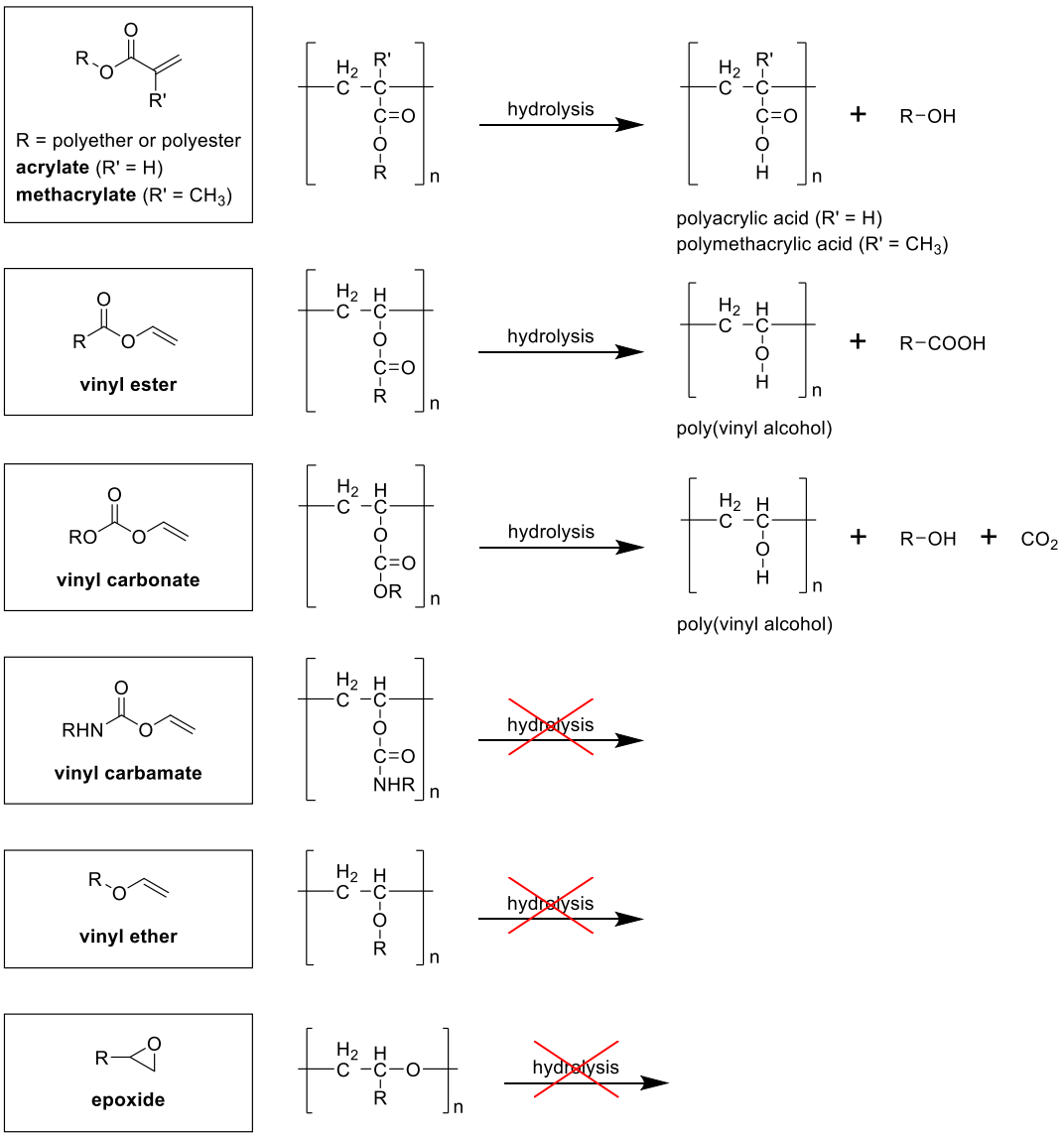

Figure 56 – Diagram highlighting hydrolysis products of radical and cationic photopolymerisation systems. Adapted and modified from Husar et al. (2014)[244].

Firstly, the effect of simple post-processing steps such as post-cleaning and post-curing on polyurethane dimethacrylate-based materials are evaluated. Cell culture studies are used to evaluate the effect of different post-processing steps on material biocompatibility (and drug loading. Secondly, strategies for facilitating SLA 3D printing of cationic photopolymer systems were explored. This will involve preparation and testing of cationic photoinitiators that operate within the same near-UV light spectrum as do commercial SLA 3D printers.

5.2. Results and Discussion

5.2.1. Post-processing materials and its effects on material biocompatibility

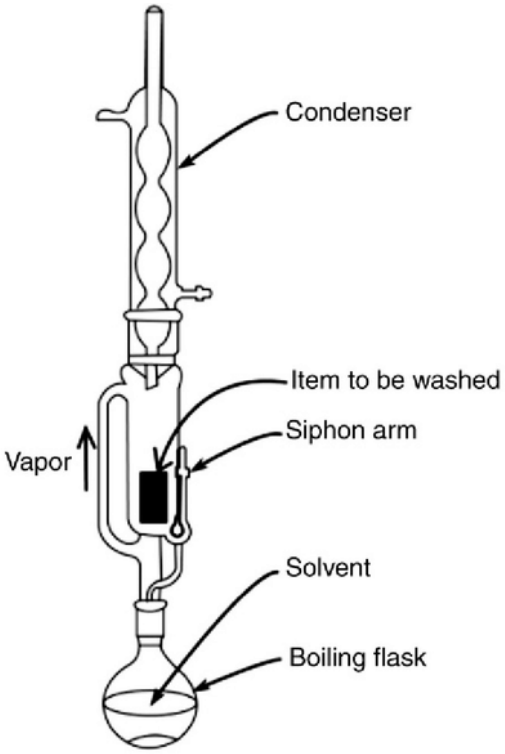

Figure 57 – Diagram showing a Soxhlet apparatus used for continuous warm acetone extraction of toxic materials from samples. Reproduced from Muhamad et al. (2017)[258].

Silicone mould cured sheet samples were post-cured in a Form Cure UV curing oven at 60 °C for 60 min. In a method similar to Elomaa et al. (2011)[259] and He et al. (2016)[210], samples were placed into a glass fibre thimble and placed into a Soxhlet apparatus setup (see Figure 57). Residual monomers, photoinitiators and additives were extracted from samples continuously with warm acetone for 24 hours. Samples were removed from the apparatus, allowed to dry at room temperature for 24 hours and then dried under vacuum at 60 °C. NIH 3T3 fibroblasts were then exposed to these samples for 24, 72 and 120 hours to investigate the biocompatibility of these materials (Figure

58). Cell line selection was due to Elomaa et al. (2011)[259] and He et al. (2016)[210] having previously used this model to evaluate biocompatibility of (meth)acrylate-based materials. In general, all cells showed excellent biocompatibility against all samples tested. An interesting trend observed was that cell viability seemingly went above 100%, especially so for PEG1000PUDMA-based materials. This was attributed to the provision of additional surfaces for cell adhesion and proliferation by the sample. It was speculated that PEG1000PUDMA-based materials, on account of their hydrophilicity, presented a more habitable surface for cell adhesion, hence the larger values for cell viability when compared to more hydrophobic materials based on PTHF1000PUDMA.

An additional reason for +100% cell viability values can be accounted to sample preparation. As mentioned previously, these materials were mould-cured through evaporation of a carrier solvent. The evaporation of solvent leaves voids within the material (see Figure 59). The presence of voids within a material greatly increases its surface area. A greater surface area means more surface for potential cell adhesion and ultimately, higher cell viability. Additionally, the unpredictability of void generation within the material due to solvent evaporation, could potentially explain the larger variances seen in cell viability for materials displaying cell viability values above 100%. Interestingly, the surface image of “cleaned” PEG1000PUDMA + 10% dithiol CTA material indicates a lack of voids. This may explain why cell viability for this material is much lower when compared to PEG1000PUDMA and PEG1000PUDMA + 20% HEA materials (82.59% versus 162.16% and 169.98% mean cell viability, respectively). A potential reason this material contains no observable voids could be attributed to a lower viscosity that results in fewer bubbles formed during solvent evaporation.

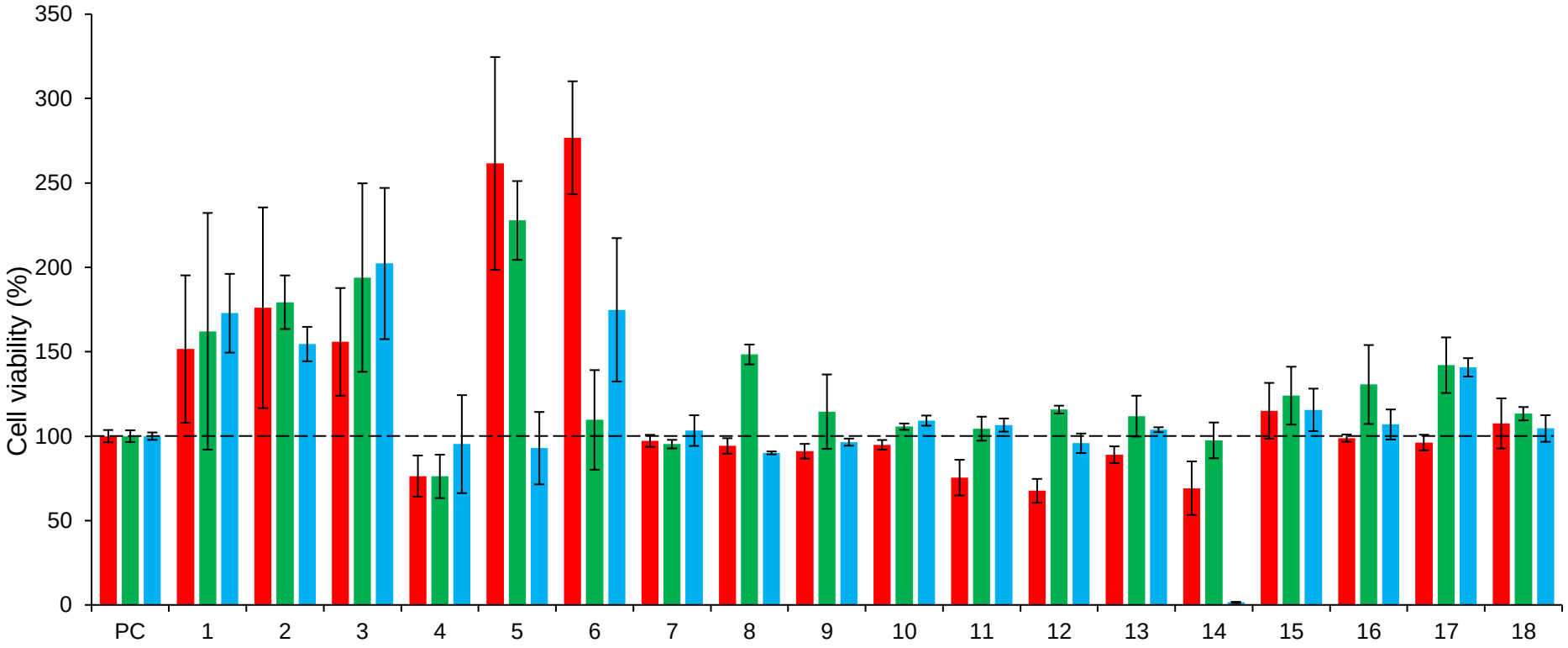

Figure 58 – Cluster column chart displaying cell viability (± 1 SE) against samples at 1, 3 and 5 days incubation. Positive control (PC) included. Samples are: **1** = "PEG1000PUDMA", **2** = "" + 20% HEA, **3** = "" + 20% TEGDA, **4** = "" + 10% dithiol CTA, **5** = "" + 10% tetrathiol CTA, **6** = "" + 20% PEG400, **7** = "PTHF1000PUDMA", **8** = "" + 20% IBOA, **9** = "" + TMPTA, **10** = "" + 10% dithiol CTA, **11** = "" + 10% tetrathiol CTA, **12** = "" + 20% PTHF650, **13** = PCL1250PUDMA, **14** = PPG1200PUDMA, **15** = PEG400PUDMA, **16** = PTHF650PUDMA, **17** = PCL530PUDMA, **18** = PPG425PUDMA.

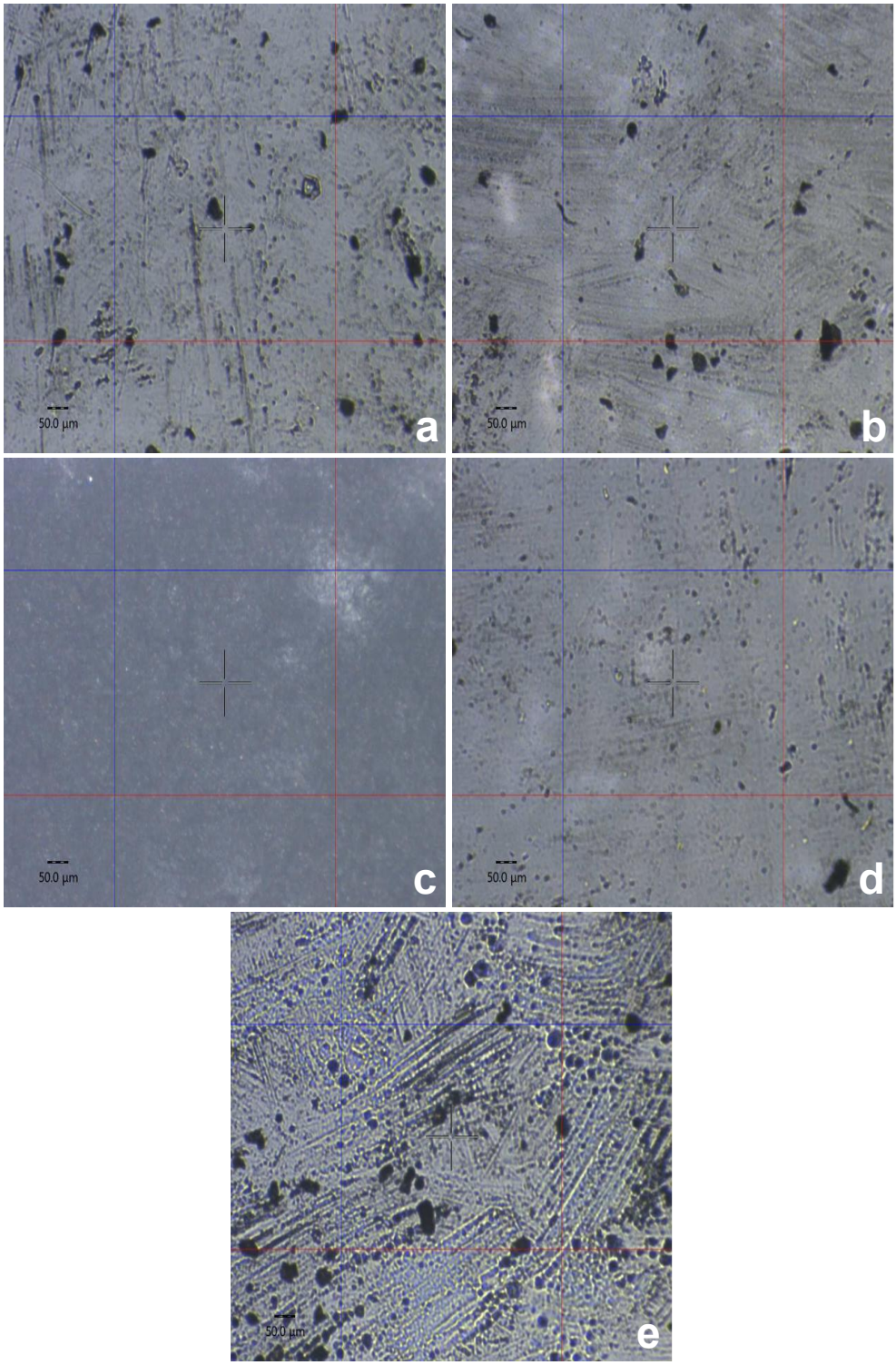

Figure 59 – Images captured via the optical video microscope feature of the Anton Paar Bioindenter™ (UNHT^3 Bio) at 5x magnification of select sample surfaces. Samples are: **a** = "PEG1000PUDMA", **b** = "" + 20% HEA, **c** = ""+ 10% dithiol CTA, **d** = "" + 20% PEG400, **e** = PEG400PUDMA.

Furthermore, materials formed from PEG1000PUDMA + 20% PEG400 do not display a significantly larger cell viability than its counterparts (187.09% mean cell viability), despite being a highly porous material (75.84% versus 94.49% (PEG1000PUDMA) gel content). From Figure 59, it can be observed that voids within the PEG1000PUDMA + 20% PEG400 material are smaller (albeit more ubiquitous) than PEG1000PUDMA and PEG1000PUDMA + 20% HEA materials. It is speculated that although materials formed from PEG1000PUDMA + 20% PEG400 are highly porous, the voids present are too small to be infiltrated by cells (diameter 18 μm), preventing additional adherence, proliferation and consequently, increased cell viability. To verify this theory, it would be necessary to measure pore size range of these materials.

PEG1000PUDMA-based materials showed greater biocompatibility in comparison to PEG400PUDMA-based materials. This was attributed to the increase hydrophobicity of PEG400PUDMA-based materials due to a shortening of the hydrophilic spacer compound resulting in an increased hydrophobic, isophorone-urethane linkage hard segment content and therefore reduced cell adhesion and proliferation. The day 5 cell viability of cells exposed to PPG1200PUDMA is worthy of comment. The sharp decrease in cell viability (69.18% (Day 1) > 97.49% (Day 3) > 1.48% (Day 5) cell viability) was unexpected. This result could be attributed to human error such as incorrect addition of cell suspension to plate well, contamination of the plate well leading to cell death and/or incorrect addition of Prestoblue assay to well. The alternative is that this result is correct. One potential theory is, as previously mentioned, the polypropylene glycol chain of PPG1200PUDMA undergoes hydrolysis which leads to the generation of degradation products bearing carboxylic acid terminal groups[208]. This could potentially lower the pH of the culture medium over time, resulting in cell death and low cell viability. Retesting of this formulation is necessary to ascertain whether this theory is credible, or if the observation was attributed to a defective sample, but if true, this could imply such materials are unsuitable as implantable materials.

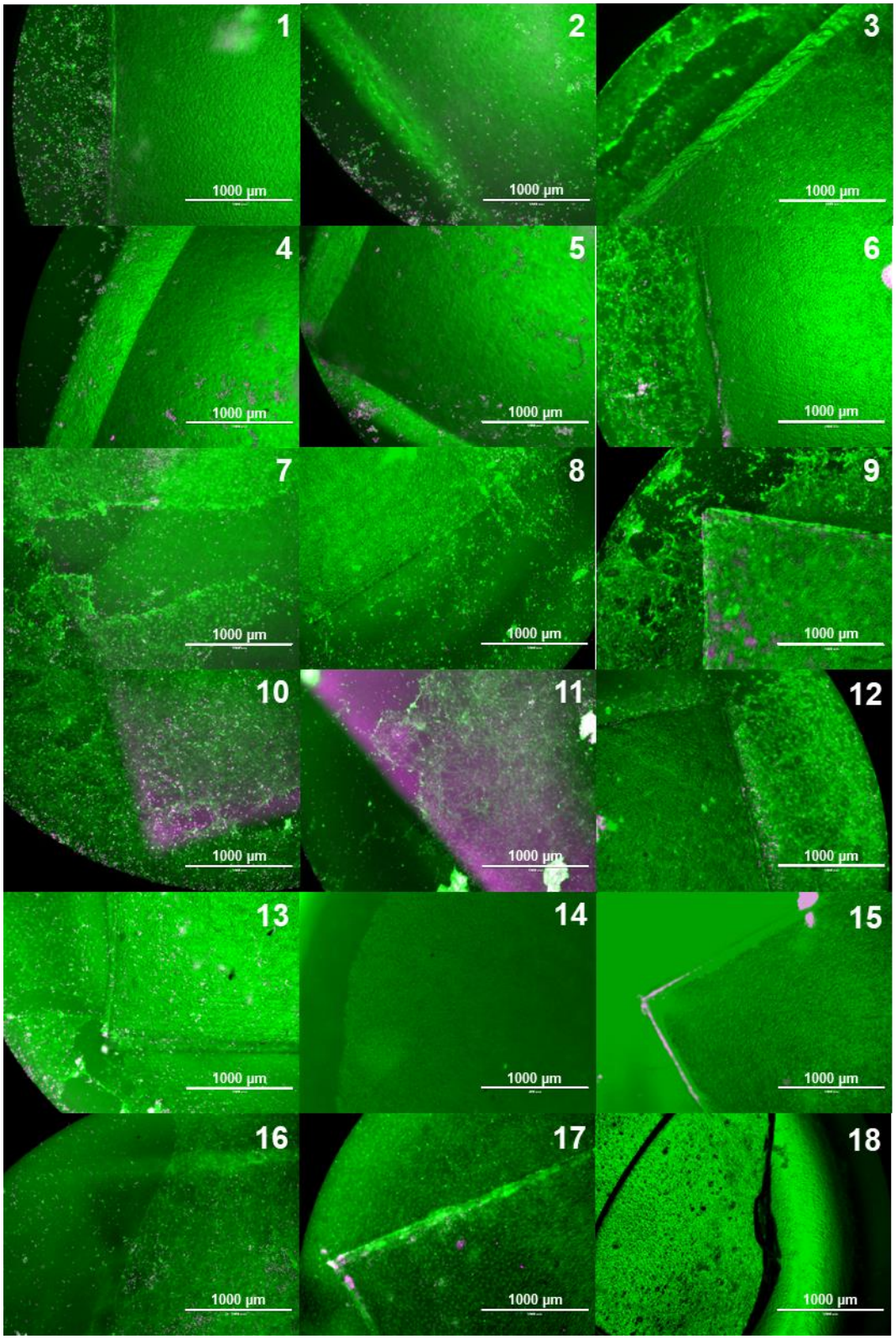

Figure 60 – Images of plate wells containing samples in cell suspension at Day 5 treated with LIVE/DEAD Cell Imaging Kit. Images are an overlap of images taken with GFP and Texas channels at 4x magnification. Numbers correspond to samples as detailed in Figure 58.

Figure 60 displays images of plate wells containing samples and cell suspension. Wells were treated with a LIVE/DEAD Cell Imaging Kit assay which allowed for differentiation between live and dead cells. Green indicates live cells whereas purple indicates dead cells. For all samples, images indicated the vast majority of cells were alive, with very few cells being dead. The intensity of green light for most samples also appears to be concentrated on the sample area, further indicating cell adhesion and proliferation on the sample. Findings presented here indicate the tested samples have good biocompatibility when post-processed using post-curing and continuous solvent extraction methods. They also indicate a range of materials which permit cell adherence to varying degrees. For example, PEG1000PUDMA-based materials may prove suitable for applications where cell growth is desired such as tissue scaffolds and grafts, or where implants are intended for long-term implantation, where biocompatibility of the device with the surrounding tissue is essential. On the other hand, PTHF1000PUDMA-based materials may prove suitable for applications where cell growth is not desired, perhaps in situations where cell adherence could affect intended purpose of a device such as drug delivery, or if the implant is only temporary such as catheters.

5.2.2. Post-processing materials and its effects on drug loading

Whilst the continuous solvent extraction method proved effective in rendering photocured materials biocompatible, it was important to consider how this post-processing step may affect the material in other ways specific to its intended use. In this case, the other factor to be considered is the effect of post-processing on material drug loading. The current dogma for incorporating drug into photocurable materials is through mixing API into the photocurable resin prior to SLA 3D printing. However, if this drug is removed during the post-processing step, either post-processing steps would need to be changed or post-drug loading protocols would need to be developed. The former may not be possible if alternative post-processing steps do not sufficiently reduce the toxicity of resultant materials. To assess the impact of continuous solvent extraction on drug loading, a test was devised. 10 square films (10.0 mm x

10.0 mm, 0.05 mm thickness) were SLA 3D printed using a formulation of PEG1000PUDMA + 20% TEGDA + 1% TPO. 5 of these films contained 3% w/w salicylic acid. The total weight of these 5 drug-loaded films was 0.4810 g. This process was repeated using a formulation of PTHF1000PUDMA + 20% HDDA + 1% TPO. Of these 10, 5 contained 3% w/w salicylic acid, and the weight of these 5 films in total were 0.44184 g. PEG1000PUDMA + 20% TEGDA and PTHF1000PUDMA + 20% HDDA samples were placed into separate glass fibre thimbles which were in turn placed into separate Soxhlet apparatus setups. Continuous extraction with warm acetone proceeded. At 1, 3, 8 and 24-hour timepoints, all of the solvent from each Soxhlet apparatus was collected, concentrated under reduced pressure and diluted to 20 mL with fresh acetone. A sample from this solution was analysed via HPLC to calculate salicylic acid content. Simultaneously, a non-drug loaded film was removed from the glass thimble for each timepoints and dried under high vacuum at 40 °C. Dried samples were subsequently cultured with NIH3T3 cell lines and cell viability was measured after 72 hours.

Figure 61 shows cell viability (%) against samples and cumulative drug release (%) from drug loaded samples over 0, 1, 3, 8 and 24 h. As observed, samples display biocompatibility of above 70% as soon as 1 h after continuous solvent extraction. Unfortunately, both materials exhibit over 100% cumulative drug release at 1 h. This implies that the quantified leachate is not solely salicylic acid, and that further revision of the HPLC method, or use of a different method to quantify salicylic acid release more accurately is required. Nevertheless, only a further 10% additional leachables were detected from 1 to 24 h for both materials (104.67 to 113.10% for PEG1000PUDMA and 115.44 to 125.97% for PTHF1000PUDMA), therefore indicating a significantly large content of salicylic acid is removed during the first hour of extraction. Consequently, this means that whilst this continuous extraction method can render materials biocompatible, the caveat is that drug content is lost. As a result, alternative methods for drug loading SLA 3D printed objects must be explored such as post-loading through immersion in a saturated drug solution.

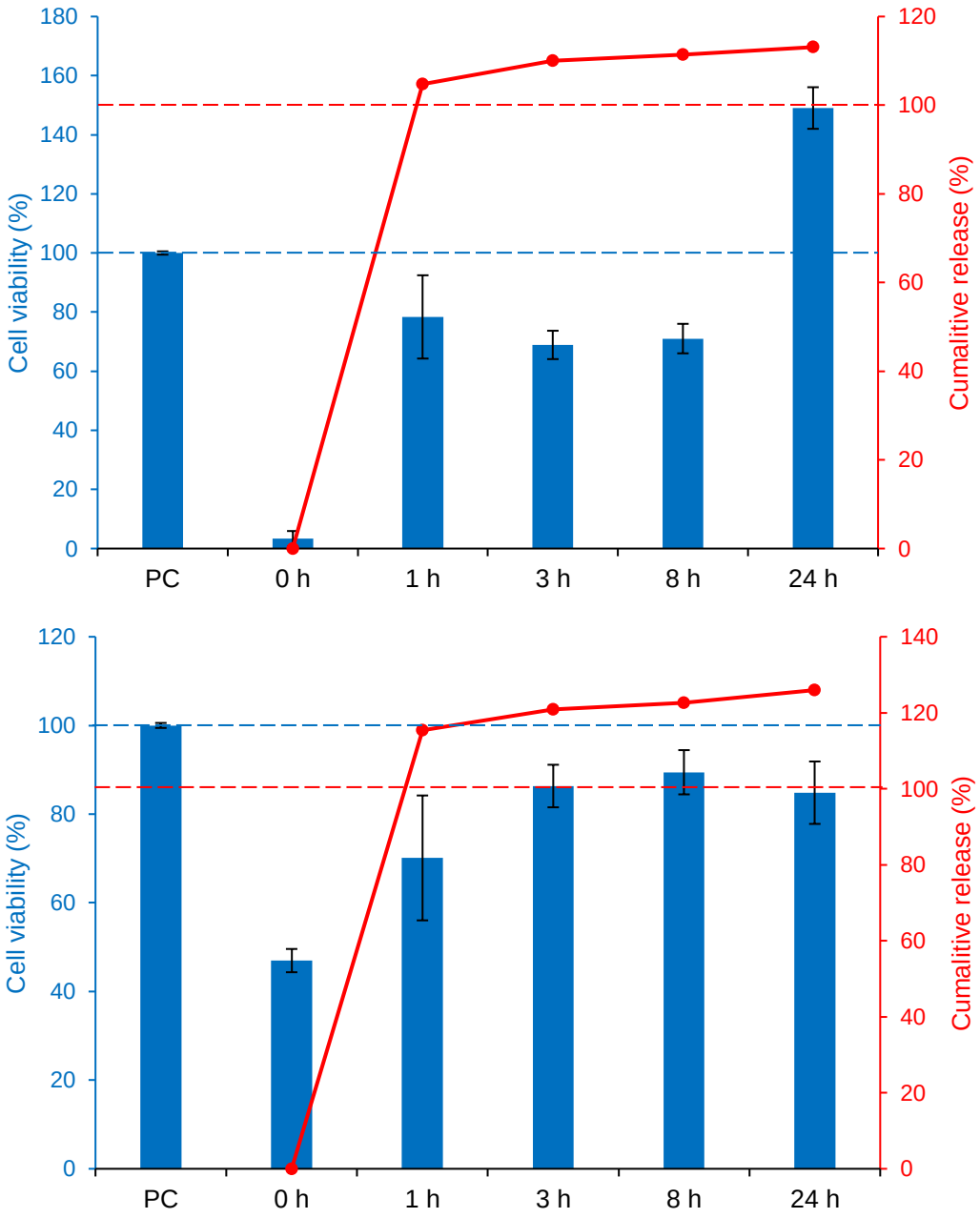

Figure 61 – Column/line chart showing simultaneous cell viability (%, ± 1 SE) and cumulative release of salicylic acid (%) of/from samples continuously extracted with acetone over different time intervals. Positive control (PC) included. Top graph = PEG1000PUDMA + 20% TEGDA + 1% TPO, bottom graph = PTHF1000PUDMA + 20% HDDA + 1% TPO.

5.2.3. Cationic photoinitiator synthesis

Few cationic photoinitiators are commercially available in comparison to radical photoinitiators. Furthermore, ones that are available such as onium salts have spectral limitations within near visible region of light that restricts their applications. This presents a problem as commercial SLA 3D printers such as the Formlabs 1+, Formlabs 2 and MiiCraft+, utilise a 405 nm wavelength (within the visible spectrum) laser or LED for resin curing. It was therefore necessary to explore and acquire cationic photoinitiators with a suitable absorption spectrum.

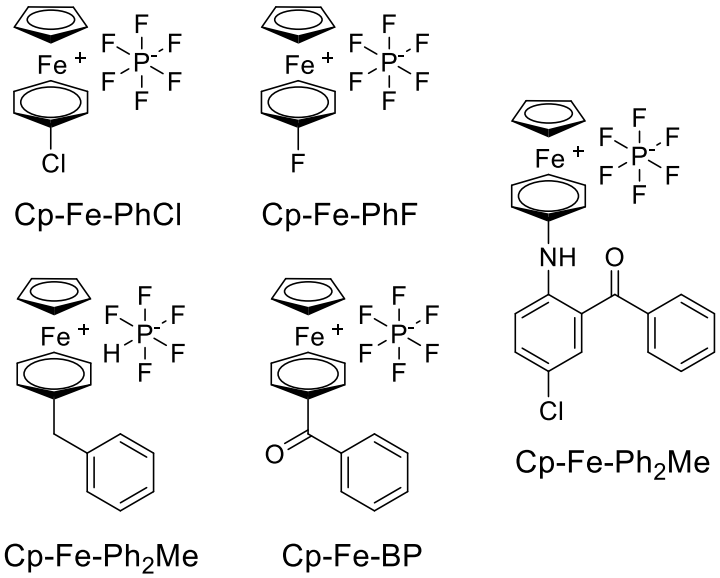

Figure 62 – Chemical structures of ferrocene-based cationic photoinitiators

Figure 62 shows ferrocenium compounds chosen for investigation. Zhang et al. demonstrated ferrocenium compounds containing halogenated arenes are more photoactive than amine-conjugated arenes, and hence (η6-chlorobenzene) (η5-cyclopentadienyl) iron hexafluorophosphate (Cp-Fe-PhCl) and (η6-fluorobenzene) (η5-cyclopentadienyl) iron hexafluorophosphate (Cp-Fe-PhF) were selected as potential candidates[260,261]. (η6-3-benzoyl-4-chlorodiphenylamine) (η5-cyclopentadienyl) iron hexafluorophosphate (Cp-Fe-NBP) and (η6-benzophenone) (η5-cyclopentadienyl) iron hexafluorophosphate (Cp-Fe-BP) were also chosen as both exhibit absorption in the visible light spectrum and

have good efficiency attributed to benzophenone structural moieties[183,184]. Serendipitously, the intermediate to Cp-Fe-BP, (η6-diphenylmethane) (η5-cyclopentadienyl) iron hexafluorophosphate (Cp-Fe-Ph_2Me), displayed greater photoinitiation activity in comparison to Cp-Fe-BP, and was also included for testing.

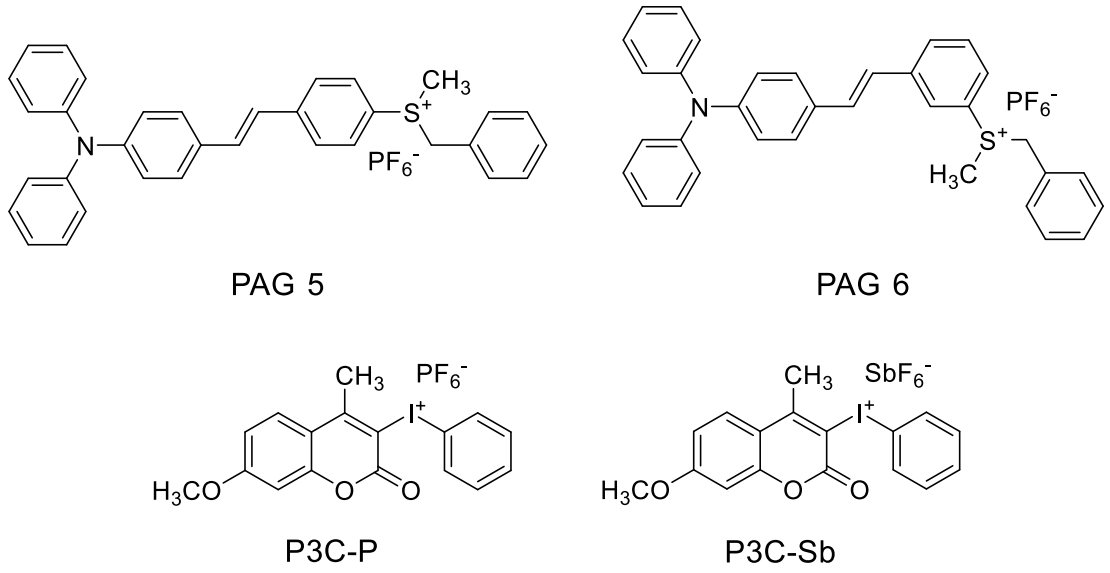

Figure 63 – Chemical structures of sulfonium and iodonium-based cationic photoinitiators

Modification of onium compounds through structural conjugation with multi-ring aromatic or chromophoric moieties and introduction of electron withdrawing groups onto aryl groups, has facilitated broadening and red-shifting of compound absorption spectra without diminishment of cationic initiating activity[260,261]. Jin et al. have reported the design and development of novel sulfonium salts para-Bz (PAG 5) and meta-Bz (PAG 6) that demonstrate moderate and high reactivity as cationic photoinitiators, respectively, and were chosen to be investigated[186,262]. Mokbel et al. investigated two iodonium salts based on a coumarin chromophore, P3C-P and P3C-Sb, as cationic photoinitiators. They observed that both compounds effectively initiate the polymerisation of epoxy- and vinyl ether-based monomers upon exposure to 405 nm wavelength light, with excellent polymerisation profiles recorded[263]. All cationic photoinitiators mentioned were synthesised apart from P3C-P and

P3C-Sb, which were purchased as Sylanto-7MP and Sylanto 7MS, respectively.

The route for synthesis of Cp-Fe-PhCl and Cp-Fe-PhF was adapted from procedures for the preparation of (η^6-aniline) (η^5-cyclopentadienyl) iron hexafluorophosphate and (η^6-2,6-dimethylchlorobenzene) (η^5-cyclopentadienyl) iron hexafluorophosphate[181,264]. Initial product yields (2 – 8%) for Cp-Fe-PhCl and Cp-Fe-PhF were lower than those reported for (η^6-aniline) (η^5-cyclopentadienyl) iron hexafluorophosphate and (η^6-2,6-dimethylchlorobenzene) (η^5-cyclopentadienyl) iron hexafluorophosphate (37.1 and 38 %, respectively). Using toluene instead of diethyl ether for product recrystallisation led to improved product yields (34 – 38 %). ^{1}H and ^{13}C NMR analysis of products corresponded with expected results based on ^{1}H and ^{13}C NMR data for (η^6-aniline) (η^5-cyclopentadienyl) iron hexafluorophosphate and (η^6-2,6-dimethylchlorobenzene) (η^5-cyclopentadienyl) iron hexafluorophosphate, and starting materials ferrocene, chlorobenzene and fluorobenzene. MS analysis corresponded with the theoretical cation molecular weight for both compounds and IR analysis confirmed the PF_6 counter-anion. All other ferrocenium salts were prepared according to their associated literature. The product yield for Cp-Fe-NBP was 41%, whereas the literature reports an 80% yield. This low yield was attributed to loss of product due to an extensive washing protocol to remove DMF. The associated literature did not provide ^{1}H or ^{13}C NMR data for this compound. ^{1}H and ^{13}C NMR analysis of the product corresponded with expected results based on ^{1}H and ^{13}C NMR data for similar compounds reported by Pearson et al.[265] and Abd-el-aziz et al.[264,266], and starting materials Cp-Fe-PhCl and 3-benzoyl-4-chlorodiphenylamine. MS analysis corresponded with the theoretical cation molecular weight for the compound and IR analysis confirmed the PF_6 counter-anion. Product yield for Cp-Fe-Ph_2Me was 25%, whereas literature reported a yield of 29%. ^{1}H NMR and IR analysis of the product corresponded with ^{1}H NMR and IR data reported by literature. MS analysis corresponded with the theoretical cation molecular weight for the compound. Product yield for Cp-Fe-BP was 12%, whereas literature reported a yield of 21%. ^{1}H NMR analysis revealed mostly unchanged Cp-Fe-Ph_2Me, with only a small quantity of Cp-

Fe-BP present. IR analysis confirmed the PF_6^- counter-anion, however the peak corresponding to the benzophenone C=O group was not observable. MS analysis confirmed Cp-Fe-Ph_2Me was the major component of the mixture and Cp-Fe-BP was the minor. It can be speculated that the reaction of the diphenylmethane complex with aqueous potassium permanganate was incomplete and, if revisited, a revision of this step is required.

Sulfonium salts PAG 5 and PAG 6 were prepared according to literature published by Jin et al.[186,262]. Starting material 4-(*N,N-diphenyl*)aminestyrene was synthesised according to literature published by Zhou et al.[185]. Product yield was 87% which was in accordance with the 89% yield reported by the literature. ^{1}H NMR and IR analysis of product corresponded with ^{1}H NMR and IR data reported by literature. Additional ^{13}C NMR analysis further confirmed the successful synthesis of the compound. 4-(Benzylthio)-4'-bromobenzene and (E)-4-(*N,N-diphenyl*)amine-4'-benzylthiostilbene, the first two intermediates in the PAG 5 synthesis protocol were afforded in yields of 49% and 35%, respectively.^{1}H and ^{13}C NMR analysis of products corresponded with ^{1}H and ^{13}C data reported by literature. 3-(Benzylthio)-4'-bromobenzene and (E)-4-(*N,N*-diphenyl)amine-3'-benzylthiostilbene, the first two intermediates in the PAG 6 synthesis protocol were obtained in yields of 58% and 34%, respectively.^{1}H and ^{13}C NMR analysis of products corresponded with ^{1}H and ^{13}C data reported by literature. Yields for the triflate salts of PAG 5 and PAG 6 were 68% and 77%. Furthermore, ^{1}H and ^{13}C NMR analysis of both compounds was obscure and of poor resolution. Despite loose comparability with literature ^{1}H and ^{13}C data, the success of compound synthesis was ambiguous. Higher than reported yields and unclear NMR data indicate several impurities are present in compound samples. Yields for hexafluorophosphate salts of PAG 5 and PAG 6 were 38% and 48%, respectively, lower than reported Zhou et al. (2002) (83% and 77%)[187]. Low yields were likely due to product loss from multiple filtration, redissolution and precipitation steps but may be associated to presence of impurities. Again, ^{1}H and ^{13}C NMR analysis of both compounds was obscure and compound validation was inconclusive. MS analysis confirmed both compounds were complex mixtures containing product and impurities. Nonetheless, all

photoinitiator products were tested for photoactivity within formulations of a cheap and readily available vinyl ether-based monomer, tri(ethylene glycol) divinyl ether (TEGDVE). Subsequent data is cautiously appraised on account of ambiguity regarding compound purities.

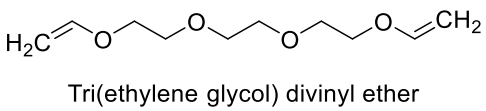

Tri(ethylene glycol) divinyl ether

Figure 64 – Chemical structure of tri(ethylene glycol) divinyl ether (TEGDVE)

5.2.4. RT-FTIR analysis of cationic photoinitiators

Photoactivity of photoinitiators was analysed using real-time FTIR spectroscopy. A thin layer of photoinitiator-containing formulation (30 µL) was directly deposited onto the FTIR optical window. A single spectrum, in absorbance mode, of the material was acquired at this point for use as a baseline. The material was subsequently irradiated with light from a collimated 405 nm LED light source at an intensity of 100 mW/cm^2. This intensity was chosen as similarly high intensities were used for analysis of cationic photoinitiator photoactivity in literature[183,184,261–263].

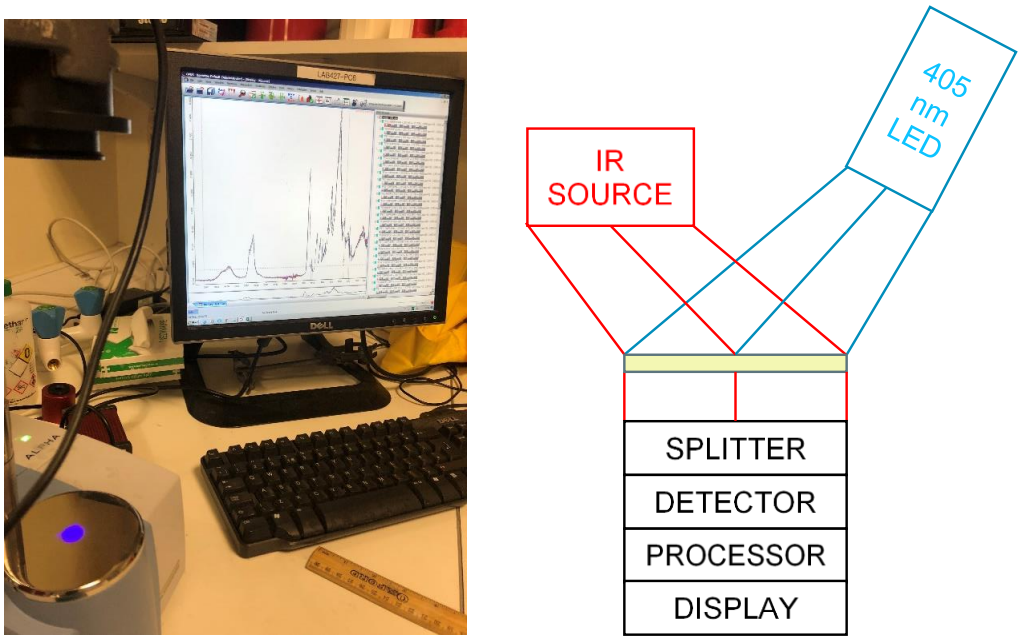

Figure 65 – Images showing actual and conceptual RT-FTIR setups

50 spectra were acquired consecutively with 1 seconds between scan times at 4000 and 400 cm^{-1}, resolution of 4 cm^{-1} and a sample and background scan time of 4 scans. This in combination meant there was approximately 5 – 7 seconds between each generated spectrum. As tri(ethylene glycol) divinyl ether homopolymerises, the content of C=C vinyl groups within the material are depleted, which can be visualised by the reduction of spectral peaks corresponding to C=C vinyl groups at 1637 cm^{-1} and 810 cm^{-1}. Peaks from each spectrum can be integrated to allow quantitative analysis of double-bond conversion (DBC) at certain timepoints. DBC (%) was calculated for each spectrum as follows:

$$\text{DBC (\%)} = \left(1 - \frac{\text{AUC}_x}{\text{AUC}_0}\right) \times 100$$

where AUC_0 is the calculated integral (area under the curve) of chosen peak for the first spectra (no light source) and AUC_x is the calculated area under the curve/peak either peak 1637 cm^{-1} or 810 cm^{-1} for spectra $x^{267–270}$.

Figure 66 displays graphs plotting mean DBC (%) values plotted against irradiation time for ferrocene cationic photoinitiator containing formulations. As is evident, plots generated via integration of the 810 cm^{-1} spectral peak consistently report a lower DBC at all points for all formulations. This is attributed to overlapping spectral peaks that result in non-precise integration of the 810 cm^{-1} peak. Formulations containing Cp-Fe-Cl (Figure 66, graph **a**) show less than 10% DBC after 10 minutes irradiation. This was unexpected, with literature indicating Cp-Fe-Cl has a higher photoactivity than Cp-Fe-F (Figure 66, graph **b**) which reached 70 – 90 % DBC after 300 s. This observation was attributed to the light source used. Zhang et al. (2016) utilise an uncollimated 405 nm LED light source when testing Cp-Fe-Cl and Cp-Fe-F containing formulations[261]. An uncollimated light source has a broader emission spectrum, and hence it is speculated Cp-Fe-Cl has a greater molar extinction coefficient (a measure of light absorption) over this wavelength range, hence displaying greater photoactivity than Cp-Fe-F when irradiated with this light source. Conversely, when irradiated with a collimated 405 nm

light source with a narrower emission spectrum, Cp-Fe-F exhibits a greater molar extinction coefficient and hence displays greater photoactivity in comparison to Cp-Fe-Cl. Low and delayed DBC for Cp-Fe-BP and Cp-Fe-Ph_2Me was similarly attributed to the collimated versus non-collimated phenomenon, with both compounds displaying a low absorption of light at 405 nm, and low photoactivity in general.

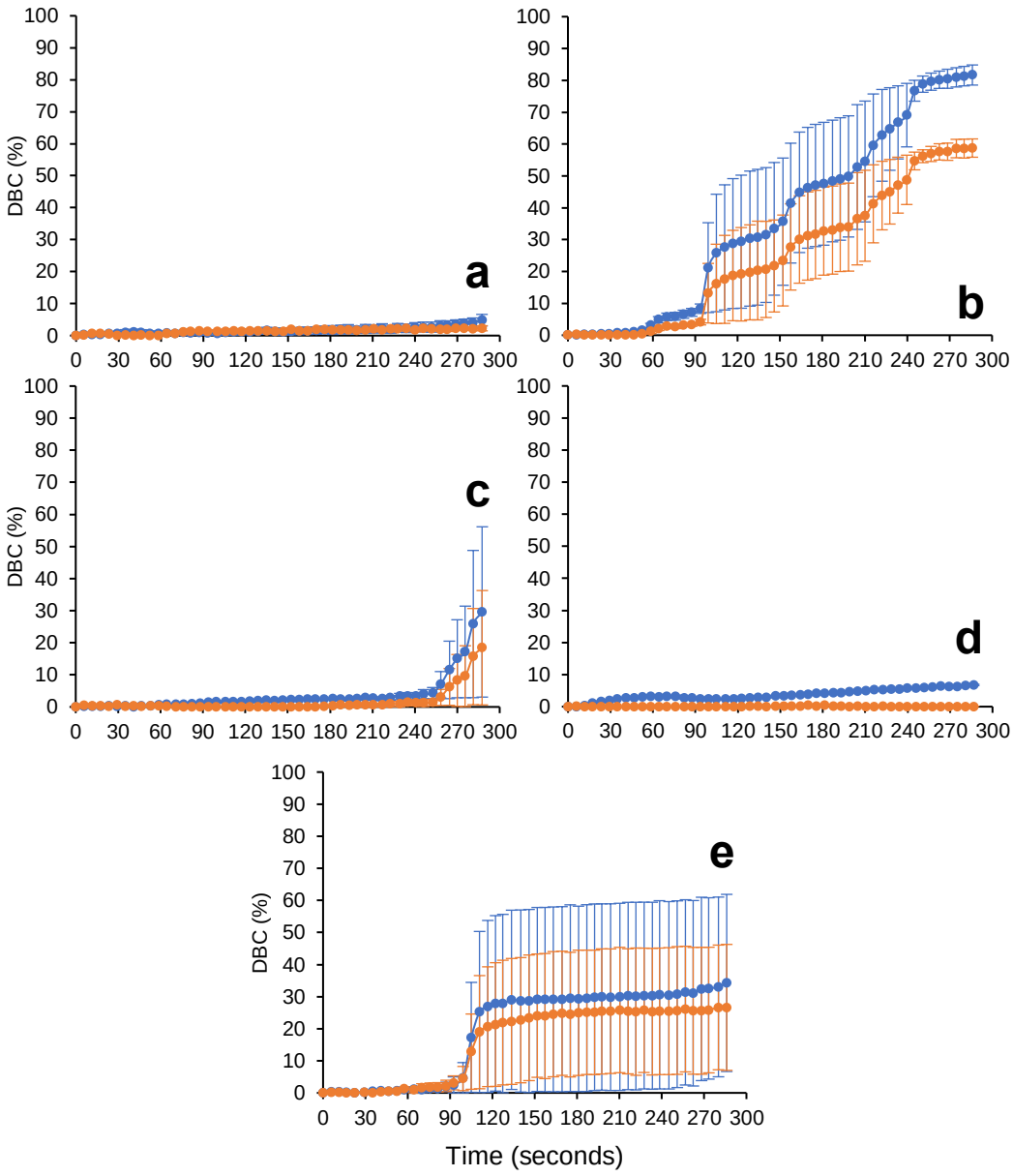

Figure 66 – Graphs plotting mean DBC (%) against irradiation time for ferrocenium cationic photoinitiator containing TEGDVE formulations. 1637 cm^{-1} (–) and 810 cm^{-1} (–). **a** = 3% w/w Cp-Fe-Cl, **b** = 3% w/w Cp-Fe-F, **c** = 3% w/w Cp-Fe-Ph_2Me, **d** = 3% w/w Cp-Fe-BP and **e** = 3% w/w Cp-Fe-NBP.

Cp-Fe-Ph_2Me showed greater photoactivity in comparison to Cp-Fe-BP, as highlighted in literature.

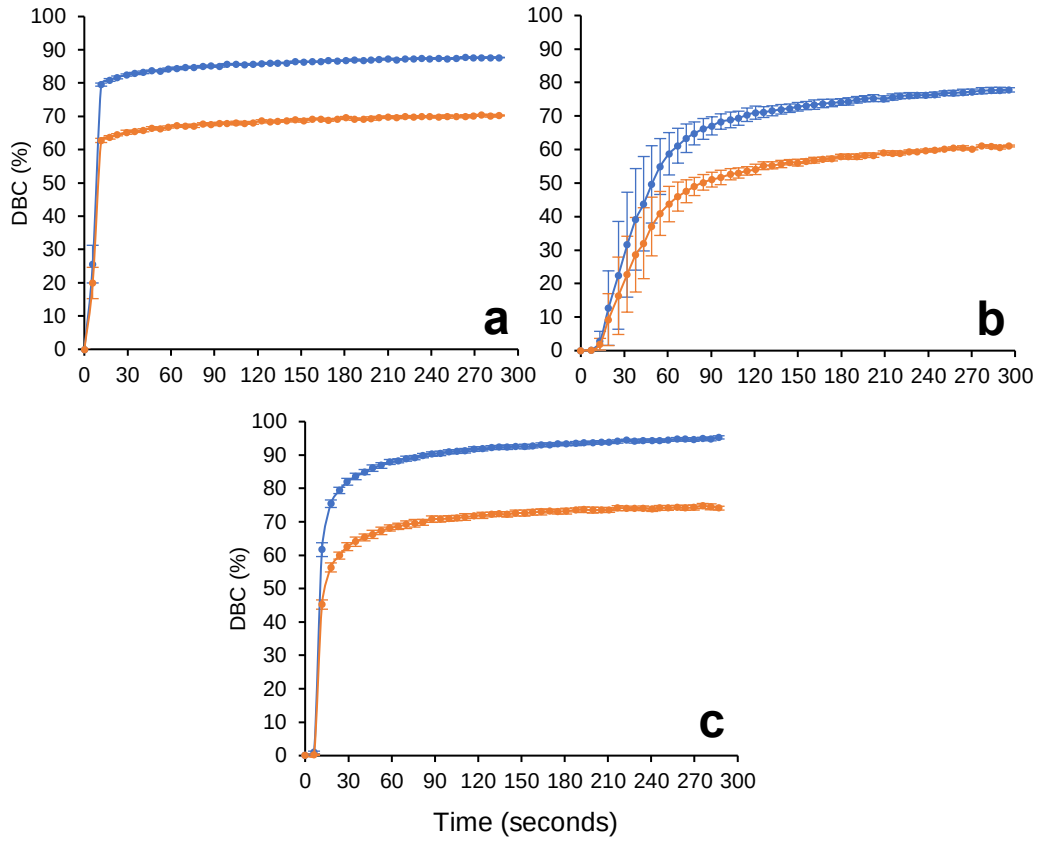

Figure 67 – Graphs plotting mean DBC (%) against irradiation time for onium cationic photoinitiator containing TEGDVE formulations. 1637 cm^{-1} (–) and 810 cm^{-1} (–). **a** = 1% w/w PAG 5, **b** = 1% w/w PAG 6, **c** = 1% w/w P3C-P.

Figure 67 displays graphs plotting mean DBC (%) values plotted against irradiation time for onium cationic photoinitiator containing formulations. P3C-Sb was not used due to insolubility in TEGDVE, attributed to the antimonate cation. In contrast to ferrocenium cationic photoinitiators, formulations containing onium cationic photoinitiators do not present a significant induction period (< 10 sec) and reach 50% DBC at times below 60 sec. PAG 6 containing formulations exhibits the poorest photoactivity out of the three onium compounds tested, with significant variation between samples. Jin et al. note that PAG 5 has a maximum absorption peak (λ_{max}) and ε_{max} at 397 nm and 34400 $M^{-1}cm^{-1}$, respectively, whereas PAG 6 has a λ_{max} and ε_{max} at 379 nm and 25200 $M^{-1}cm^{-1}$, respectively[262]. This may explain why PAG 5 displays a

slightly improved photoactivity when irradiated with a 405 nm collimated light source, in comparison to PAG 6. Surprisingly, P3C-P formulations display similar photoactivity at 405 nm, albeit with a slightly larger induction period, despite much lower ε values at 405 nm than sulfonium compounds PAG 5 and PAG 6. Interestingly, the authors found P3C-P had similar photo-efficiency to ferrocenium salt, [(1,2,3,4,4a,8a-η)-naphthalene](1,2,3,4,5-η)-2,4-cyclopentadien-1-yl]-iron hexafluorophosphate, suggesting ferrocenium salts may yet be useful within 3D printing applications[263].

5.3. Conclusions and Future Work

Through a process of post-curing at an elevated temperature, followed by continuous extraction with warm acetone in Soxhlet apparatus for 24 hours, and finally drying in a vacuum, polyurethane dimethacrylate-based materials were rendered biocompatible, which was verified through cell viability studies. The ability to produce biocompatible SLA 3D printed parts overcomes a huge hurdle that previously prevented or limited the use of SLA 3D printing for implantable devices and other medical applications that require absolute non-toxicity. Furthermore, “cleaned” samples permitted surface adhesion of fibroblasts, which potentially broaden their range of applications to areas such as tissue engineering. A potential continuation of this work would be to investigate the long term (weeks, months) biocompatibility of post-processed (meth)acrylate-based parts, as eventual hydrolytic degradation of materials, yielding polyacids, could pose a toxicity risk. Furthermore, the discussed post-processing method resulted in removal of material drug loading, and hence another extension of this work could take the form of exploring alternative post-processing methods for yielding material biocompatibility, without affecting drug loading, or exploring methods for incorporating drug into materials after post-processing.

In addition to rendering polyurethane dimethacrylate materials biocompatible, a range of cationic photoinitiator that operate in the near UV light spectrum were successfully prepared. From these, 3 compounds, PAG 5, PAG 6 and P3C-P were identified as suitably photoactive cationic photoinitiators that could find potential use within photocurable materials for a range of commercial SLA 3D printers. If cationic photopolymer systems prove compatible with SLA technology, future work could look to explore and develop epoxide and/or vinyl-ether based monomers/macromers for use as photocurable systems. Furthermore, exploration and development of novel synthetic routes to vinyl ester, carbonate and carbamate-based monomers/macromers could prove a worthy endeavour, yielding 3D printable radical photopolymer systems with theoretical long term biocompatibility.

6. Adapting a SLA 3D printer to fabricate drug-eluting materials

6.1. Introduction

Stereolithography (SLA) was first introduced in 1988 by 3D Systems Inc[114]. Stereolithography is based on light source facilitated (usually UV-emitting lasers), by spatially controlled crosslinking and solidification of liquid resin by photopolymerisation. An advantage of the SLA method is a high spatial resolution (10-50 µm) afforded by the spot size of a focussed laser beam[108].

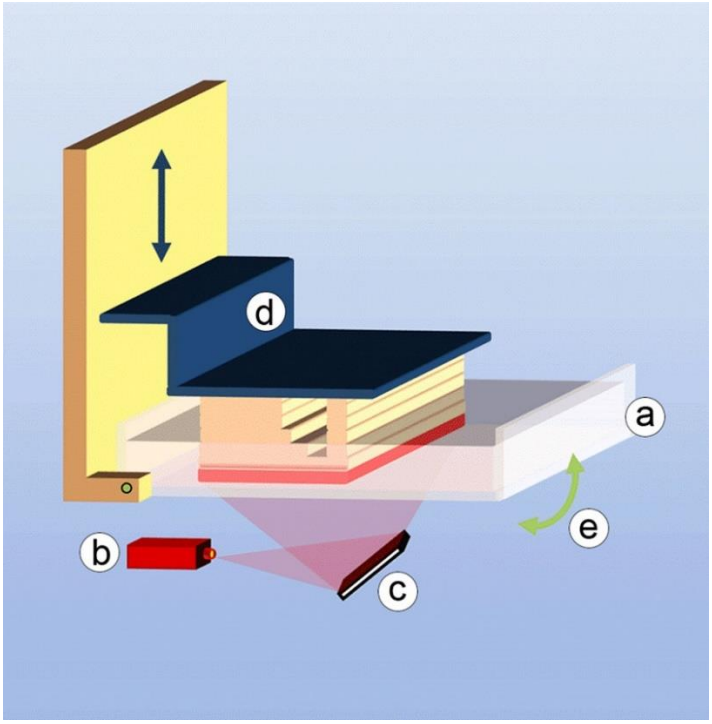

Figure 68 – Digital light processing (DLP) consisting of (a) vat filled with photopolymer resin, (b) light source, (c) micromirror array, (d) vertically movable building platform, and (e) tilting device to replenish the uncured bottom layer. Reproduced from Ligon et al. (2017)[108].

With conventional SLA methods light exposure is performed sequentially by laser beam scanning within the plane on the surface of photosensitive material. The x-y orientation of the laser beam is controlled by a pair of mirrors

within a galvanoscanner. The SLA printing process is executed in a layer by layer manner, with each individual layer expressed as a separate set of coordinates that define tilt angles of the two mirrors, guiding the position of the laser beam along the plane. Every pixel within a layer is irradiated sequentially.

Digital light processing (DLP), an adapted SLA method, instead utilises a selectively masked light source as opposed to a pixel-by-pixel approach, curing entire layers of resin at a time, hence considerably reducing build times[196]. Furthermore, continuous direct light processing (CLIP), a more recent development, is very similar to DLP. In this method, the build plate moves continuously in the z-axis, further improving print times[107]. After the first layer, the platform is moved away allowing the built layer to be recoated with liquid resin and the process cycles until the final object is formed. Layer adherence to the build platform and previous layers requires over-curing in the z-axis. Photoinitiator type and quantity and light penetration depth, altered through exposure dose (light intensity and illumination time) and light absorber additives, are elements that must be fine-tuned to ensure sufficient over-curing without diminished vertical resolution. Excess resin is drained and washed off and the object is further irradiated with UV light to ensure maximal conversion of unreacted monomers thus improving biocompatibility and mechanical properties[196]. Bottom-up approaches, meaning the print platform moves from bottom to top, are increasingly applied in SLA, affording several advantages over top-down systems. Advantages include eliminating the need for structure recoating, the illuminated surface is always smooth, less amounts of resin are required and the illuminated layer is not exposed to oxygen – a known inhibitor of radical-based photopolymerisation[108,196].

The main limitations of the stereolithography method arise from the limited number of commercially available resins suitable for the process. However, the properties of parts built with SLA are improving, extending their use beyond rapid prototyping to manufacture of functional parts for varying end-use applications. The manufacturing speed these methods afford can facilitate rapid fabrication of personalised drug delivery systems at the point of care. The high accuracy and resolution of SLA and DLP printed structures provide

an attractive approach for preparation of surgical implants and drug delivery systems with complex 3D inner structures. It is noteworthy that UV light, as opposed to heat melting, shows no significant degradation of additives such as thermolabile APIs during processing[109]. Resins that imbue cured parts with biodegradable properties have found applications within medicine[196]. Most available 3D printable resins are based on low molecular weight (< 2000 Da) multi-functional monomers[114], which produce highly crosslinked, glassy, rigid and brittle materials. Few resins offer elastomeric material properties. Those that do include macromers of high molecular weights that require dilution with (non-)reactive diluents such as isobornyl acrylate and water, to provide SLA compatibility. Despite the number of available resins increasing, the technique is limited to use of a single resin at one time hence multi-material SLA objects are yet to be fully realised[196].

Another limitation with the stereolithography process, is the somewhat limited printing parameters offered by commercial SLA 3D printers. For example, during the “mini-project”, attempts were made to print with a formulation containing Formlabs Flexible FLGR01 (FLFLGR01) resin and 1% w/w copper chloride. Despite the use of different pre-set print settings it was not possible to 3D print objects using the ($CuCl_2 \cdot 2H_2O$) containing resin. Print failure was associated with available printing parameter configurations being unsuitable for object construction using a ($CuCl_2 \cdot 2H_2O$) containing FLFLGR01 resin. It was speculated that ($CuCl_2 \cdot 2H_2O$) may act as a photo-absorber which prevents sufficient photopolymerisation of the layer of pre-defined depth with the printing parameter configurations offered by Formlabs Form 1+ SLA 3D printer software. An explanation for how this led to print failure can be deduced through consideration of equations developed by Jacobs dictating the SLA process[271]. For SLA, the critical light exposure E_c to cause gelation of a photoresin can be defined as;

$$E_c = E_0 \exp\left(-\frac{C_d}{D_p}\right),$$

where E_0 is the light exposure dose at the photopolymer surface, C_d is the curing depth and D_p is the penetration depth (or layer height) as defined by;

$$D_p = 1/(2.3\varepsilon[I])$$

which assumes light absorption is solely dependent of photoinitiator concentration [I] and molar extinction coefficient (ε). Though the strength and modulus of a polymer at gelation is too low to survive the SLA build process. To compensate, Jacobs defines the excess energy (E_x) required to sufficiently cross-link photopolymer with adequate physical strength to withstand the SLA process – referred to as “green” strength – as;

$$E_x = E_c(D_p/C_d)\left(\exp\left(\frac{C_d}{D_p}\text{-}1\right)\text{-}1\right)$$

Excess energy is directly proportional to the critical exposure dose for gelation and inversely proportional to the cure depth[108,271]. This means “green” strength can be achieved and/or improved by increasing energy dosage or by lowering layer height. However, as cure depth is directly proportional to layer height, the addition of a photoabsorber such as ($CuCl_2 \cdot 2H_2O$) will lead to a reduced layer height. The Formlabs Form 1+ SLA 3D printer software has a pre-set print setting for FLFLGR01 resin with variable layer height options. For each layer height option the exposure dose is fine-tuned for the FLFLGR01 resin to ensure curing of layers with sufficient “green” strength and successful layer-to-layer adhesion without excessive “over-curing” and loss of resolution. The addition of ($CuCl_2 \cdot 2H_2O$) disrupts this balance with consequential cure depth reduction, layer thinning, failed layer-to-layer adhesion and ultimately a failed print. The obvious solution to this situation is to increase the exposure dose, in an empirical fashion until the balance is re-established. However, Formlabs Form 1+ SLA 3D printer software restricts adjustment of exposure dose, and therefore printing with ($CuCl_2 \cdot 2H_2O$) containing FLFLGR01 resin was not possible. Nevertheless, other SLA 3D printers allow extensive customisation of print settings. For example, the MiiCraft+ SLA 3D printer allows the user to define exposure time per layer (analogous to exposure dose) among a host of

other settings, that can capacitate successful 3D printing using ($CuCl_2 \cdot 2H_2O$) containing FLFLGR01 resin and other photopolymer systems[272].

Within this chapter, a method for adapting the Formlabs Form 1+ to facilitate printing of multiple materials, in low volumes, is detailed. Furthermore, a RT-FTIR spectroscopy tool is developed and utilised to identify required photoinhibitor content to yield a photopolymer formulation compatible with the Formlabs Form 1+. Options for improvement of this tool are also explored and discussed. Subsequently, drug loaded samples were printed from a range of different photocurable formulations, and subsequent release of drug was measured over a period of 4 weeks, to determine material, drug and design-dependent release kinetics.

6.2. Results and discussion

6.2.1. Adapting the Formlabs Form 1+ and Form 2 SLA 3D printers

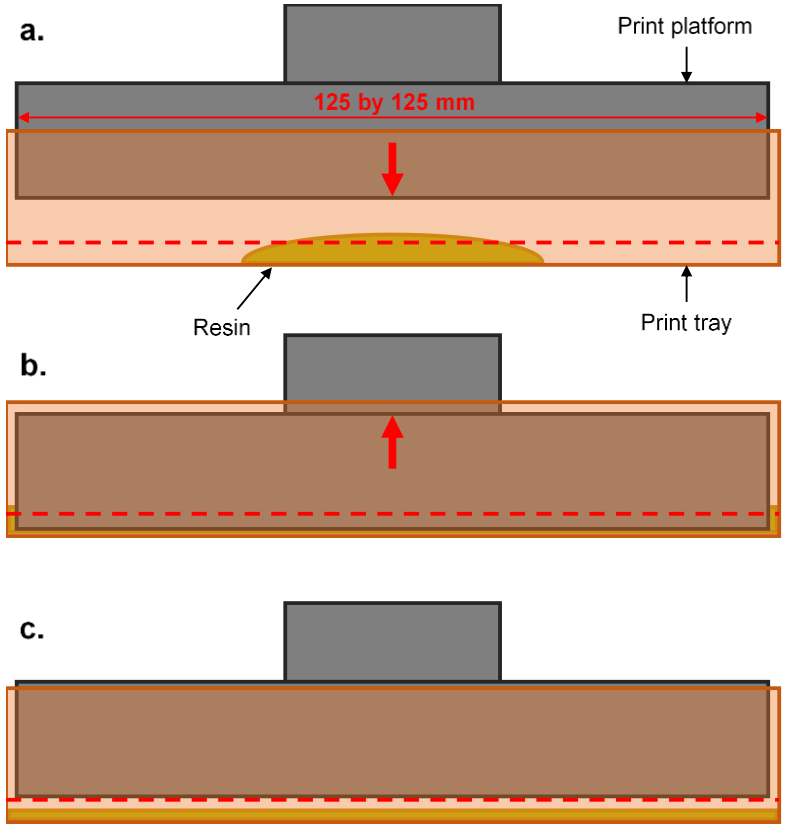

Figure 69 – Illustration depicting the concept of resin levelling on the Formlabs Form 1+ SLA 3D printer

As previously discussed, there are several limitations that hinder the use of custom resin printing with most commercial 3D printers, including the Formlabs Form 1+ and Form 2 SLA 3D printers. Certain limitations pertain to the hardware of both Formlabs, where proprietary print trays require large excess of resins for printing of small objects and only a single resin can be used per print. Considering the former, Formlabs recommend that their Form 1+ resin tank be filled up to the maximum fill line, equating to 200 mL of resin. This does not present an issue when printing with Formlabs materials in plentiful supply. However, when printing with experimental custom resin formulations of low quantity, preparing 200 mL is impractical and costly. Print success is not guaranteed with experimental formulations. Hence preparing a

large amount of a custom resin for a small print that is unsuccessful leads to a potential costly waste of material. Furthermore, even if printing is successful, the excess material may be unusable for future experimental printing if it contains a complex mixture of additives or has a short expiration.

Figure 69 illustrates the dilemma of 3D printing with small volumes on the Form 1+ SLA 3D printer using proprietary print platforms and trays. Red dashed lines indicate the minimum level of resin required to print a theoretical small object. The initial movement of the print platform lowers it until it touches the resin tray surface (Figure 69a.). This results in resin being pushed outwards and up the sides of the platform (Figure 69b.). The platform then raises one layer in the z-direction, allowing resin to redistribute over the resin tray surface (Figure 69c). With a small amount of resin this process can lead to either all or parts of the resin tray being insufficiently covered with resin to allow print success. In practice, it has been possible to print small objects with a low amount of resin (approx. 30 mL resin) with the standard Form 1+ setup.

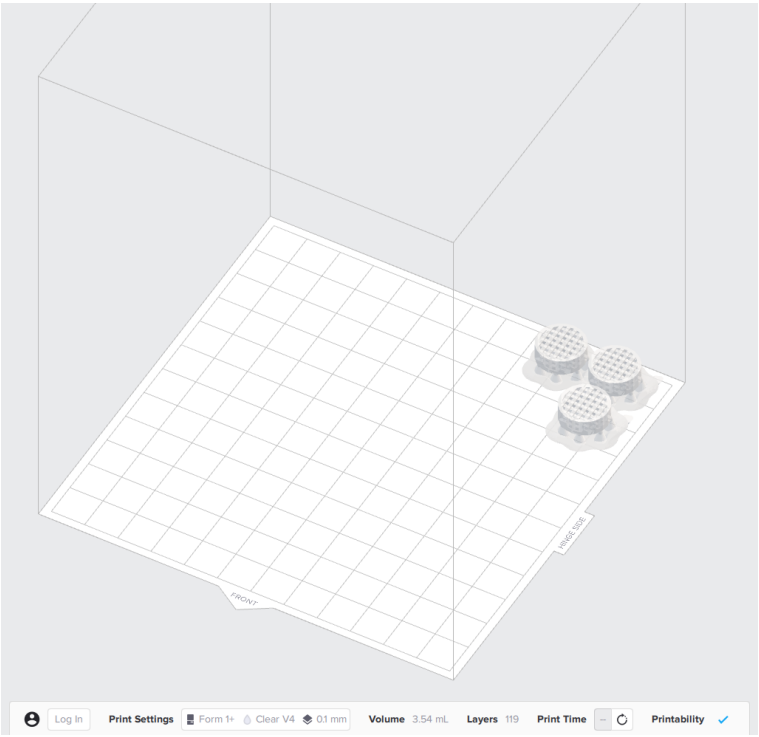

Figure 70 – Screenshot of print layout required for printing of objects with low resin volumes.

This is due to the natural pooling of resin towards the top hinge side corner during object peeling, and therefore prints are strategically positioned towards this corner using PreForm software (see Figure 70). This, however, still presents a number of problems. Firstly, only a limited number of objects can be positioned to print near the hinge side corner, preventing the utilisation of the entire print platform. Secondly, positioning prints near the top hinge side corner meant prints experienced significant z-displacement and subsequent resin drag during peeling between layers, which often resulted in prints detaching from the platform during peeling, especially with high viscosity resins. Finally, approximately 30 mL resin to print objects that require approximately 5 mL of resin still represents a large excess of resin.

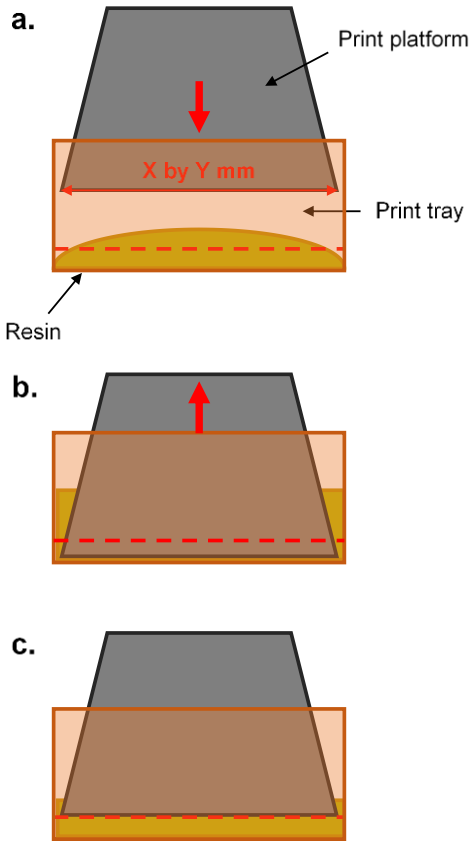

Figure 71 – Illustration depicting the concept of an adapted print platform and tray setup and subsequent resin levelling on the Formlabs Form 1+ SLA 3D printer

Figure 71 illustrates the concept of an adapted print platform and tray setup. The x-y dimensions of the custom print platform print interface (the surface upon which the printed object adheres to – henceforth referred to as printhead) are 6 mm, in both dimensions which is larger than the object (+ supports) to be printed. Resin displacement and redistribution during resin levelling is commensurate with the print platform area and hence a smaller area results in less resin dispersion, reducing “non-relevant” resin redistribution over areas of the print platform not involved in printing.

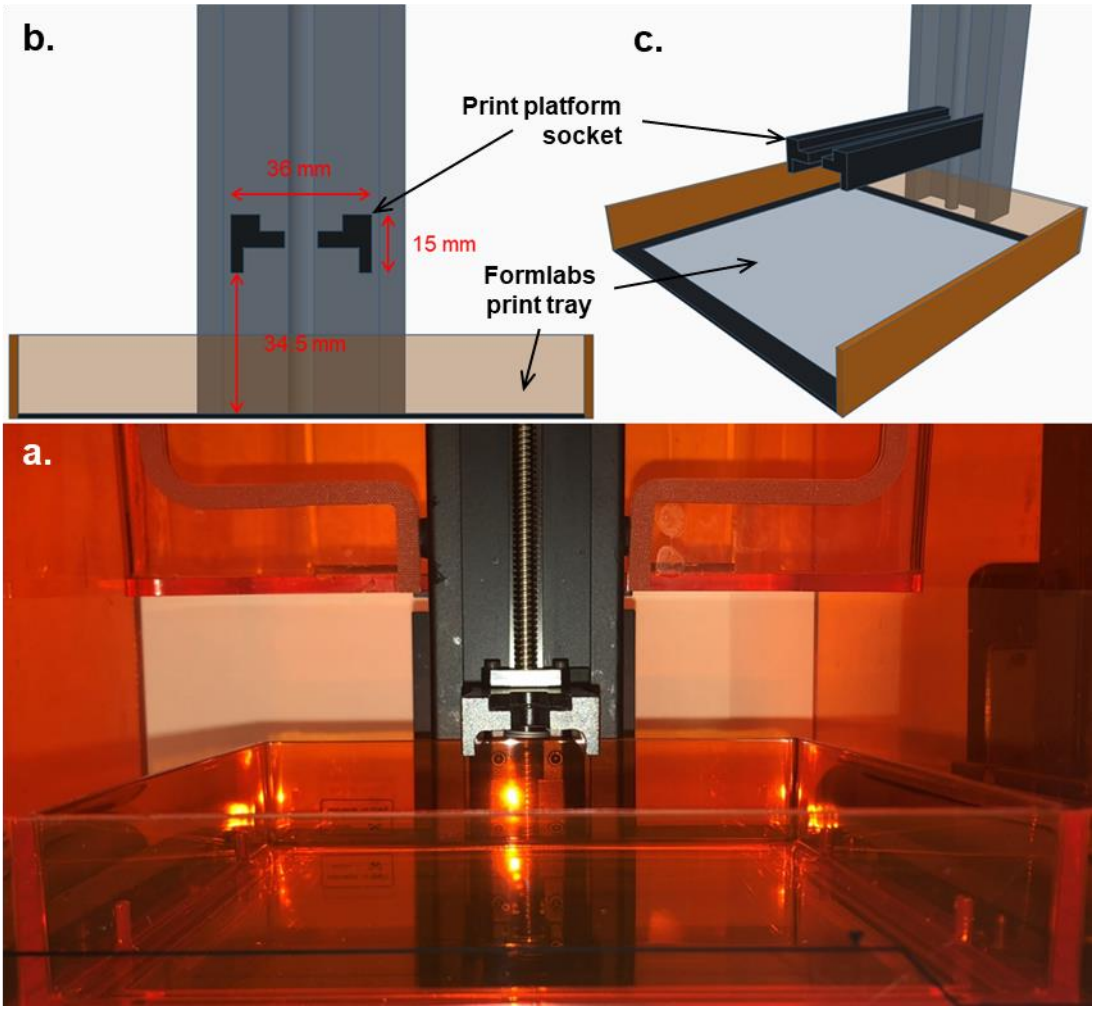

Figure 72 – Illustration highlighting key dimensions of Formlabs Form 1+ SLA 3D printer: **a.** shows printer with print platform socket in its start position **b.** and **c.** show dimensions of print platform socket and its z-distance from the print tray surface.

Furthermore, the inner x-y dimensions of the custom print tray/well are only 6 mm larger than the x-y dimensions of the print head, reducing “non-relevant” resin redistribution during resin levelling. To prevent resin overflow of print wells, the y-dimension of the print platform was slanted. The absolute x-y-z dimensions of a tensile test sample were 15 x 50 x 3 mm. The ideal printing orientation involved printing three tensile test samples on their sides. Including supports, the x-y dimensions of three tensile test samples were 19 x 54 mm and consequently the x-y dimensions of each printhead were 25 x 60 mm. The print platform was built with three printheads to ensure full use of the available print area. The inner dimensions of a single printing well were 31 x 66 mm. The print tray contained three printing wells to match the print platform.

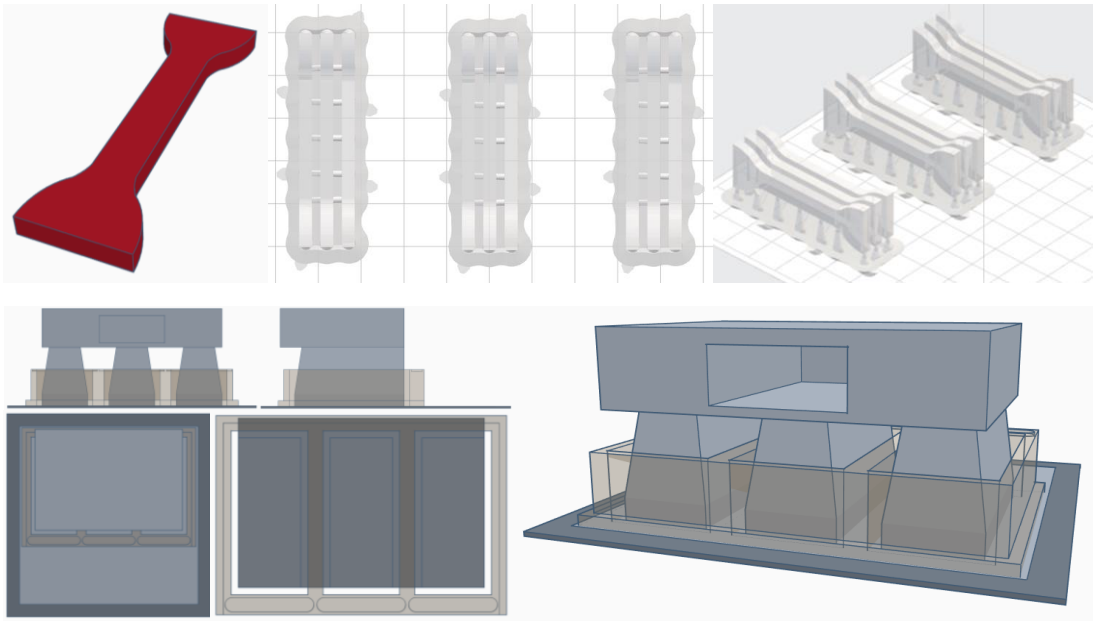

Figure 73 – Top; Tinkercad and PreForm generated images showing tensile test sample design and printing orientations with supports. Bottom; Tinkercad images showing adapted print platform and tray setup for printing of tensile test samples

The print platform was printed on an Ultimaker 3 FFF 3D printer using black poly(lactic acid) (PLA) filament (Figure 74). FFF 3D printing was favoured over SLA 3D printing as it allows for control over object infill.

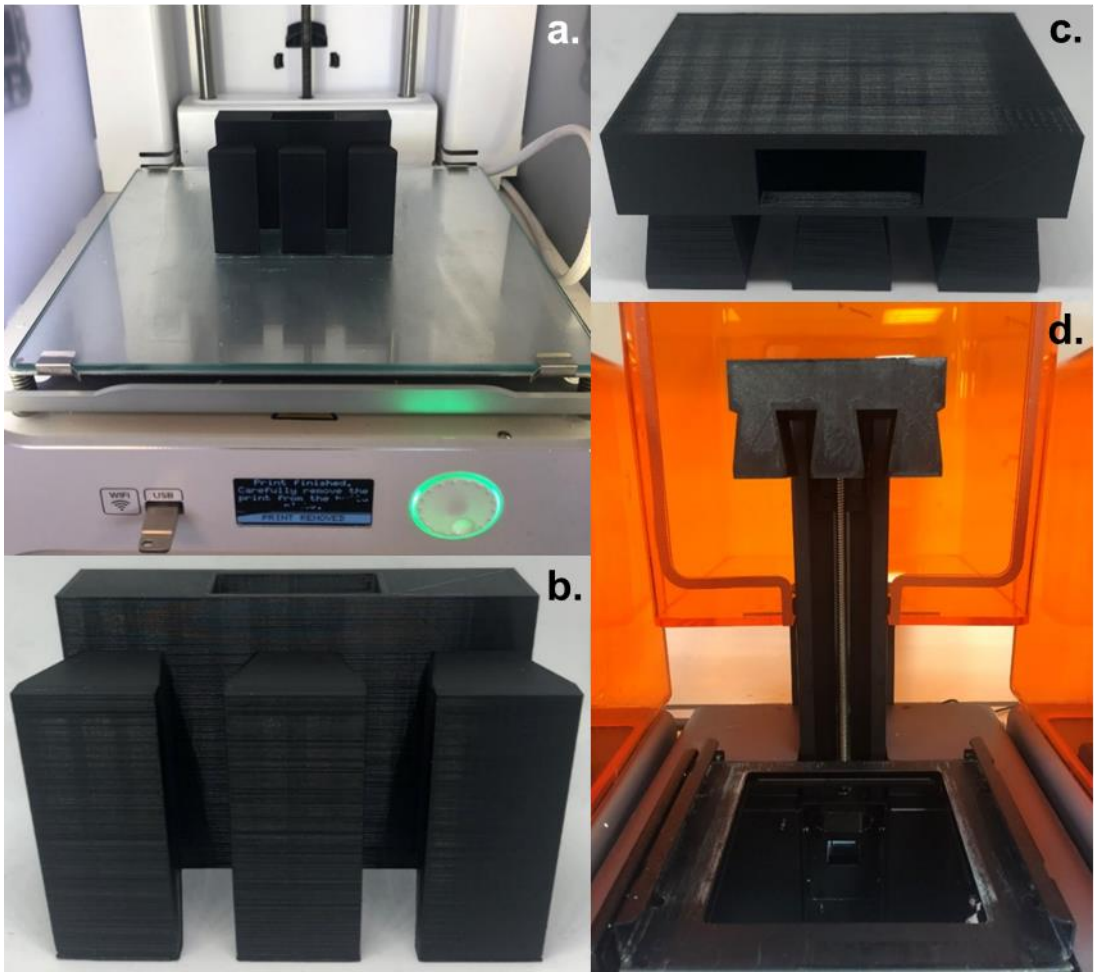

Figure 74 – Images showing FFF 3D printed print platform for tensile test sample printing: **a.** finished FFF 3D printed print platform, **b.**, and **c.** two different views of the custom print platform, and **d.** print platform attached to Formlabs Form 1+ SLA 3D printer print platform socket.

This permits fabrication of a lightweight print platform that applies less pressure upon the build platform arm than a heavier SLA 3D printed print platform might, which could negatively affect print accuracy or success. On the contrary, SLA 3D printing was preferred over FFF 3D printing for fabricating print trays (Figure 75). Print trays were printed on a Formlabs Form 2 SLA 3D printer using Clear V4 (FLGPCL04) photocurable resin. Initially, an FFF 3D printed tray was first trialled but proved problematic. Firstly, it displayed a tendency to leak and/or absorbed and swelled with resin over time. This was attributed to the lower infill and resolution of FFF 3D printing resulting in a relatively porous object. The high infill and resolution of SLA 3D printing leads to a more “moisture tight” print tray which proved ideal. Secondly, the FFF 3D

printed tray did not adhere well to the proprietary print tray silicone surface, despite use of a silicone-plastic adhesive. It was speculated that rough surface finish and/or PLA incompatibility may have resulted in poor adhesion. The print tray was printed on a Formlabs Form 2 SLA 3D printer using Clear V4 (FLGPCL04) photocurable resin. The printed object was removed from the build platform and washed with IPA. The object was placed in a Form Cure for post-curing to reduce the content of uncured monomers. A time of 60 minutes at 45 °C was chosen to minimise any object warping or shrinkage.

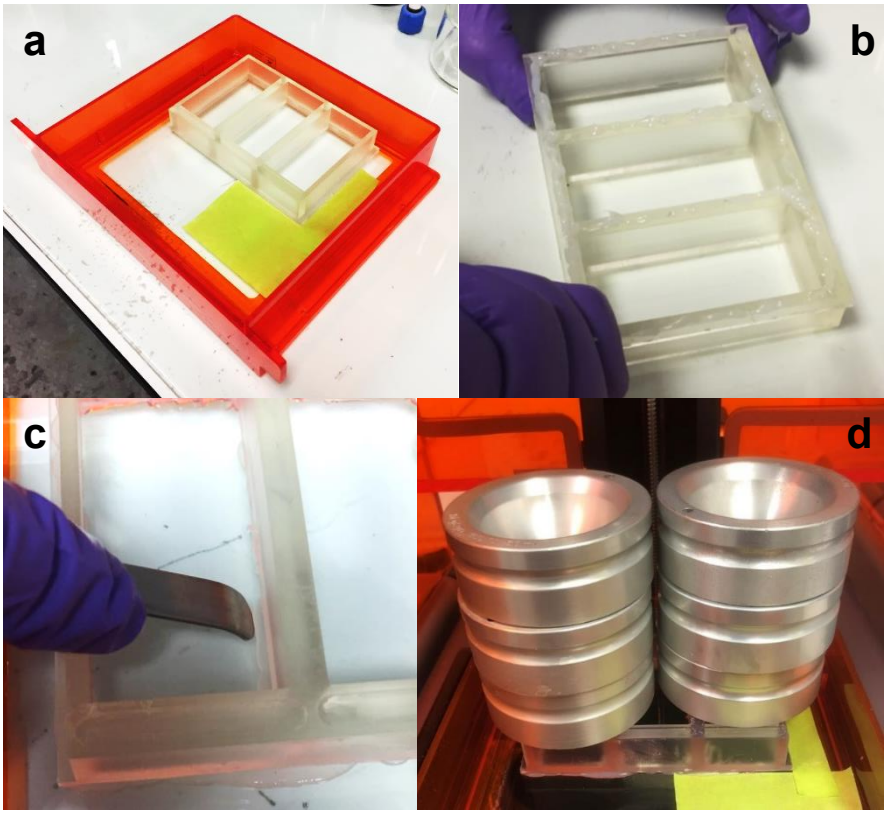

Figure 75 – Images detailing the preparation of an adapted tray setup for the Formlabs Form 1+ SLA 3D printer

Figure 75 illustrates the stepwise preparation of an adapted tray setup. The first step involved deducing the correct position for the print tray on the proprietary print tray surface (Figure 75a). Next, silicone-plastic adhesive was syringed onto the bottom of the tray which was promptly placed onto the standard print tray surface in the correct position (Figure 75b). Excess adhesive that encroached print areas was scraped away with a spatula (Figure 75c).

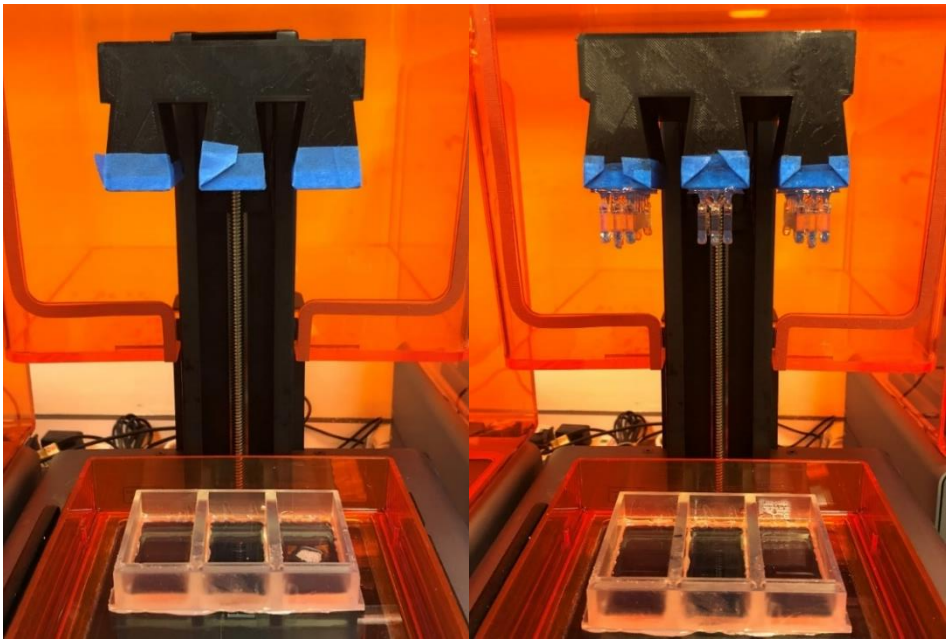

Figure 76 – Images showing Formlabs Form 1+ SLA 3D printer with adapted print setup before (left) and after (right) printing.

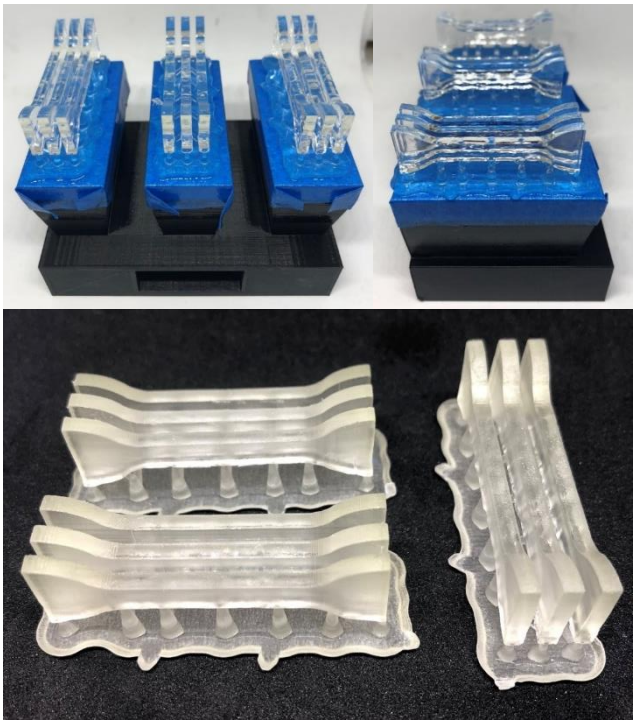

Figure 77 – Images showing fabricated objects before (top) and after post-processing (bottom)

Weights were placed on top of the tray for 24 hours to ensure a good seal was achieved (Figure 75d). Prior to printing, masking tape was applied to the print

head surface(s) which provided a pliant surface for object building and permitted easy removal of object(s) from print head(s) post-print. PreForm calculated that each supported object required 6.93 mL resin. Each well was filled with 8 mL of resin, representing a small excess of approximately 1 mL. Figure 76 and 77 shows the successful 3D printing of tensile test samples. No visible defects were observed for any objects.

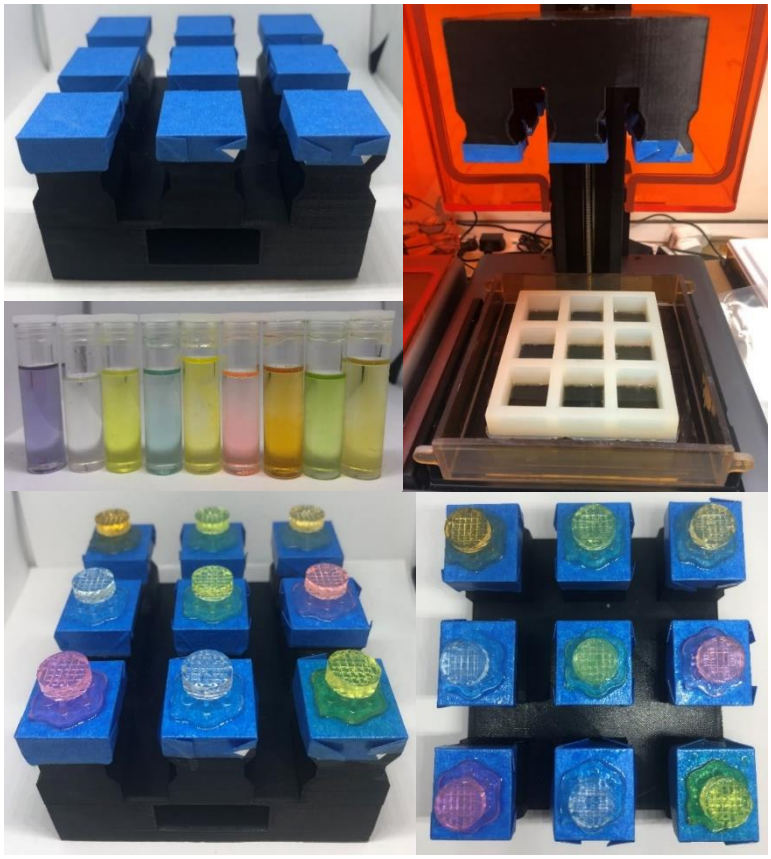

Figure 78 – Images showing an adapted Formlabs Form 1+ SLA 3D printer setup including 9 printheads and printing wells, and successful multi-material printing of 9 small objects

In addition to facilitating printing of small objects with small resin volumes, the adapted setup method can drastically reduce the printing time of multiple objects. For example, to print 9 small objects with 9 different materials utilising the standard Form 1+ setup takes 9 x 35 min = 5 hours 15 minutes plus additional time required to empty, clean and refill a proprietary resin tray. However, using an adapted Form 1+ setup that comprises of 9 printheads and printing wells, the printing time of 9 objects with 9 different materials is reduced

to 1 hour 19 minutes (Figure 78). This represents approximately a 4 times faster process, reducing the bottleneck impact 3D printing has on the workflow when compared to other manufacturing techniques. A 9 times faster process is not observed as a result of layer curing times increasing due to an increased number of objects in a single print. A caveat to this is that a single print uses a pre-defined PreForm print setting and hence, without formulation revision, all objects may not successfully print. A solution to this problem involves formulating all materials with certain quantities of additives such as photoinitiators, photoinhibitors and photoabsorbers so that all subsequent resin formulations print successfully using a single pre-defined print setting. The RT-FTIR method previously used to measure photoactivity of cationic photoinitiator containing formulations is utilised to achieve the above and is discussed later.

6.2.2. Preliminary 3D printing

Preliminary 3D printing using both the MiiCraft+ and Formlabs Form 1+ SLA 3D printers yielded mixed results. Firstly, initial attempts to print with cationic photopolymer systems were unsuccessful. Figure 79 shows the unsuccessful printing of a TEGDVE formulation containing 1% w/w P3C-P using Formlabs Clear V4 print settings with 0.2 mm layer height. It is apparent that the object did not have sufficient “green” strength to fully print and hence it fell from the platform during printing. Numerous print settings were trialled and none were able to result in successful printing with this formulation. A decision was made to alter the formulation to achieve print success. Figure 80 shows failed prints using a TEGDVE formulation containing 5% w/w P3C-P + 3% benzoyl peroxide, a photosensitiser. During the first attempt no object adhered to the print and instead the resin within the vat polymerised. In the second attempt, an object did adhere to the print platform. Unfortunately, a large amount of overpolymerisation occurred. This overpolymerisation was attributed to a phenomenon known as “shadow” curing, which is an exclusive property of cationic photopolymerisation systems.

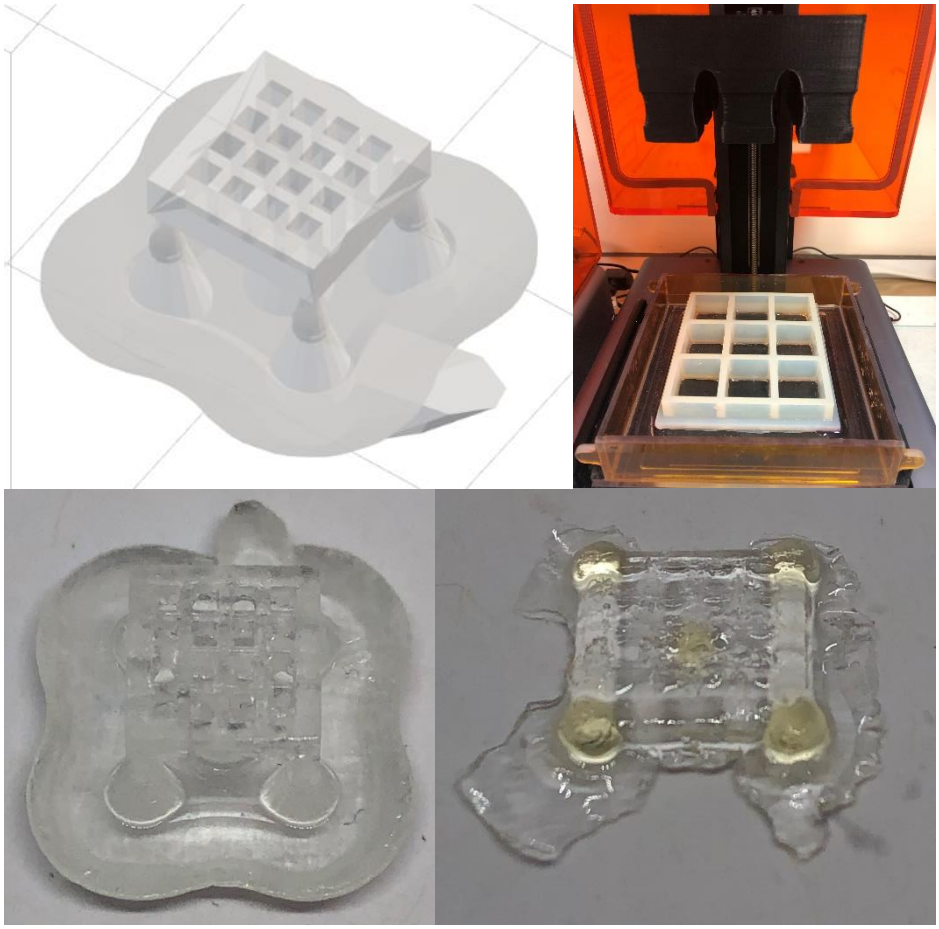

Figure 79 – Top left image shows desired object for printing in Formlabs PreForm software. Top right image shows print setup using an adapted print head and print tray. Bottom left image shows successful print using Formlabs Clear V4 resin. Bottom right image shows failed printing using a TEGDVE + 3% P3C-P formulation.

Figure 80 – Left image shows desired object, generated using Tinkercad, for printing. Middle and right images show subsequent failed prints using a TEGDVE + 5% w/w P3C-P + 3% benzoyl peroxide formulation on the MiiCraft+ SLA 3D printer

Photo-generated acids from cationic photoinitiators persist within formulations for days unlike free-radicals that persist for fractions of a second. As a result, cationic photopolymer systems will continue to polymerise without continued exposure to UV radiation[252]. While this phenomenon can prove useful for other applications, it is unfavourable for 3D printing. With increased print time, the effect of “shadow” curing becomes greater, therefore limiting printing with cationic photopolymer systems to small objects, using the lowest resolution setting. A potential solution to be explored involves the addition of organic bases in small quantities to cationic photopolymer formulations the with aim to neutralise photoacid migration in non-irradiated print areas. Despite the desirability of cationic photopolymer systems and the promising results shown for cationic photoinitiators operating within the near-UV light spectrum, a decision was made to discontinue exploration of these system for the immediate project. This was due to anticipation that development of 3D printable cationic photopolymer systems would involve a substantial amount of work and therefore may be better approached as a separate project.

Figure 81 highlights the main issue encountered when 3D printing custom photopolymer formulations. Numerous prints (15 in total) were required to finetune a PEG575DA + 20% w/w trithiol CTA formulation to ensure prints fabricated using the MiiCraft+ SLA 3D printer were successful and accurate to their design. This trial and error approach to find an optimised resin formulation led to a waste of both time and material. Although literature often provides values for photoinitiator, photoinhibitor and/or photoabsorbers content within 3D printable formulations, these values are specific to a certain photopolymer system and/or SLA 3D printing apparatus or are somewhat arbitrary. It is therefore necessary to develop a method that identifies precise content values of additives that render a resin formulation printable with high resolution and accuracy, without the need for trial and error 3D printing. To simplify this process, it was necessary to have a reference material that prints with high resolution and accuracy under its own optimised print settings. A decision was therefore made to use Formlabs Clear V4 resin as a reference material, due to it possessing its own optimised print settings within the PreForm software.

Furthermore, experimental SLA 3D printing was exclusively performed using the Formlabs Form 1+ apparatus from hereon.

Figure 81 – Images showing multiple consecutive prints utilising a PEG575DA + trithiol + 1% TPO (unless stated otherwise) formulation with varying layer exposures and amounts of photoinhibitor HQ.

6.2.3. Development and assessment of an RT-FTIR spectroscopy method as a tool for identifying 3D printable resin formulations

The use of real-time Fourier-transform infrared spectroscopy to monitor extent of curing within (meth)acrylate-based photopolymer systems has been widely researched. As mentioned previously, the content of C=C vinyl groups within a (meth)acrylate-based material is depleted and can be visualised by the reduction of spectral peaks corresponding to C=C vinyl groups at 1637 cm^{-1} and 810 cm^{-1}. The Formlabs Form 1+ SLA 3D printer offers a single print setting for each of its own materials. An assumption is made that each pre-set print setting is optimised to its corresponding material. A hypothesis was made that altering the curing profile of a custom photopolymer formulation to match that of a Formlabs resin material, would yield a resin formulation printable using the print setting of that select Formlabs material. The means for altering the curing profile of a custom photopolymer formulation involves varying amounts of photoinitiator, photoinhibitor and/or photoabsorber within the formulation.

To allow for 3D printing of aspirin (ASA) loaded mesh samples, a pilot study using the aforementioned RT-FTIR spectroscopy method was conducted to elucidate 3D printable formulations of varying base monomers. These base monomers were PEG575DA, PTHF650DA, PPG425DA, PEG1000PUDMA, PTHF1000PUDMA and PPG1200PUDMA. PEG1000PUDMA was diluted with 20% HEA whereas PTHF1000PUDMA and PPG1200PUDMA was diluted with 20% HDDA. Photoactivity of photoinitiators was analysed using real-time FTIR spectroscopy. The setup and approach used for assessing photoreactivity of cationic photopolymer formulations was utilised for this pilot study, with a few adjustments. The light intensity used for curing was reduced to 2.653 mW/cm^2. This value was measured using a Thorlabs power meter from the Form 1+ SLA 3D printer light source during a blank print using Clear V4 print settings at 0.1 mm layer thickness. This was the print setting intended to be used for printing of the above resin formulations. For this pilot study, all formulations contained 1% w/w TPO as photoinitiator and a variable amount of hydroquinone (HQ) as photoinhibitor. For example, stock formulations of

PEG575DA + 1% w/w TPO and PEG575DA + 1% w/w TPO + 25.6% w/w HQ were produced. The 25.6% w/w HQ stock formulation was serially diluted to produce formulations containing 12.8, 3.2, 0.8, and 0.2% w/w HQ. The rationale behind these experiments was that increasing HQ content would reduce formulation curing rate (DBC (%) over time) in a commensurate fashion. Each formulation was analysed in triplicate. As before when measuring curing rates of cationic photopolymer systems, plots generated via integration of the 810 cm^{-1} spectral gave lower and widely varied values for DBC. This was again attributed to overlapping of spectral peaks, leading to inaccurate integrations, and were therefore not used.

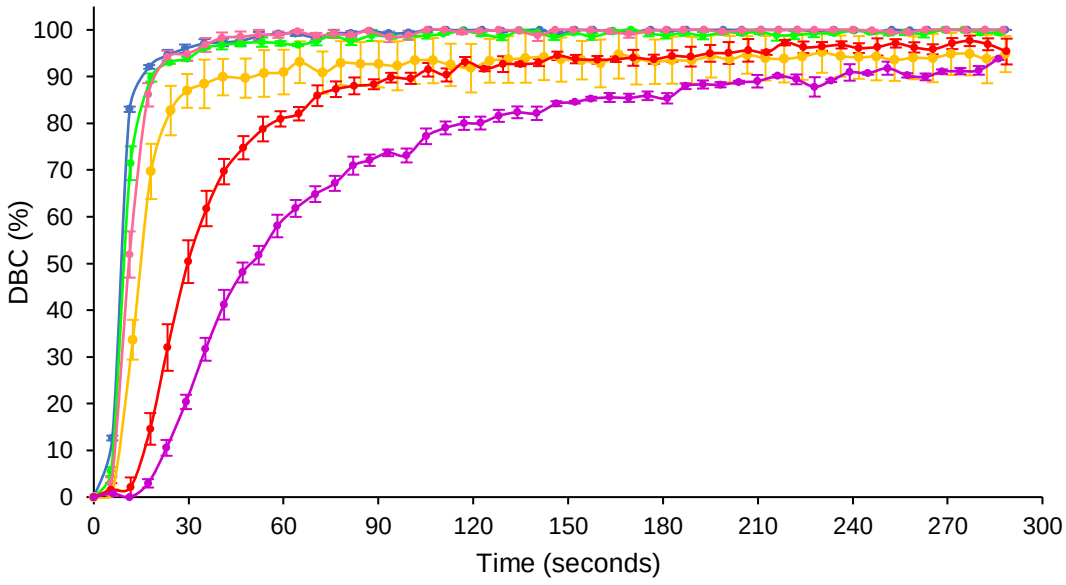

Figure 82 – Graph plotting mean DBC (%) against irradiation time for PEG575DA + 1% w/w TPO formulations containing variable amounts of photoinhibitor HQ. Plot results shown are: No HQ (–), 0.2% w/w HQ (–), 0.8% w/w HQ (–), 3.2% w/w HQ (–), 12.8% w/w HQ (–) and 25.6% w/w HQ (–).

Figure 82 highlights the effect of HQ content on DBC (%) of PEG575DA + 1% w/w TPO over irradiation time. With increasing HQ content, curing rate and overall DBC (%) of the sample is reduced. There are two explanations for this observation. Firstly, HQ operates as a free radical scavenger, reducing the rate of initiation and propagation of photopolymerisation, resulting in a slowed and/or reduced curing process. Secondly, the gradual increase in HQ content

leads to a sparser dispersion of acrylate functional groups within the formulation. A more dilute photopolymer systems results in a slower and/or reduced curing process.

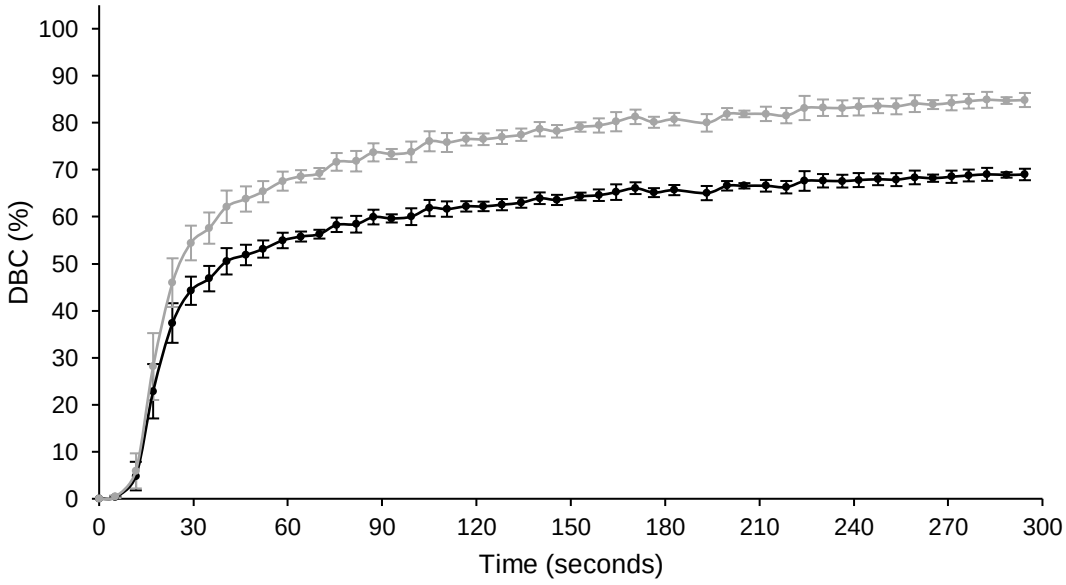

Figure 83 – Graph plotting mean DBC (%) against irradiation time for Formlabs Clear V4 resin. Plot results shown are unmodified (**–**) and modified (–).

Figure 83 shows DBC (%) of Formlabs Clear V4 resin over time when irradiated with a 2.653 mW/cm^2 intensity 405 nm wavelength light source. As the exact composition of the Formlabs Clear V4 resin is unknown, it is impossible to determine whether the peak at 1637 cm^{-1} fully corresponds to C=C bonds that participate in and disappear during photopolymerisation, or whether the peak partly corresponds to C=C bonds that do not participate in photopolymerisation. A separate RT-FTIR spectroscopy study of Formlabs Clear V4 resin was conducted where a light intensity of 100 mW/cm^2 was utilised and 200 spectra were collected instead of 50. This was done to identify a DBC (%) value at which curing plateaus. An assumption was made that the DBC (%) value at which curing plateaus (81.32 %) corresponds to 100 % DBC. Individual points from the unmodified plot in Figure 83 were adjusted based on this value (y % / 81.32 % x 100 %), generating a new modified data plot.

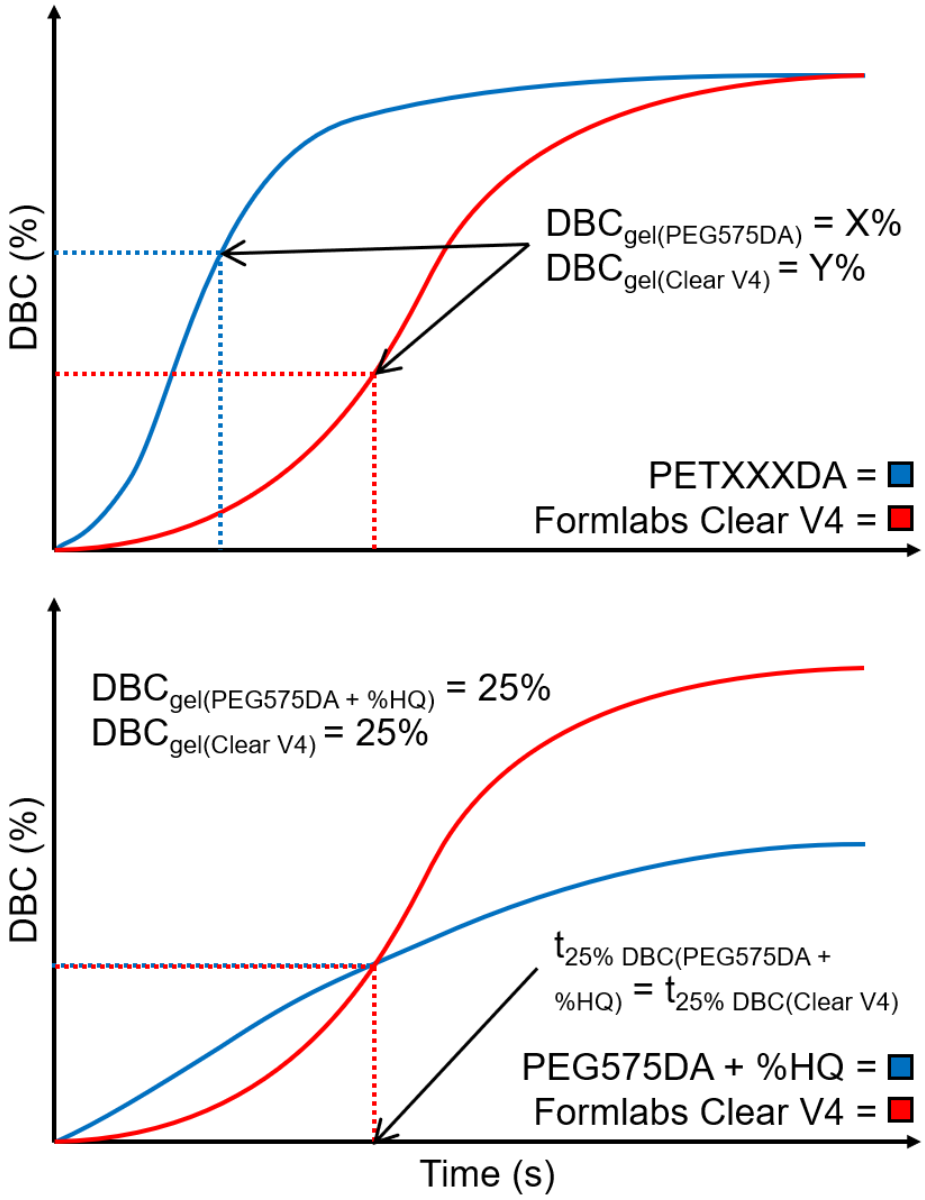

Figure 84 – Graphs detailing the concepts behind the proposed RT-FTIR spectroscopy method.

The next step for this method was to calculate the amount of HQ required to modify the rate of curing of the PEG575DA formulation to match that of Formlabs Clear V4 resin. Complete adjustment of the curing profile of PEG575DA so that it matches that of Formlabs Clear V4, point for point, is not possible and therefore it was decided that achieving an interception of both curing profiles at a designated time point was a good approach (Figure 84). To start, matching the times at which both formulations achieve arbitrary DBCs of 25% or 50% DBC were chosen.

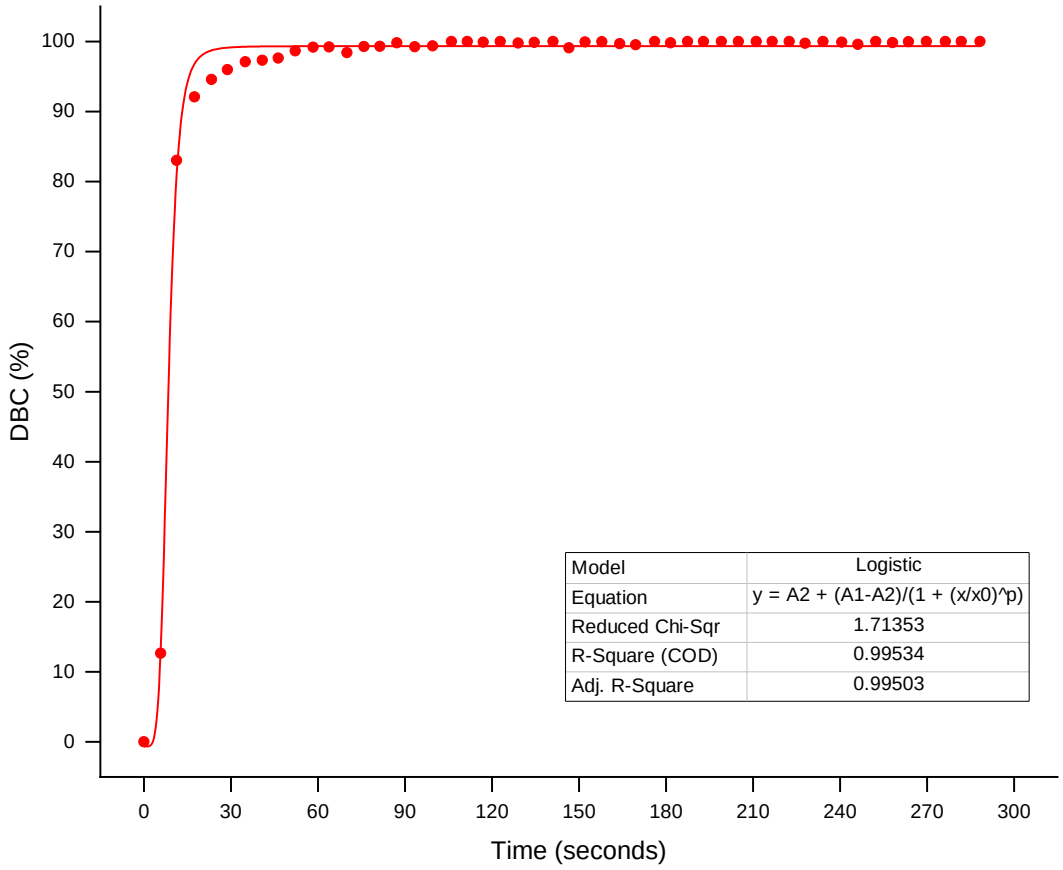

Figure 85 – Graph plotting mean DBC (%) against irradiation time for PEG575DA + 1% w/w TPO + no HQ, with a logistic dose response curve fitted.

Table 25 – Table showing t@25%DBC and t@50%DBC values for PEG575DA + 1% w/w TPO formulations containing different HQ contents

HQ content (% w/w)	Time (s, @ 25% DBC)	Time (s, @ 50% DBC)
0	6.76924	8.44439
0.2	7.38728	9.65039
0.8	8.56822	11.19134
3.2	10.8723	14.71533
12.8	20.41215	31.04866
25.6	30.93985	52.00585

To calculate values for times at 25% (t@25% DBC) and 50% DBC (t@50% DBC) from plots, it was necessary to use statistical scientific graphing software

(OriginPro 2019). All plots were fitted with a logistic dose response curve model.

Utilising the fitted curve from Figure 85, values for t@25%DBC and t@50%DBC values could be generated for PEG575DA + 1% w/w TPO formulations containing variable HQ contents. These values were then used to produce a calibration curve, plotting HQ content (% w/w) against both t@25%DBC and t@50%DBC (Figure 86). A second order polynomial curve model was used to fit the dataset with good accuracy reported (R-squared value > 0.99). Values for t@25%DBC and t@50%DBC were 18.2442 and 43.9143 seconds for Formlabs Clear V4 – unmodified, respectively; and 15.33903 and 30.88437 seconds for Formlabs Clear V4 – modified, respectively. Inputting these values into the calibration curve (Figure 86) yielded values for HQ content ranging from 7.49 to 20.57 % w/w. PEG575DA + 1% w/w TPO containing both lower and upper range HQ contents printed successfully, displaying high accuracy in correspondence to the original design. However, objects printed with higher contents of HQ were mechanically weak which attributed to the amount of HQ present which led to a material with low polymer crosslinking. As these HQ content values were generated from t@50%DBC values, a decision was made to consider only HQ content values generated from t@25%DBC values.

This method of calculating ideal HQ contents to ensure printability with Formlabs Clear V4 settings was utilised for all resin formulations, with all subsequent data compiled in both Figure 87 and Table 26.

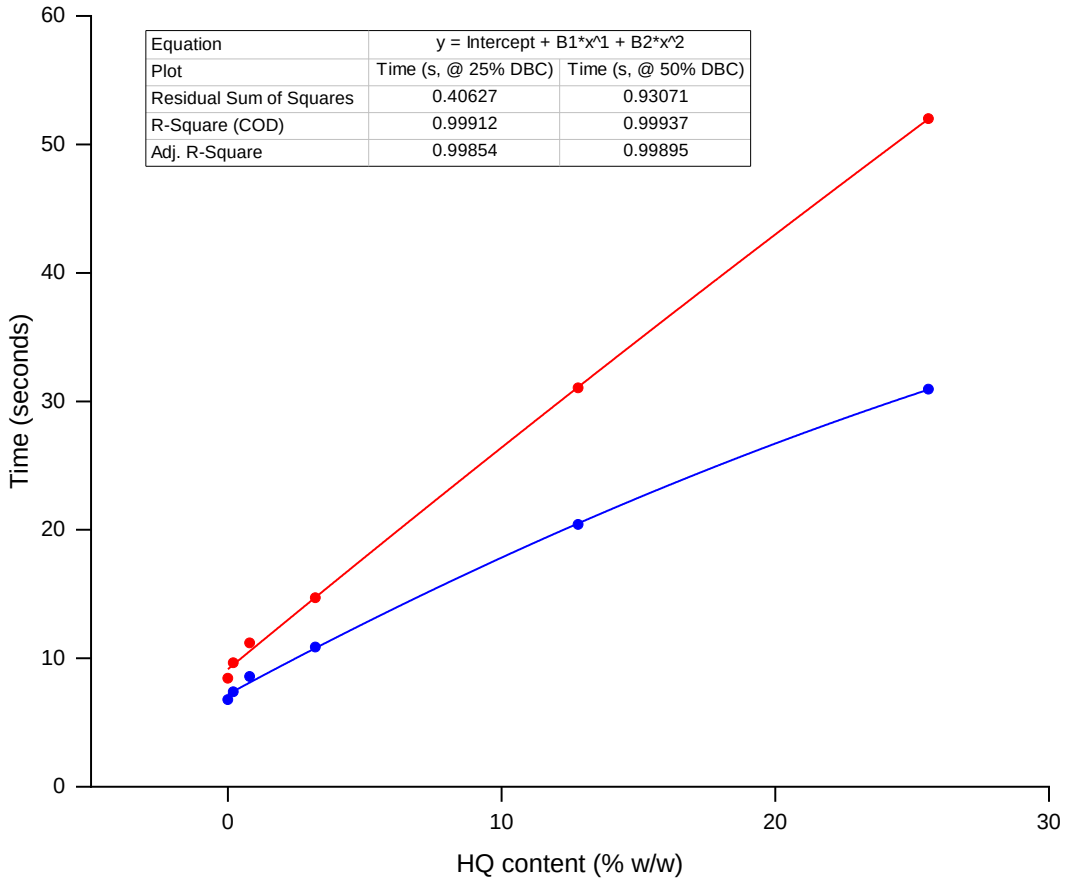

Figure 86 – Calibration curve plotting HQ content (% w/w) against both t@25%DBC and t@50%DBC for PEG575DA + 1% w/w TPO formulations. Plot results shown are time at 25% DBC (–) and time at 50% DBC (–).

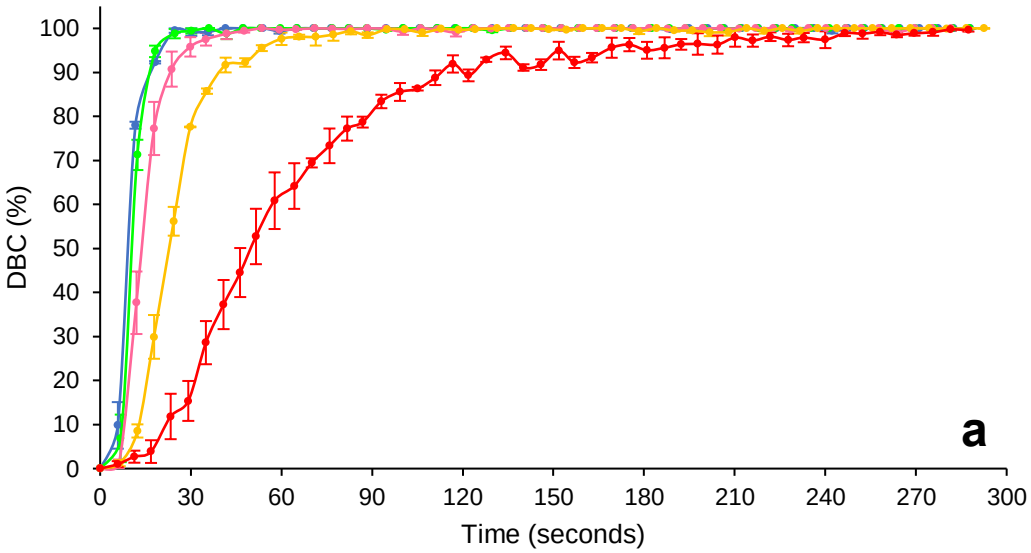
DBC (%)
Time (seconds)
a

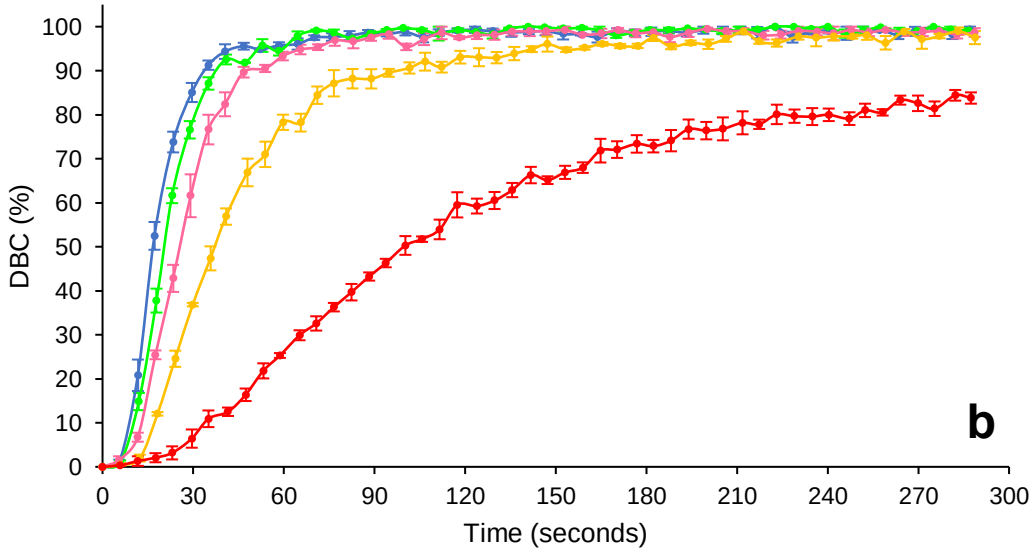
DBC (%)
Time (seconds)
b

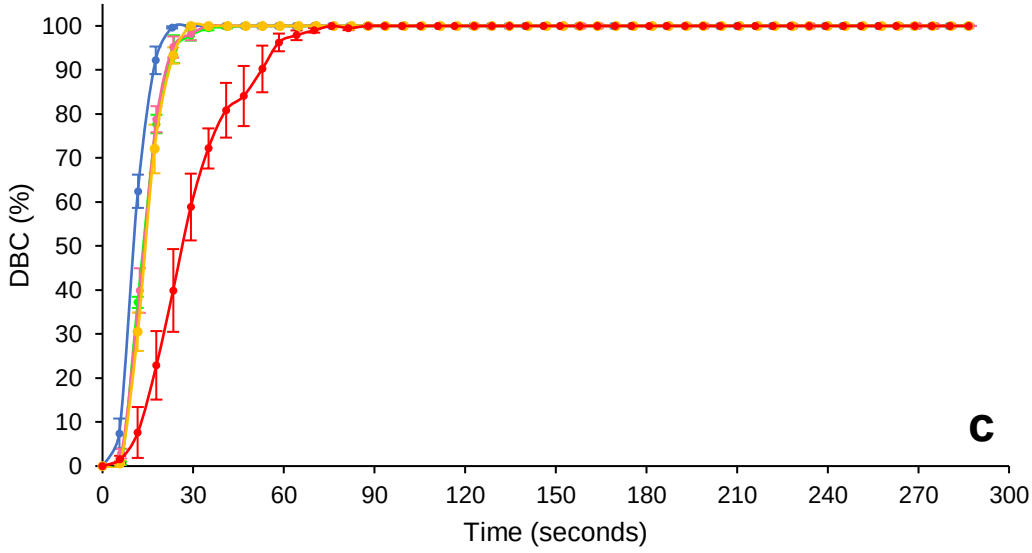
DBC (%)
Time (seconds)
c

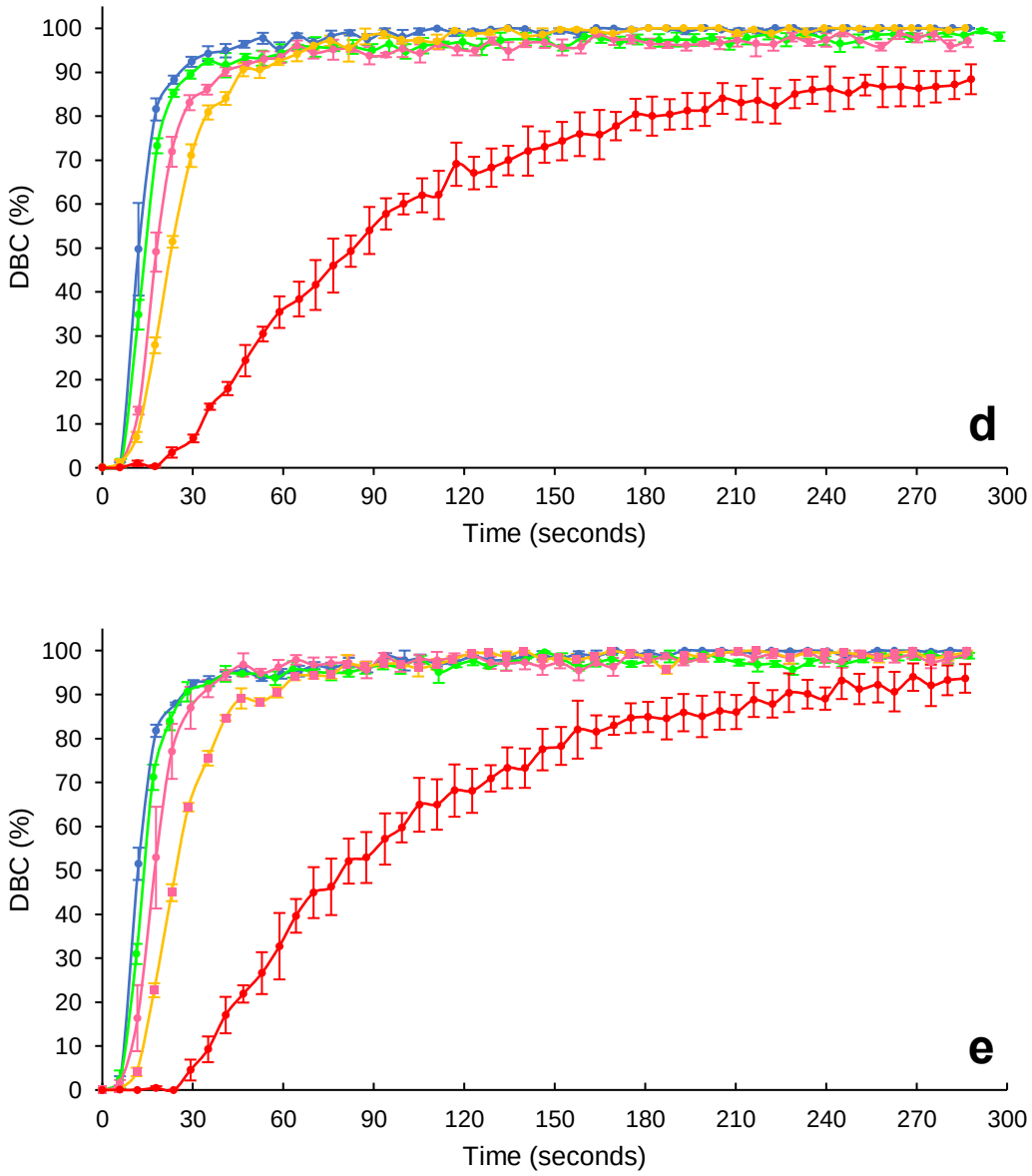

Figure 87 – Graphs plotting mean DBC (%) against irradiation time for different resin formulations containing variable amounts of photoinhibitor HQ. Graphs shown are: **a** – PTHF650DA + 1% w/w TPO, **b** – PPG425DA + 1% w/w TPO, **c** – PEG1000PUDMA + 20% w/w HEA + 1% w/w TPO, **d** – PTHF1000PUDMA + 20% w/w HDDA + 1% w/w TPO, and **e** – PPG1200PUDMA + 20% w/w + 1% w/w TPO. Plots for all graphs are as follows: No HQ (–), 0.2% w/w HQ (–), 0.8% w/w HQ (–), 3.2% w/w HQ (–) and 12.8% w/w HQ (–).

Table 26 – Table showing data generated from DBC(%) versus time (s) plots and time (s) versus HQ content (% w/w) calibration plots for various resin formulations. Adjusted R-squared values for all graphs are provided to display accuracy of data modelling.

Formulation	DBC (%) versus time (s) plots			Time (s) versus HQ content (% w/w) calibration plot		
	Adjusted R-squared	HQ content (% w/w)	t@25%DBC (s)	Adjusted R-squared	HQ content (% w/w) to match t@25%DBC values	
					Formlabs Clear V4 - unmodified	Formlabs Clear V4 - modified
PEG575DA + 1% TPO	0.9950	0	6.77	0.9985	10.4188	7.4971
	0.9949	0.2	7.39			
	0.9986	0.8	8.57			
	0.9965	3.2	10.87			
	0.9958	12.8	20.41			
	0.9962	25.6	30.94			
PTHF650DA + 1% TPO	0.9988	0	7.21	0.9979	3.7097	2.5895
	0.9998	0.2	8.72			
	0.9996	0.8	10.49			
	0.9992	3.2	16.84			
	0.9984	12.8	33.20			
PPG425DA + 1% TPO	0.9990	0	12.25	0.9940	1.3149	0.4843
	0.9989	0.2	14.75			
	0.9991	0.8	17.89			
	0.9986	3.2	24.37			
	0.9990	12.8	58.99			
PEG1000 PUDMA + 20% HEA + 1% TPO	0.9995	0	8.19	0.9091	12.1363	8.6033
	0.9995	0.2	10.37			
	0.9998	0.8	10.76			
	0.9995	3.2	11.14			
	0.9986	12.8	18.84			
PTHF1000 PUDMA + 20% HDDA + 1% TPO	0.9948	0	9.04	0.9896	3.7065	2.4893
	0.9949	0.2	10.49			
	0.9955	0.8	13.72			
	0.9982	3.2	16.41			
	0.9981	12.8	48.87			
PPG1200 PUDMA + 20% HDDA + 1% TPO	0.9915	0	8.77	0.9946	3.2787	2.2095
	0.9953	0.2	10.30			
	0.9977	0.8	13.15			
	0.9977	3.2	17.56			
	0.9972	12.8	50.54			

From Table 26, it can be observed PEG-based photopolymer systems require a larger content of HQ to convert their t@25%DBC values to those for Formlabs Clear V4 unmodified and modified. This implies the photoreactivity of PEG-based photopolymer systems is less affected by HQ content, which could potentially explain premature polymerisation of these materials during preparation. PPG425DA + 1% TPO formulations showed low values for t@25%DBC and hence lower curing rates, in comparison to all other formulations. It was speculated that the adapted workup protocol for PPG-based di(meth)acrylates which omitted washing steps for removal of hydroquinone, may have led to this reduced photoreactivity. As with PEG575DA formulations, a second order polynomial curve model was used to fit datasets for calibration curves. In general, this model fit datasets for acrylate-based materials and PPG1200PUDMA formulations with high accuracy (adjusted R-squared value > 0.99), however this was not the case for PTHF1000PUDMA (R-squared value = 0.9896) and PEG1000PUDMA (R-squared value = 0.9091) formulations. This either implies that the relationship between time at 25% DBC and HQ content for these formulations does not follow a second order polynomial model, or datasets for these specific formulations were inaccurate. Exploring the latter hypothesis, it was noted that integration of IR spectra peaks at 1637 cm^{-1} for polyurethane methacrylate formulations were less precise due to reduced peak size and resolution. Peak size and resolution were reduced due to the ratio between oligomer molecular weight and methacrylate functional groups increasing. Nonetheless, lower end values for HQ content were used to produce a range of aspirin (ASA) containing resin formulations for 3D printing.

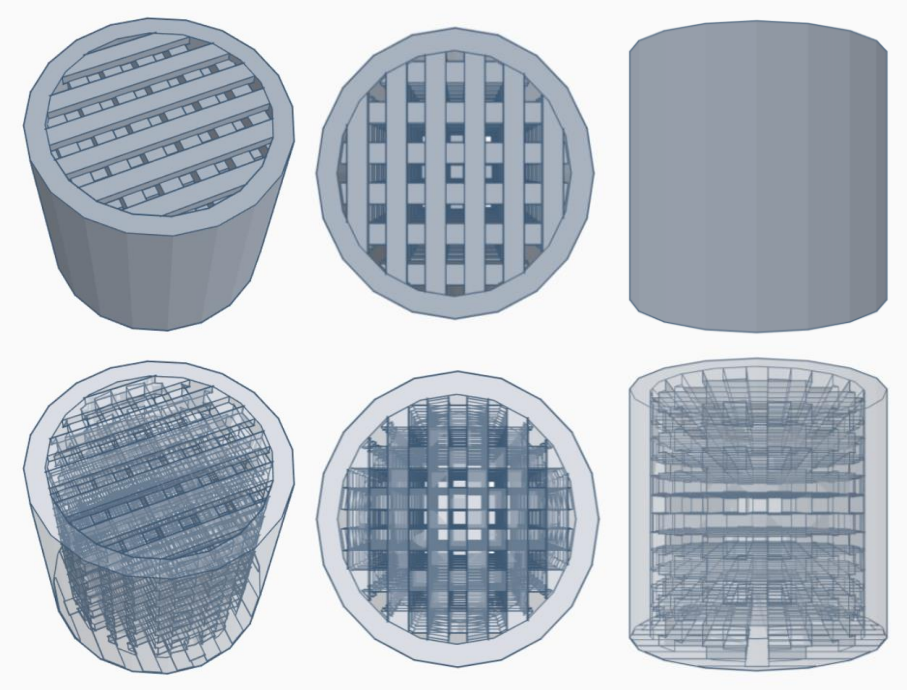

Figure 88 – Tinkercad generated images showing cylindrical mesh design used for samples for preliminary drug release studies

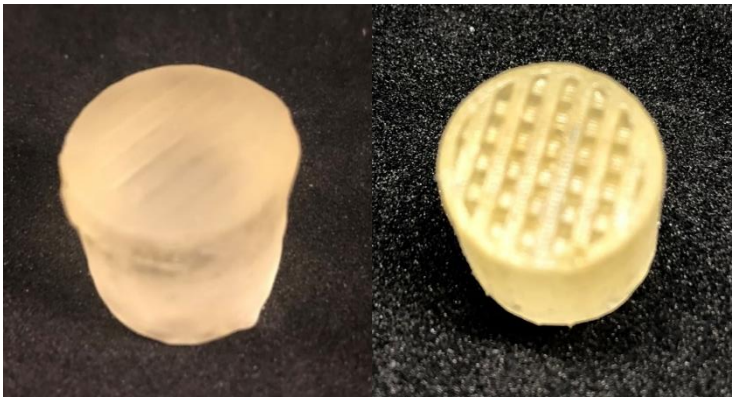

Figure 89 – Images showing effect of HQ addition on printing quality. Left image shows PEG575DA formulation containing no HQ and right image shows PEG575DA formulation containing HQ.

Figure 88 shows the intricate design chosen for 3D printing. When it was attempted to 3D print this design prior to modification of PEG575DA + 1% w/w TPO formulations, the overall resolution and accuracy to original design of the object was poor as illustrated in Figure 89 (left). Considering that drug release profiles of such implants heavily depend on object design, poor reproduction

of said design will lead to unpredictable and imprecise drug release kinetics, representing a failure in personalised treatment. It is therefore paramount that objects are fabricated with high resolution and accuracy to original design. Developing a method is essential, as discussed here, to ensure this is of high importance. Figure 89 (right) demonstrates the successful printing of custom resin formulations using the design illustrated in Figure 88. From observation, all objects printed were accurate to the above design, with no apparent print defects.

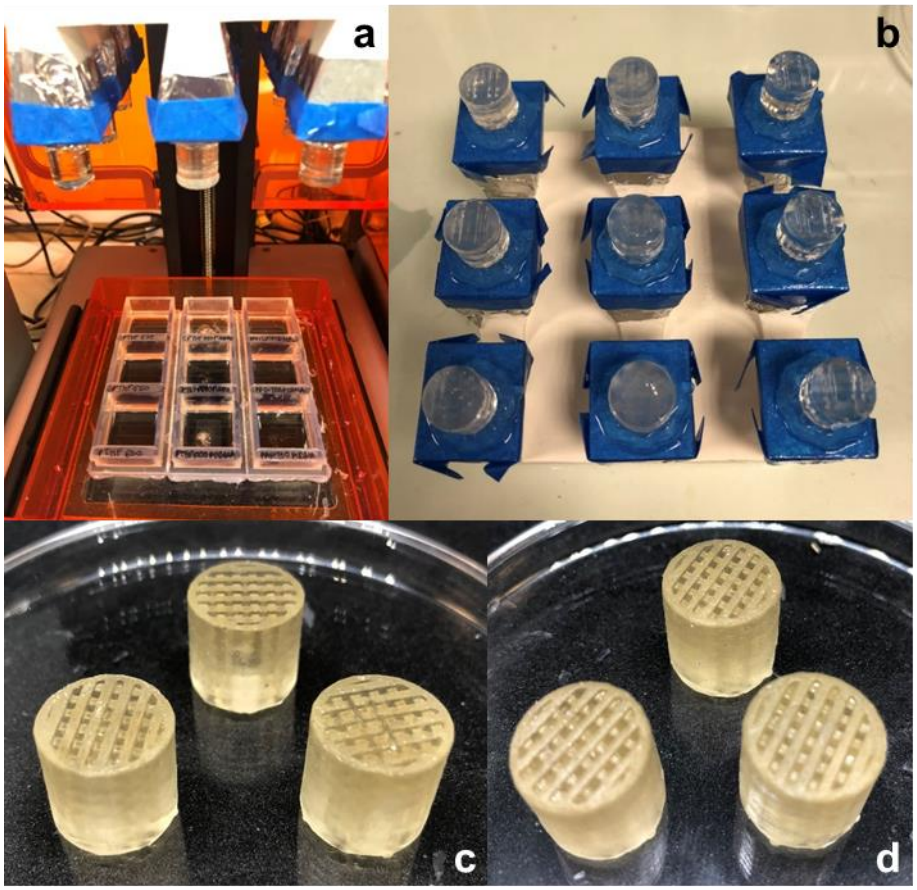

Figure 90 – Top images **a.** and **b.** show showing successful printing of cylindrical mesh samples using custom resin formulations with calculated contents of HQ. Bottom images show meshes fabricated from **c** – PEG575DA + 1% w/w TPO + 7.5% w/w HQ + 5% ASA, and **c** – PEG1000PUDMA + 20% w/w HEA + 1% w/w TPO + 8.6% HQ + 5% ASA.

These results confirm that the RT-FTIR spectroscopy method successfully identified resin formulations that when printed on the Form 1+ SLA 3D printer

using Form Clear V4 settings at a layer thickness of 0.1 mm, produced objects of high resolution with high accuracy to the chosen design. Whilst the above approach proved to be an effective method for the fabrication of objects from different photopolymer formulations using the same print settings, revisions were still necessary.

6.2.4. Utilisation of RT-FTIR spectroscopy tool to identify different roles of photoinhibitors and photoabsorbers in the 3D printing process

Firstly, utilising photoinhibitor as the sole additive for controlling print resolution and accuracy is short-sighted. Photoinhibitors are effective at controlling polymerisation in the x-y dimensions but are not renowned for their ability to control cure depth (z-dimension). As discussed above, the use of photoabsorbers are an effective way of controlling cure depth, and it was therefore logical to explore how photoinhibitors and photoabsorbers impact the printing process. An RT-FTIR method was once again used to investigate, albeit with a slightly different setup (see Figure 91). Previously, considerations were not made regarding the replication of the SLA 3D printing conditions. For example, sample exposure to oxygen was not limited and sample thickness did not correspond with that of the print layer height. To remedy the former, samples were sandwiched between the FTIR spectrometer optical window and a PMMA cover slip. This alteration was expected to limit oxygen exposure, which can hinder resin curing. To remedy the latter, square spacer blocks of thickness 0.2 mm were FFF 3D printed and placed around the sample. When the PMMA coverslip was placed on top of the sample, the spacer block ensured the sample was compressed to a thickness of 0.2 mm. In accordance, print settings for Formlabs Clear V4 with layer height 0.2 mm were chosen. Intensity of light used for this print setting was measured to be 4.05 mW/cm^2 and hence the intensity of light used for testing was also 4.05 mW/cm^2. A black cover sleeve was fabricated from Formlabs Black V2 resin on the Formlabs Form 2 SLA 3D printer and placed over the sample during testing. This was to prevent interference from other light sources. Furthermore, calculation of an “adjusted” Formlabs Clear V4 curing profile was abandoned. This was due to

the lack of evidence that suggested Formlabs Clear V4 resin contained C=C bonds that do not participate in DBC.

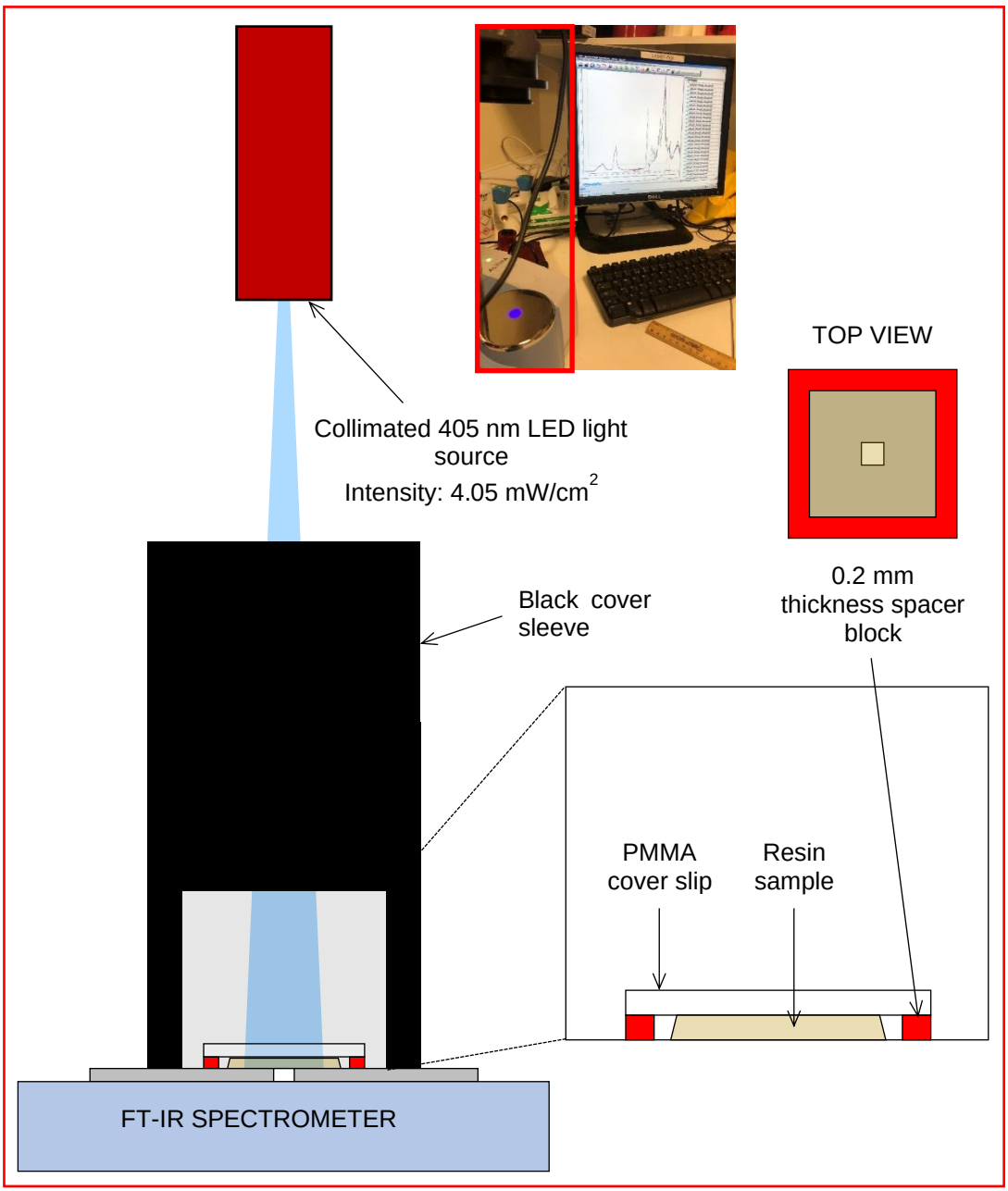

Figure 91 – Diagram showing previous actual setup and revised setup for RT-FTIR spectroscopy tool. Aim of setup was to replicate SLA 3D printing conditions including a black sleeve cover to limit ambient light interference and a cover slip to limit oxygen exposure. Setup was specific to use of Formlabs Clear V4 resin as reference material (4.05 mW/cm^2) and 0.2 mm layer height print settings.

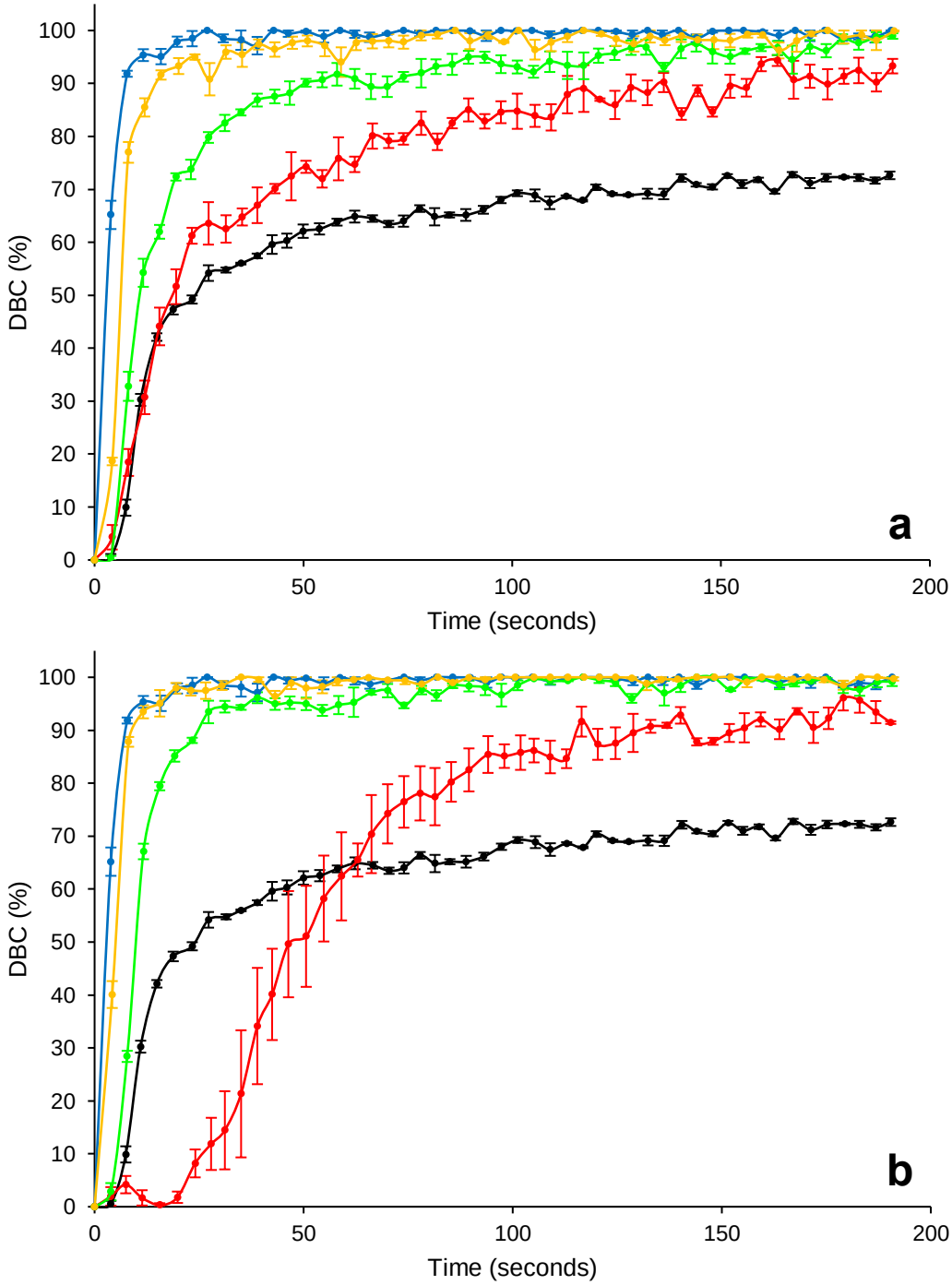

Figure 92 – Graph plotting mean DBC (%) against irradiation time for PEG575DA + 1% w/w TPO formulations containing variable amounts of photoinhibitor AT (**a**) and photoabsorber OG (**b**). Plot results shown are: Formlabs Clear V4 resin (**–**), No HQ (–); **a** – 2% w/w AT (–), 10% w/w AT (–), 20% w/w AT (–); **b** – 0.02% w/w OG (–), 0.1% w/w OG (–), 0.2% w/w OG (–).

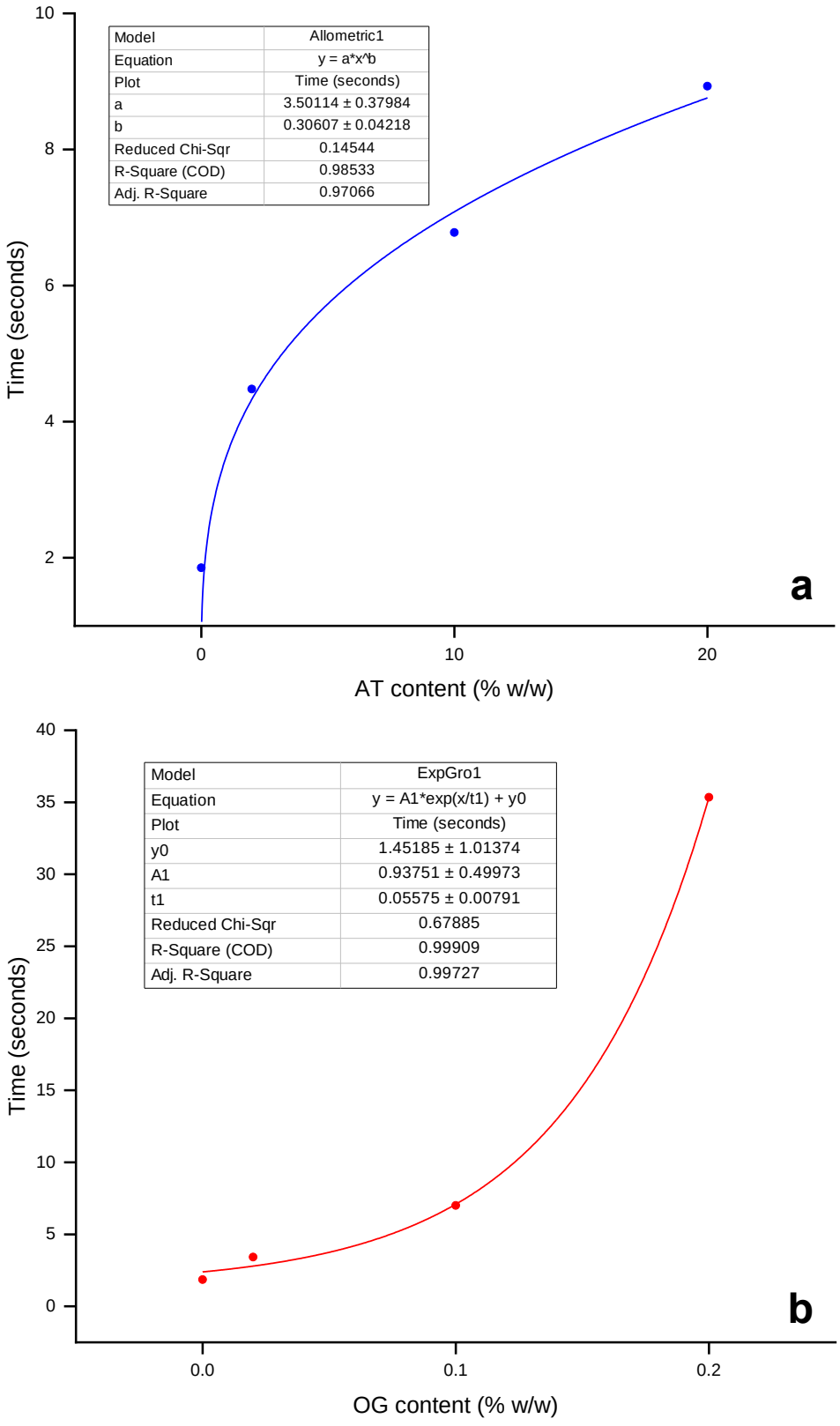

Figure 93 – Calibration curves plotting increasing AT (–) and OG (–) content (% w/w) against t@25% DBC for PEG575DA + 1% w/w TPO formulations.

PEG575DA + 1% TPO formulations containing varying amounts of photoinhibitor α-tocopherol (vitamin E, 20%, 10% and 2% w/w) and cobalt complex-based photoabsorber Orasol Orange G dye (0.2%, 0.1% and 0.02% w/w). Each formulation was tested using the above setup in triplicate, along with Formlabs Clear V4 resin. Initial observations of Figure 92 indicated that the photoabsorber displayed a more profound effect on DBC rate than the photoinhibitor. For example, only a small amount (0.2% w/w) of OG was required to extend the t@25%DBC for PEG575DA beyond that of Formlabs Clear V4 resin whereas a large concentration (20% w/w) of AT was required to approximately match t@25% DBC for both PEG575DA and Formlabs Clear V4 resin. Figure 93 shows calibration curves plotting increasing AT and OG content (% w/w) against t@25% DBC for PEG575DA + 1% w/w TPO formulations. The AT content calibration curve was modelled with a power function, indicating that a linear increase in AT content (% w/w) leads to a logarithmic growth in t@25%DBC for PEG575DA. The OG content calibration curve was modelled with an exponential growth function, indicating the opposite, that a linear increase in OG content (% w/w) leads to an exponential increase in t@25%DBC for PEG575DA. For the latter, this correlates with the above discussion, whereby excess energy (required to give a material “green” strength) is inversely proportional to cure depth[108,271]. As photoabsorber decreases cure depth, higher excess energy is required. As all tests were performed using the same conditions, this would have inevitably led to a reduction in curing rate with increasing photoabsorber content. Table 27 shows the calculated amounts of AT and OG (% w/w) required to match the t@25%DBC of PEG575DA and Formlabs Clear V4 resin.

For example, at low AT contents (2% w/w) the free radical scavenging function of AT was likely the primary mechanism causing DBC variances, whereas at higher contents (20% w/w), increasing photopolymer dilution may present an addition mechanism causing DBC variance, and hence a simple power function may not accurately model the data. PEG575DA + 1% TPO formulations containing AT and OG contents (% w/w) as detailed in Table 27 were prepared and used for SLA 3D printing.

Table 27 – Table showing data generated from time (s) versus AT or OG content (% w/w) calibration plots for PEG575DA formulations. Adjusted R-squared values for each calibration curve is provided to display accuracy of data modelling.

Formulation	Additive	Time (s) versus additive content (% w/w) calibration plot	
		Adjusted R-squared	Additive content (% w/w) to match Formlabs Clear V4 t@25% DBC values
PEG575DA + 1% TPO	AT	0.97066	> 20.00
	OG	0.99727	0.1241

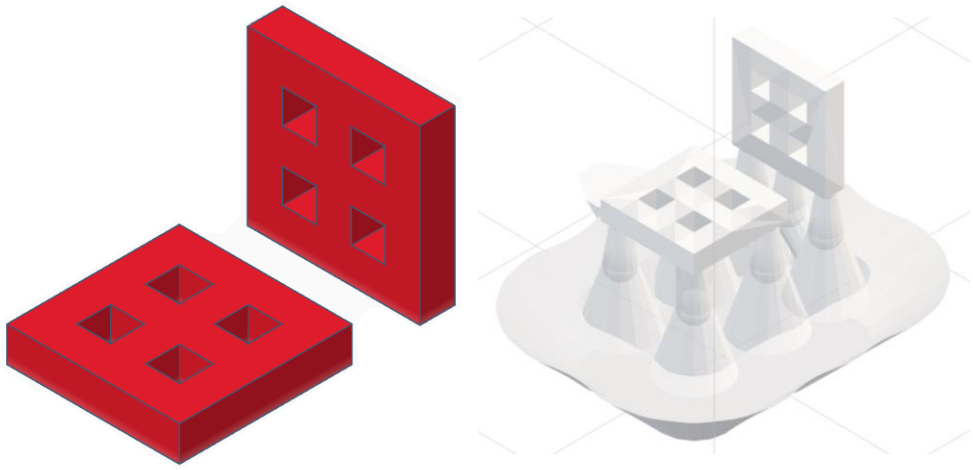

Figure 94 – Images showing (left) Tinkercad generated designs of grids with 1.0 mm x 1.0 mm pore size in horizontal and vertical orientations, and (right) print layout for horizontal and vertical grids with supports.

Figure 94 shows grid designs that were to be printed with prepared formulations. The hypothesis was that horizontal grids would be printed with high pore accuracy with AT-containing formulations, due to greater control of x-y dimension polymerisation whereas vertical grids would be printed with high pore accuracy with OG-containing formulations, due to greater control of cure depth (z dimension) polymerisation.

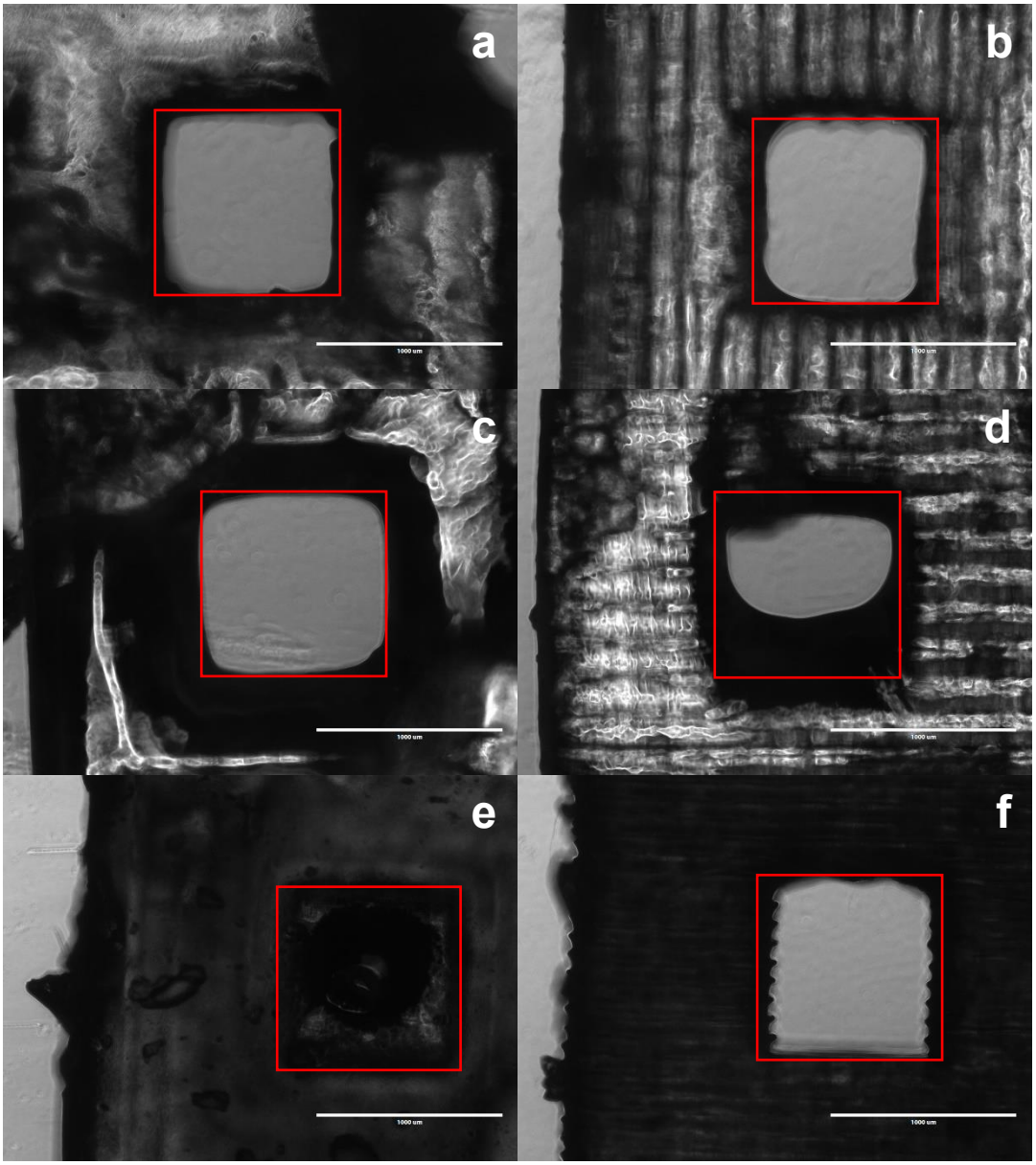

Figure 95 – Images of horizontal and vertical grids at 4x magnification taken using an inverted microscope. Images of grids are: **a** and **b** = Formlabs Clear V4 horizontal and vertical grids, respectively, **c** and **d** = PEG575DA + 1% w/w TPO + 20% w/w AT horizontal and vertical grids, respectively, **e** and **f** = PEG575DA + 1% TPO w/w TPO + 0.1241% w/w OG horizontal and vertical grids, respectively.

Figure 95 shows images of grids printed in both vertical and horizontal orientations. Red squares on images represent the theoretical pore size of 1.0 mm x 1.0 mm. Figure 95a and b show pore sizes for horizontal and vertical grids, respectively, printed from Formlabs Clear V4 resin. As expected, pore

sizes in both these grids are close to the theoretical, further highlighting how Formlabs Clear V4 print settings are optimised for its respective material. Figure 95c and d show pore sizes for horizontal and vertical grids, respectively, printed from a formulation of PEG575DA + 20% w/w AT + 1% TPO. As hypothesised, pore formation in the vertical grid was relatively accurate, showing close similarity to that of the theoretical pore size. However, pore formation in the horizontal grid was less accurate with only half the pore area having formed. This was to be expected, as the 20% w/w AT content was below what would have been the calculated value. Testing and printing with PEG575DA formulations containing above 20% w/w AT was opted against, as it was considered an unreasonable amount of additive that could severely affect material properties. Figure 95e and f show pore sizes for horizontal and vertical grids, respectively, printed from PEG575DA + 0.1241% w/w OG + 1% TPO formulations. Again the hypothesis proved correct, with excellent pore formation observed within the vertical grid. No pore formation was observed within the horizontal grid. This confirms that Orasol Orange G dye (and perhaps all photoabsorbers) have no effect on x-y dimension polymerisation. On the other hand, α-tocopherol and hydroquinone photoinhibitors exhibit excellent control over x-y dimension polymerisation and modest control over z dimension polymerisation. Ideally, to achieve prints with accurate x-y-z dimensions according to design, the formulation must contain both photoinhibitor and photoabsorber. A question raised, is whether the content of photoinhibitor calculated via this RT-FTIR spectroscopy method is the precise value required to achieve control of x-y dimension polymerisation. The likely answer is no. The method described measures the effect of photoinhibitor/photoabsorber on formulation cure depth (z dimension polymerisation) as opposed to x-y dimension polymerisation. It is a coincidence that calculated photoinhibitor contents yielded z-dimension polymerisation control, albeit limited. It is therefore reasonable to assume the calculated photoinhibitor content calculated via this method is grossly overestimated and that this method is better suited for calculation of photoabsorber content. With that said, it is expected that this method can be adapted facilitate measurement of photoinhibitor effect on formulation x-y dimension polymerisation.

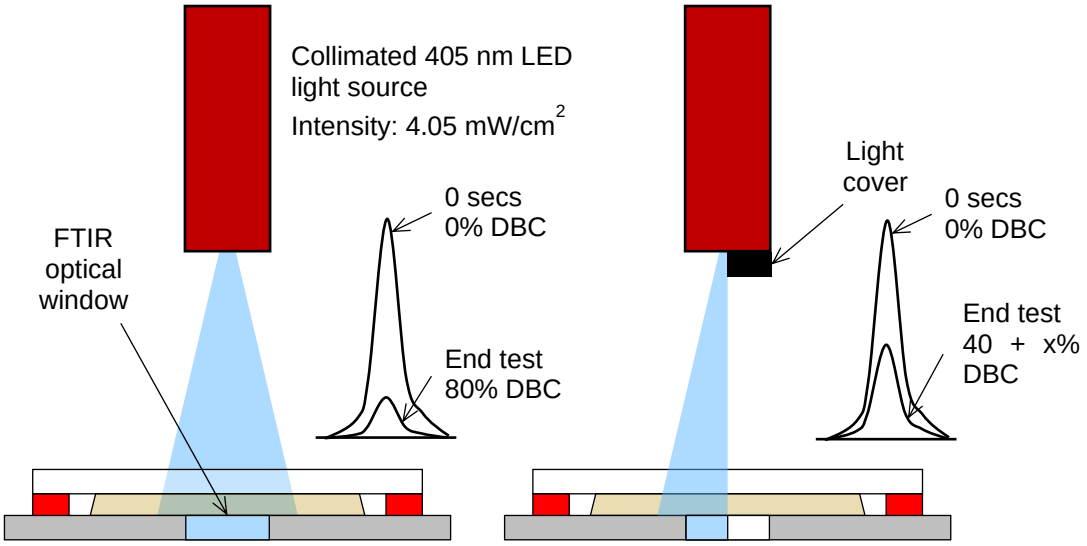

Figure 96 – Diagram detailing a modified version of the setup shown in Figure 91 to facilitate the measurement of photoinhibitor effect on formulation x-y dimension polymerisation. The left diagram shows a setup where all resin that covers the FTIR optical window is irradiated during testing. The right diagram shows the same setup except only half the resin that covers the optical window is irradiated.

Figure 96 shows a proposed setup for measurement of photoinhibitor effect on formulation x-y dimension polymerisation and determination of photoinhibitor content to precisely control x-y dimension polymerisation. Firstly, a reference material, with known good x-y dimension print resolution, is tested using the standard setup as before. DBC (%) is recorded after testing. A cover is then placed in front of the lamp so that only half of the optical window is irradiated during testing. As a result, only half of the resin sample covering the optical window will irradiated and cured. Theoretically, values for DBC (%) from these “half” tests would be half that generated from standard testing. However, it is more likely DBC (%) values from “half” tests would be larger than half, attributed to polymerisation in non-irradiated areas. This “overage” in DBC (%) could represent the target custom photopolymer formulations need to meet if similar x-y dimension print resolution were to be achieved. For example, if a standard test of a reference material yielded an end test DBC (%) value of 80% and a “half-light” test yielded an end test value of 44%, the overage would be 4%. If a standard test of a photopolymer formulation yielded

an end test value of 90%, the target end test value would be 49% ((90% / 2) + 4%). As before, modification of end test values to reach this target value, could be achieved through increasing amounts of photoinhibitor. Combination of the established method for identifying ideal photoabsorber content, and the proposed method for identifying ideal photoinhibitor content for a chosen formulation would, in theory, yield a photopolymer formulation optimised for reference material print settings.

6.2.5 Improving accuracy of the RT-FTIR spectroscopy tool through combination with photorheology

A major flaw in the presented RT-FTIR spectroscopy tool is that it is assumed that all formulations gel at the same DBC (%) value. This assumption is inadvertently made when attempting to match t@25%DBC values of photopolymer formulations with those of reference materials. In reality, photopolymer formulations do not all gel at the same DBC (%) value and hence matching of t@25%DBC values will not necessarily confer printability.

Table 28 – Table showing DBC (%) at gel point (DBC_{gel}) values for various photopolymer formulations. Adapted from Gorsche et al. (2017)[273].

Formulation	TPO-L content (% w/w)	DBC_{gel} (%)
IBOA	0.5	60 ± 2
IBOA + 10% w/w HDDA	0.5	17 ± 2
IBOA + 50% w/w HDDA	0.5	12 ± 1
HDDA	0.5	28 ± 2
HDDA + 20 rg% trithiol CTA	0.5	41 ± 3
HDDA + 40 rg% trithiol CTA	0.5	62 ± 4

Table 28 shows DBC_{gel} (%) values for monofunctional and difunctional acrylates (and their combinations) and mixtures of difunctional acrylates and trithiol chain transfer agents. Combination of acrylates with different functionalities appear to reduce DBC_{gel} (%) compared to their homopolymer equivalents whereas combination with difunctional acrylate HDDA with 20 and 40 rg% (reactive groups in formulation) trithiol CTA leads to an increase in DBC_{gel}. Incorrectly calculating additive values through matching of

t@25%DBC values can potentially lead to overpolymerisation and poor resolution in materials with DBC_{gel} (%) values lower than that of the reference material, or too little polymerisation, insufficient “green” strength and subsequent print failure in materials with DBC_{gel} (%) values above that of the reference material. It may therefore be more appropriate to calculate additives values through matching t@DBC_{gel} (%) values instead. Having a material that achieves gelation (and therefore “green” strength) at the same time as a reference material during the 3D printing process is more likely to result in printing success, than if two materials achieve an arbitrary DBC (%) at the same timepoint. In light of this, a decision was made to elucidate DBC_{gel} (%) values of photopolymer formulations of interest. Photorheology is a technique that allows for real-time measurement of sample rheological properties during UV-light irradiation. This allows for monitoring of rapid changes in mechanical properties such as gelation and vitrification.

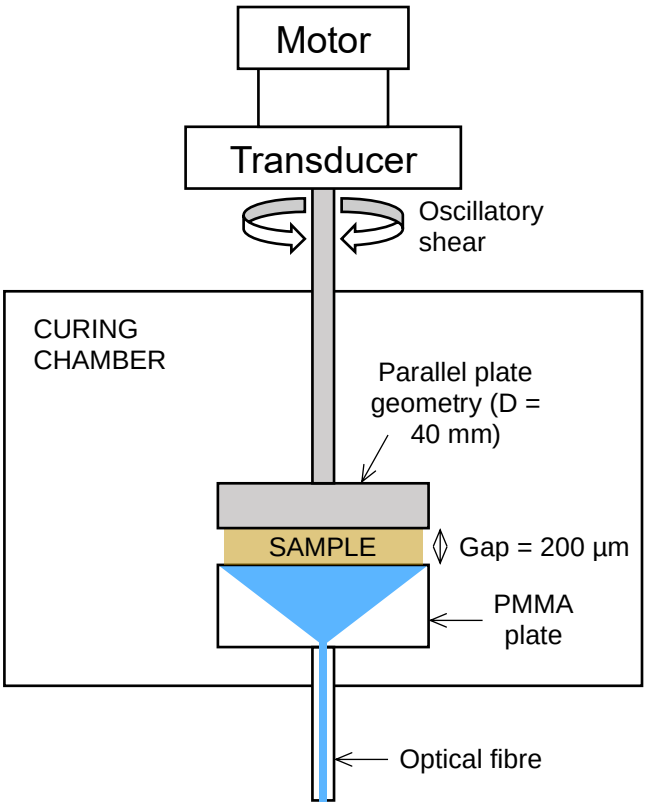

Figure 97 – Schematic diagram of a rotational rheometer attached with a UV curing system. Adapted from Park et al. (2014)[274].

Utilising both technologies in tandem, should in theory, allow for calculation of DBC_{gel} values of photocurable formulations of interest. To ensure reliability of tandem data, it was vital that conditions such as light intensity and sample thickness were kept the same. A light intensity of 2.00 mW and a sample thickness of 200 µm was chosen. Firstly, a range of different materials were tested using our standard RT-FTIR spectroscopy tool.

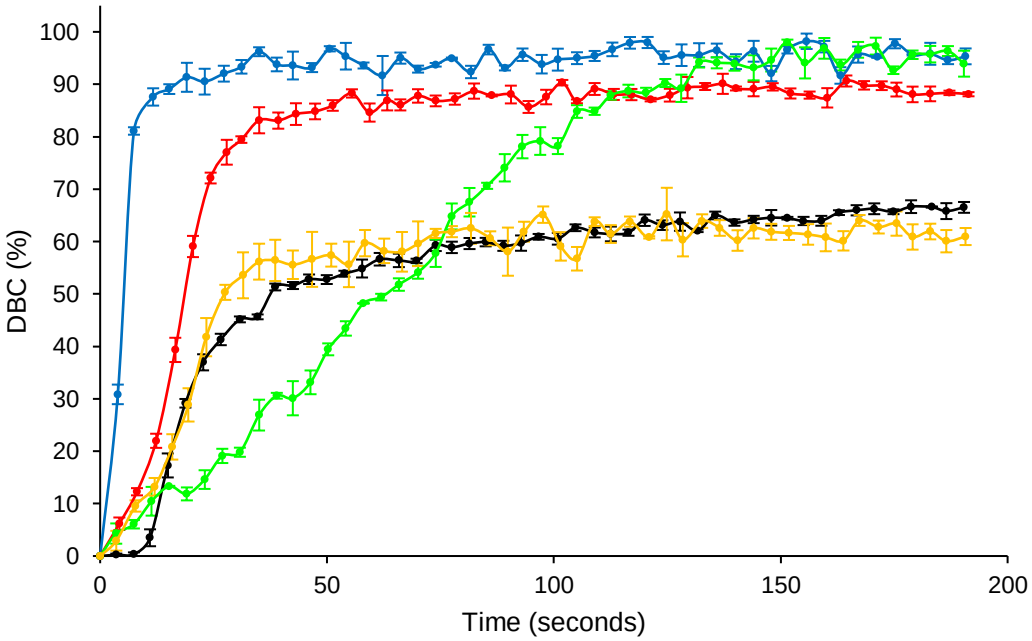

Figure 98 – Graph plotting mean DBC (%) against irradiation time for different photopolymer formulations. Plot results shown are: Formlabs Clear V4 resin (**–**), PEG575DA + 1% TPO (–); PEG550DMA + 1% TPO (–), PEG550DMA + 10% dithiol CTA + 1% TPO (–) and PEG550DMA + 10% ethyl lactate (–).

These materials were chosen as they were expected to display a range of t_{gel} due to different functional groups and addition of thiol CTAs or non-reactive diluents. From these plots (Figure 98), t@25% DBC values were calculated. These materials were then subjected to photorheology testing (Figure 99). Samples were allowed to equilibrate for 30 secs before irradiation with UV light. Material storage (elastic) and loss (viscous) moduli were measured continuously over a period of 10 minutes. The crossover of storage and loss moduli indicated material gelation. The time at which gelation occurred was recorded.

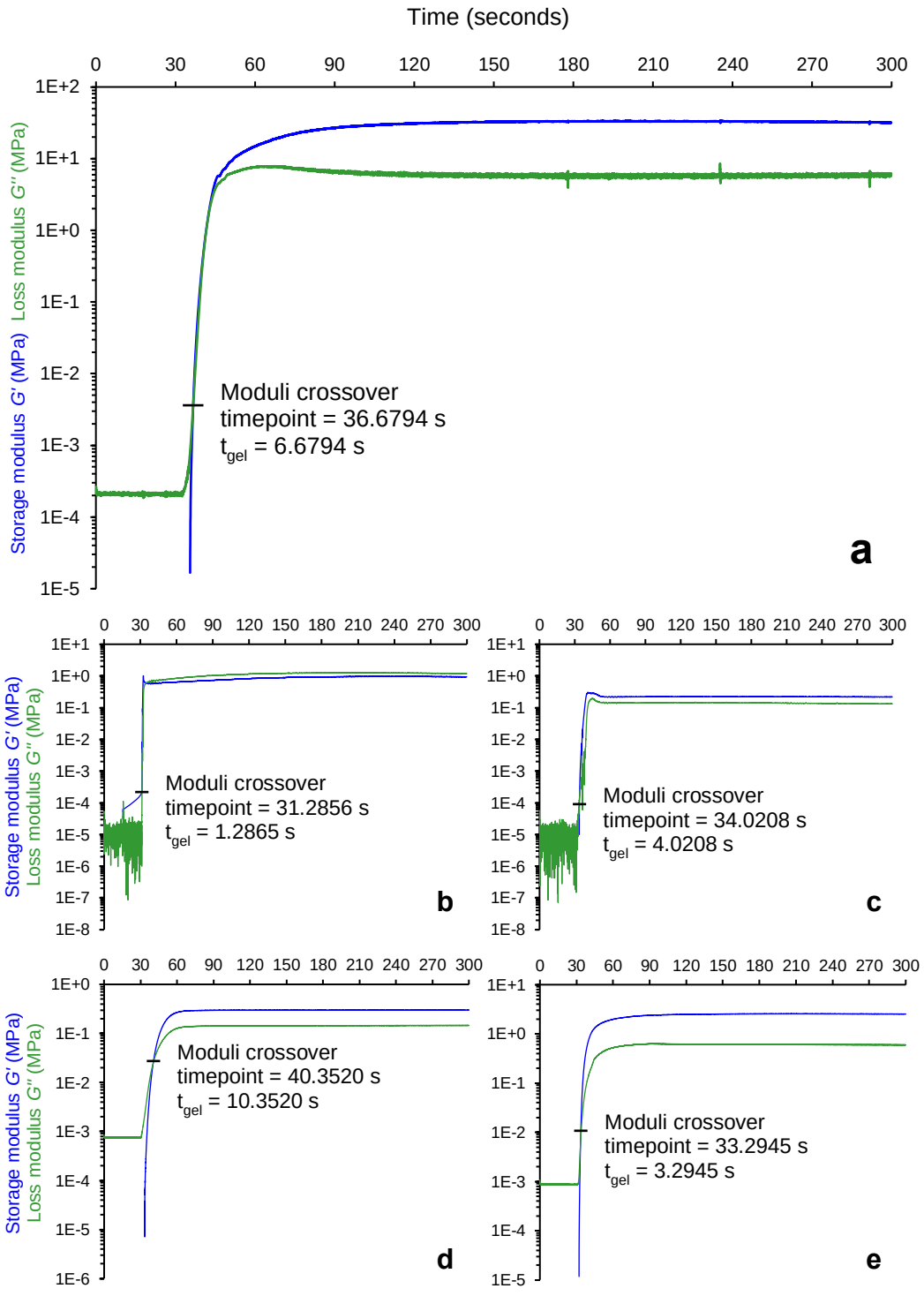

Figure 99 – Graphs plotting storage modulus *G'* (MPa) and loss modulus *G''* (MPa) versus time (seconds) for different photopolymer formulations. Plot results shown are for: **a** = Formlabs Clear V4 resin, **b** = PEG575DA + 1% TPO; **c** = PEG550DMA + 1% TPO, **d** = PEG550DMA + 10% dithiol CTA + 1% TPO, and **e** = PEG550DMA + 10% ethyl lactate.

Table 29 – Compilation of values obtained from tandem RT-FTIR spectroscopy and photorheology testing.

Formulation	TPO content (% w/w)	t@25% DBC (s)	t_{gel} (s)	DBC_{gel} (%)
Formlabs Clear V4	-	17.71	6.68	3.06
PEG575DA	1	3.52	1.29	0.78
PEG550DMA	1	12.92	4.02	4.23
PEG550DMA + 10% DT	1	36.97	10.35	8.05
PEG550DMA + 10% EL	1	16.78	3.29	2.94

Values for t_{gel} (s) of each material were input into above RT-FTIR spectroscopy constructed plots to generate values for DBC_{gel} (%). Table 29 compiles t@25% DBC (s), t_{gel} (s) and DBC_{gel} (%) values for all materials. At first glance, DBC_{gel} (%) values were of a lower magnitude than those reported by Gorsche et al. (2017)[273]. This was associated to poor correlation of data obtained from RT-FTIR and photorheology testing. Firstly, due to limited access to a photorheometer, each sample was only tested once, and hence photorheology data was potentially inaccurate. Secondly, although efforts were made to ensure testing conditions were similar, achieving the exact same conditions with the resources available was not possible. For example, the UV light source used for RT-FTIR spectroscopy exhibits a narrow emission spectra (λ 370 – 450 nm) whereas the UV light source for the photorheometer exhibits a large emission spectra (λ 250 – 650 nm). This leads to different curing conditions which would ultimately lead to different results. Other small differences between testing conditions (sample thickness, ambient light shielding, temperature, sample age etc.) can potentially lead to poor correlation of data and hence incorrect reporting of DBC_{gel} (%). Furthermore, the RT-FTIR spectrometer tool is limited as it can only capture data every 3 seconds (approximately). The inability to rapidly capture data leads to inaccurate data modelling and generation of inaccurate values for DBC_{gel} (%).

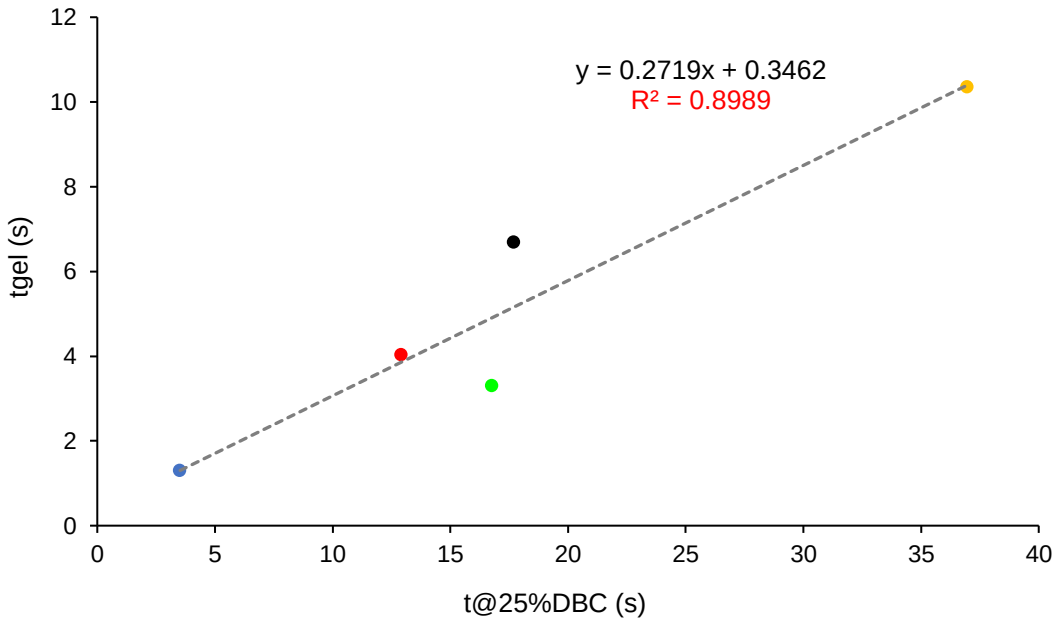

Figure 100 – Graph plotting t_{gel} (s) against t@25%DBC (s). Individual points correspond to: Formlabs Clear V4 resin (–), PEG575DA + 1% TPO (–); PEG550DMA + 1% TPO (–), PEG550DMA + 10% dithiol CTA + 1% TPO (–) and PEG550DMA + 10% ethyl lactate (–).

Nonetheless, a linear correlation between t@25%DBC (s) and t_{gel} (s) values exists (Figure 100). This validates the previous approach of using t@25%DBC (s) values for calculating additives. Formulations of PEG575DA, PEG550DMA, and PEG550DMA + 10% EL all exhibit t_{gel} (s) values below that of Formlabs Clear V4 resin. This implies that all of these materials are 3D printable using Formlabs Clear V4 print settings, albeit with formulation adjustments. Preliminary 3D printing confirmed the printability of all these formulations. PEG550DMA + 10% DT formulations display a t_{gel} (s) above that of Formlabs Clear V4 resin. This indicates that this material is not 3D printable using Formlabs Clear V4 print settings due to insufficient layer gelation rates. This was confirmed through preliminary 3D printing whereby printing with this material, using Formlabs Clear V4 print settings, resulted in successful prints. To obtain printability with this material it would be necessary to change the formulation. For example, reformulation with acrylates could sufficiently lower t_{gel} (s) of the resultant material to yield 3D printability. However, this would potentially lead to a change in material properties. The alternative option involves using a different print setting or using a different SLA 3D printer

apparatus that allows better control of print settings. For example, formulations containing thiol CTAs were printable using the MiiCraft+ SLA 3D printer, a machine that allowed wide control over light exposure time per layer.

6.2.6. Drug release studies

Initial drug release studies

A drug release study was designed and conducted in order to develop a baseline understanding of the drug release potential of synthesised materials. Aspirin (ASA) was chosen as a model compound to analyse drug release due to its cost, accessibility, reasonable solubility in all media included in the study, and numerous HPLC analysis methods that are well described in the literature. Photopolymer materials that were chosen for the preliminary drug release studies include PEG575DA, PTHF650DA, PPG425DA, PEG1000PUDMA, PTHF1000PUDMA and PPG1200PUDMA.

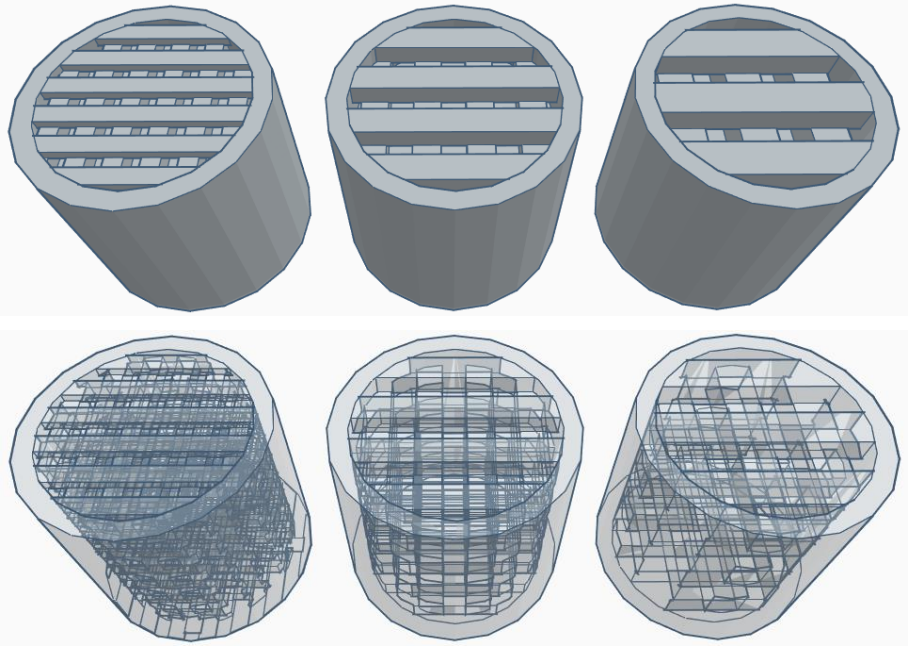

Figure 101 – Tinkercad generated images showing cylindrical mesh designs with different surface areas. Left images show 1.0 x 1.0 mm mesh with 1.0 x 1.0 mm pore size, middle images show 1.5 x 1.5 mm mesh with 1.5 x 1.5 mm pore size and right images show 2.0 x 2.0 mm mesh with 2.0 x 2.0 mm pore size.

Polyester-based materials were reserved for a separate analysis. PTHF1000PUDMA and PPG1200PUDMA were diluted with 20% w/w IBOA, and PEG1000PUDMA was diluted with 20% w/w HEA. All materials were formulated with 1% w/w TPO. For all samples, a cylindrical mesh structure was utilised as detailed in the previous chapter. Each layer of the mesh structure was a sheet composed of 1.0 x 1.0 mm cuboids, spaced 1.0 mm apart. Each stacked layer was rotated 90 °. This design was opted for to ensure each sample had a large surface area for drug diffusion.

Full descriptions for each resin formulation are detailed below (Table 30). Photoinhibitor concentrations of hydroquinone (HQ) were determined using the RT-FTIR method in the previous chapter. 5% w/v ASA loading was chosen for all samples to ensure each sample contained the same amount of drug. The total volume of the cylindrical mesh was determined, using Formlabs PreForm software, as 1.32 mL. Subsequently, it was calculated that each sample should contain 66 mg of ASA. Diluents and additives were added to base resins and mixed using a magnetic stirrer with heating until all additives had dissolved. Resins were degassed under vacuum prior to use.

Table 30 – Table showing full contents of photopolymer formulations used for preliminary drug release studies

Base resin	Reactive diluents	TPO content (% w/w)	HQ content (% w/w)	ASA content (% w/w)
PEG575DA	-	1	7.6	5
PTHF650DA	-	1	2.6	5
PPG425DA	-	1	0.5	5
PEG1000PUDMA	20% w/w HEA	1	8	5
PTHF1000PUDMA	20% w/w IBOA	1	2.3	5
PPG1200PUDMA	20% w/w IBOA	1	2	5

Samples were SLA 3D printed using an adapted tray setup, discussed earlier in the chapter, using pre-defined print settings for Clear V4 at a layer thickness of 0.1 mm. Three different formulations were used in a single print, limiting number of prints to 2, instead of 6. Time of printing was reduced from 33 mins x 6 = 3 hrs 18 mins to 56 mins x 2 = 1 hr 52 mins. It was observed that simple immersion of samples in IPA for 5 – 10 minutes did not fully remove uncured

resin from the mesh samples. Longer immersion was unadvisable as this could risk leaching of drug. Instead, a simple apparatus was devised that involved a 3D printed funnel fitted into a Hirsch funnel. Each sample was used to tightly plug the bottom of the 3D printed funnel.

Figure 102 – Images showing pilot drug release study setup.

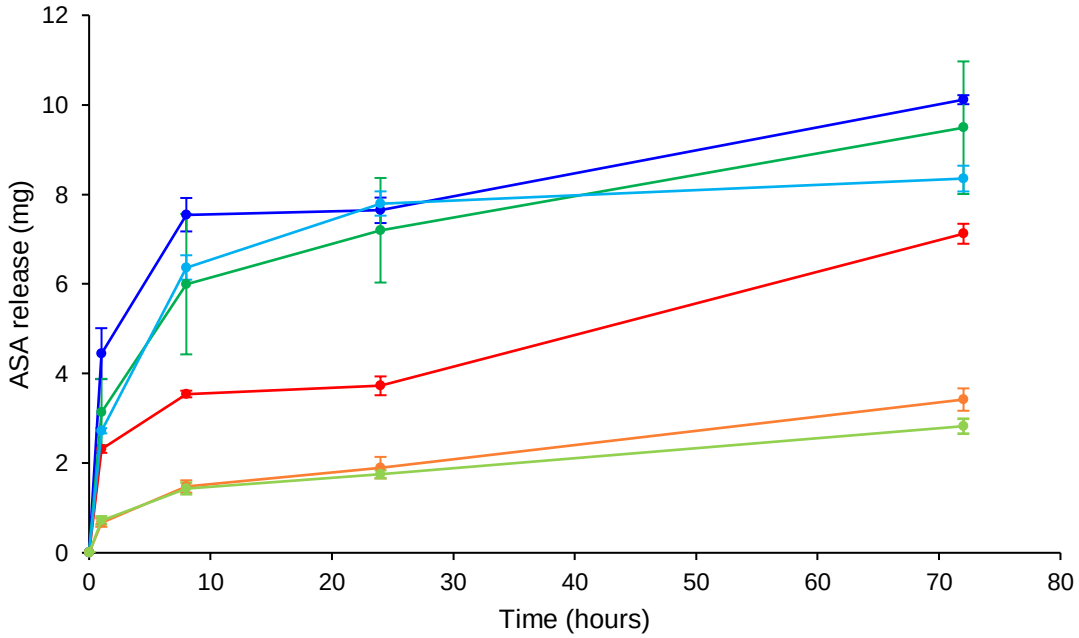

Figure 103 – Graph showing ASA drug release from mesh samples over a period of three days (72 hours). Plot results shown are: (–) PEG575DA, (–) PTHF650DA, (–) PPG425DA, (–) PEG1000PUDMA, (–) PTHF1000PUDMA and (–) PPG1200PUDMA.

A vacuum was applied, and a large quantity of IPA was added to the funnel. IPA was pulled through the mesh structure, resulting in clean mesh structures. Sleeves for mesh samples were also printed. These were fabricated to limit release of drug from a single mesh face, so drug content released could be attributed to a uni-directional release, as is intended for the proposed implant.

A TEGDVE formulation containing 1% P3C-P was used to fix the mesh sample into the sleeve. A cationic photopolymer system was utilised for this step to take advantage of “shadow” curing. This ensured that all the TEGDVE formulation fully polymerised, despite not fully irradiated, thereby preventing detachment of the mesh sample from the sleeve during analysis. Figure 103 highlights the drug release from cylindrical meshes over a period of 3 days. With all meshes, an initial burst release can be observed followed by a more gradual sustained release. Further monitoring over a larger time period would be required to ascertain whether drug release profiles adopt zero-order kinetics, and for how long this is maintained. Meshes fabricated from PEG575DA displayed the greatest overall release of drug (15.3% total drug content after 3 days), and the highest burst release after 1 and 8 h (6.7% and 11.4%, respectively). This is attributed to the hydrophilic nature of PEG575DA, facilitating water penetration into the mesh structure and thereby permitting an increased rate of drug diffusion. Meshes fabricated from PTHF650DA exhibit the second greatest overall release of drug (14.4% total drug content after 3 days), and the second highest burst release after 1 h (4.8%). In comparison, meshes fabricated from PPG425DA exhibit a lower overall release of drug (10.8% total drug content after 3 days) and a lower burst release (3.5%). Differences in burst release and overall 3-day release between PEG575DA, PTHF650DA and PPG425DA meshes were attributed to material hydrophilicity/lipophilicity and material pore size. Log P, is the logarithm of partition coefficient, defined as the ratio of the concentrations of a solute between two solvents, in most cases *n*-octanol and water. Log P is used to measure lipophilicity of compounds, where large log P values indicate lipophilicity and small log P values indicate hydrophilicity. Calculated log P (cLogP) values for PEGDA of molecular weight between 566.29 – 610.32 g/mol, calculated using ChemBioDraw Ultra software, were between

0.0172018 and -0.158397. cLogP values were also calculated for PTHFDA of molecular weights between 702.49 – 774.55 g/mol (cLog P values = 3.19 – 3.366) and PPGDA of molecular weights between 532.32 – 590.75 g/mol (cLog P values = 2.707 – 2.8404). As expected, PEG575DA has a low cLogP value, indicative of its hydrophilic nature. Both PTHF650DA and PPG425DA possess larger values for cLog P (2.707 – 3.366), indicating a more lipophilic nature. Materials of a lipophilic nature will permit less water penetration, less drug diffusion and therefore, less drug release. Despite lower cLogP values and therefore a more hydrophilic nature, PPG425DA meshes displayed lower burst and overall ASA release than PTHF650DA meshes. It is speculated that this is due to differences in material pore size. The pore size of materials formed from linear PTHF650DA, in theory, is larger than those formed from PPG425DA, due to reduced spacer size. Larger pores, irrespective of lipophilicity, facilitate greater water uptake, diffusion of entrapped compounds into the surrounding aqueous media. Subsequently, a larger burst and overall release of drug from the PTHF650DA mesh, in comparison to the PPG425DA mesh, is observed.

Pertaining to polyurethane dimethacrylate-based materials, all polyurethane dimethacrylate-based meshes displayed lower burst and overall ASA release in comparison to their diacrylate counterparts. This was attributed to an increase in lipophilicity due to inclusion of lipophilic isophorone isocyanate moieties within compound structures. PEGPUDMA of molecular weights between 1690.99 – 1735.01 g/mol possessed cLog P values of between 4.1376 and 3.96199, PTHFPUDMA of molecular weights between 1659.16 – 1703.18 g/mol possessed cLog P values of between 9.8244 and 8.9624, and PPGPUDMA of molecular weights between 1883.25 – 1941.29 possessed cLogP values of between 10.6688 and 10.8022. Drug release rates from PEG575DA (6.8% at 1 h and 15.3% at 3 d) and PEG1000PUDMA (4.1% at 1 h and 12.7% at 3 d) meshes were comparable, whereas drug release rates from PTHF1000PUDMA (1.1% at 1 h and 4.3% at 3 d) and PPG1200PUDMA (1.0% at 1 h and 5.2% at 3 d) were markedly below that of their diacrylate counterparts (4.8% at 1 h, 14.4% at 3 d; and 3.5% at 1 h, 10.8% at 3 d, respectively). There is a larger difference between ΔcLog P values for

PTHFPUDMA and PTHFDA materials (ΔcLog P = 6.6344 – 5.5964), and PPGPUDMA and PPGDA materials (ΔcLog P = 7.8284 – 8.0952), than between PEGPUDMA and PEGDA materials (ΔcLog P = 4.295997 – 3.9447882). The marked increased in lipophilicity of PTHFPUDMA and PPGPUDMA in comparison to diacrylate counterparts, compared to a less marked increased in lipophilicity of PEGPUDMA in comparison to PEGDA, may explain the above observed differences in drug release rates. The larger theoretical pore size of PEG1000PUDMA materials in comparison to PEG575DA and formulation with 20% w/w water soluble HEA likely further contribute to the similar drug release rates of both materials.

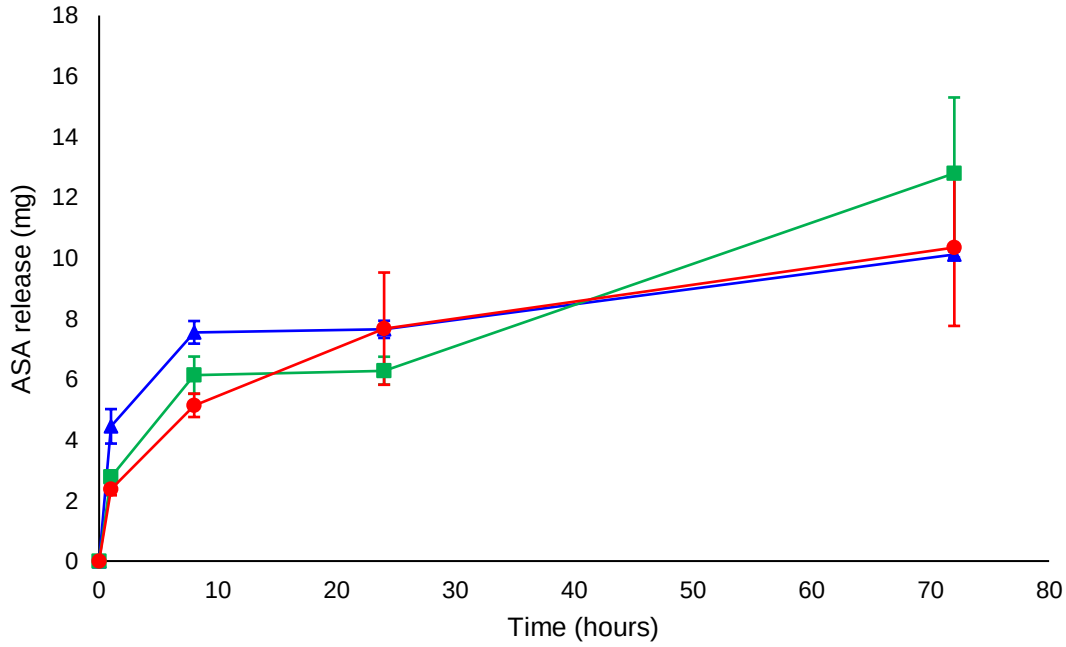

Figure 104 – Graph showing ASA drug release from PEG575DA mesh samples over a period of three days (72 hours). Plot results shown are: (–) 1.0 x 1.0 mm mesh w/ 1.0 x 1.0 mm pore size, (–) 1.5 x 1.5 mm mesh w/ 1.5 x 1.5 mm pore size, (–) 2.0 x 2.0 mm mesh w/ 2.0 x 2.0 mm pore size.

Figure 104 shows drug release from cylindrical meshes formed from PEG575DA, all containing, as before, 5% w/w ASA. In addition to the 1.0 x 1.0 mm mesh w/ 1.0 x 1.0 mm pore size design as used before, a 1.5 x 1.5 mm mesh w/ 1.5 x 1.5 mm pore size and 2.0 x 2.0 mm mesh w/ 2.0 x 2.0 mm pore size mesh designs were also used to facilitate analysis of how sample design contributes to material drug release properties. Whilst the 1.0 x 1.0 mm mesh

and 1.5 x 1.5 mm mesh designs required 1.32 mL of resin for construction, and hence had the same drug content, the 2.0 x 2.0 mm mesh design required 1.33 mL of resin for construction and hence contained 66.5 mg of ASA. Prior to analysis, it was expected that the 1.0 x 1.0 mm mesh design would exhibit a higher drug release rate than other designs, due to an increased surface area. An increased surface area permits greater diffusion of drug into the aqueous medium. This hypothesis is somewhat confirmed at early timepoints, where the 1.0 x 1.0 mm mesh sample released 6.7 and 11.4 % ASA at 1 and 8 h timepoints, respectively, whereas the 1.5 x 1.5 mm mesh sample released 4.1 and 9.3 % ASA at 1 and 8 h timepoints, respectively, and the 2.0 x 2.0 mm mesh sample released 3.6 and 7.7 % ASA at 1 and 8 h timepoints. These observations support the hypothesis that drug release correlates positively with increasing surface area. Past the 8 h timepoint, data for drug release for all samples displays greater variance and does not support the initial hypothesis.

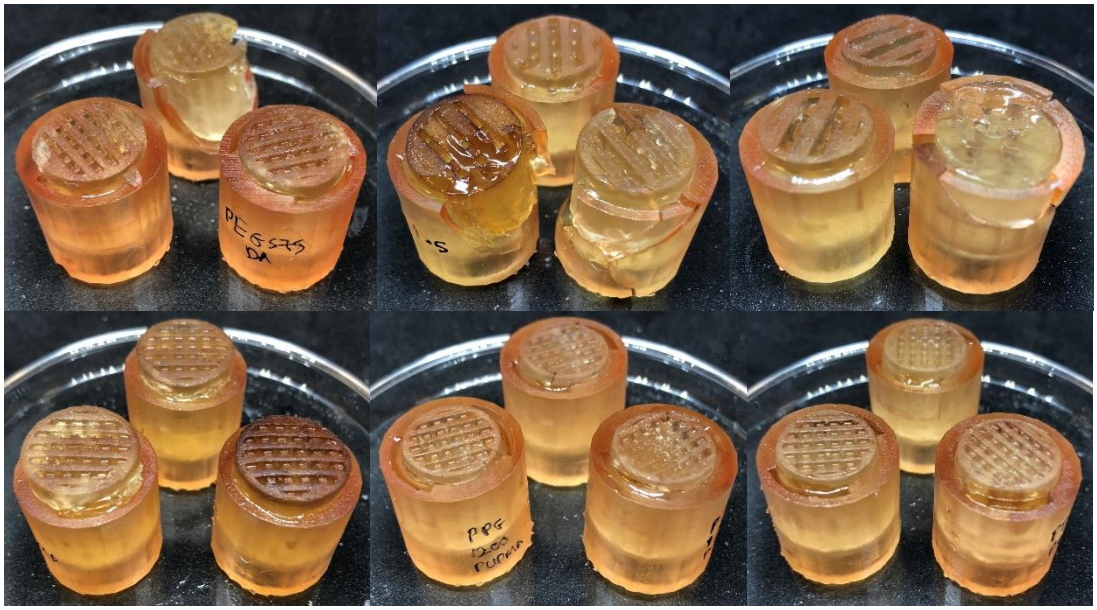

Figure 105 – Images showing sleeved samples after 3-day drug release study. The top row shows PEG575DA samples with 1.0 x 1.0 (left), 1.5 x 1.5 (middle) and 2.0 x 2.0 mm (right) meshes and pores. The bottom row shows PEG1000PUDMA (left), PPG1200PUDMA (middle) and PTHF1000PUDMA (right) samples.

The 1.5 x 1.5 mm mesh sample has the greatest ASA release after 3 days (19.4 %), whereas the 1.0 x 1.0 mm mesh and 2.0 x 2.0 mm mesh samples displayed similar ASA releases after 3 days (15.3 and 15.7 %, respectively). This was unusual, as it was expected the mesh samples with the greatest surface area (2.0 x 2.0 mm mesh) would show greatest ASA release at this timepoint. These varied and unpredictable results were attributed to sample sleeves breaking *in situ* due to mesh swelling (see Figure 105 – top row), leading to increased mesh surface area and consequently, increased drug release. The above again highlights the mechanical shortcomings of diacrylate-based materials, where breaking of the mesh after a 1 d period led to an unpredictable drug release profile, and ultimately treatment failure. It is worth noting that no polyurethane dimethacrylate-based samples broke in situ after 3 days (Figure 105) and all samples gave coherent data with low variance. Drug release studies beyond this pilot study will abandon the use of sleeves so as to prevent any damage to the mesh sample, and will be carried out over a larger time period (1 month) so that the amount of drug release and drug release kinetics can be fully elucidated for each material and/or design.

Wider drug release studies

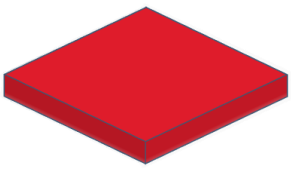

Figure 106 – Tinkercad generated image showing design of square film used for general drug release studies.

Pilot drug release studies were utilised as a learning curve for further drug release studies, with a number of alterations made to in relation to sample preparation and drug release testing. As mentioned, sleeves with the aim of permitting uni-directional release of drug were abandoned in the next phase of drug release testing. This was due to sleeves breaking *in situ*, resulting in variant surface area and ultimately drug release. Furthermore, the size of drug release meshes were reduced to more accurately represent dimensions of a

drug release mesh/film. For general samples, the complicated mesh design was also abandoned. This was done for two reasons. Firstly, a simpler design meant a lower variance in effective surface area. Only the effect of material properties on drug release was to be considered for general studies and hence maintaining a constant sample surface area ensured this. Secondly, a large range of materials were examined. Using a print design with complicated x-y-z dimensions would require a large amount of time to elucidate ideal printing formulations for these materials. Use of a simpler design meant time efficient arbitrary material formulations could be used. The design used was a simple square film (10.0 mm x 10.0 mm x 1.0 mm).

Table 31 – Table showing all material formulations used for general drug release studies.

Base monomer (+ 1% w/w TPO)	Additive 1 (% w/w)	Additive 2 (% w/w)	Drug (% w/w)
PEG550DMA			3% SA
PEG575DA			3% SA
PTHF650DMA			3% SA
PTHF650DA			3% SA
PLA400DMA			3% SA
PLGA400DMA			3% SA
PGA400DMA			3% SA
PEG1000PUDMA	20% HEA		3% SA
PEG1000PUDMA	20% TEGDA		3% SA
PEG1000PUDMA	20% TMPTA		3% SA
PEG1000PUDMA	20% TEGDA	10% DT	3% SA
PEG1000PUDMA	20% TEGDA	10% QT	3% SA
PEG1000PUDMA	20% TEGDA	10% EL	3% SA
PTHF1000PUDMA	20% IBOA		3% SA
PTHF1000PUDMA	20% HDDA		3% SA
PTHF1000PUDMA	20% TMPTA		3% SA
PTHF1000PUDMA	20% HDDA	10% DT	3% SA
PTHF1000PUDMA	20% HDDA	10% QT	3% SA
PTHF1000PUDMA	20% HDDA	10% EL	3% SA
PLA1000PUDMA	15% EL		3% SA
PLGA1000PUDMA	15% EL		3% SA
PEG400PUDMA	15% EL		3% SA
PTHF650PUDMA	15% EL		3% SA

To reduce the amount of resin required per print, objects were printed directly onto the print platform, forgoing the use of supports. Testing conditions were simplified. This involved placing samples into PBS containing vials instead of suspending samples. An incubated shaker was also utilised to provide temperature and shaking conditions, as opposed to an oil bath and magnetic stirring, respectively. This was done to simplify the process of aliquot sampling and to avoid potential sample damage caused by magnetic stirring. Table 31 lists all the material formulations used for general drug release studies. Salicylic acid (SA) was used instead of acetylsalicylic acid (ASA) as a model drug. This was due to a concern that the drug may hydrolyse over a long time period (28 days), leading to an inaccurate drug release calculation from HPLC chromatograms.

Figure 107 shows SA drug release (%) against time (hours) for non-polyurethane dimethacrylate materials. Plots show drug release (%) at specific timepoints for each material. PEG550DMA and PEG575DA materials display burst releases (26.27 and 31.47% drug release, respectively) within the first two hours, followed by a steady decrease in drug release (per timepoint) attributed to solution saturation. The observation of a burst release can be attributed to rapid diffusion of drug at or near the polymer matrix surfaces. The slower, sustained release of drug that follows is associated to gradual penetrance of media into the polymer matrix that facilitates diffusion of deeper entrapped drug. At the 3 day timepoint, both materials released approximately 5% of drug between aliquot samples. It was presumed that the removal of an aliquot permitted an additional 5% drug release from materials before a saturation point was once again reached. Therefore, it was assumed that solution saturation for these materials occur at the 3 day timepoint. PTHF650DMA and PTHF650DA materials also display burst releases (16.53 and 14.37% drug release, respectively) like PEG550DMA and PEG575DA materials, but to a lesser extent. This was expected due to PTHF being more hydrophobic than PEG and hence less marked swelling and drug release from PTHF650DMA and PTHF650DA materials was observed.

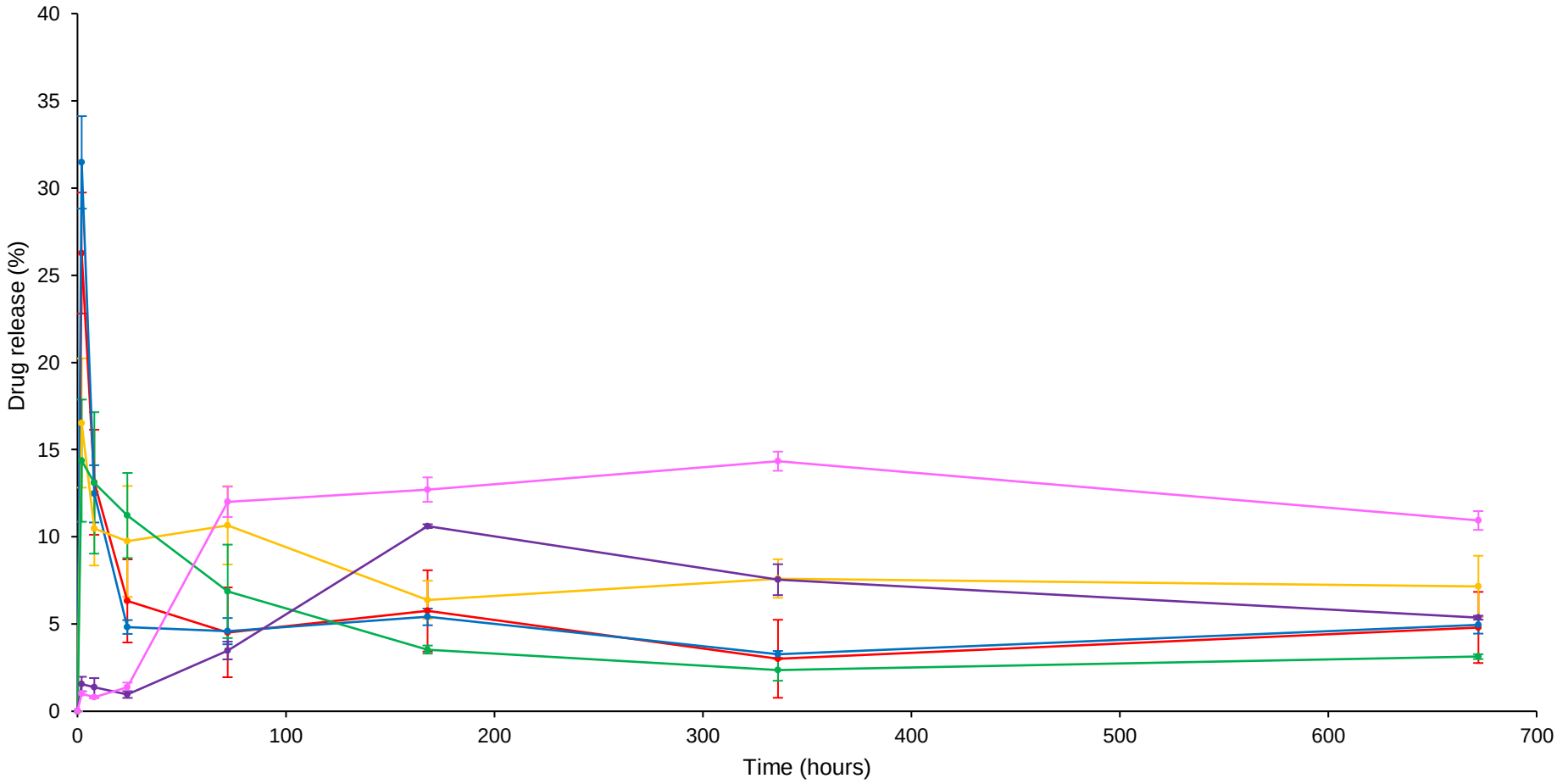

Figure 107 – Graph plotting SA drug release (%) at specific time intervals (hours) for non-PUDMA materials. Plot results shown are: PEG550DMA (–), PEG575DA (–); PTHF650DMA (–), PTHF650DA (–), PLGA400DMA (–) and PGA400DMA (–).

A less marked decrease in drug release (per timepoint) was observed before solution saturation was reached at approximately 1 week for both materials. No burst release was observed from PLGA400DMA and PGA400DMA materials. PLGA400DMA and PGA400DMA materials displayed sharp increases in drug release from 24 hours to 1 week (3.90 to 18.00% drug release) and from 24 hours to 3 days (3.19 to 15.19% drug release). Both PLA and PLGA are more hydrophilic PTHF, so the lack of burst release from these materials cannot be attributed to lack of hydrophilicity.

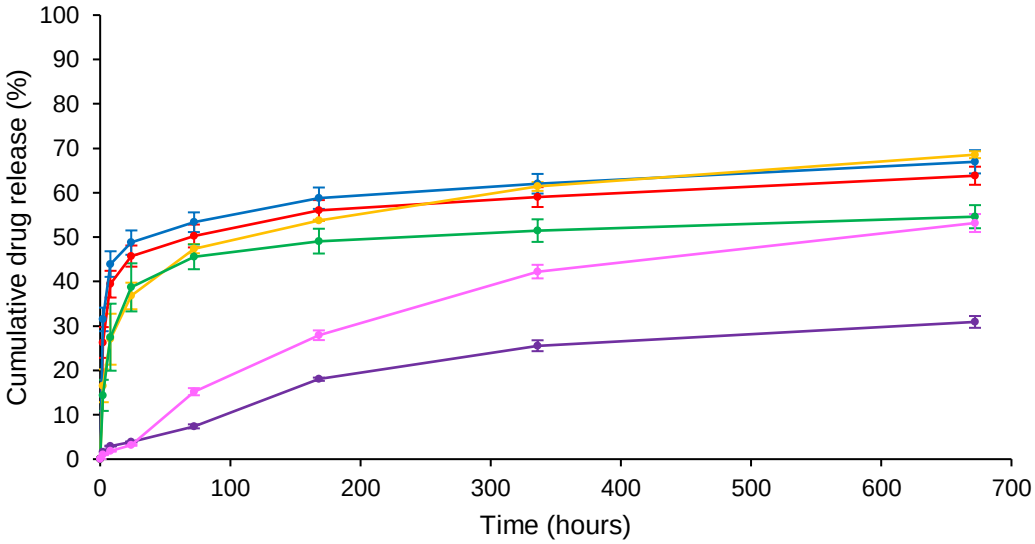

Figure 108 – Graph plotting cumulative SA drug release (%) against time (hours) for non-PUDMA materials. Plot results shown are: PEG550DMA (–), PEG575DA (–); PTHF650DMA (–), PTHF650DA (–), PLGA400DMA (–) and PGA400DMA (–).

Instead, it is speculated that increased crosslinking density (PLGA400/PGA400 versus PTHF650) and increased glass transition temperature may lead to an attenuated drug release. With the latter, drug diffusion is faster in rubbery amorphous networks (Tg below 37 °C) than in glassy crystalline networks (Tg above 37 °C)[210]. The Tg of PLGA400DMA and PGA400DMA were calculated to be above 37 °C, which may explain their associated reduced drug release rates. Sharper increases in drug release from 3 to 7 days onwards for these formulations could be attributed to bulk polymer matrix degradation but may also result from a prolonged initial release (no

burst release). Further investigation of these polyester-based formulations is required to ascertain whether polymer matrix degradation significantly influence drug release kinetics. Figure 108 shows cumulative SA drug release (%) against time (hours). Here it is observable that PEG and PTHF di(meth)acrylate materials displayed a burst release followed by a steady zero order release after approximately 3 days or 1 week. In contrast, PLGA/PGA dimethacrylate materials showed a relatively steady first order release over a 28 day period.

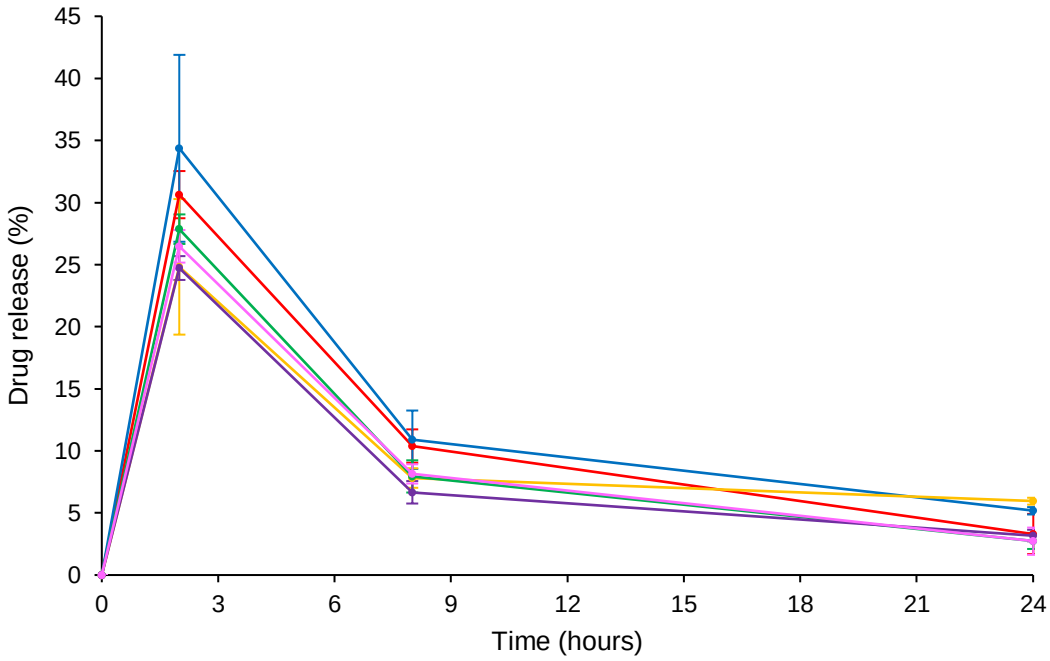

Figure 109 – Graph plotting SA drug release (%) at specific time intervals (hours) within 24 hours for PEG1000PUDMA heteropolymer materials. Plot results shown are: “PEG1000PUDMA” + 20% HEA (–), “” + 20% TEGDA (–); “” + 20% TMPTA (–), “” + 20% TEGDA + 10% dithiol CTA (–), “” + 20% TEGDA + 10% tetrathiol CTA (–), and “” + 20% TEGDA + 10% EL (–).

Figure 109 and Figure 110 show SA drug release (%) against time (hours) for PEG1000PUDMA materials. Both plots indicate that all PEG1000PUDMA materials displayed a similar burst release at 2 hours followed by a gradual decrease in drug release (per timepoint) until a solution saturation was reached at approximately 1 week.

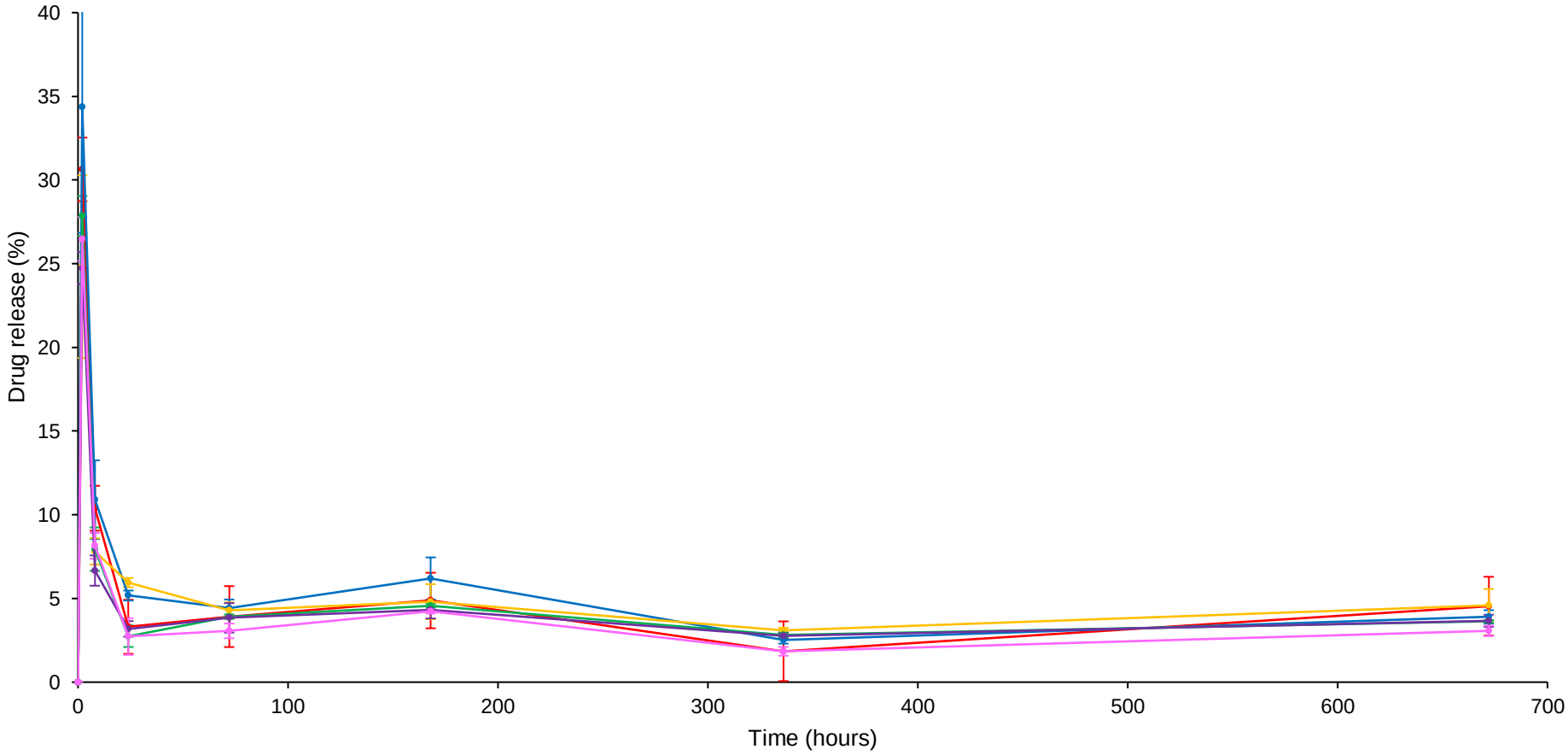

Figure 110 – Graph plotting SA drug release (%) at specific time intervals (hours) for PEG1000PUDMA heteropolymer materials. Plot results shown are: “PEG1000PUDMA” + 20% HEA (–), “” + 20% TEGDA (–); “” + 20% TMPTA (–), “” + 20% TEGDA + 10% dithiol CTA (–), “” + 20% TEGDA + 10% tetrathiol CTA (–), and “” + 20% TEGDA + 10% EL (–).

“PEG1000PUDMA” + 20% HEA and “” + 20% TEGDA materials displayed the highest burst releases at 2 days (30.64 and 34.37%, respectively) whereas “” + 20% TMPTA and “” + 20% HDDA + 10% tetrathiol CTA displayed the lower burst releases at 2 days (24.82 and 24.73%, respectively). This was associated with lower crosslinking density within materials containing monofunctional HEA and difunctional TEGDA, that facilitated material water penetration and drug diffusion, as opposed to materials with higher crosslinking density containing trifunctional TMPTA and tetrafunctional tetrathiol CTA. Furthermore, HEA and TEGDA are more hydrophilic than TMPTA and tetrathiol CTA, further aiding water penetration and drug diffusion. Unexpectedly, ethyl lactate containing materials displayed a relatively low burst release and a subsequently lower cumulative release (%).

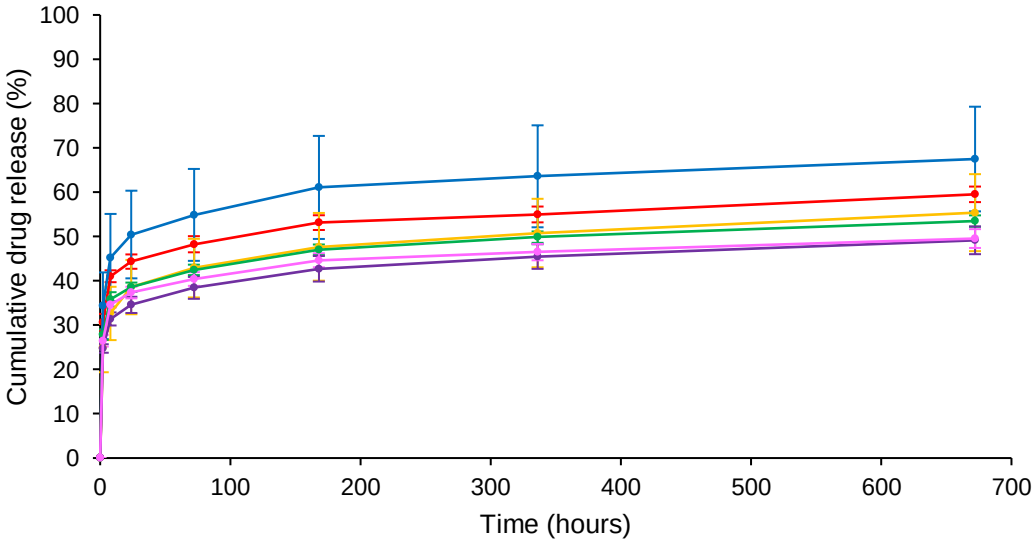

Figure 111 – Graph plotting cumulative SA drug release (%) against time (hours) for PEG1000PUDMA heteropolymer materials. Plot results shown are: “PEG1000PUDMA” + 20% HEA (–), “” + 20% TEGDA (–); “” + 20% TMPTA (–), “” + 20% TEGDA + 10% dithiol CTA (–), “” + 20% TEGDA + 10% tetrathiol CTA (–), and “” + 20% TEGDA + 10% EL (–).

Materials containing non-reactive diluents are porous, theoretically increasing material surface area and ultimately drug diffusion. It was hypothesised that ethyl lactate altered the solution saturation point, curtailing the release of salicylic acid from the sample. PEG1000PUDMA materials display similar drug

release kinetics to PEG di(meth)acrylate materials. They both showed comparable burst release at 2 hours (PEG1000PUDMA materials, 34.37 – 24.73%, PEG di(meth)acrylate materials, 31.47 – 26.27%), followed by gradual decrease in drug release (per time point) until a zero order release (attributed to solution saturation) was obtained at approximately 1 week. This is a positive note for PEG1000PUDMA materials, as there was previous concern that improved and customisable mechanical properties of PEG1000PUDMA materials in comparison to PEG di(meth)acrylate materials would be offset by stunted drug release kinetics.

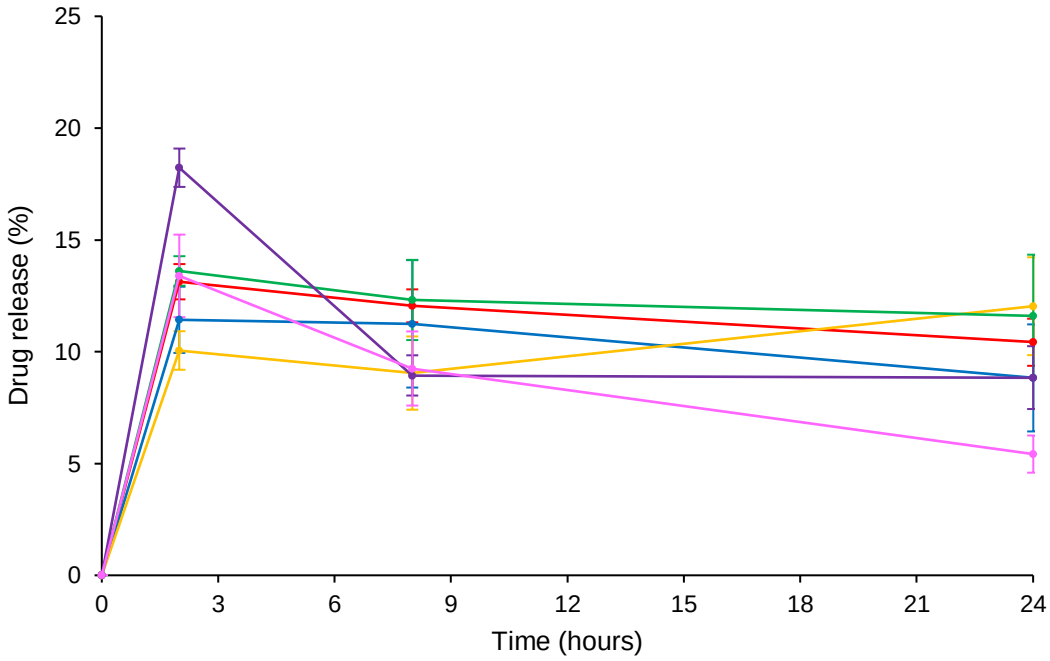

Figure 112 – Graph plotting SA drug release (%) at specific time intervals (hours) within 24 hours for PTHF1000PUDMA heteropolymer materials. Plot results shown are: “PTHF1000PUDMA” + 20% IBOA (–), “” + 20% HDDA (–); “” + 20% TMPTA (–), “” + 20% HDDA + 10% dithiol CTA (–), “” + 20% HDDA + 10% tetrathiol CTA (–), and “” + 20% HDDA + 10% EL (–).

Figure 112 and Figure 113 show SA drug release (%) against time (hours) for PTHF1000PUDMA materials.

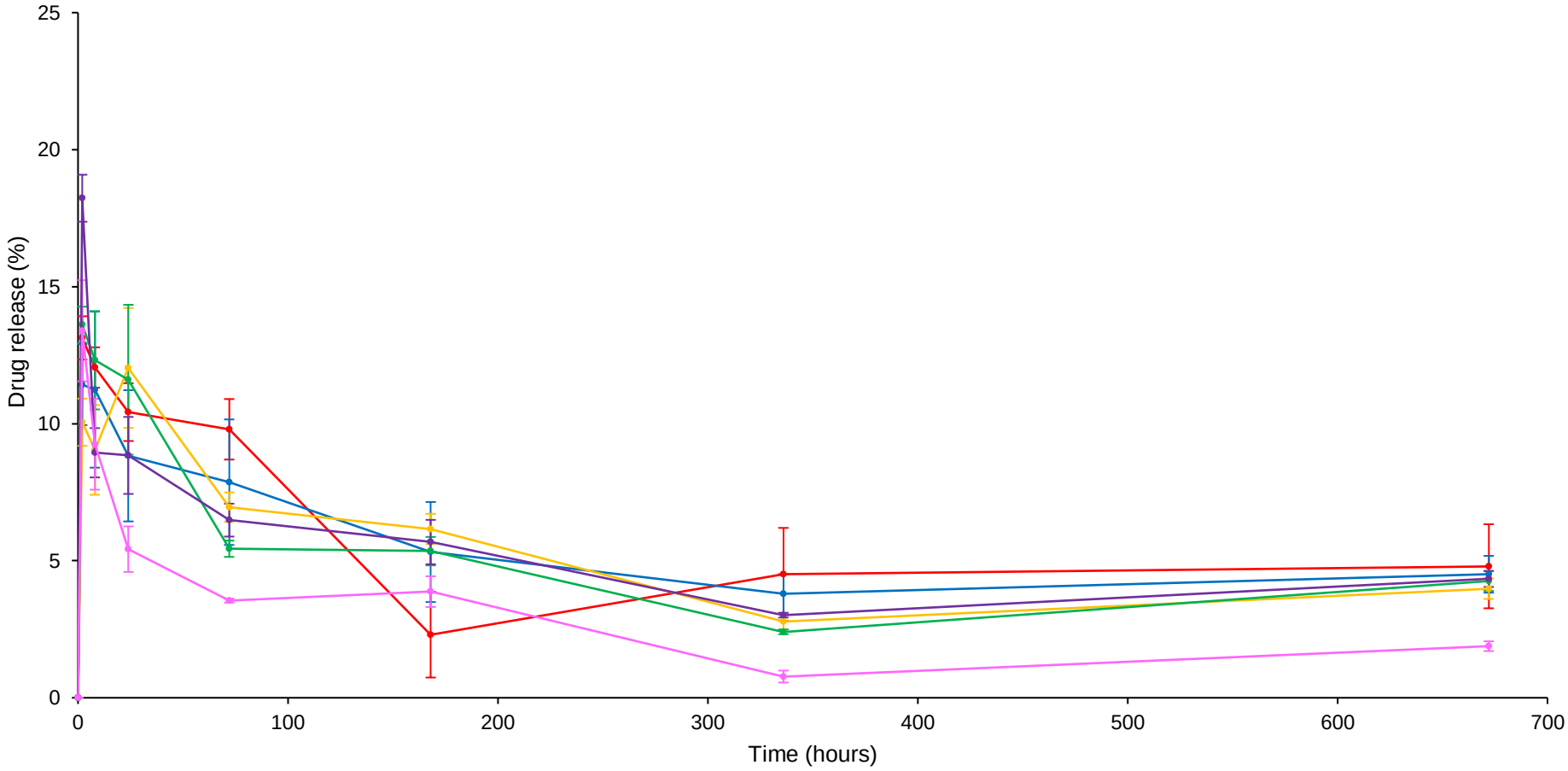

Figure 113 – Graph plotting SA drug release (%) at specific time intervals (hours) for PTHF1000PUDMA heteropolymer materials. Plot results shown are: “PTHF1000PUDMA” + 20% IBOA (–), “” + 20% HDDA (–); “” + 20% TMPTA (–), “” + 20% HDDA + 10% dithiol CTA (–), “” + 20% HDDA + 10% tetrathiol CTA (–), and “” + 20% HDDA + 10% EL (–).

As with PEG1000PUDMA, PTHF1000PUDMA materials displayed similar drug release kinetics to one another, displaying burst release at 2 hours of between 18.23 and 10.06%, followed by a gradual decrease in drug release (per timepoint) until a zero order release was established between 3 days and 1 week.

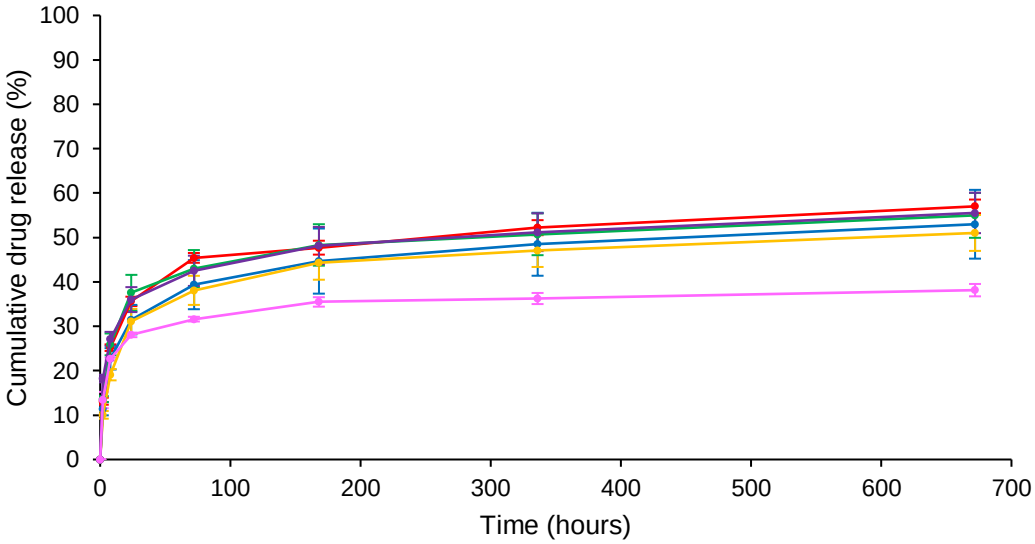

Figure 114 – Graph plotting cumulative SA drug release (%) against time (hours) for PTHF1000PUDMA heteropolymer materials. Plot results shown are: “PTHF1000PUDMA” + 20% IBOA (–), “” + 20% HDDA (–); “” + 20% TMPTA (–), “” + 20% HDDA + 10% dithiol CTA (–), “” + 20% HDDA + 10% tetrathiol CTA (–), and “” + 20% HDDA + 10% EL (–).

These drug release kinetics are comparable to those of PTHF di(meth)acrylate materials which exhibited burst release at 2 hours of between 16.53 and 14.37% and zero order release after 3 days. As with PEG1000PUDMA materials, this implies that PTHF1000PUDMA materials possess superior mechanical properties to those of PTHF di(meth)acrylate with a wide breadth for variation, whilst maintaining reliable drug release kinetics akin to PTHF (di)methacrylates.

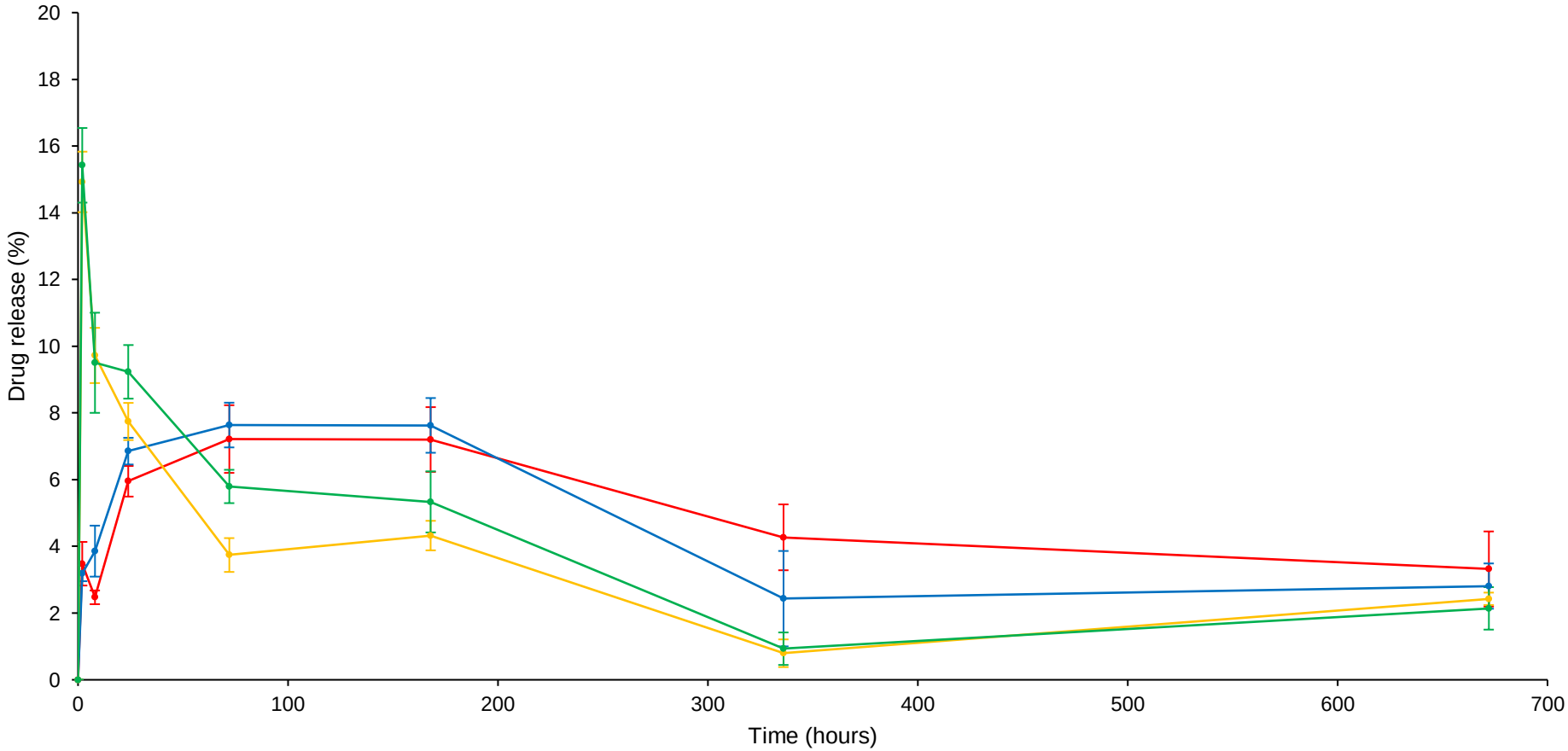

Figure 115 – Graph plotting SA drug release (%) at specific time intervals (hours) for select polyurethane dimethacrylate materials. Plot results shown are: PLA1000PUDMA + 20% TEGDA + 8% ethyl lactate (–), PLGA1000PUDMA + 20% TEGDA + 8% ethyl lactate (–), PEG400PUDMA + 15% ethyl lactate (–) and PTHF650PUDMA + 15% ethyl lactate (–).

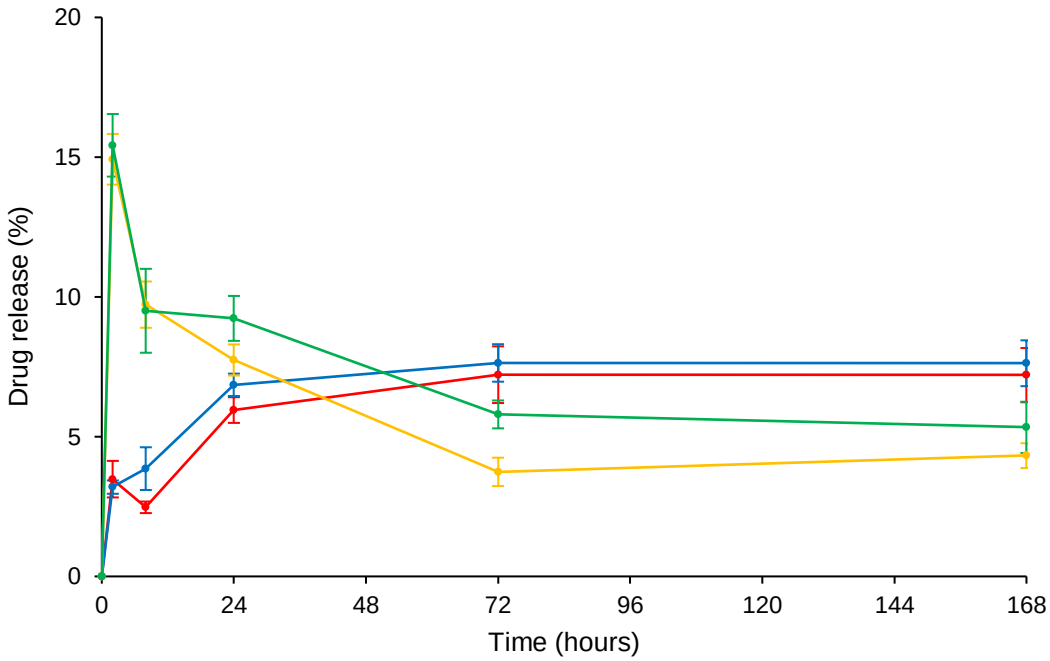

Figure 116 – Graph plotting SA drug release (%) at specific time intervals (hours) within 24 hours for select polyurethane dimethacrylate materials. Plot results shown are: PLA1000PUDMA + 20% TEGDA + 8% ethyl lactate (–), PLGA1000PUDMA + 20% TEGDA + 8% ethyl lactate (–), PEG400PUDMA + 15% ethyl lactate (–) and PTHF650PUDMA + 15% ethyl lactate (–).

Figure 115 and Figure 116 show SA drug release (%) against time (hours) for PL(G)A1000PUDMA, PEG400PUDMA and PTHF650PUDMA materials. All samples for these materials displayed attenuated drug release and low cumulative drug release over 48 days. Coincidently, all these formulations were formulated with ethyl lactate. This further supports the hypothesis that ethyl lactate alters the solution saturation point, reducing salicylic acid release.

This may find use as an additive for delaying release of drugs that require controlled release rates over long periods of time. As with their polyester dimethacrylate counterparts, PL(G)A1000PUDMA materials did not show a considerable burst release, instead showing a near zero order release of drug from 2 hours onwards. Unlike previously, PTHF650PUDMA materials showed a greater burst release at 2 hours than PEG400PUDMA (15.4 versus 14.9%, respectively). This was attributed to the shortening of spacer compounds

leading to an increased proportion of “hard” hydrophobic isophorone diurethane linkage segments. Differences in hydrophilicity between PEG400PUDMA and PTHF650PUDMA materials are likely negligible and it is more probable that crosslinking density dictates drug release kinetics of these two materials. As PEG400 is a shorter spacer compound than PTHF650, crosslinking density of PEG400PUDMA is higher and hence a lower burst release is to be expected. This indicates polyester-based photocurable materials may benefit the release of drugs that require controlled release over long periods of time. Next, release of different salicylic acid concentrations and different drugs from PEG1000PUDMA and PTHF1000PUDMA materials was investigated.

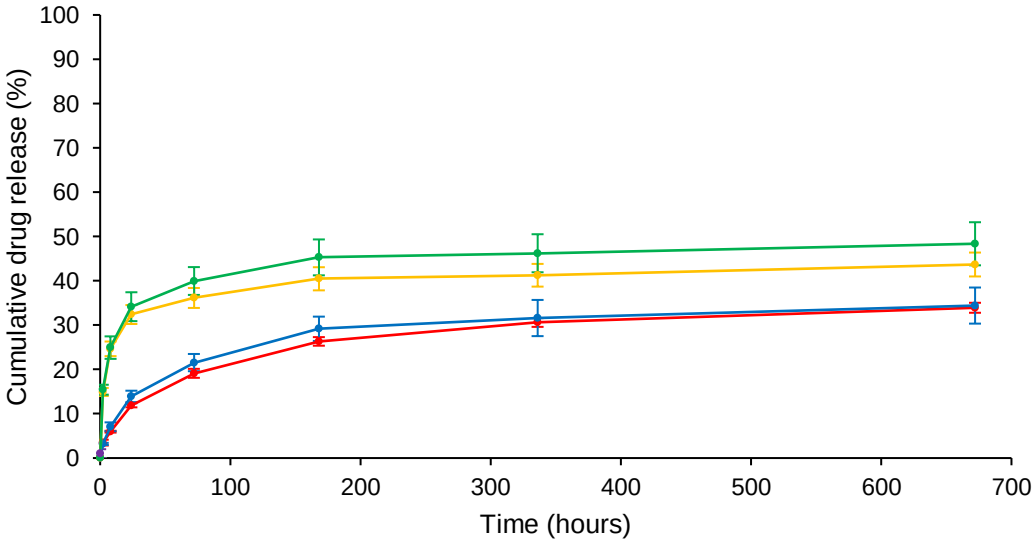

Figure 117 – Graph plotting SA drug release (%) against time (hours) for select polyurethane dimethacrylate materials. Plot results shown are: PLA1000PUDMA + 20% TEGDA + 8% ethyl lactate (–), “” + PLGA1000PUDMA + 20% TEGDA + 8% ethyl lactate (–), PEG400PUDMA + 15% ethyl lactate (–) and PTHF650PUDMA + 15% ethyl lactate (–).

Exploring drug release rates from materials containing different concentrations is important, as drug release kinetics will change depending on solution saturation and media turnover (modelled by aliquot sample). For example, in the gastric compartment, solution saturation is rarely achieved, due to large

media volumes and a high media turnover, whereas in bone compartments, solution saturation is readily achieved due to low media turnover.

Table 32 – Table showing material formulations used to investigate release kinetics of different SA concentrations and different drugs from PEG1000PUDMA and PTHFPUDMA materials.

Base monomer (+ 1% w/w TPO)	Additive 1 (% w/w)	Drug
PEG1000PUDMA	20% w/w TEGDA	1% w/w SA
PEG1000PUDMA	20% w/w TEGDA	5% w/w SA
PEG1000PUDMA	20% w/w TEGDA	3% w/w PM
PEG1000PUDMA	20% w/w TEGDA	3% w/w NX
PTHF1000PUDMA	20% w/w HDDA	1% w/w SA
PTHF1000PUDMA	20% w/w HDDA	5% w/w SA
PTHF1000PUDMA	20% w/w HDDA	3% w/w PM
PTHF1000PUDMA	20% w/w HDDA	3% w/w NX

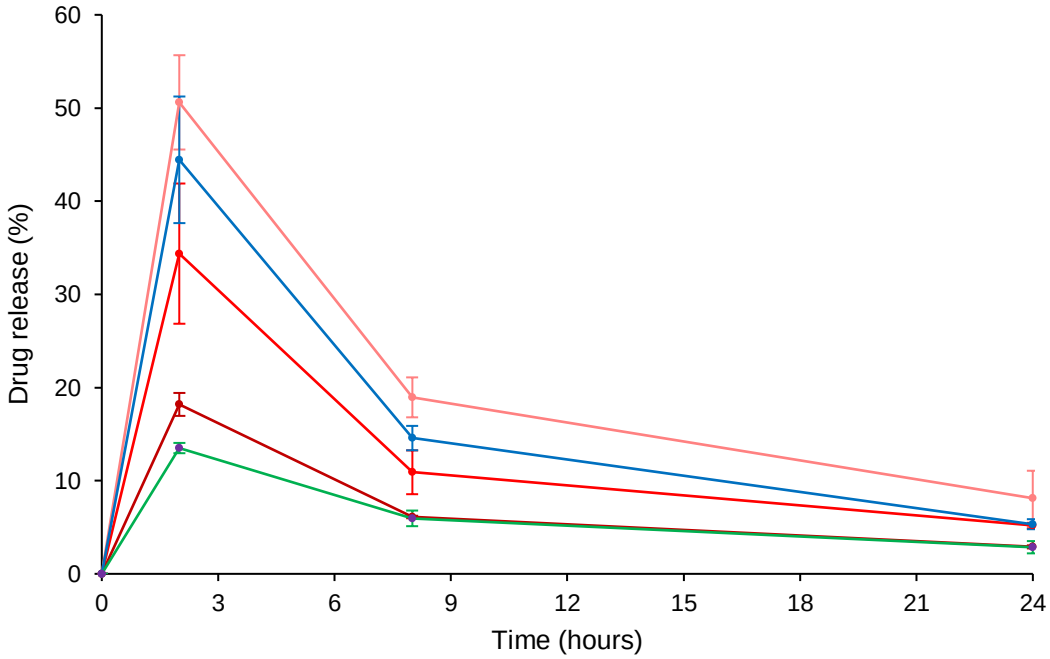

Figure 118 – Graph plotting drug release (%) at specific time intervals (hours) within 24 hours for PEG1000PUDMA + 20% TEGDA materials. Plot results shown are: 1% w/w salicylic acid (–), 3% w/w salicylic acid (–), 5% w/w salicylic acid (–), 3% w/w acetaminophen (–) and 3% w/w naproxen (–).

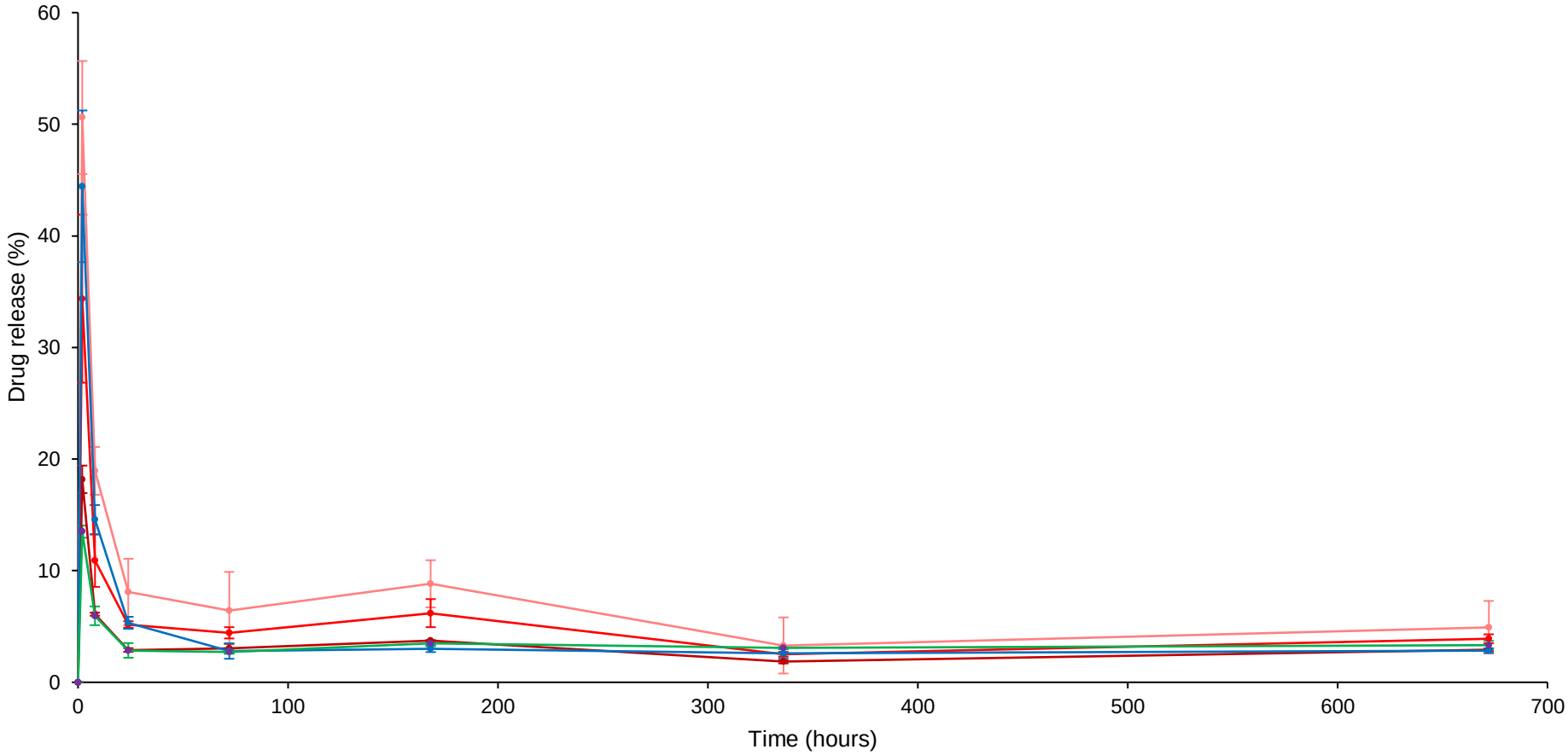

Figure 119 – Graph plotting drug release (%) at specific time intervals (hours) for PEG1000PUDMA + 20% TEGDA materials. Plot results shown are: 1% w/w salicylic acid (–), 3% w/w salicylic acid (–), 5% w/w salicylic acid (–), 3% w/w acetaminophen (–) and 3% w/w naproxen (–).

Burst release (%) at 2 hours increases for PEG1000PUDMA materials with decreasing salicylic acid contents (5% w/w > 3% w/w > 1% w/w, 18.19% > 34.37% > 50.60% drug release, respectively). Looking at the actual release of salicylic acid (mg), approximately the same amounts of drug are released at 2, 8 and 24 hour timepoints. As with other PEG1000PUDMA materials, drug release plateaus to a zero order release at 1 week. These findings imply controlled zero order drug release in body compartments where media turnover is high (and subsequently solution saturation is not approached) which is not achieved through PEG1000PUDMA materials However, PEG1000PUDMA materials may prove suitable for applications where burst release of drug is desirable. Furthermore, burst release (%) at 2 hours increases with decreasing log P values for incorporated drug (13.50% > 18.19% > 44.44% drug release, 3.29 (naproxen log P) > 1.96 (salicylic acid log P) > 0.51 (acetaminophen log P), respectively). Log P values were calculated using ALOGPS 2.1, an online log P predictive tool[275,276]. This was anticipated, as decreased compound hydrophilicity will decrease diffusion into aqueous layers.

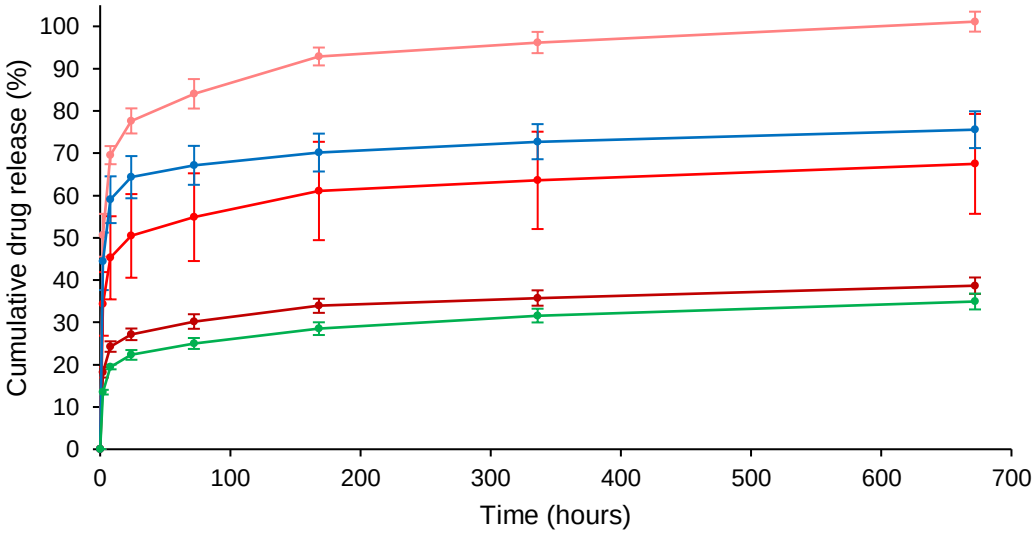

Figure 120 – Graph plotting cumulative drug release (%) against time (hours) for PEG1000PUDMA + 20% TEGDA materials. Plot results shown are: 1% w/w salicylic acid (–), 3% w/w salicylic acid (–), 5% w/w salicylic acid (–), 3% w/w acetaminophen (–) and 3% w/w naproxen (–).

Furthermore, solution saturation will be achieved at a faster rate due to increasing compound log P correlating with decreased solution saturation concentrations. These findings imply PEG1000PUDMA may yet prove suitable for controlled long-term release of drug in high media turnover compartments, albeit with more hydrophobic APIs. Figure 120 shows PEG1000PUDMA materials containing 1% w/w SA expend almost 100% of drug content over a period of 4 weeks (77.64% cumulatively at 24 hours, 101.14% cumulatively at 4 weeks). Conversely, 5% w/w SA loaded materials expend approximately expends 33% drug content over a period of 4 weeks. This highlights how solution saturation (and media turnover rate) dictate (%) drug release from drug-loaded materials.

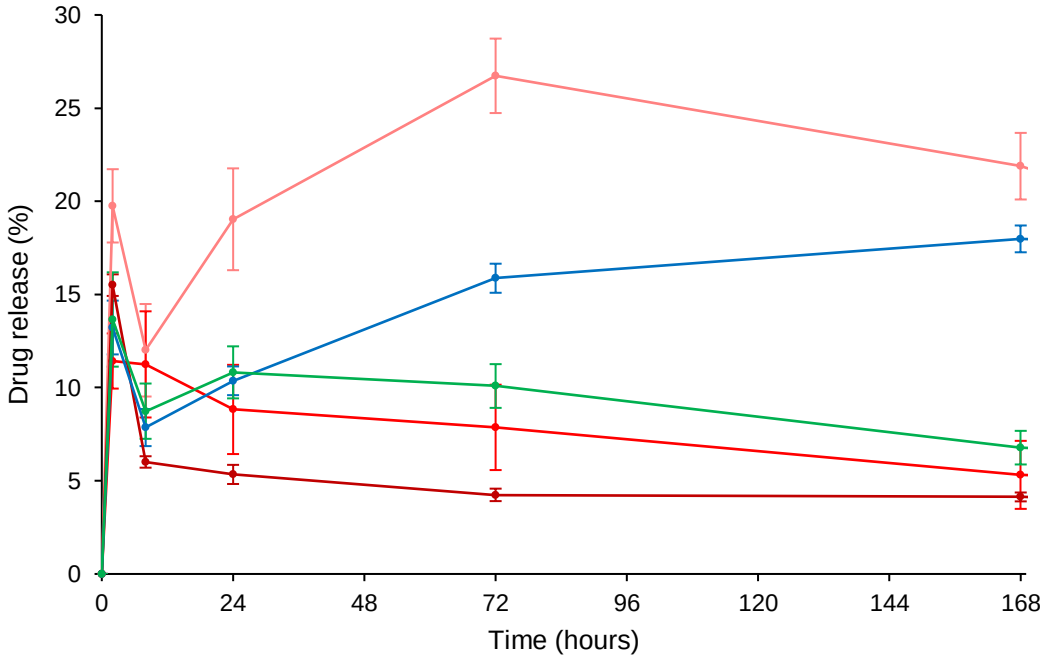

Figure 121 – Graph plotting drug release (%) at specific time intervals (hours) within 24 hours for PTHF1000PUDMA + 20% HDDA materials. Plot results shown are: 1% w/w salicylic acid (–), 3% w/w salicylic acid (–), 5% w/w salicylic acid (–), 3% w/w acetaminophen (–) and 3% w/w naproxen (–).

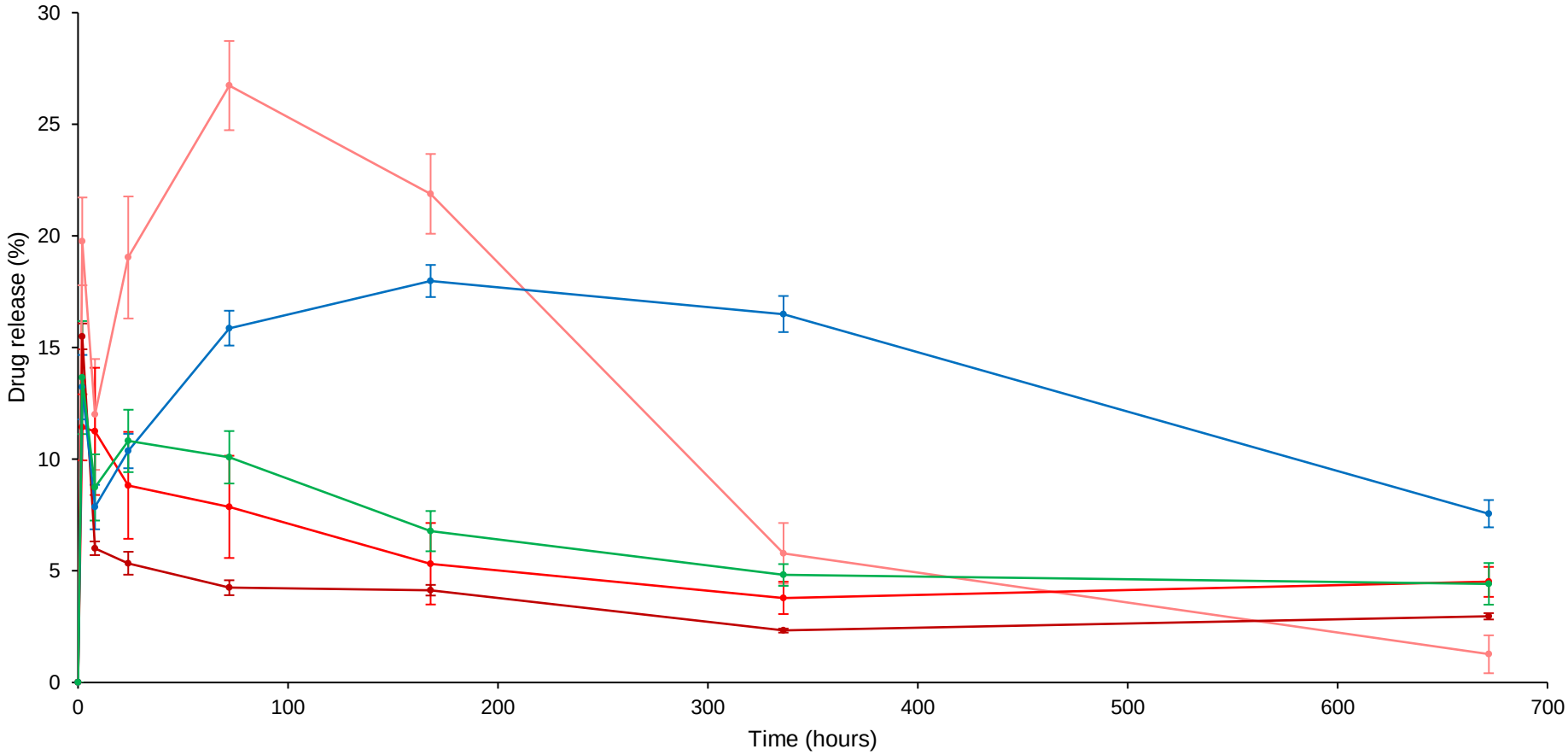

Figure 122 – Graph plotting drug release (%) at specific time intervals (hours) for PTHF1000PUDMA + 20% HDDA materials. Plot results shown are: 1% w/w salicylic acid (–), 3% w/w salicylic acid (–), 5% w/w salicylic acid (–), 3% w/w acetaminophen (–) and 3% w/w naproxen (–).

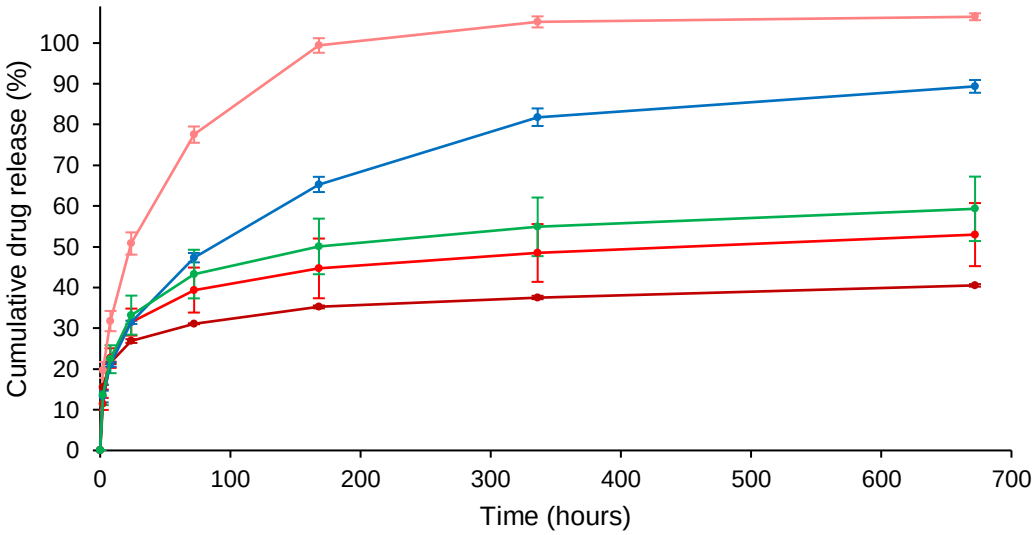

Figure 123 – Graph plotting cumulative SA drug release (%) against time (hours) for PTHF1000PUDMA + 20% HDDA materials. Plot results shown are: 1% w/w salicylic acid (–), 3% w/w salicylic acid (–), 5% w/w salicylic acid (–), 3% w/w acetaminophen (–) and 3% w/w naproxen (–).

Figure 121 and Figure 122 show release rates of salicylic acid, in different concentrations, and other drugs from PTHF1000PUDMA materials. Of interest, peak release rates for materials containing 1% w/w salicylic acid and 3% w/w acetaminophen are observed at 3 days and 1 week respectively. This was attributed to lack of solution saturation dictating drug release kinetics. This allowed for the “true” drug release kinetics for these materials to be observed, unimpeded by solution saturation. Nonetheless, with the intended application of these materials being drug release in tumour resection cavities, where presumably media turnover is low, solution saturation will always play a significant role in drug release kinetics.

Materials containing 3% and 5% w/w salicylic acid, and 3% w/w naproxen showed the highest drug release (per timepoint) at 2 hours. This is attributed to solution saturation and it is speculated that removal of the solution saturation factor may yield maximum drug release (per timepoint) at a later time.

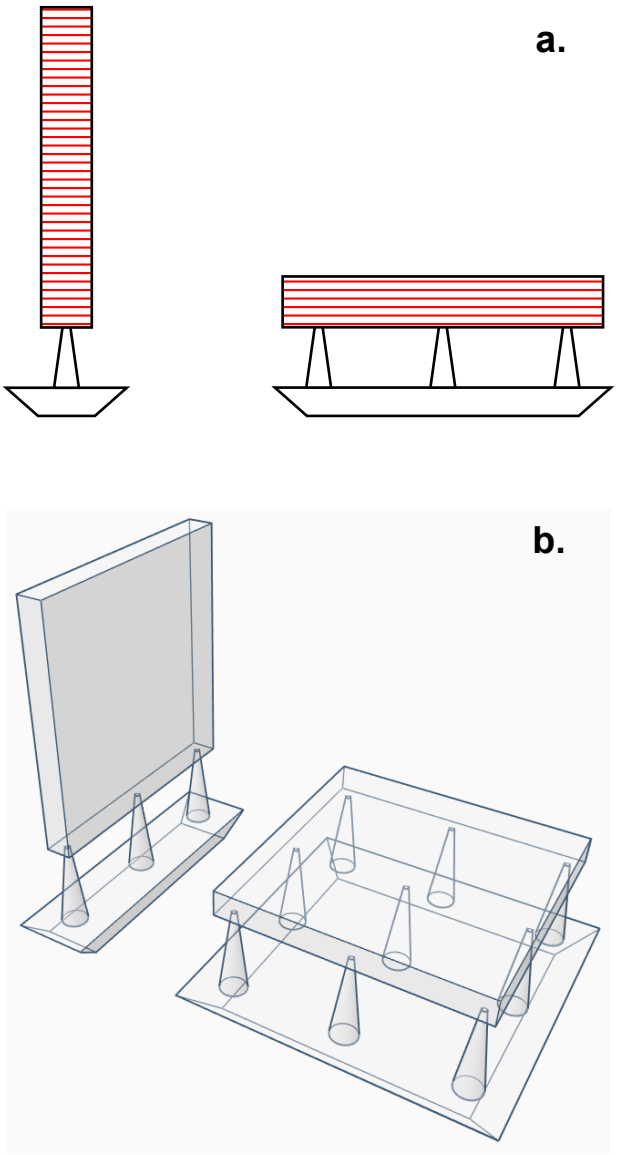

Figure 124 – Images showing **a.** vertical (left) and horizontal (right) printing orientations of a square film and **b.** 3D view of vertical and horizontal orientations of a square film generated with Tinkercad.

The effect of 3D printing and design were next investigated. PEG1000PUDMA and PTHF1000PUDMA containing 3% w/w salicylic were once again chosen as model formulations. Firstly, a decision was made to explore whether print orientation affects drug release. Figure 124 shows vertical and horizontal printing orientation of a square film (10.0 mm x 10.0 mm, 1.0 mm thickness). Red lines indicate layer formations within objects.

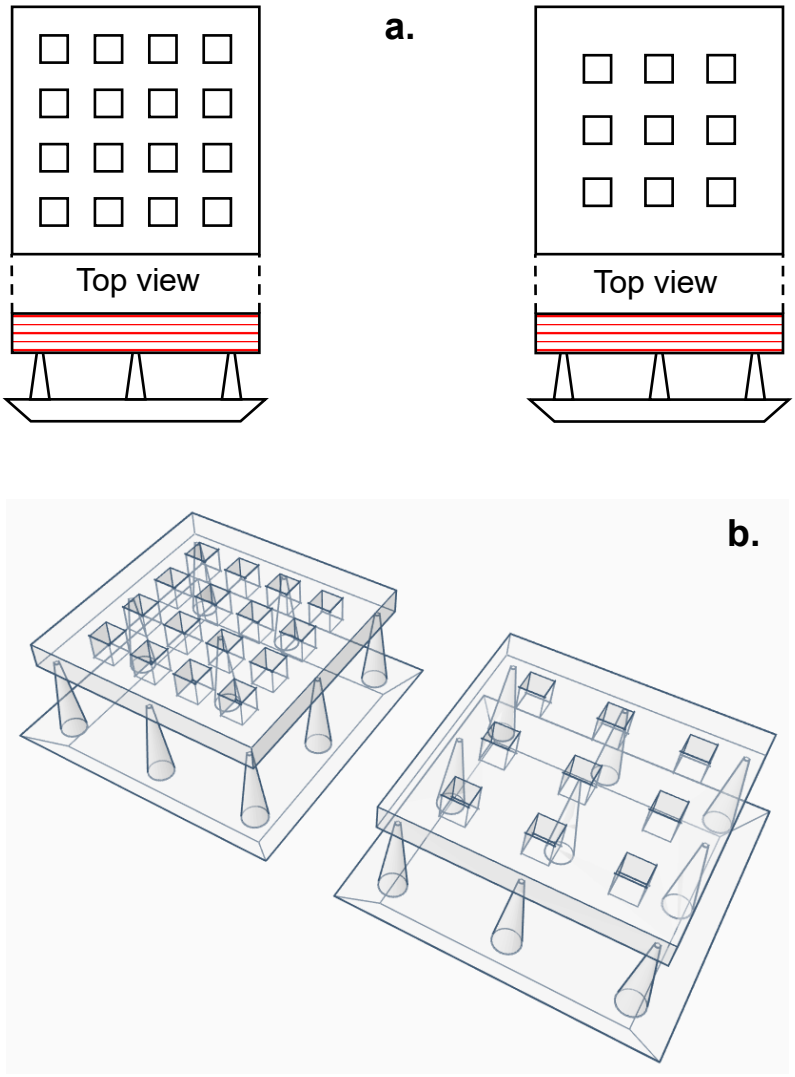

Figure 125 – Images showing **a.** 1.0 x 1.0 mm (left) and 2.0 x 2.0 mm (right) square mesh films w/ 1.0 x 1.0 mm pore size (horizontal print orientation) and **b.** 3D view of 1.0 x 1.0 mm and 2.0 x 2.0 mm square mesh films generated with Tinkercad.

Vertical orientation samples are referred to as V, and horizontal orientation samples are referred to as H. In addition, the effect of object design was explored. Square films (10.0 x 10.0 mm, 1.0 mm thickness) containing either 1.0 x 1.0 mm (referred to as 1 x 1) or 2.0 x 2.0 mm meshes (referred to as 2 x 2) with 1.0 x 1.0 mm pore size were designed and printed in the horizontal orientation (Figure 125). It must be noted that the weight of SLA 3D printed samples with supports were greater than those printed directly onto the print

platform. This was attributed to z-dimension overpolymerisation of prints with supports, associated with printing with formulations containing an arbitrary amount of hydroquinone and no photoabsorber. As previously discussed, time constraints did not permit calculation ideal additive contents for each formulation.

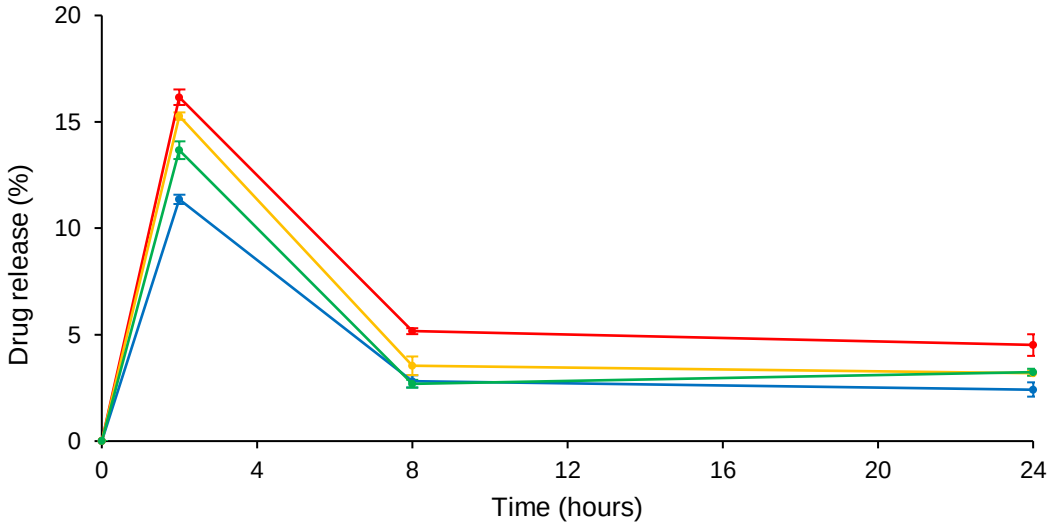

Figure 126 – Graph plotting drug release (%) at specific time intervals (hours) within 24 hours for PEG1000PUDMA + 20% w/w TEGDA + 3% w/w SA materials. Plot results shown are: V (–), H (–), 1 x 1 (–) and 2 x 2 (–).

Figure 126 and Figure 127 show SA drug release (%) against time (hours) for PEG1000PUDMA + 20% w/w TEGDA + 3% w/w SA materials printed with different orientation and different object designs. PEG1000PUDMA V materials display a higher burst release (16.16%) at 2 hours in comparison to PEG1000PUDMA H materials (11.36%). Salicylic acid release (mg) at 2 hours for both materials is however similar. This difference in (%) drug release is attributed to the increased weight of PEG1000PUDMA H compared to V.

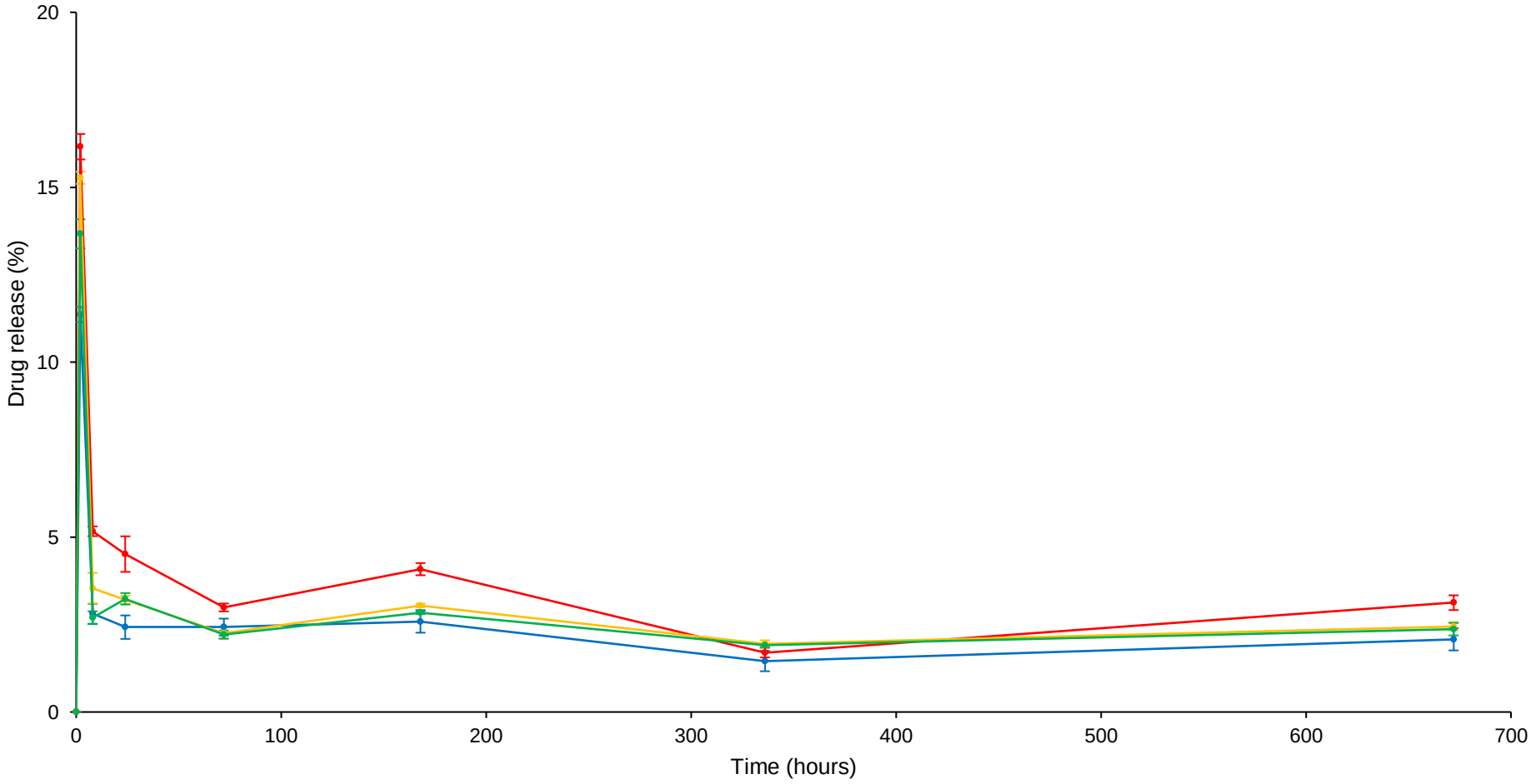

Figure 127 – Graph plotting drug release (%) at specific time intervals (hours) for PEG1000PUDMA + 20% w/w TEGDA + 3% w/w SA materials. Plot results shown are: V (–), H (–), 1 x 1 (–) and 2 x 2 (–).

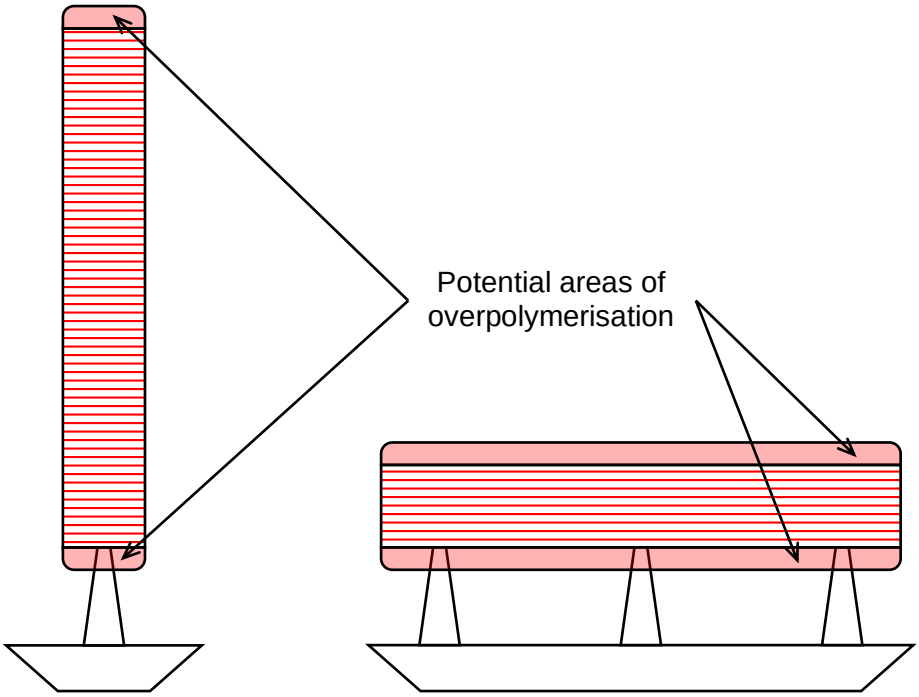

Figure 128 – Images showing vertical (left) and horizontal (right) printing orientations of a square film. Red shading depicts potential z-dimension overpolymerisation, of both orientations, when printing with formulations not containing photoabsorbers.

Figure 128 shows vertical and horizontal printing orientations of square films, with red shading indicating potential z-dimension overpolymerisation for both orientations. As can be seen, there is far greater potential for z-dimension overpolymerisation in horizontal orientations when compared to vertical orientations, hence the weight difference. As mentioned, this is a consequence of formulating without photoabsorbers. It is therefore critical to obtain an optimised material formulation, containing both photoinhibitor and photoabsorber, so as to achieve a product with accurate drug content and release kinetics. PEG1000PUDMA 1 x 1 materials display a slight increase in burst release (%) at 2 days (15.27%) compared to that of PEG1000PUDMA 2 x 2 (13.67%) and PEG1000PUDMA H (11.36%) materials. This is associated to a larger surface area implemented through object design.

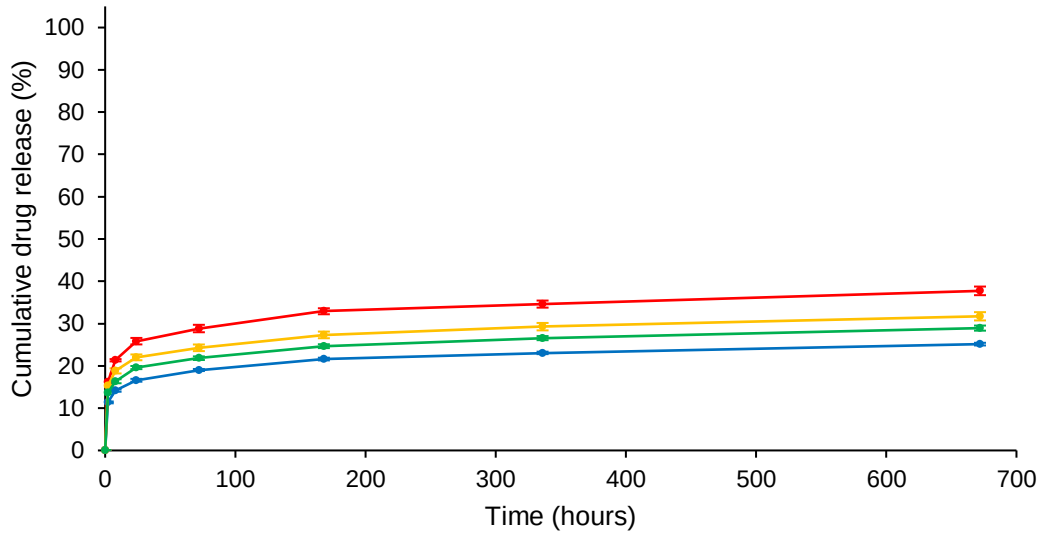

Figure 129 – Graph plotting cumulative drug release (%) against time (hours) for PEG1000PUDMA + 20% w/w TEGDA + 3% w/w SA materials. Plot results shown are: V (–), H (–), 1 x 1 (–) and 2 x 2 (–).

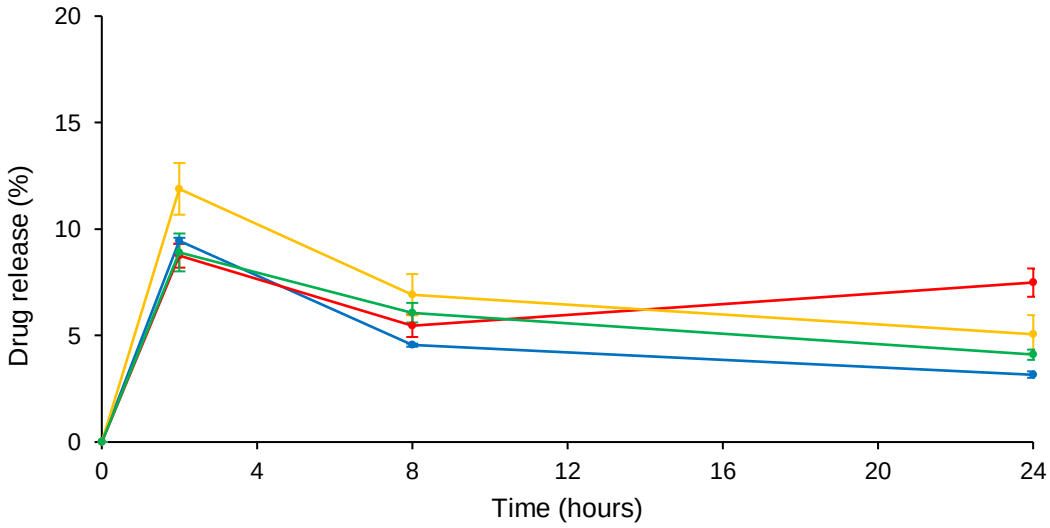

Figure 130 – Graph plotting drug release (%) at specific time intervals (hours) within 24 hours for PTHF1000PUDMA + 20% w/w HDDA + 3% w/w SA materials. Plot results shown are: V (–), H (–), 1 x 1 (–) and 2 x 2 (–).

However, this increase is not considerable. There are two explanations for this finding. Firstly, the increase in surface area is not of a subsequent magnitude to facilitate a significant change in drug release kinetics. To fabricate a mesh with greatly increased surface would require fine control over x-y-x printing dimensions and hence is only achievable with an optimised photopolymer

formulation. Secondly, material hydrophilicity may dictate, to a greater degree, drug release kinetics of PEG1000PUDMA materials than surface area (at least in its current magnitude), hence the similarity in burst release rates.

PTHF1000PUDMA H materials display a slightly higher burst release (9.45%) compared to PTHF1000PUDMA V (8.75%) materials. Beyond this time point, PTHF1000PUDMA V materials show higher cumulative release of drug in comparison to PTHF1000PUDMA H materials. It was noted, on average that PTHF1000PUDMA H materials were 45.71% greater in mass than PTHF1000PUDMA V. PTHF1000PUDMA H materials therefore have a lower surface area to volume ratio, perhaps explaining lower cumulative release of drug. PTHF1000PUDMA 1x1 materials display a higher burst release (11.89%) at 2 hours than PTHF1000PUDMA H materials (8.75%). This can be attributed to an increase in surface area, although as observed with PEG1000PUDMA materials, this does not appear significant, suggesting magnitude of surface area differences are not large enough to alter drug release kinetics to a large degree.

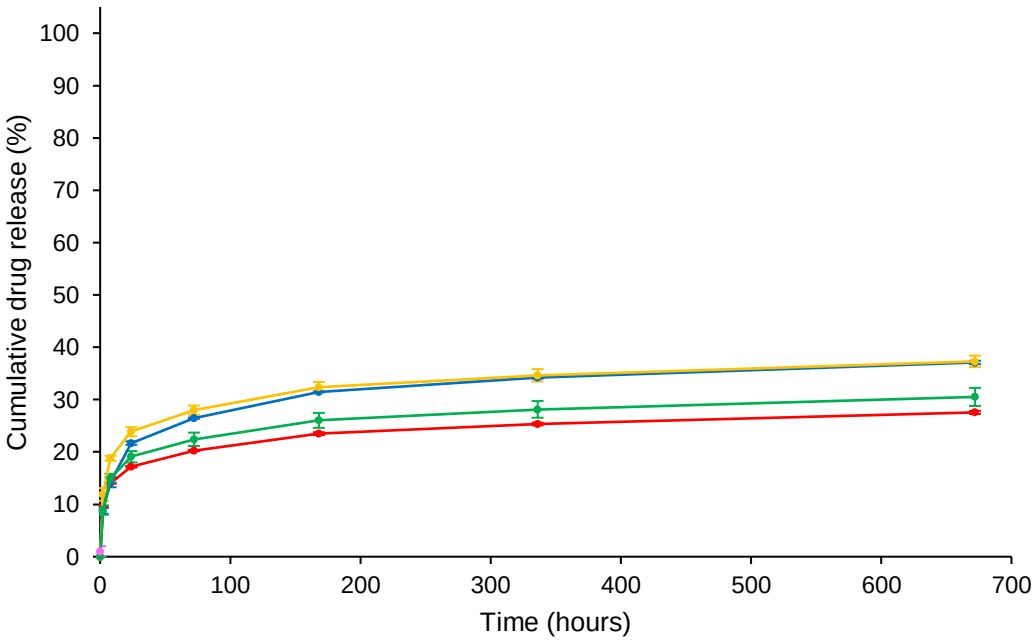

Figure 131 – Graph plotting cumulative drug release (%) against time (hours) for PTHF1000PUDMA + 20% w/w HDDA + 3% w/w SA materials. Plot results shown are: V (–), H (–), 1 x 1 (–) and 2 x 2 (–).

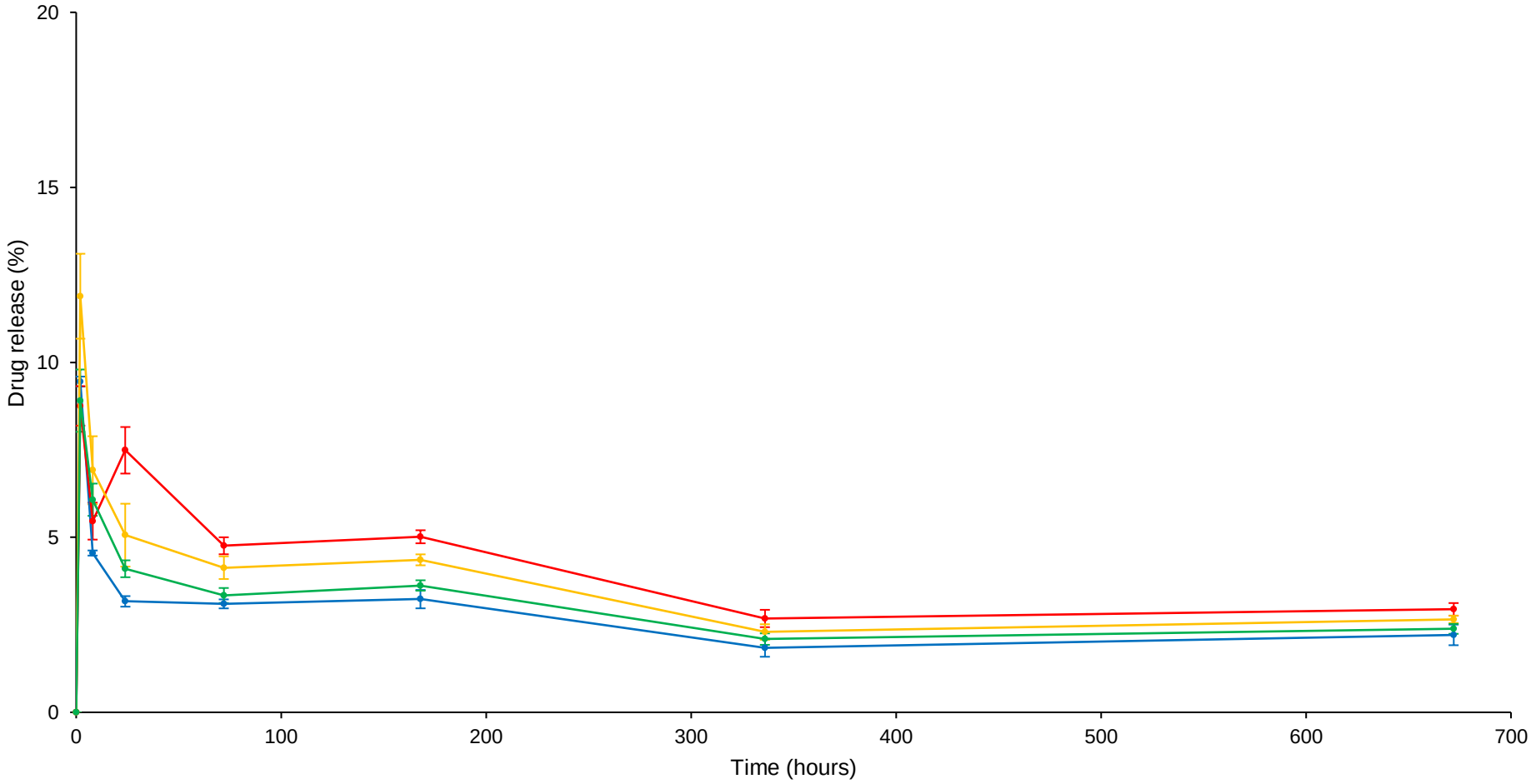

Figure 132 – Graph plotting drug release (%) at specific time intervals (hours) for PTHF1000PUDMA + 20% w/w HDDA + 3% w/w SA materials. Plot results shown are: V (–), H (–), 1 x 1 (–) and 2 x 2 (–).

6.2.7. Physical properties of SLA 3D printed materials

Nanoindentation was utilised to assess the mechanical properties of SLA 3D printed samples in comparison to mould cured samples. The reason tensile testing was not used was due to variance in the printing of tensile testing strips. Small variances in printing quality can significantly affect the accuracy of results obtained from tensile testing. On the other hand, nanoindentation can avoid such inaccuracies due to surface probing prior to test. In addition, a small amount of resin (0.41 mL) is required to print a single square film for multiple nanoindentations, whereas a large amount of resin (8.03 mL) is required to print DIN EN ISO 527-3 conforming tensile test strips (in triplicate). Figure 133 shows load versus penetration depth curves for load-unload nanoindentation testing of SLA 3D printed samples. Table 33 shows values obtained from nanoindentation testing. Mould cured samples (PEG1000PUDMA + 20% TEGDA and PTHF1000 display different nanoindentation plots (Figure 133 a and c) to their SLA 3D printed counterparts (Figure 133 b and d). Furthermore, indentation hardness (kPa) and moduli (MPa) increased for mould cured samples in comparison to SLA 3D printed samples. It was speculated that as SLA 3D printed samples had not undergone a continuous solvent extraction process and subsequent drying, that this “cleaning” process was the cause. A potential explanation is that, in a similar manner to how hydration of dried PEG-based networks form soft and flexible hydrogels, unreacted monomers within the SLA 3D printed films act to “hydrate” the polymer network, leading to softer, more flexible materials.

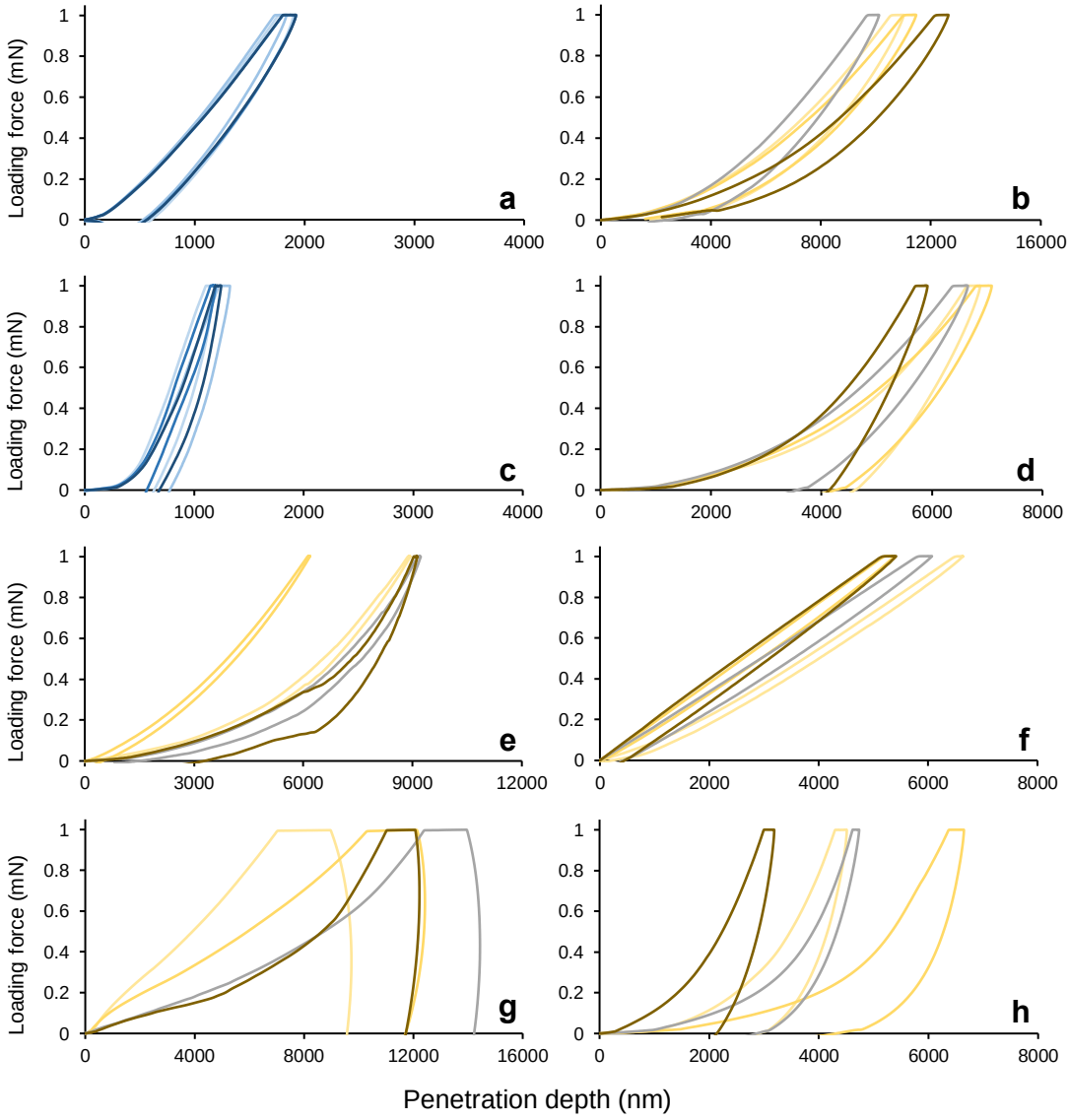

Figure 133 – Load (mN) versus penetration depth (nm) curves for load-unload nanoindentation testing. Plot results shown are: **a** = PEG1000PUDMA + 20% TEGDA – mould cured, **b** = PEG1000PUDMA + 20% TEGDA – SLA 3D printed, **c** = PTHF1000PUDMA + 20% HDDA + 1% TPO – mould cured, **d** = PTHF1000PUDMA + 20% HDDA + 1% TPO – SLA 3D printed, **e** = PEG575DA + 1% TPO – SLA 3D printed, **f** = PTHF650DA + 1% TPO – SLA 3D printed.

Table 33 – Nanoindentation results for select mould cured and SLA 3D printed formulations

Sample name	Indentation hardness (HIT, kPa)	Indentation modulus (EIT, MPa)	Indentation creep (CIT, %)	Shore*	
				A	D
PEG1000PUDMA + 20% TEGDA - mould	250.04 ± 4.82	14.68 ± 0.38	8.13 ± 0.25	76.90	-
PEG1000PUDMA + 20% TEGDA - 3DP	37.57 ± 2.02	1.34 ± 0.05	5.56 ± 0.15	32.63	-
PTHF1000PUDMA + 20% HDDA - mould	314.22 ± 11.31	47.67 ± 3.57	6.84 ± 1.01	-	48.66
PTHF1000PUDMA + 20% HDDA - 3DP	56.92 ± 2.18	4.46 ± 0.43	4.75 ± 0.18	54.90	-
PEG575DA - 3DP	54.82 ± 10.81	2.33 ± 0.33	-0.99 ± 1.13	42.89	-
PTHF650DA - 3DP	140.64 ± 13.56	2.06 ± 0.14	6.64 ± 0.76	40.63	-
PLGA1000PUDMA + 8% ethyl lactate + 20% TEGA - 3DP	28.67 ± 2.76	13.34 ± 2.51	17.59 ± 4.10	75.13	-
PLGA400DMA - 3DP	78.46 ± 12.30	13.56 ± 2.01	5.06 ± 0.83	75.43	-

It is also possible that the aforementioned cleaning process, especially the vacuum drying step, “fully cures” the material resulting in increased crosslinking density and subsequent increase in stiffness and hardness. Alternatively, SLA 3D printed formulations contained 0.1% w/w α-tocopherol whereas mould cured formulations did not. It is possible that this small amount of additive alters the polymer network sufficiently to result in different mechanical properties. Finally, differences in how the polymer architecture is constructed during mould curing and SLA 3D printing procedures could result in the observed different mechanical properties. As noted, a number of variables could be the cause of these differences in mechanical properties, warranting further study. Nanoindentation results worthy of comment include those of PEG575DA and PTHF650 materials, which exhibit similar indentation moduli (correlating with similar elastic moduli of these materials obtained via

tensile testing in Chapter 1), but different hardness values. Furthermore, PLGA1000PUDMA and PLGA400DMA materials exhibit similar indentation moduli, yet PLGA400DMA displays a higher hardness value higher than that of its polyurethane dimethacrylate counterpart. Determination of hardness via other means are required to confirm whether this observation is true.

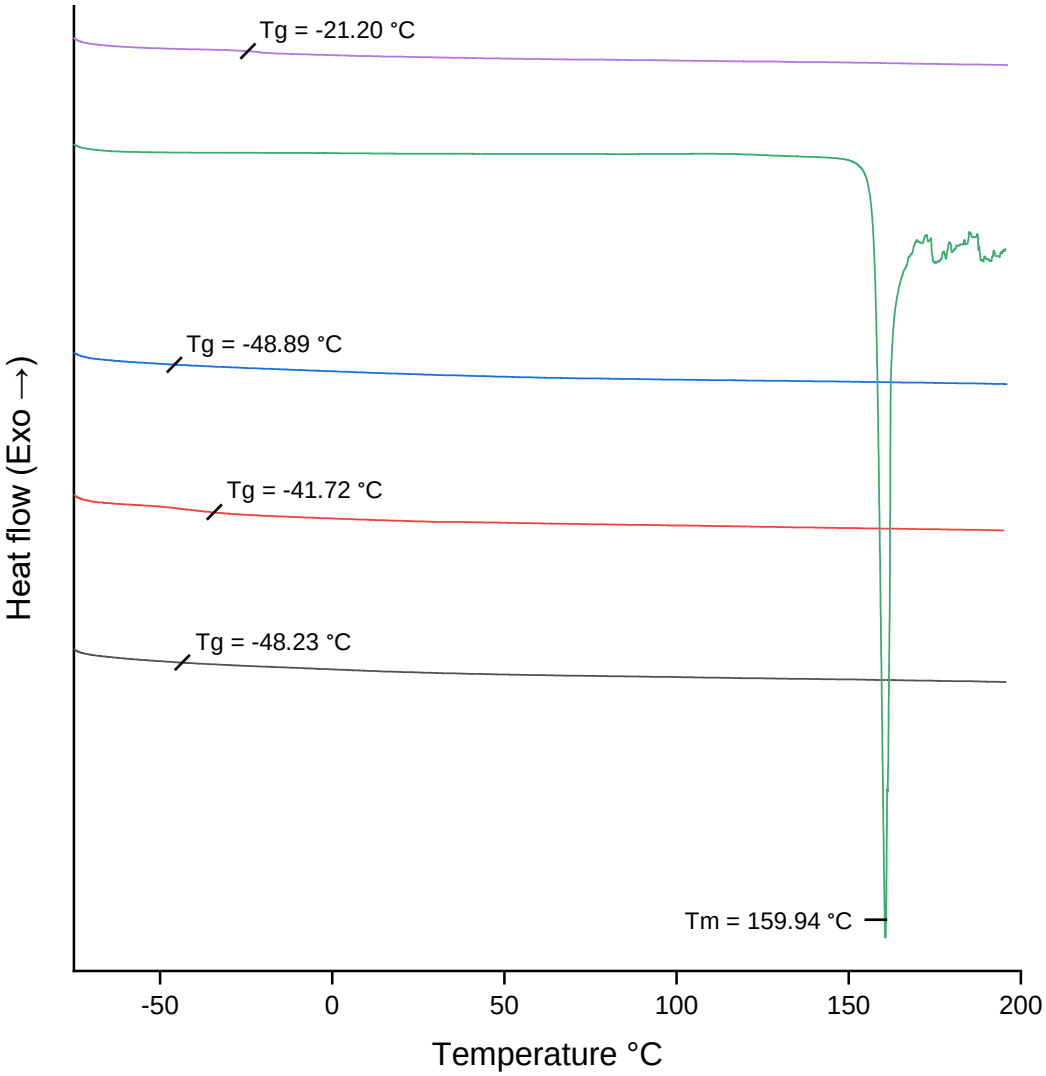

Figure 134 – DSC thermograms of SLA 3D printed PTHF1000PUDMA + 20% HDDA materials containing variable amounts of salicylic acid. Thermogram results shown are: (—) Blank; (—) Neat salicylic acid; (—) + 1% w/w salicylic acid; (—) + 3% w/w salicylic acid; (—) + 5% w/w salicylic acid.

Figures 134 and 135 show DSC thermograms of PTHF1000PUDMA and PEG1000PUDMA materials containing variable amounts of salicylic acid. All

formulations do not show a melting peak corresponding to salicylic acid, indicating amorphous distribution of drug in both materials. This is important, as presence of crystalline drug in polymer networks can lead to unpredictable drug release kinetics and weakened mechanical properties.

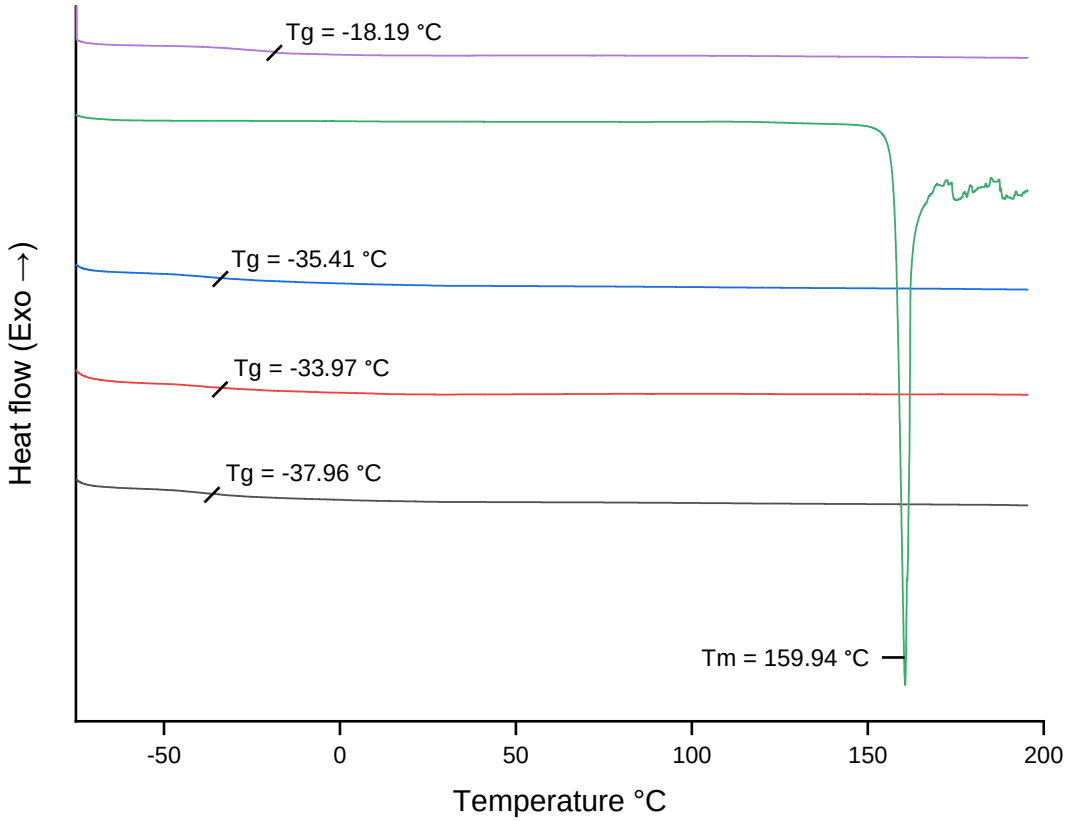

Figure 135 – DSC thermograms of SLA 3D printed PEG1000PUDMA + 20% TEGDA materials containing variable amounts of salicylic acid. Thermogram results shown are: (—) Blank; (—) Neat salicylic acid; (—) + 1% w/w salicylic acid; (—) + 3% w/w salicylic acid; (—) + 5% w/w salicylic acid.

Figure 136 also indicates amorphous dispersion of acetaminophen and naproxen in PEG1000PUDMA and PTHF1000PUDMA-based materials. The Tg values for PEG1000PUDMA (-37.96 to -18.19 °C) and PTHF1000PUDMA (-48.89 to -21.20 °C) based materials are speculative as glass transitions were subtle and difficult to identify. As mentioned previously, to verify Tg values for these materials, or ascertain new Tg values, it may prove necessary to repeat DSC testing utilising different conditions until clearer, more accurate glass transitions are observed.

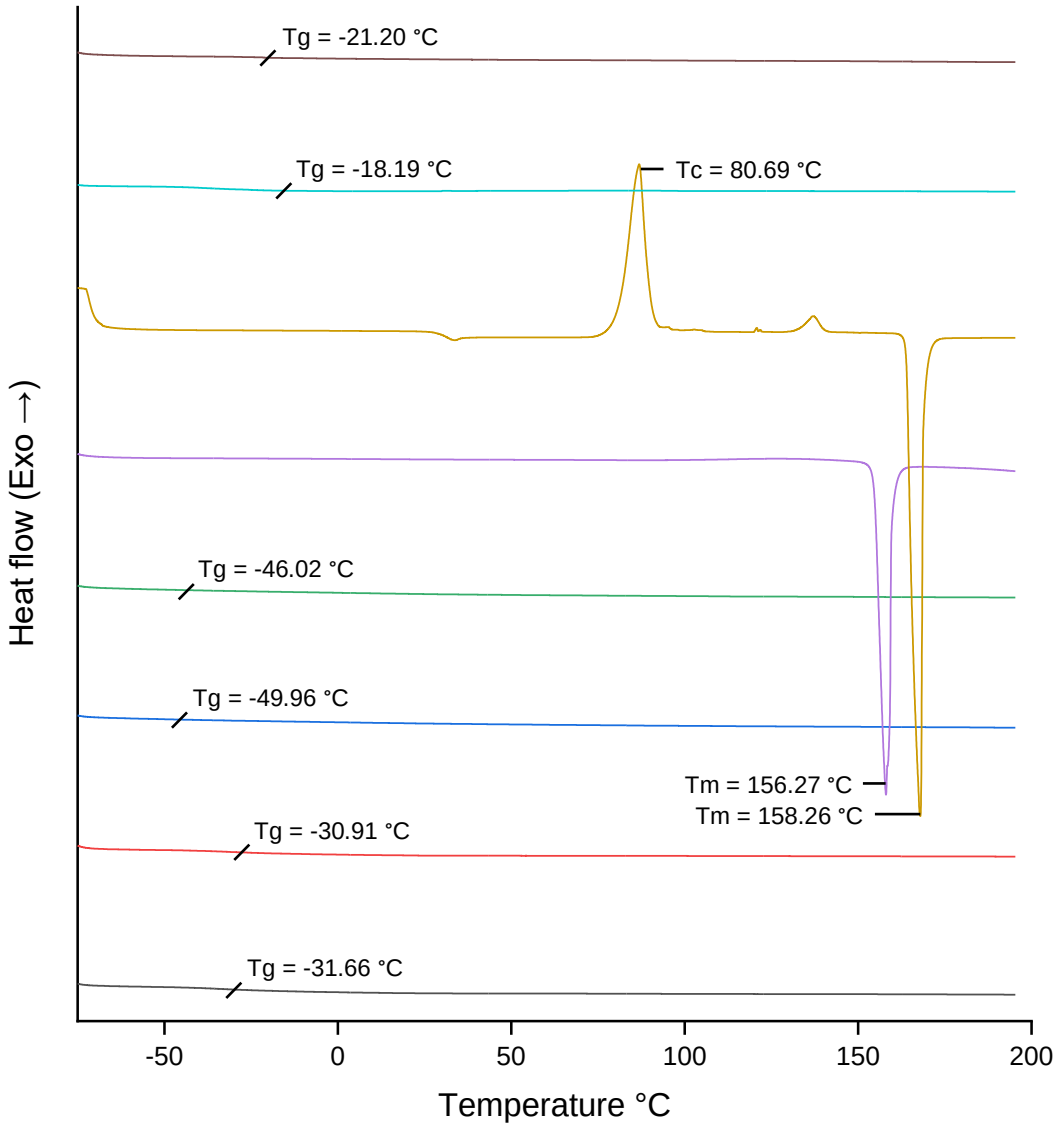

Figure 136 – DSC thermograms of SLA 3D printed materials containing 3% w/w of acetaminophen or naproxen. Thermogram results shown are: (—) PTHF1000PUDMA + 20% HDDA; (—) PEG1000PUDMA + 20% TEGDA; (—) Neat acetaminophen; (—) Neat naproxen; (—) PTHF1000PUDMA + 20% HDDA + 3% acetaminophen; (—) PTHF1000PUDMA + 20% HDDA + 3% naproxen; (—) PEG1000PUDMA + 20% TEGDA + 3% acetaminophen; (—) PEG1000PUDMA + 20% TEGDA + 3% naproxen.

Figure 137 shows thermograms of various SLA 3D printed materials, where mould cured counterparts would fracture when fashioned (by guillotine) into samples for various tests. PTHF and PEG di(methacrylates) display glass transition states between -51.24 and -39.68 °C, and -23.09 and -39.68 °C, respectively. This indicates these materials are in a rubbery elastic state at

room temperature, suggesting that fracturing of material when mould cures were guillotined, was not associated with the materials being in a glassy state but was rather due to weak polymer architecture as a result of rapid and irregular polymer crosslinking. On the other hand, polyester (polyurethane) dimethacrylates display clear glass transitions between 30.76 and 53.24 °C.

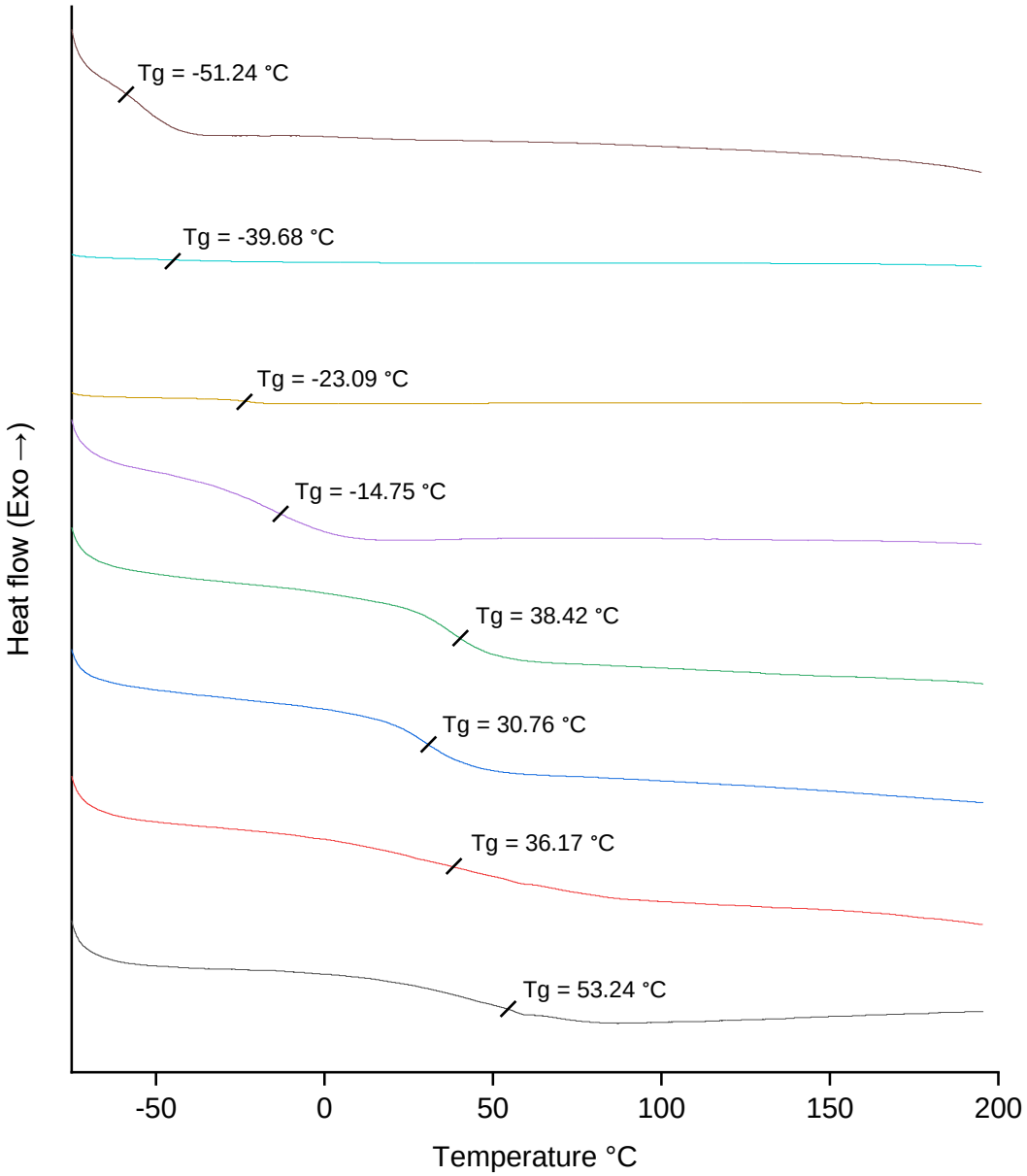

Figure 137 – DSC thermograms of SLA 3D printed materials containing 3% w/w of salicylic acid. Thermogram results shown are: (—) PTHF650DA; (—) PTHF650DMA; (—) PEG575DA; (—) PEG550DMA; (—) PLA1000PUDMA + 20% TEGDA + 8% EL; (—) PLGA1000PUDMA + 20% TEGDA + 8% EL; (—) PLGA400DMA; (—) PGA400DMA.

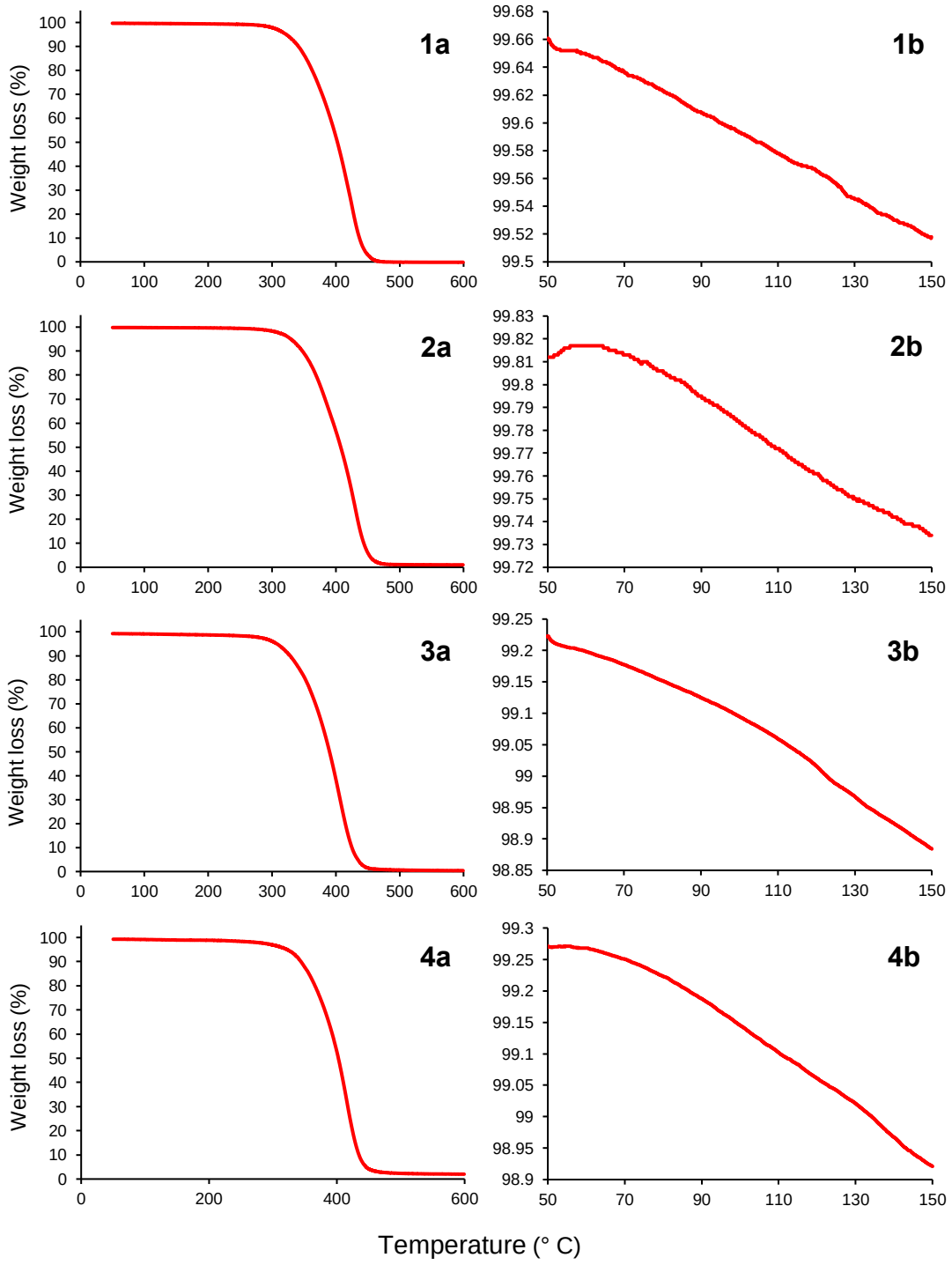

Figure 138 – TGA thermograms of "cleaned" PEG1000PUDMA + 20% TEGDA and PTHF1000PUDMA + 20% HDDA materials, both mould cured, and 3D printed. Thermogram results shown are: **1** = PTHF1000PUDMA + 20% HDDA – mould cured; **2** = PTHF1000PUDMA + 20% HDDA – 3DP; **3** = PEG1000PUDMA + 20% TEGDA – mould cured; **4** = PEG1000PUDMA + 20% TEGDA – 3DP.

At room temperature, these materials exist in a glassy state, which explains their tendency to fracture when mould cured sheets were guillotined into samples. Figure 138 shows TGA thermograms of “cleaned” PEG1000PUDMA + 20% TEGDA and PTHF1000PUDMA + 20% HDDA materials, either mould cured or 3D printed (3DP).

Table 34 – Table showing results obtained from TGA of mould cured and SLA 3D printed samples

Sample name		Weight loss (%)		Onset of thermal decomposition (°C)
		at 150 °C	at 600 °C	
PTHF1000PUDMA + 20% HDDA + 1% TPO	mould cured	0.482	100.168	365.03
	SLA 3D printed	0.266	98.987	371.26
PEG1000PUDMA + 20% TEGDA + 1% TPO	mould cured	1.098	99.672	351.53
	SLA 3D printed	1.079	97.983	369.81

Table 34 shows values obtained from these thermograms such as weight loss (%) at specific temperatures and onset of thermal decomposition (°C). Of greatest interest were values for material weight loss (%) at 150 °C. Weight loss at this temperature typically corresponds to loss of volatiles such as solvents and moisture. Mould cured and SLA 3D printed all underwent a “cleaning” process of continuous acetone extraction for 24 hours followed by drying under vacuum. USP <467> (ICH Q3C) guidelines set certain limits for residual solvents in pharmaceutical products. The limit for class 3 solvents such as acetone are 5000 ppm (0.5% w/w)[277]. PTHF1000PUDMA materials shows weight loss of below 0.5% w/w at 150 °C. Assuming all volatiles are lost at 150 °C, these materials are in accordance to USP <467>. Conversely, PEG1000PUDMA materials shows a weight loss of above 0.5% w/w at 150 °C. These materials are not in accordance to USP <467>. This additional mass loss is attributed to moisture accrued during storage, owed to the hygroscopic nature of PEG-based materials. To be able to measure loss of specific volatiles, more specific techniques such as tandem TGA-MS, gas chromatography and dynamic headspace chromatography may allow more precise detection and quantification of volatiles from samples[278].

6.3. Conclusions and Future Work

Customised printheads and print trays were constructed, permitting printing of low volume objects with minimal waste. Furthermore, through the use of an RT-FTIR spectroscopy tool, it was possible to calculate required amounts of photoadditives for a photocurable formulation to facilitate high resolution 3D printing using the Formlabs Form 1+ SLA 3D printer. In combination, it was possible to reduce the time it took to print 9 separate objects with 9 separate resins by almost 4 fold. These approaches can be implemented to expand the versatility and convenience of a range of commercial SLA 3D printers for researchers wishing to experiment with custom photopolymer systems. As mentioned, potential continuation of this work could involve improving the accuracy of this tool by developing an adapted test for measuring x-y dimension overpolymerisation and use of photorheology in tandem. Furthermore, understanding the key features an SLA 3D printer with experimental capabilities must possess, a potential spin-off from this work could entail the development of an “open-source” SLA 3D printer designed for the researcher.

3D printed samples composed from a range of different photocurable materials and drugs were prepared. Drug release studies showed drug release kinetics from samples were dependent on material composition, drug type and content and object design. Furthermore, polyurethane dimethacrylate materials, which in previous sections were shown to have suitable mechanical properties and biocompatibility, were shown to be sufficiently versatile to permit programmable drug release kinetics. This work paves the wave for SLA 3D printing to not only be considered for fabrication of implantable drug-eluting materials, but also for a range of medical and non-medical applications, where versatile, tough, and non-toxic materials are required. Extension to this work could involve development of a high throughput approach with aim to accurately characterise, and ultimately predict drug release kinetics of certain materials and payloads, under specific conditions with scope to facilitate the development of programmable drug eluting devices for cancer treatment.

7. References

1. Fitzmaurice, C. *et al.* Global, Regional, and National Cancer Incidence, Mortality, Years of Life Lost, Years Lived With Disability, and Disability-Adjusted Life-years for 32 Cancer Groups, 1990 to 2015. *JAMA Oncol.* **3**, 524 (2017).
2. Cancer mortality for common cancers. *Cancer Research UK* Available at: http://www.cancerresearchuk.org/health-professional/cancer-statistics/mortality/common-cancers-compared#heading-One. (Accessed: 30th October 2017)
3. Cancer Statistics for the UK. *Cancer Research UK* Available at: http://www.cancerresearchuk.org/health-professional/cancer-statistics-for-the-uk. (Accessed: 30th October 2017)
4. Cancer survival for common cancers. *Cancer Research UK* (2019). Available at: http://www.cancerresearchuk.org/health-professional/cancer-statistics/survival/common-cancers-compared#heading-Zero. (Accessed: 30th October 2017)
5. Cole, A. *et al. Improving Efficiency and Resource Allocation in Future Cancer Care*. (2016).
6. Bristol-Myers Squibb & The Patients Association. *Transforming the Cycle in Cancer Care*. (2017).
7. NHS England Cancer Drugs Fund Team. Appraisal and Funding of Cancer Drugs from July 2016 (including the new Cancer Drugs Fund) - A new deal for patients, taxpayers and industry. (2016). Available at: https://www.england.nhs.uk/wp-content/uploads/2013/04/cdf-sop.pdf. (Accessed: 30th October 2017)
8. Royal College of Radiologists. *Equipment, Workload and Staffing for Radiotherapy in the UK 1997–2002*. (2003).
9. Sciubba, D. M. *et al.* Diagnosis and management of metastatic spine disease. *J. Neurosurg. Spine* **13**, 94–108 (2010).
10. Fornaro, L., G., M., F., L., E., V. & A., F. Palliative treatment of unresectable metastatic colorectal cancer. *Expert Opin. Pharmacother.* **11**, 63–77 (2010).
11. Stephens, F. O. & Aigner, K. R. Treating Cancer. in *Basics of Oncology* 14–15 (Springer, 2009).
12. Wolinsky, J., Colson, Y. & Grinstaff, M. Local Drug Delivery Strategies for Cancer Treatment: Gels, Nanoparticles, Polymeric Films, Rods, and Wafers.

J. Control. Release **159**, 1–34 (2012).

13. Gavhane, Y. *et al.* Solid Tumors : Facts, Challenges and Solutions. *Int. J. Pharma Sci. Res.* **2**, 1–12 (2011).
14. Kelsey, C. R. *et al.* Local recurrence after surgery for early stage lung cancer: An 11-year experience with 975 patients. *Cancer* **115**, 5218–5227 (2009).
15. Sjövall, A., Granath, F., Cedermark, B., Glimelius, B. & Holm, T. Loco-regional Recurrence from Colon Cancer: A Population-based Study. *Ann. Surg. Oncol.* **14**, 432–440 (2007).
16. About surgery. *Cancer Research UK* Available at: http://www.cancerresearchuk.org/about-cancer/cancer-in-general/treatment/surgery/about. (Accessed: 30th October 2017)
17. Baskar, R., Lee, K. A., Yeo, R. & Yeoh, K.-W. Cancer and Radiation Therapy: Current Advances and Future Directions. *Int. J. Med. Sci.* **9**, 193–199 (2012).
18. Baudino, T. Targeted Cancer Therapy: The Next Generation of Cancer Treatment. *Curr. Drug Discov. Technol.* **12**, 3–20 (2015).
19. Sparreboom, A., van Tellingen, O., Nooijen, W. J. & Beijnen, J. H. Tissue distribution, metabolism and excretion of paclitaxel in mice. *Anti-Cancer Drugs* **7**, 78–86 (1996).
20. Abdulkareem, I. H. & Zurmi, I. B. Review of hormonal treatment of breast cancer. *Niger. J. Clin. Pract.* **15**, 9–14 (2012).
21. Goldspiel, B. R. & Kohler, D. R. Flutamide: anantiandrogen for advanced prostate cancer. **24**, 616–623 (1990).
22. Fernando, N. H. Targeted Therapy of Colorectal Cancer: Clinical Experience with Bevacizumab. *Oncologist* **9**, 11–18 (2004).
23. Prasad, V. & Kaestner, V. Nivolumab and pembrolizumab: Monoclonal antibodies against programmed cell death-1 (PD-1) that are interchangeable. *Semin. Oncol.* **44**, 132–135 (2017).
24. Graff, J. N. & Chamberlain, E. D. Sipuleucel-T in the treatment of prostate cancer: An evidence-based review of its place in therapy. *Core Evid.* **10**, 1–10 (2014).
25. Choudhry, H. *et al.* Prospects of IL-2 in Cancer Immunotherapy. *Biomed Res. Int.* **2018**, (2018).
26. Smith, H. G. *et al.* Isolated Limb Perfusion with Melphalan and Tumour Necrosis Factor α for In-Transit Melanoma and Soft Tissue Sarcoma. *Ann. Surg. Oncol.* **22**, 356–361 (2015).
27. Duensing, S. & Duensing, A. Targeted therapies of gastrointestinal stromal tumors (GIST)-The next frontiers. *Biochem. Pharmacol.* **80**, 575–583 (2010).

28. Oikawa, T. *et al.* Clinical usefulness of gefitinib for non-small-cell lung cancer with a double epidermal growth factor receptor mutation. *Mol. Clin. Oncol.* **3**, 329–333 (2015).
29. Exner, A. A. & Saidel, G. M. Drug-eluting polymer implants in cancer therapy. *Expert Opin. Drug Deliv.* **5**, 775–788 (2008).
30. Krukiewicz, K. & Zak, J. K. Biomaterial-based regional chemotherapy: Local anticancer drug delivery to enhance chemotherapy and minimize its side-effects. *Mater. Sci. Eng. C* **62**, 927–942 (2016).
31. Su, J. L., Bouchard, R. R., Karpiouk, A. B., Hazle, J. D. & Emelianov, S. Y. Photoacoustic imaging of prostate brachytherapy seeds. *Biomed. Opt. Express* **2**, 2243 (2011).
32. Odell, D. D., Kent, M. S. & Fernando, H. C. Sublobar resection with brachytherapy mesh for stage I non-small cell lung cancer. *Semin. Thorac. Cardiovasc. Surg.* **22**, 32–37 (2010).
33. Toita, T. Current status and perspectives of brachytherapy for cervical cancer. *Int. J. Clin. Oncol.* **14**, 25–30 (2009).
34. Polgár, C. & Major, T. Current status and perspectives of brachytherapy for breast cancer. *Int. J. Clin. Oncol.* **14**, 7–24 (2009).
35. Santos, R. *et al.* Comparison between sublobar resection and 125Iodine brachytherapy after sublobar resection in high-risk patients with Stage I non-small-cell lung cancer. *Surgery* **134**, 691–697 (2003).
36. Juratli, T. A., Schackert, G. & Krex, D. Current status of local therapy in malignant gliomas - A clinical review of three selected approaches. *Pharmacol. Ther.* **139**, 341–358 (2013).
37. Wyse, E., Handa, J. T., Friedman, A. D. & Pearl, M. S. A review of the literature for intra-arterial chemotherapy used to treat retinoblastoma. *Pediatr. Radiol.* **46**, 1223–1233 (2016).
38. Homma, A., Onimaru, R., Matsuura, K., Robbins, K. T. & Fujii, M. Intra-arterial chemoradiotherapy for head and neck cancer. *Jpn. J. Clin. Oncol.* **46**, 4–12 (2016).
39. Zhang, W. *et al.* Efficacy of intraarterial chemoinfusion therapy for locally advanced breast cancer patients: A retrospective analysis of 28 cases. *Onco. Targets. Ther.* **6**, 761–765 (2013).
40. Clancy, T. E., Dixon, E., Perlis, R., Sutherland, F. R. & Zinner, M. J. Hepatic arterial infusion after curative resection of colorectal cancer metastases: a meta-analysis of prospective clinical trials. *J. Gastrointest. Surg.* **9**, 198–206 (2005).

41. Vogl, T. *et al.* Preliminary experience with transarterial chemoembolization (TACE) in liver metastases of uveal malignant melanoma: Local tumor control and survival. *J. Cancer Res. Clin. Oncol.* **133**, 177–184 (2007).
42. Vogl, T. J., Zangos, S., Eichler, K., Yakoub, D. & Nabil, M. Colorectal liver metastases: Regional chemotherapy via transarterial chemoembolization (TACE) and hepatic chemoperfusion: An update. *Eur. Radiol.* **17**, 1025–1034 (2007).
43. Marelli, L. *et al.* Transarterial therapy for hepatocellular carcinoma: Which technique is more effective? A systematic review of cohort and randomized studies. *Cardiovasc. Intervent. Radiol.* **30**, 6–25 (2007).
44. Shen, Z., Shen, T., Wientjes, M. G., O'Donnell, M. A. & Au, J. L. S. Intravesical treatments of bladder cancer: Review. *Pharm. Res.* **25**, 1500–1510 (2008).
45. Lawler, S. E., Speranza, M.-C., Cho, C.-F. & Chiocca, E. A. Oncolytic Viruses in Cancer Treatment. *JAMA Oncol.* **3**, 841 (2017).
46. Andtbacka, R. H. I. *et al.* Talimogene laherparepvec improves durable response rate in patients with advanced melanoma. *J. Clin. Oncol.* **33**, 2780–2788 (2015).
47. Vogelbaum, M. A. Convection enhanced delivery for treating brain tumors and selected neurological disorders: Symposium review. *J. Neurooncol.* **83**, 97–109 (2007).
48. Sampson, J. H. *et al.* Comparison of intratumoral bolus injection and convection-enhanced delivery of radiolabeled antitenascin monoclonal antibodies. *Neurosurg. Focus* **20**, E14 (2006).
49. Lidar, Z. *et al.* Convection-enhanced delivery of paclitaxel for the treatment of recurrent malignant glioma: a Phase I/II clinical study. *J. Neurosurg.* **100**, 472–479 (2004).
50. Maier-Hauff, K. *et al.* Efficacy and safety of intratumoral thermotherapy using magnetic iron-oxide nanoparticles combined with external beam radiotherapy on patients with recurrent glioblastoma multiforme. *J. Neurooncol.* **103**, 317–324 (2011).
51. Raghavan, R. *et al.* Convection-enhanced delivery of therapeutics for brain disease, and its optimization. *Neurosurg. Focus* **20**, E12 (2006).
52. Minchinton, A. I. & Tannock, I. F. Drug penetration in solid tumours. *Nat. Rev. Cancer* **6**, 583–592 (2006).
53. Jain, R. K. Barriers to drug delivery in solid tumors. *Sci. Am.* **2**, e29528 (1994).
54. Jain, R. K. Delivery of molecular medicine to solid tumors. *Adv. Drug Deliv. Rev.* **271**, 1079–1080 (1997).

55. Liu, Q. & Liu, B. Local Drug Delivery Strategies for Gastric Cancer Treatment. in *Personalized Management of Gastric Cancer - Translational and Precision Medicine* (eds. Wei, J. & Liu, B.) 203–214 (2017).
56. Chew, S. A. & Danti, S. Biomaterial-Based Implantable Devices for Cancer Therapy. *Adv. Healthc. Mater.* **6**, (2017).
57. Packhaeuser, C. B., Schnieders, J., Oster, C. G. & Kissel, T. In situ forming parenteral drug delivery systems: An overview. *Eur. J. Pharm. Biopharm.* **58**, 445–455 (2004).
58. Kempe, S. & Mäder, K. In situ forming implants - An attractive formulation principle for parenteral depot formulations. *J. Control. Release* **161**, 668–679 (2012).
59. Fakhari, A. & Anand Subramony, J. Engineered in-situ depot-forming hydrogels for intratumoral drug delivery. *J. Control. Release* **220**, 465–475 (2015).
60. Obara, K. *et al.* Controlled release of paclitaxel from photocrosslinked chitosan hydrogels and its subsequent effect on subcutaneous tumor growth in mice. *J. Control. Release* **110**, 79–89 (2005).
61. Sharifi, S. *et al.* Injectable in situ forming drug delivery system based on poly(ε-caprolactone fumarate) for tamoxifen citrate delivery: Gelation characteristics, in vitro drug release and anti-cancer evaluation. *Acta Biomater.* **5**, 1966–1978 (2009).
62. Zhang, H. *et al.* Near-infrared-triggered in situ hybrid hydrogel system for synergistic cancer therapy. *J. Mater. Chem. B* **3**, 6310–6326 (2015).
63. Balakrishnan, B. & Jayakrishnan, A. Self-cross-linking biopolymers as injectable in situ forming biodegradable scaffolds. *Biomaterials* **26**, 3941–3951 (2005).
64. Emoto, S. *et al.* Intraperitoneal administration of cisplatin via an in situ cross-linkable hyaluronic acid-based hydrogel for peritoneal dissemination of gastric cancer. *Surg. Today* **44**, 919–926 (2014).
65. Swanson, G. P. Management of Locally Advanced Prostate Cancer: Past, Present, Future. *J. Urol.* **176**, S34–S41 (2006).
66. Sawyer, A. J., Piepmeier, J. M. & Saltzman, W. M. New methods for direct delivery of chemotherapy for treating brain tumors. *Yale J. Biol. Med.* **79**, 141–152 (2006).
67. Thompson, I. M., Tangen, C. M. & Paradelo, J. Adjuvant Radiotherapy for Pathologically Advanced Prostate Cancer: A Randomized Clinical Trial. *JAMA Oncol.* **76**, 180–182 (2006).

68. James, S. J., Pogribna, M., Miller, B. J., Bolon, B. & Muskhelishvili, L. Characterization of cellular response to silicone implants in rats: Implications for foreign-body carcinogenesis. *Biomaterials* **18**, 667–675 (1997).

69. Coleman, D. L., King, R. N. & Andrade, J. D. The foreign body reaction: A chronic inflammatory response. *J. Biomed. Mater. Res.* **8**, 199–211 (1974).

70. Jain, R. A. The manufacturing techniques of various drug loaded biodegradable poly(lactide-co-glycolide) (PLGA) devices. *Biomaterials* **21**, 2475–2490 (2000).

71. von Burkersroda, F., Schedl, L. & Gopferich, A. Why degradable polymers undergo surface erosion or bulk erosion. *Biomaterials* **23**, 4221–4231 (2002).

72. Fung, L. L. K., Shin, M., Tyler, B., Brem, H. & Saltzman, W. M. Chemotherapeutic Drugs Released from Polymers: Distribution of 1,3-bis(2-chloroethyl)-l-nitrosourea in the Rat Brain. *Pharmaceutical Research* **13**, 671–682 (1996).

73. Gao, J., Qian, F., Szymanski-Exner, A., Stowe, N. & Haaga, J. In vivo drug distribution dynamics in thermoablated and normal rabbit livers from biodegradable polymers. *J. Biomed. Mater. Res.* **62**, 308–314 (2002).

74. Krupka, T. M., Weinberg, B. D., Ziats, N. P., Haaga, J. R. & Exner, A. a. Injectable polymer depot combined with radiofrequency ablation for treatment of experimental carcinoma in rat. *Invest. Radiol.* **41**, 890–7 (2006).

75. Qian, F., Szymanski, A. & Gao, J. Fabrication and characterization of controlled release poly (D , L -lactide-co-glycolide) millirods. *J. Biomed. Mater. Res.* **55**, 512–522 (2000).

76. Qian, F., Stowe, N., Liu, E. H., Saidel, G. M. & Gao, J. Quantification of in vivo doxorubicin transport from PLGA millirods in thermoablated rat livers. *J. Control. Release* **91**, 157–166 (2003).

77. Weinberg, B. D. *et al.* Combined radiofrequency ablation and doxorubicineluting polymer implants for liver cancer treatment. *J. Biomed. Mater. Res.* **81**, 205–213 (2007).

78. Blanco, E., Weinberg, B. D., Stowe, N. T., Anderson, J. M. & Gao, J. Local release of dexamethasone from polymer millirods effectively prevents fibrosis after radiofrequency ablation. *J. Biomed. Mater. Res. - Part A* **76**, 174–182 (2006).

79. Haaga, J. R., Exner, A. A., Wang, Y., Stowe, N. T. & Tarcha, P. J. Combined tumor therapy by using radiofrequency ablation and 5-FU-laden polymer implants: evaluation in rats and rabbits. *Radiology* **237**, 911–8 (2005).

80. Weinberg, B. D. Intratumoural Chemotherapy For Liver Cancer Using

Biodegradable Polymer Implants. (Case Western Reserve University, 2007).

81. Wolinsky, J. B. *et al.* Prevention of in vivo lung tumor growth by prolonged local delivery of hydroxycamptothecin using poly(ester-carbonate)-collagen composites. *J. Control. Release* **144**, 280–287 (2010).
82. Liu, R. *et al.* Paclitaxel-Eluting Polymer Film Reduces Locoregional Recurrence and Improves Survival in a Recurrent Sarcoma Model: A Novel Investigational Therapy. *Ann. Surg. Oncol.* **19**, 199–206 (2012).
83. Muldoon, L. L. *et al.* Chemotherapy delivery issues in central nervous system malignancy: A reality check. *J. Clin. Oncol.* **25**, 2295–2305 (2007).
84. Ramachandran, R. *et al.* Theranostic 3-Dimensional nano brain-implant for prolonged and localized treatment of recurrent glioma. *Sci. Rep.* **7**, 43271 (2017).
85. Saini, M. Implant biomaterials: A comprehensive review. *World J. Clin. Cases* **3**, 52 (2015).
86. Ewend, M. G. *et al.* Local Delivery of Chemotherapy and Concurrent External Beam Radiotherapy Prolongs Survival in Metastatic Brain Tumor Models. *Cancer Res.* **56**, 5217–5223 (1996).
87. Hsu, W., Lesniak, M. S., Tyler, B. & Brem, H. Local delivery of interleukin-2 and adriamycin is synergistic in the treatment of experimental malignant glioma. *J. Neurooncol.* **74**, 135–140 (2005).
88. Bow, H. *et al.* Local delivery of angiogenesis-inhibitor minocycline combined with radiotherapy and oral temozolomide chemotherapy in 9L glioma. *J. Neurosurg.* **120**, 662–669 (2014).
89. Brem, H. *et al.* Placebo-controlled trial of safety and efficacy of intraoperative controlled delivery by biodegradable polymers of chemotherapy for recurrent gliomas. The Polymer-brain Tumor Treatment Group. *Lancet* **345**, 1008–1012 (1995).
90. Westphal, M. *et al.* A phase 3 trial of local chemotherapy with biodegradable carmustine (BCNU) wafers (Gliadel wafers) in patients with primary malignant glioma. *Neuro. Oncol.* **5**, 79–88 (2003).
91. Fleming, A. B. & Saltzman, W. M. Pharmacokinetics of the Carmustine Implant. *Clin. Pharmacokinet.* **41**, 403–419 (2002).
92. Arbor Pharmaceuticals, L. *Carmustine: Drug information*. (2013).
93. Jelonek, K. *et al.* Novel poly(l-lactide-co-ε-caprolactone) matrices obtained with the use of zr[acac]as nontoxic initiator for long-term Release of Immunosuppressive Drugs. *Biomed Res. Int.* **2013**, (2013).
94. Hendricks, B. K., Cohen-gadol, A. A. & Miller, J. C. Novel delivery methods

bypassing the blood-brain and blood-tumor barriers. *Neurosurg Focus* **38**, 1–15 (2015).

95. Mitchell, H. Goserelin ('Zoladex') - Offering patients more choice in early breast cancer. *Eur. J. Oncol. Nurs.* **8**, (2004).
96. Chaplin, S. & Persad, R. Histrelin acetate : gonadorelin analogue given once a year. *Prescriber* 31–33 (2010).
97. Woolen, S., Holzmeyer, C., Nesbitt, E. & Siami, P. F. Long-Term Efficacy and Tolerability of Abdominal Once-Yearly Histrelin Acetate Subcutaneous Implants in Patients with Advanced Prostate Cancer. *Prostate Cancer* **2014**, 1–5 (2014).
98. Herrlich, S., Spieth, S., Messner, S. & Zengerle, R. Osmotic micropumps for drug delivery. *Adv. Drug Deliv. Rev.* **64**, 1617–1627 (2012).
99. Daneshmand, S., Pohar, K. S., Steinberg, G. D., Aron, M. & Cutie, C. Effect of GemRIS (gemcitabine-releasing intravesical system, TAR-200) on antitumor activity in muscle-invasive bladder cancer (MIBC). *J. Clin. Oncol.* **35**, (2017).
100. Struss, W. J. *et al.* Magnetically-actuated drug delivery device (MADDD) for minimally invasive treatment of prostate cancer: An in vivo animal pilot study. *Prostate* **77**, 1356–1365 (2017).
101. Cima, M. J. Microsystem Technologies for Medical Applications. *Annu. Rev. Chem. Biomol. Eng.* **2**, 355–378 (2011).
102. Masi, B. C. *et al.* Intracranial MEMS based temozolomide delivery in a 9L rat gliosarcoma model. *Biomaterials* **33**, 5768–5775 (2012).
103. Ge, J. *et al.* Initiation of Targeted Nanodrug Delivery in Vivo by a Multifunctional Magnetic Implant. *ACS Appl. Mater. Interfaces* **9**, 20771–20778 (2017).
104. Rawat, S., Vengurlekar, S., Rakesh, B., Jain, S. & Srikarti, G. Transdermal Delivery by Ionotophoresis. *Indian J. Pharm. Sci.* **70**, 5–10 (2008).
105. Byrne, J. D. *et al.* Iontophoretic device delivery for the localized treatment of pancreatic ductal adenocarcinoma. *Proc. Natl. Acad. Sci.* **113**, 2200–2205 (2016).
106. Elzey, bennett *et al.* A totally absorbable multilayer PLGA implant device containing doxorubicin inhibited tumor growth and metastasis without systemic toxicity in murine breast cancer and an ideal pharmacological paradigm for regional chemotherapy. *J. Biosci. Med.* **4**, 66–81 (2016).
107. Liaw, C.-Y. & Guvendiren, M. Current and emerging applications of 3D printing in medicine. *Biofabrication* **9**, 024102 (2017).
108. Ligon, S. C., Liska, R., Stampfl, J., Gurr, M. & Mülhaupt, R. Polymers for 3D Printing and Customized Additive Manufacturing. *Chem. Rev.* **117**, 10212–

10290 (2017).

109. Palo, M., Holländer, J., Suominen, J., Yliruusi, J. & Sandler, N. 3D printed drug delivery devices: perspectives and technical challenges. *Expert Rev. Med. Devices* **14**, 685–696 (2017).
110. Ho, C. M. B., Ng, S. H. & Yoon, Y. J. A review on 3D printed bioimplants. *Int. J. Precis. Eng. Manuf.* **16**, 1035–1046 (2015).
111. Norman, J., Madurawe, R. D., Moore, C. M. V., Khan, M. A. & Khairuzzaman, A. A new chapter in pharmaceutical manufacturing: 3D-printed drug products. *Adv. Drug Deliv. Rev.* **108**, 39–50 (2017).
112. Prasad, L. K. & Smyth, H. 3D Printing technologies for drug delivery: a review. *Drug Dev. Ind. Pharm.* **9045**, 1–13 (2016).
113. Kumar, S. Selective Laser Sintering : A Qualitative and Objective Approach. 43–47
114. Hutmacher, D. W., Sittinger, M. & Risbud, M. V. Scaffold-based tissue engineering: Rationale for computer-aided design and solid free-form fabrication systems. *Trends Biotechnol.* **22**, 354–362 (2004).
115. Gibson, I. & Shi, D. Material properties and fabrication parameters in selective laser sintering process. *Rapid Prototyp. J.* **3**, 129–136 (1997).
116. Kruth, J., Mercelis, P., Van Vaerenbergh, J., Froyen, L. & Rombouts, M. Binding mechanisms in selective laser sintering and selective laser melting. *Rapid Prototyp. J.* **11**, 26–36 (2005).
117. Schmid, M., Amado, A. & Wegener, K. Materials perspective of polymers for additive manufacturing with selective laser sintering. *J. Mater. Res.* **29**, 1824–1832 (2014).
118. Goodridge, R. D., Tuck, C. J. & Hague, R. J. M. Laser sintering of polyamides and other polymers. *Prog. Mater. Sci.* **57**, 229–267 (2012).
119. Berretta, S., Ghita, O. & Evans, K. E. Morphology of polymeric powders in Laser Sintering (LS): From Polyamide to new PEEK powders. *Eur. Polym. J.* **59**, 218–229 (2014).
120. Vasquez, M., Cross, J., Hopkinson, N. & Haworth, B. Developing new laser sintering materials for snowboarding applications. *Procedia Eng.* **34**, 325–330 (2012).
121. Yamane, M. & Kawaguchi, T. Apparatus for forming three-dimensional article. (1992).
122. Napadensky, E. Compositions and methods for use in three dimensional model printing. (2003).
123. Renn, M. J. Direct Write™ System. (2006).

124. Kim, N.-S. & Han, K. N. Future direction of direct writing. *J. Appl. Phys.* **108**, 102801 (2010).
125. Sachs, E., Cima, M. & Cornie, J. Three-dimensional printing: rapid tooling and prototypes directly form a CAD model. *CIRP Ann. - Manuf. Technol.* **39**, 201–204 (1990).
126. Pfister, A. *et al.* Biofunctional Rapid Prototyping for Tissue-Engineering Applications: 3D Bioplotting versus 3D Printing. *J. Polym. Sci. Part A Polym. Chem.* **42**, 624–638 (2004).
127. Krishnan, V. The insider's guide to Invisalign® Treatment (2017). *J. World Fed. Orthod.* **6**, 139–140 (2017).
128. Abdulmohsen, B., Parker, S., Braden, M. & Patel, M. P. A study to investigate and compare the physicomechanical properties of experimental and commercial temporary crown and bridge materials. *Dent. Mater.* **32**, 200–210 (2016).
129. Leong, K. F., Cheah, C. M. & Chua, C. K. Solid freeform fabrication of three-dimensional scaffolds for engineering replacement tissues and organs. *Biomaterials* **24**, 2363–2378 (2003).
130. Yeong, W.-Y., Chua, C.-K., Leong, K.-F. & Chandrasekaran, M. Rapid prototyping in tissue engineering: challenges and potential. *Trends Biotechnol.* **22**, 643–652 (2004).
131. The 4WEB Difference. *4WEB Medical* (2018). Available at: https://4webmedical.com/about/. (Accessed: 14th January 2018)
132. Tritanium® PL Posterior Lumbar Cage - Technical Summary. *Built to fuse* 1–12 (2017). Available at: http://www.stryker.com/builttofuse/media/assets/TRITA-BR-3 Tritanium Technical Summary FINAL.pdf. (Accessed: 14th January 2018)
133. Bulanova, E. A. *et al.* Bioprinting of functional vascularized mouse thyroid gland construct. *Biofabrication* **93**, 1–28 (2017).
134. L'Oreal And Poietis Sign An Exclusive Research Partnership To Develop Bioprinting Of Hair. *Press Releases* (2016). Available at: http://www.loreal.com/media/press-releases/2016/sep/loreal-and-poietis-sign-an-exclusive-research-partnership-to-develop-bioprinting-of-hair. (Accessed: 14th January 2018)
135. Nyga, A., Cheema, U. & Loizidou, M. 3D tumour models: Novel in vitro approaches to cancer studies. *J. Cell Commun. Signal.* **5**, 239–248 (2011).
136. Jang, J., Yi, H.-G. & Cho, D.-W. 3D Printed Tissue Models: Present and Future. *ACS Biomater. Sci. Eng.* **2**, 1722–1731 (2016).

137. Zhang, Y. S. *et al.* Bioprinting the Cancer Microenvironment. *ACS Biomater. Sci. Eng.* **2**, 1710–1721 (2016).
138. Zhao, Y. *et al.* Three-dimensional printing of Hela cells for cervical tumor model in vitro. *Biofabrication* **6**, (2014).
139. Chang, R., Nam, J. & Sun, W. Direct Cell Writing of 3D Microorgan for *In Vitro* Pharmacokinetic Model. *Tissue Eng. Part C Methods* **14**, 157–166 (2008).
140. Matsusaki, M., Sakaue, K., Kadowaki, K. & Akashi, M. Three-dimensional human tissue chips fabricated by rapid and automatic inkjet cell printing. *Adv. Healthc. Mater.* **2**, 534–539 (2013).
141. Nguyen, D. G. *et al.* Bioprinted 3D primary liver tissues allow assessment of organ-level response to clinical drug induced toxicity in vitro. *PLoS One* **11**, 1–17 (2016).
142. Lee, V. *et al.* Design and Fabrication of Human Skin by Three-Dimensional Bioprinting. *Tissue Eng. Part C Methods* **20**, 473–484 (2014).
143. L'Oreal USA Announces Research Partnership with Organovo to Develop 3-D Bioprinted Skin Tissue. *Organovo* (2015). Available at: http://ir.organovo.com/phoenix.zhtml?c=254194&p=irol-newsArticle&ID=2129344. (Accessed: 14th January 2018)
144. Kolesky, D. B., Homan, K. A., Skylar-Scott, M. A. & Lewis, J. A. Three-dimensional bioprinting of thick vascularized tissues. *Proc. Natl. Acad. Sci.* **113**, 3179–3184 (2016).
145. Kunz, M., Waldman, S. D., Rudan, J. F., Bardana, D. D. & Stewart, A. J. Computer-assisted mosaic arthroplasty using patient-specific instrument guides. *Knee Surgery, Sport. Traumatol. Arthrosc.* **20**, 857–861 (2012).
146. Rankin, T. M. *et al.* Three-dimensional printing surgical instruments: Are we there yet? *J. Surg. Res.* **189**, 193–197 (2014).
147. Scolozzi, P. Maxillofacial reconstruction using polyetheretherketone patient-specific implants by 'mirroring' computational planning. *Aesthetic Plast. Surg.* **36**, 660–665 (2012).
148. Frigg, R. Advanced bone marker and custom implants. (2013).
149. Hollister, S. J. *et al.* Mitigation of tracheobronchomalacia with 3D- printed personalized medical devices in pediatric patients. **7**, 1–12 (2016).
150. Sandström, C. G. The non-disruptive emergence of an ecosystem for 3D Printing - Insights from the hearing aid industry's transition 1989-2008. *Technol. Forecast. Soc. Change* **102**, 160–168 (2016).
151. Jones, D. B., Sung, R., Weinberg, C., Korelitz, T. & Andrews, R. Three-Dimensional Modeling May Improve Surgical Education and Clinical Practice.

Surg. Innov. **23**, 189–195 (2016).

152. Spritam. (2017). Available at: https://www.spritam.com/#/patient. (Accessed: 11th January 2018)
153. Jacob, J. *et al.* Rapid Disperse Dosage Form Containing Levetiracetam. (2014).
154. Goyanes, A., Robles Martinez, P., Buanz, A., Basit, A. W. & Gaisford, S. Effect of geometry on drug release from 3D printed tablets. *Int. J. Pharm.* **494**, 657–663 (2015).
155. Lin, S. *et al.* In vitro and in vivo evaluations of biodegradable implants for hormone replacement therapy: Effect of system design and PK-PD relationship. *AAPS PharmSciTech* **2**, 55–65 (2001).
156. Gbureck, U., Vorndran, E., Müller, F. A. & Barralet, J. E. Low temperature direct 3D printed bioceramics and biocomposites as drug release matrices. *J. Control. Release* **122**, 173–180 (2007).
157. Inzana, J. A., Trombetta, R. P., Schwarz, E. M., Kates, S. L. & Awad, H. A. 3D printed bioceramics for dual antibiotic delivery to treat implant-associated bone infection. *Eur. Cells Mater.* **30**, 232–247 (2015).
158. Rowe, C. . *et al.* Multimechanism oral dosage forms fabricated by three dimensional printing™. *J. Control. Release* **66**, 11–17 (2000).
159. Yu, D. G. *et al.* Tablets with material gradients fabricated by three-dimensional printing. *J. Pharm. Sci.* **96**, 2446–2456 (2007).
160. Yu, D. G. *et al.* Novel drug delivery devices for providing linear release profiles fabricated by 3DP. *Int. J. Pharm.* **370**, 160–166 (2009).
161. Lee, K. J. *et al.* Evaluation of Critical Formulation Factors in the Development of a Rapidly Dispersing Captopril Oral Dosage Form. *Drug Dev. Ind. Pharm.* **29**, 967–979 (2003).
162. Alhnan, M. A. *et al.* Emergence of 3D Printed Dosage Forms: Opportunities and Challenges. *Pharm. Res.* **33**, 1817–1832 (2016).
163. Goyanes, A. *et al.* 3D Printing of Medicines: Engineering Novel Oral Devices with Unique Design and Drug Release Characteristics. *Mol. Pharm.* **12**, 4077–4084 (2015).
164. Sandler, N. *et al.* Towards fabrication of 3D printed medical devices to prevent biofilm formation. *Int. J. Pharm.* **459**, 62–64 (2014).
165. Boetker, J. *et al.* Modifying release characteristics from 3D printed drug-eluting products. *Eur. J. Pharm. Sci.* **90**, 47–52 (2016).
166. Holländer, J. *et al.* Three-Dimensional Printed PCL-Based Implantable Prototypes of Medical Devices for Controlled Drug Delivery. *J. Pharm. Sci.* **105**,

2665–2676 (2016).

167. Genina, N. *et al.* Ethylene vinyl acetate (EVA) as a new drug carrier for 3D printed medical drug delivery devices. *Eur. J. Pharm. Sci.* **90**, 53–63 (2016).
168. Rattanakit, P., Moulton, S. E., Santiago, K. S., Liawruangrath, S. & Wallace, G. G. Extrusion printed polymer structures: A facile and versatile approach to tailored drug delivery platforms. *Int. J. Pharm.* **422**, 254–263 (2012).
169. Khaled, S. A., Burley, J. C., Alexander, M. R., Yang, J. & Roberts, C. J. 3D printing of five-in-one dose combination polypill with defined immediate and sustained release profiles. *J. Control. Release* **217**, 308–314 (2015).
170. Song, T. H., Jang, J., Choi, Y. J., Shim, J. H. & Cho, D. W. 3D-printed drug/cell carrier enabling effective release of cyclosporin a for xenogeneic cell-based therapy. *Cell Transplant.* **24**, 2513–2525 (2015).
171. Min, Z., Kun, L., Yufang, Z., Jianhua, Z. & Xiaojian, Y. 3D-printed hierarchical scaffold for localized isoniazid/rifampin drug delivery and osteoarticular tuberculosis therapy. *Acta Biomater.* **16**, 145–155 (2015).
172. Yi, H.-G. *et al.* A 3D-printed local drug delivery patch for pancreatic cancer growth suppression. *J. Control. Release* **238**, 231–241 (2016).
173. Salmoria, G. V. *et al.* Development of functionally-graded reservoir of PCL/PG by selective laser sintering for drug delivery devices: This paper presents a selective laser sintering-fabricated drug delivery system that contains graded progesterone content. *Virtual Phys. Prototyp.* **7**, 107–115 (2012).
174. Wang, J., Goyanes, A., Gaisford, S. & Basit, A. W. Stereolithographic (SLA) 3D printing of oral modified-release dosage forms. *Int. J. Pharm.* **503**, 207–212 (2016).
175. Guan, Y., Zhang, W., Wan, G. & Peng, Y. Polytetrahydrofuran amphiphilic networks. I. Synthesis and characterization of polytetrahydrofuran acrylate ditelechelic and polyacrylamide-l-polytetrahydrofuran networks. *J. Polym. Sci. Part A Polym. Chem.* **38**, 3812–3820 (2000).
176. Sinh, L. H. *et al.* Novel photo-curable polyurethane resin for stereolithography. *RSC Adv.* **6**, 50706–50709 (2016).
177. Patil, D. M., Phalak, G. A. & Mhaske, S. T. Design and synthesis of bio-based UV curable PU acrylate resin from itaconic acid for coating applications. *Des. Monomers Polym.* **20**, 269–282 (2017).
178. Feng, P., Li, W. & Zou, Y. Synthesis and ultraviolet-curing behaviors of vinyl ether functionalized polyurethane oligomers. *J. Appl. Polym. Sci.* **131**, 1–9 (2014).
179. V, K. I. Synthesis and Properties of Urethane Acrylate Oligomers: Direct versus

Reverse Addition. *Ind. Eng. Chem. Res.* **43**, 6281 (2004).

180. Li, H. & Gu, L. Controllable synthesis of bio-based polylactide diols using an organocatalyst in solvent-free conditions. *J. Polym. Sci. Part A Polym. Chem.* **56**, 968–976 (2018).
181. Wang, T., Li, B. S. & Zhang, L. X. Carbazole-bound ferrocenium salt as an efficient cationic photoinitiator for epoxy polymerization. *Polym. Int.* **54**, 1251–1255 (2005).
182. Abd-el-aziz, A. S., Lee, C. C., Piorko, A. & Sutherland, R. G. Arylation of Diethyl Malonate via Nucleophilic Substitution Reactions with Cyclopentadienyliron Complexes of Chloroarenes. *Synth. Commun.* **18**, 291–300 (1988).
183. Wang, T., Li, Z., Zhang, Y. & Lu, M. Synthesis and photoactivity of novel cationic photoinitiators: (η6-Diphenylmethane) (η5-cyclopentadienyl) iron hexafluorophosphate and (η6-benzophenone) (η5-cyclopentadienyl) iron hexafluorophosphate. *Prog. Org. Coatings* **65**, 251–256 (2009).
184. Li, M., Chen, Y., Zhang, H. & Wang, T. A novel ferrocenium salt as visible light photoinitiator for cationic and radical photopolymerization. *Prog. Org. Coatings* **68**, 234–239 (2010).
185. Zhou, H. *et al.* Fluorenylvinylenes bridged triphenylamine-based dyes with enhanced performance in dye-sensitized solar cells. *Tetrahedron* **67**, 8477–8483 (2011).
186. Jin, M. *et al.* Design of D–π–A type photoacid generators for high efficiency excitation at 405 nm and 800 nm. *Chem. Commun.* **49**, 8480 (2013).
187. Zhou, W., Kuebler, S. M., Carrig, D., Perry, J. W. & Marder, S. R. Efficient Photoacids Based upon Triarylamine Dialkylsulfonium Salts. *J. Am. Chem. Soc.* **124**, 1897–1901 (2002).
188. Robles-Martinez, P. *et al.* 3D printing of a multi-layered polypill containing six drugs using a novel stereolithographic method. *Pharmaceutics* **11**, (2019).
189. Moghimi, A., Omrani, I., Nabid, M. R. & Mahmoodi, M. Quantification of hydroxyl group in polymers containing trace water by 19F NMR spectroscopy. *Eur. Polym. J.* **49**, 228–234 (2013).
190. dos Santos, V., Brandalise, R. N. & Savaris, M. Biomaterials: Characteristics and Properties. in *Engineering of Biomaterials* 5–15 (Springer International Publishing, 2017). doi:10.1007/978-3-319-58607-6
191. Teo, A. J. T. T. *et al.* Polymeric Biomaterials for Medical Implants and Devices. *ACS Biomater. Sci. Eng.* **2**, 454–472 (2016).
192. WHO. *The TCu380A Intrauterine Contraceptive Device (IUD): Specification, Prequalification and Guidelines for Procurement 2010*. (2010).

193. Formlabs. *Materials Data Sheet Photopolymer Resin for Form 1+ and Form 2 FORMLABS MATERIAL PROPERTIES*. (2017).
194. Materials and Processes - Toughness. *NDT Education Resource Center* (2014). Available at: https://www.nde-ed.org/EducationResources/CommunityCollege/Materials/Mechanical/Toughness.htm. (Accessed: 2nd February 2018)
195. Smith, K. E., Trusty, P., Wan, B. & Gall, K. Long-term toughness of photopolymerizable (meth)acrylate networks in aqueous environments. *Acta Biomater.* **7**, 558–567 (2011).
196. Melchels, F. P. W., Feijen, J. & Grijpma, D. W. A review on stereolithography and its applications in biomedical engineering. *Biomaterials* **31**, 6121–6130 (2010).
197. Decker, C. Real-Time Monitoring of Polymerization Quantum Yields. *Macromolecules* **23**, 5217–5220 (1990).
198. Ligon-Auer, S. C., Schwentenwein, M., Gorsche, C., Stampfl, J. & Liska, R. Toughening of photo-curable polymer networks: a review. *Polym. Chem.* **7**, 257–286 (2016).
199. Torres-Filho, A. Mechanical Properties of Acrylate Networks Formed by Visible Laser-Induced Polymerization. 2. Control of the Mechanical Properties. *Chem. Rev.* **7**, 744–753 (1995).
200. Lee, K. Y., Kim, K. Y., Hwang, I. R., Choi, Y. S. & Hong, C. H. Thermal, tensile and morphological properties of gamma-ray irradiated epoxy-clay nanocomposites toughened with a liquid rubber. *Polym. Test.* **29**, 139–146 (2010).
201. Hoyle, C. E., Lee, T. Y. & Roper, T. Thiol-enes: Chemistry of the past with promise for the future. *J. Polym. Sci. Part A Polym. Chem.* **42**, 5301–5338 (2004).
202. McNair, O. D. *et al.* Impact Properties of Thiol-Ene Networks. *Appl. Mater. Interfaces* **5**, 11004–11013 (2013).
203. Decker, C., Viet, T. N. T. & Decker, D. UV-radiation curing of acrylate / epoxide systems. *Polymer (Guildf).* **42**, 5531–5541 (2001).
204. Jansen, B. J. P., Rastogi, S., Meijer, H. E. H. & Lemstra, P. J. Rubber-modified glassy amorphous polymers prepared via chemically induced phase separation. 4. Comparison of properties of semi- and full-IPNs, and copolymers of acrylate-aliphatic epoxy systems. *Macromolecules* **32**, 6290–6297 (1999).
205. Sandmann, B. *et al.* Incorporation of core-shell particles into methacrylate based composites for improvement of the mechanical properties. *Polym.*

Chem. **6**, 5273–5280 (2015).

206. Miao, S. *et al.* 4D printing smart biomedical scaffolds with novel soybean oil epoxidized acrylate. *Sci. Rep.* **6**, 27226 (2016).
207. Hoare, T. R. & Kohane, D. S. Hydrogels in drug delivery: Progress and challenges. *Polymer (Guildf).* **49**, 1993–2007 (2008).
208. Malucelli, G., Gozzelino, G., Ferrero, F., Bongiovanni, R. & Priola, A. Synthesis of poly(propylene glycol-diacrylates) and properties of the photocured networks. *J. Appl. Polym. Sci.* 491–497 (1996).
209. Atzet, S., Curtin, S., Trinh, P., Bryant, S. & Ratner, B. Degradable poly(2-hydroxyethyl methacrylate)-co-polycaprolactone hydrogels for tissue engineering scaffolds. *Biomacromolecules* **9**, 3370–3377 (2008).
210. He, Y. *et al.* A new photocrosslinkable polycaprolactone-based ink for three-dimensional inkjet printing. *J. Biomed. Mater. Res. - Part B Appl. Biomater.* 1–13 (2016). doi:10.1002/jbm.b.33699
211. Burke, A. and Hasirci, N. Polyurethanes in Biomedical Applications. in *Biomaterials: From Molecules to Engineered Tissues* 83–105 (2004).
212. Tong, X. Uv-Curable Hybrid Polyurethanes. 84 (2014).
213. Liao, F., Zeng, X. R., Li, H. Q., Lai, X. J. & Zhao, F. C. Synthesis and properties of UV curable polyurethane acrylates based on two different hydroxyethyl acrylates. *J. Cent. South Univ. Technol. (English Ed.* **19**, 911–917 (2012).
214. Kunwong, D., Sumanochitraporn, N. & Kaewpirom, S. Curing behavior of a UV-curable coating based on urethane acrylate oligomer: The influence of reactive monomers. *Songklanakarin J. Sci. Technol.* **33**, 201–207 (2011).
215. Sultan, M. *et al.* Modification of cellulosic fiber with polyurethane acrylate copolymers. Part I: Physicochemical properties. *Carbohydr. Polym.* **87**, 397–404 (2012).
216. Chung, Y.-C., Kim, H. Y., Choi, J. W. & Chun, B. C. Preparation of urethane-acrylates by the photo-polymerization of acrylate monomers using a benzophenone initiator grafted onto a polyurethane copolymer. *Macromol. Res.* **22**, 1115–1124 (2014).
217. Feng, X. *et al.* Synthesis and characterization of biodegradable poly(ether-ester) urethane acrylates for controlled drug release. *Mater. Sci. Eng. C* **74**, 270–278 (2016).
218. Alcock, B. Single Polymer Composites Based on Polypropylene : Processing and Properties. (Queen Mary, University of London, 2004).
219. Lomolder, R., Plogmann, F. & Speier, P. Selectivity of Isophorone Diisocyanate in the Urethane Reaction Influence of Temperature, Catalysis, and Reaction

Partners. *J. Coatings Technol.* **69**, 51–57 (1997).

220. Srivastava, A., Agarwal, D., Mistry, S. & Singh, J. UV curable polyurethane acrylate coatings for metal surfaces. *Pigment Resin Technol. Pigment & Resin Technol. Iss Pigment & Resin Technol. Iss Pigment & Resin Technol. Iss* **37**, 217–223 (2008).
221. Shukla, S. & Rai, J. S. P. Synthesis and kinetic study of diacrylate and dimethacrylate. *Int. J. Plast. Technol.* **17**, 182–193 (2013).
222. Evans, S. B., Mulvaney, J. E. & Hall, H. K. On the synthesis of pure (meth) acrylate esters and their corresponding homopolymers. *J. Polym. Sci. Part A Polym. Chem.* **28**, 1073–1078 (1990).
223. Im, S. J., Choi, Y. M., Subramanyam, E., Huh, K. M. & Park, K. Synthesis and characterization of biodegradable elastic hydrogels based on poly(ethylene glycol) and poly(ε-caprolactone) blocks. *Macromol. Res.* **15**, 363–369 (2007).
224. Matsuda, T. & Mizutani, M. Liquid acrylate-endcapped biodegradable poly(e-caprolactone-co-trimethylene carbonate). II. Computer-aided stereolithographic microarchitectural surface photoconstructs. *J. Biomed. Mater. Res.* **62**, 395–403 (2002).
225. Schüller-Ravoo, S., Zant, E., Feijen, J. & Grijpma, D. W. Preparation of a Designed Poly(trimethylene carbonate) Microvascular Network by Stereolithography. *Adv. Healthc. Mater.* **3**, 2004–2011 (2014).
226. Bens, A. *et al.* Non-toxic flexible photopolymers for medical stereolithography technology. *Rapid Prototyp. J.* **13**, 38–47 (2007).
227. Su, S., Wang, H., Zhou, C., Wang, Y. & Liu, J. Study on epoxy resin with high elongation-at- break using polyamide and polyether amine as a two-component curing agent. *e-Polymers* **18**, 433–439 (2018).
228. Taylor, R. A Guide to Shore Durometers. (2015). Available at: https://albrightsilicone.com/a-guide-to-shore-durometers/#.
229. Crow. Polymer Properties Database. (2015). Available at: polymerdatabase.com.
230. Glass transition temperature. *Omnexus* (2020). Available at: https://omnexus.specialchem.com/polymer-properties/properties/glass-transition-temperature.
231. Woodard, L. N. & Grunlan, M. A. Hydrolytic Degradation and Erosion of Polyester Biomaterials. *ACS Macro Lett.* **7**, 976–982 (2018).
232. Husár, B. & Liska, R. Vinyl carbonates, vinyl carbamates, and related monomers: synthesis, polymerization, and application. *Chem. Soc. Rev.* **41**, 2395–2405 (2012).

233. Heller, C. *et al.* Vinylcarbonates and vinylcarbamates: Biocompatible monomers for radical photopolymerization. *J. Polym. Sci. Part A Polym. Chem.* **49**, 650–661 (2011).
234. Schuster, M. *et al.* Evaluation of Biocompatible Photopolymers I: Photoreactivity and Mechanical Properties of Reactive Diluents. *J. Macromol. Sci. Part A Pure Appl. Chem.* **44**, 547–557 (2007).
235. Schuster, M. *et al.* Evaluation of biocompatible photopolymers II: Further reactive diluents. *Monatshefte fur Chemie* **138**, 261–268 (2007).
236. Carve, M. & Wlodkowic, D. 3D-Printed Chips: Compatibility of Additive Manufacturing Photopolymeric Substrata with Biological Applications. *Micromachines* **9**, 91 (2018).
237. Bayraktar, G., Guvener, B., Bural, C. & Uresin, Y. Influence of polymerization method, curing process, and length of time of storage in water on the residual methyl methacrylate content in dental acrylic resins. *J. Biomed. Mater. Res. - Part B Appl. Biomater.* **76**, 340–345 (2006).
238. Charasseangpaisarn, T., Wiwatwarrapan, C. & Leklerssiriwong, N. Ultrasonic cleaning reduces the residual monomer in acrylic resins. *J. Dent. Sci.* **11**, 443–448 (2016).
239. Alifui-Segbaya, F., Varma, S., Lieschke, G. J. & George, R. Biocompatibility of Photopolymers in 3D Printing. *3D Print. Addit. Manuf.* **4**, 185–191 (2017).
240. FormLabs. *DentalSG: Instructions for Use*. (2016). doi:10.1515/9783110824469.X
241. Oskui, S. M. *et al.* Assessing and Reducing the Toxicity of 3D-Printed Parts. *Environ. Sci. Technol. Lett.* **3**, 1–6 (2016).
242. Inoue, Y. & Ikuta, K. Detoxification of the photocurable polymer by heat treatment for microstereolithography. *Procedia CIRP* **5**, 115–118 (2013).
243. Popov, V. K. *et al.* Laser stereolithography and supercritical fluid processing for custom-designed implant fabrication. *J. Mater. Sci. Mater. Med.* **15**, 123–128 (2004).
244. Husar, B. *et al.* An overview on low cytotoxic alternatives to (meth)acrylates: vinyl esters and vinyl carbonates. *Conf. Pap.* (2014).
245. Dworak, C., Koch, T., Varga, F. & Liska, R. Photopolymerization of biocompatible phosphorus-containing vinyl esters and vinyl carbamates. *J. Polym. Sci. Part A Polym. Chem.* **48**, 2916–2924 (2010).
246. Liska, R. *et al.* Composition that can be cured by polymerisation for the production of biodegradable, biocompatible, cross-linkable polymers on the basis of polyvinyl alcohol. (2010).

247. Heller, C. *et al.* Vinyl Esters: Low Cytotoxicity Monomers for the Fabrication of Biocompatible 3D Scaffolds by Lithography Based Additive Manufacturing. *J. Polym. Sci. Part A Polym. Chem.* **47**, 6941–6954 (2009).
248. Russmueller, G. *et al.* 3D Printable Biophotopolymers for in Vivo Bone Regeneration. *Materials (Basel).* **8**, 3685–3700 (2015).
249. Staffel, W., Kessinger, R. & Henkelmann, J. Method for the production of o-vinylcarbamates and vinylcarbonates. (2008).
250. Sangermano, M. Advances in cationic photopolymerization. *Pure Appl. Chem.* **84**, 2089–2101 (2012).
251. Chatani, S., Kloxin, C. J. & Bowman, C. N. The power of light in polymer science: photochemical processes to manipulate polymer formation, structure, and properties. *Polym. Chem.* **5**, 2187–2201 (2014).
252. Endruweit, A., Johnson, M. S. & Long, A. C. Curing of Composite Components by Ultraviolet Radiation: A Review. *Polym. Compos.* **27**, 119–128 (2006).
253. Calhoun, A. & Peacock, A. J. *Synthesis of poly(allyl 2-ylidene-acetate) and subsequent postpolymerization modification via thiol-ene reaction*. (Hanser, 2006). doi:10.1039/c6py00818f
254. Decker, C. Photoinitiated Crosslinking Polymerisation. *Prog. Polym. Sci.* **21**, 593–650 (1996).
255. Decker, C. & Decker, D. Photoinitiated Polymerization of Vinyl Ether and Acrylate Monomer Mixtures. *J. Macromol. Sci. Part A Pure Appl. Chem.* **34**, 605–625 (2006).
256. Matake, R., Adachi, Y. & Matsubara, H. Synthesis of vinyl ethers of alcohols using calcium carbide under superbasic catalytic conditions (KOH/DMSO). *Green Chem.* **18**, 2614–2618 (2016).
257. Teong, S. P., Chua, A. Y. H., Deng, S., Li, X. & Zhang, Y. Direct vinylation of natural alcohols and derivatives with calcium carbide. *Green Chem.* **19**, 1659–1662 (2017).
258. Muhamad, I. I. *et al. Extraction Technologies and Solvents of Phytocompounds From Plant Materials : Physicochemical Characterization and Identification of Ingredients and Bioactive Compounds From Plant Extract Using Various Instrumentations*. *Ingredients Extraction by Physicochemical Methods in Food* (Elsevier Inc., 2017). doi:10.1016/b978-0-12-811521-3.00014-4
259. Elomaa, L. *et al.* Preparation of poly(ε-caprolactone)-based tissue engineering scaffolds by stereolithography. *Acta Biomater.* **7**, 3850–3856 (2011).
260. Shao, J., Huang, Y. & Fan, Q. Visible light initiating systems for photopolymerization: status, development and challenges. *Polym. Chem.* **5**,

4195 (2014).

261. Zhang, J. *et al.* Cationic Photoinitiators for Near UV and Visible LEDs: A Particular Insight into One-Component Systems. *Macromol. Chem. Phys.* **217**, 1214–1227 (2016).
262. Jin, M. *et al.* Π-Conjugated Sulfonium-Based Photoacid Generators: an Integrated Molecular Approach for Efficient One and Two-Photon Polymerization. *Polym. Chem.* **5**, 4747 (2014).
263. Mokbel, H. *et al.* Specific cationic photoinitiators for near UV and visible LEDs: Iodonium versus ferrocenium structures. *J. Appl. Polym. Sci.* **132**, 1–10 (2015).
264. Abd-el-aziz, A. S., Schriemer, D. C. & Denus, C. R. De. Bis(cyclopentadienyliron)arene Complexes : A New Route to the Synthesis and Functionalization of Polyaromatic Ethers. *Organometallics* **13**, 374–384 (1994).
265. Pearson, A. J. & Gelormini, A. M. Selective Arylation of Diols Using Arene-Iron Chemistry. *J. Org. Chem.* **60**, 281–284 (1995).
266. Abd-el-aziz, A. S., Lei, Y. U. N. & Denus, C. R. D. E. Aliphatic diols in the synthesis of bis(cyclopentadienyliron) arene complexes. *Polyhedron* **14**, 1585–1591 (1995).
267. Stansbury, J. W. & Dickens, S. H. Determination of double bond conversion in dental resins by near infrared spectroscopy. *Dent. Mater.* **17**, 71–79 (2001).
268. Chen, Y., Li, G., Zhang, H. & Wang, T. Visible light curing of bisphenol-A epoxides and acrylates photoinitiated by (?? 6-benzophenone)(?? 5-cyclopentadienyl) iron hexafluorophosphate. *J. Polym. Res.* **18**, 1425–1429 (2011).
269. Sangermano, M., Meier, P. & Tzavalas, S. Infrared Spectroscopy as a Tool to Monitor Radiation Curing. in *Infrared Spectroscopy - Materials Science, Engineering and Technology* (ed. Theophile, T.) 325–336 (InTech, 2012). doi:10.5772/2055
270. Jin, C., Xianling, L. & Zhenli, Z. The Application of FT-IR Spectrum Method in Photocuring Process for Polyester Acrylate. in *Proceedings of the 6th Japan-China bilateral symposium on radiation chemistry* 428–433 (1995).
271. Jacobs, P. F. Fundamentals of Stereolithography. *Soc. Manuf. Eng.* 196–211 (1992). doi:10.1017/CBO9781107415324.004
272. Miicraft. *MiiCraft+ 3D Printer User's Manual*. (2014).
273. Gorsche, C. *et al.* Real Time-NIR/MIR-Photorheology: A Versatile Tool for the in Situ Characterization of Photopolymerization Reactions. *Anal. Chem.* **89**, 4958–4968 (2017).

274. Park, S. *et al.* Rheology and curing characteristics of dual-curable clearcoats with hydroxyl functionalized urethane methacrylate oligomer: Effect of blocked isocyanate thermal crosslinkers. *Korea Aust. Rheol. J.* **26**, 159–167 (2014).
275. Tetko, I. V. *et al.* Virtual computational chemistry laboratory - Design and description. *J. Comput. Aided. Mol. Des.* **19**, 453–463 (2005).
276. VCCLAB. Virtual Computational Chemistry Laboratory. (2005). Available at: http://www.vcclab.org.
277. *USP <467> Residual Solvents*. *United States Pharmacopeia and National Formulary (USP30 -NF25)* (United States Pharmacopeial Convention, 2005). doi:10.1021/js960213f
278. Witschi, C. & Doelker, E. Residual solvents in pharmaceutical products: Acceptable limits, influences on physicochemical properties, analytical methods and documented values. *European Journal of Pharmaceutics and Biopharmaceutics* **43**, 215–242 (1997).

8. Appendix

8.1. Appendix 1 1H NMR spectra of photocurable monomers/macromers

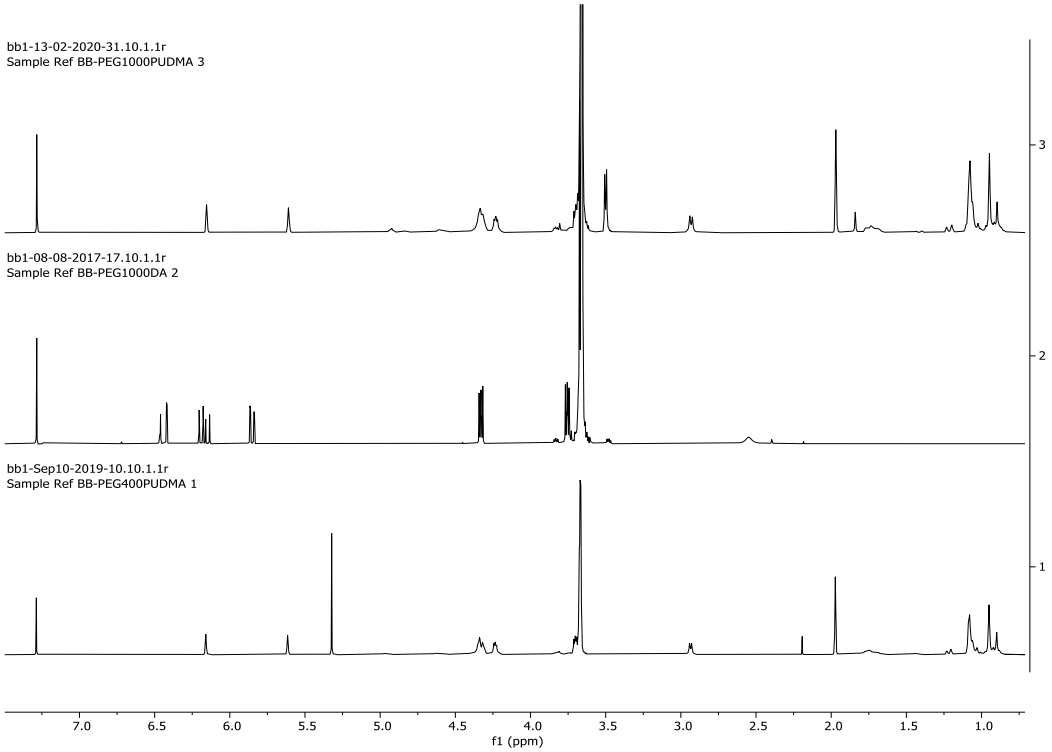

Figure 139 – ^{1}H NMR of synthesised compounds: bottom = PEG400PUDMA, middle = PEG1000DA, and top = PEG1000PUDMA

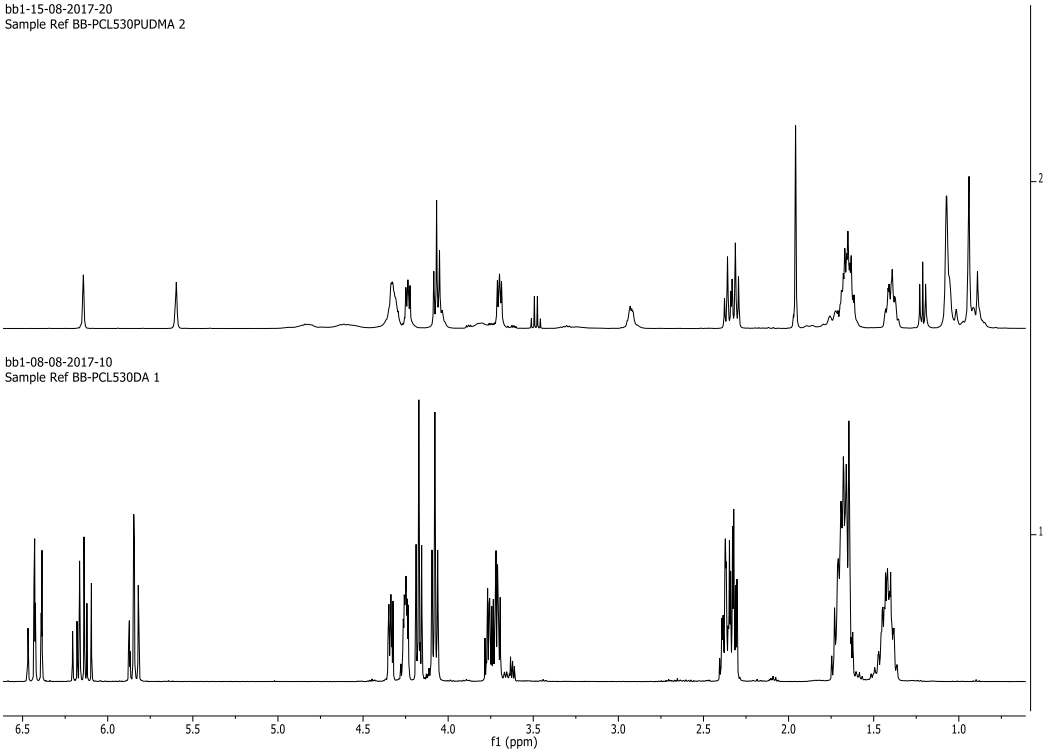

Figure 140 – ^{1}H NMR of synthesised compounds: bottom = PCL530DA and top = PCL530PUDMA

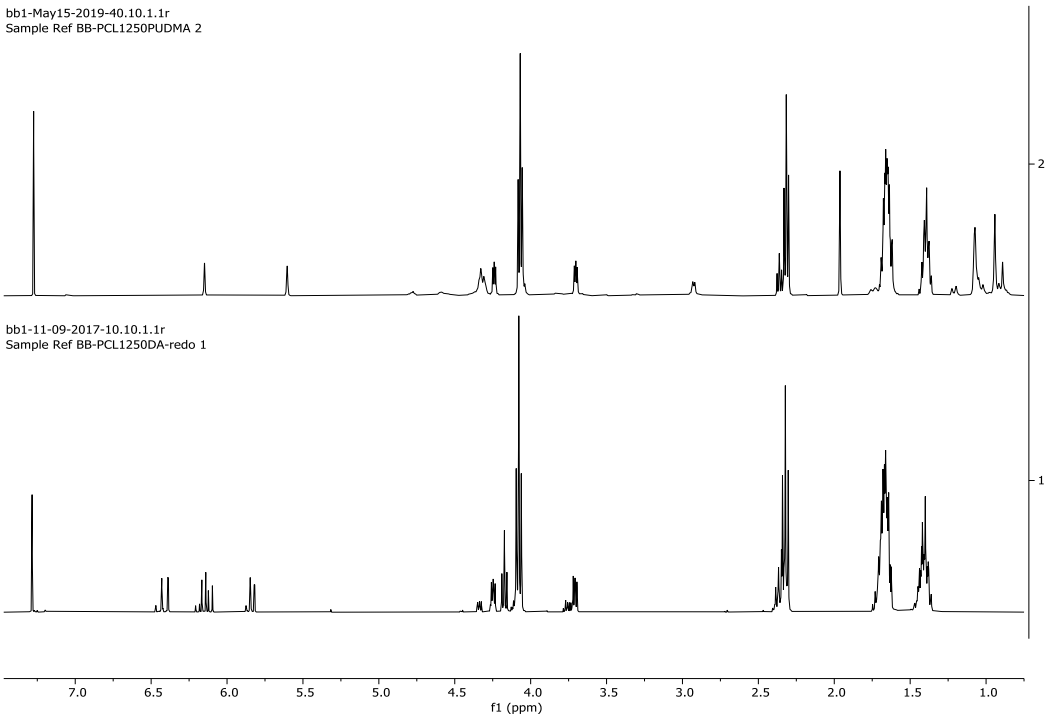

Figure 141 – ^{1}H NMR of synthesised compounds: bottom = PCL1250DA and top = PCL1250PUDMA

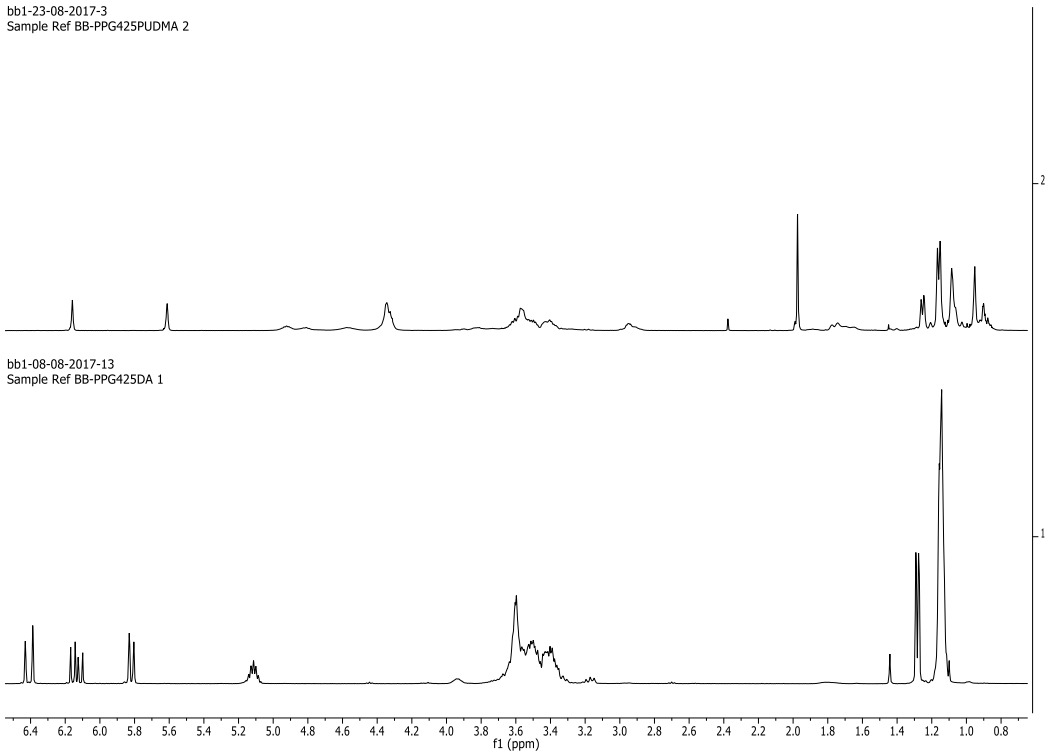

Figure 142 – ^{1}H NMR of synthesised compounds: bottom = PPG425DA and top = PPG425PUDMA

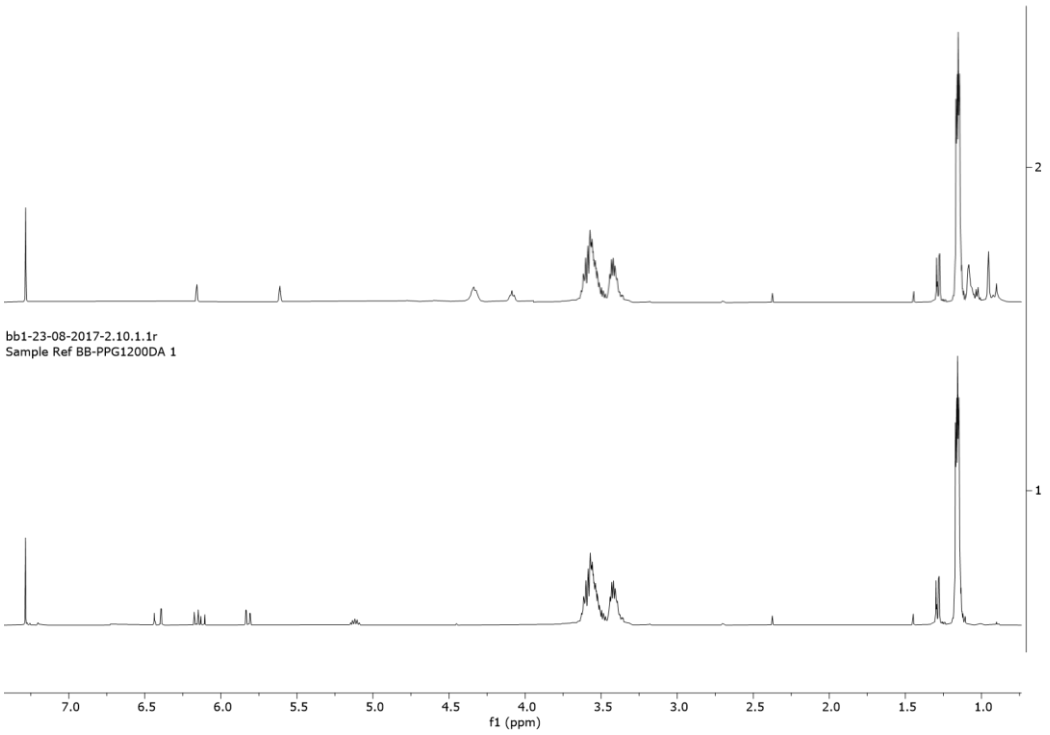

Figure 143 – ^{1}H NMR of synthesised compounds: bottom = PPG1200DA and top = PPG1200PUDMA

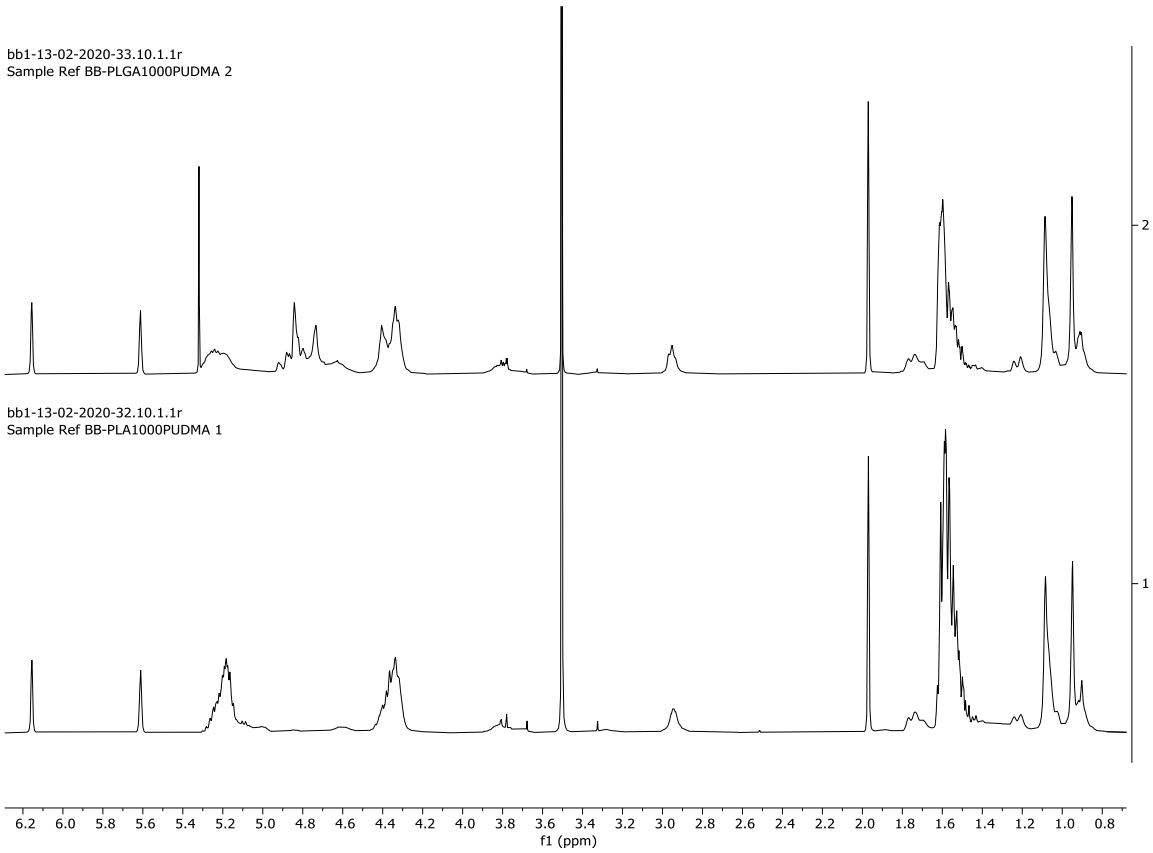

Figure 144 – ^{1}H NMR of synthesised compounds: bottom = PLA1000PUDMA and top = PLGA1000PUDMA